INVESTIGATING TRANSIENT PATTERNS OF HUMAN BRAIN ACTIVITY IN NORMAL AGEING

by

Lindsey Power

Submitted in partial fulfilment of the degree requirements
for the degree of Doctor of Philosophy

at

Dalhousie University
Halifax, Nova Scotia
June 2024

Dalhousie University is located in Mi'kma'ki, the
ancestral and unceded territory of the Mi'kmaq.
We are all Treaty people.

Table of Contents

List of Tables

List of Figures

Abstract

The global population is ageing rapidly, and with the increasing population age, comes an increasing need to understand the neurophysiological effects of ageing. Human brain activity consists of a complex combination of spontaneous transient bursts of neural activity with varying spatial and temporal characteristics. The characteristics of these transient bursts change during task performance and normal ageing in ways that can inform about the underlying neurophysiology. This thesis investigates the spatiotemporal characteristics and cortical sources of typical and atypical transient bursts in a large cohort of healthy participants and relates the findings to participant age. The thesis is comprised of three projects, each of which introduces and validates novel methods for investigating transient patterns of human brain activity in normal ageing.

Project 1 implements source localization techniques to detect the cortical sources of sensorimotor beta bursts in MEG data from a cohort of 561 healthy participants acquired by the Cambridge Centre for Ageing and Neuroscience (CamCAN). Age-related trends were then investigated by applying regression analysis between participant age and average source power within several cortical regions of interest. This analysis revealed that beta bursts localized primarily to the sensorimotor cortex under the sensor used for their detection. Region of interest analysis revealed that there were age-related changes in the beta burst localization pattern, including an expansion of source with age.

Project 2 applies a data-driven convolutional dictionary learning (CDL) approach to detect transient bursts in MEG data from 538 participants in the CamCAN dataset. CDL was used to extract repeating spatiotemporal motifs in each participant during a sensorimotor task. Motifs were then clustered across participants based on similarity, and relevant task-related clusters were analysed for age-related trends in their spatiotemporal characteristics. Seven task-related motifs resembling known transient burst types were identified through this analysis, including beta, mu, and alpha type bursts. All burst types showed positive trends in their activation levels with age that could be explained by increasing burst rate with age.

Project 3 investigated atypical transient patterns of slow cortical activity (i.e., paroxysmal slow wave events (PSWEs)) in resting state MEG recordings from 623 healthy participants in the CamCAN dataset. PSWEs were detected in approximately 20% of healthy participants in the dataset, and participants with PSWEs tended to be older and have lower cognitive performance than those without PSWEs. In addition, event features changed linearly with age and cognitive performance, resulting in longer and slower events in older adults, and more widespread events in those with low cognitive performance. These findings provide the first evidence of PSWEs in a subset of purportedly healthy adults.

Together, these projects validate new methods for exploring human brain signals, provide insights into the neural mechanisms of healthy ageing, and have the potential to inform future clinical applications.

List of Abbreviations Used

ACE-R	Addenbrooke's Cognitive Examination - Revised
AD	Alzheimer's Disease
AIC	Akaike information criterion
ANOVA	Analysis of variance
APOE	Apolipoprotein E
BAU	Brief amplitude undulation
BOSC	Better oscillation detection
BBB(d)	Blood-brain barrier (disruption)
CamCAN	Cambridge Centre for Ageing and Neuroscience
CDL	Convolutional dictionary learning
DICS	Dynamic imaging of coherent sources
DSPM	Dynamic statistical parametric mapping
ECD	Equivalent current dipole
ECG	Elecrtocardiogram
EEG	Electroencephalography
EOG	Electrooculogram
(f)MRI	(Functional) Magnetic resonance Imaging
HMM	Hidden Markov modelling
HNN	Human Neocortical Neurosolver
ICA	Independent component analysis
ISI	Inter-stimulus interval
LCMV	Linearly constrained minimum variance
LFP	Local field potential
MEG	Magnetoencephalography
MNE	Minimum norm estimation
MPF	Median power frequency
OPM	Optically pumped magnetometer
PAPTO	Periodic/aperiodic parameterization of transient oscillations
PD	Parkinson's Disease
PSWE	Paroxysmal slow wave event
ROC	Receiver operating characteristic
RMS(E)	Root mean squares (error)
SAM	Synthetic aperture magnetometry
sLORETA	Standardized low-resolution brain electromagnetic tomography
SQUID	Superconducting quantum interference device
TFR	Time-frequency representation
TGF-beta	Transforming growth factor - beta
TOT	Tip-of-tongue task
tSSS	Temporal signal space separation
VSTM	Visual short-term memory task

Acknowledgements

I am extremely fortunate to have been surrounded by so many incredibly supportive friends, family members, mentors, and colleagues throughout my PhD journey.

I would first like to thank my supervisor, Dr. Tim Bardouille for his unwavering support and mentorship throughout all aspects of my scientific career so far. When I began working with Tim as an undergraduate volunteer seven years ago, I never imagined that I would end up coming out of the lab with a PhD. But Tim's passion for research and dedication to mentorship inspired me to continue down this path and to grow my own passion for scientific research. Tim went above and beyond the requirements of a supervisor and has provided me with every opportunity to help me grow as a researcher. I will be forever grateful for his mentorship.

I would also like to thank my committee members, Dr. Alon Friedman and Dr. Kim Brewer for their insightful feedback and guidance throughout my PhD studies. My thesis has come a long way since my initial transfer proposal due in large part to their input.

Thank you to all those who contributed to the work presented in this thesis. To our collaborators in Paris, Dr. Alexandre Gramfort, Dr. Thomas Moreau, and Dr. Cédric Allain, for their machine learning expertise and software contributions, and to all of the current and past Biosignal lab members who have contributed ideas, feedback, and unique expertise to this work.

I would also like to acknowledge the research team at the Cambridge Centre for Ageing and Neuroscience (CamCAN) for their efforts in collecting and maintaining the dataset used in this work. Without this amazing resource, much of this work would not have been possible.

This work would also not have been possible without financial support from the National Sciences and Engineering Research Council of Canada, Research Nova Scotia, the Killam Trust, and Dalhousie University.

Finally, I want to thank all of my friends and family for their support and encouragement every step of the way. To my friends and peers in the BME community, thank you for commiserating, motivating, and being the best support network I could have asked for. To my parents, sisters, extended family, and friends outside of BME, thank you for always cheering me on, listening to me vent, and trying to understand my science ramblings. And finally, to my fiancé, Nathan, for being my number one supporter, confidant, and proof-reader, and for being there for me throughout all of the craziness that comes with doing a PhD. I appreciate each and every one of you and could not have done this on my own.

Chapter 1

Introduction

1.1 Ageing

1.1.1 The Ageing Population

According to recent projections by the United Nations, it is expected that by 2050, 17% of the global population and up to 25% of the North American population will be over the age of 65. In Canada, as of 2021, there were 7 million people (19% of the population) over the age of 65, and 861,000 (2.3% of the population) over the age of 85 (Statistics Canada, 2021). Over the next 25 years, these numbers are expected to climb to more than 12 million (24.9% of the projected population) over 65 and 2.7 million (5.6% of the projected population) over 85, respectively (Statistics Canada, 2021). With the increasing age of the population, comes an increased prevalence of age-related illness and disease, and an increasing need to study the effects of ageing on the human body and brain.

1.1.2 The Ageing Brain

Ageing has particularly pronounced effects on the anatomy and function of the brain. Ageing is associated with anatomical changes including reductions in brain volume (Taki et al., 2011; Fjell & Walhovd, 2010; Hedman et al., 2012; Murman, 2015), reductions in synaptic connections (Esiri, 2007; Murman, 2015), demyelination of neurons (Fjell & Walhovd, 2010; Murman, 2015), and neurochemical alterations (Cleeland et al., 2019). In addition, ageing is associated with reductions in cognitive function, particularly in the domains of memory, processing speed, and executive function (Fjell & Walhovd, 2010; Murman, 2015). Along with these normal age-related changes in brain structure and function, ageing is also considered one of the most prominent risk factors for many neuropathologies including stroke, neurodegenerative disease, dementia, and movement disorders, which can result in further functional and anatomical deficits.

Reductions in brain volume across the lifespan have been consistently observed in longitudinal magnetic resonance (MR) studies (Hedman et al., 2012; Murman, 2015).

These brain volume changes manifest as cortical thinning and enlargement of the ventricles, which are apparent in MR images as well as post-mortem investigations. Gray matter (i.e., darker brain tissue consisting primarily of neuronal cell bodies) has been shown to decrease in volume relatively consistently throughout the lifespan, beginning shortly after childhood (Taki et al., 2011; Fjell & Walhovd, 2010; Hedman et al., 2012). White matter (i.e., lighter brain tissue made up of bundles of axons) on the other hand, continues to increase in volume until middle age before beginning to decrease later in life (Taki et al., 2011; Fjell & Walhovd, 2010; Hedman et al., 2012). The spatial pattern of volume loss is highly heterogeneous, with particularly large changes observed in the frontal, prefrontal, and temporal cortices, as well as the putamen, thalamus, and nucleus accumbens (Fjell & Walhovd, 2010). However, other regions, such as the brainstem, are comparably well-preserved throughout the lifespan (Fjell & Walhovd, 2010). The observed reductions in brain volume are thought to be the result of alterations in neuronal structure such as cell shrinkage, loss of dendritic and axonal arborizations, and reductions in synaptic connections (Morrison & Hof, 1997; Esiri, 2007; Murman, 2015). Contrary to what might be expected, the volume reductions are not likely caused by neuronal cell death, as this is relatively restricted in healthy ageing (< 10% of neurons lost between age 20-90) (Morrison & Hof, 1997; Fjell & Walhovd, 2010; Murman, 2015). In addition to changes in brain volume, healthy ageing is thought to be associated with network-level changes including a shift from focal to widespread patterns of brain activation during task performance (Cabeza et al., 2002), and changes in the complexity of local and long-range network connections (McIntosh et al., 2014). These physiological changes may reflect compensatory mechanisms that emerge as a result of the age-related changes in the cellular architecture.

The neuroanatomical changes observed with age are likely the result of a combination of underlying chemical and molecular factors. Ageing is associated with increased demands of neural cells for oxidative metabolism which can lead to damage to proteins, nucleic acids, lipids, DNA, and mitochondria (Esiri, 2007). In addition, ageing is associated with elevated levels of intracellular calcium which can have damaging effects including apoptosis and selective death of dendrites (Esiri, 2007). Additional factors such as neurochemical changes (Cleeland et al., 2019), increases in iron

concentration (Esiri, 2007), reductions in glucoregulation, and increased inflammation (Cleeland et al., 2019) can further contribute to cellular damage. These effects may be modulated by genetic factors. Certain genes, such as those involved in synaptic function and plasticity, vesicular transport, mitochondrial function and calcium homeostasis in the frontal cortex are reduced in expression with age (Esiri, 2007), while others, such as those that respond to oxidative stress, increase in expression with age (Esiri, 2007).

Perhaps unsurprisingly given the extensive neuroanatomical changes, ageing is also associated with functional changes in cognitive performance. However, not all cognitive processes are affected to the same extent. In most cases, fluid intelligence (e.g., real-time cognitive processing, problem solving, decision making, etc.), attention, perception, and short-term memory decline with age, while crystallized intelligence (e.g., general knowledge, autobiographical history, vocabulary), speech and language function, and procedural memory tend to remain intact (Murman, 2015). The functions that show significant decline with age tend to align with the functionally specific brain regions that show the most pronounced age-related anatomical changes. For example, the executive functions that decline with age are heavily dependent on the fronto-striatal circuits in the frontal and pre-frontal cortices, which show some of the most drastic reductions in volume with age (Fjell & Walhovd, 2010). Similarly, older adults who show more extensive cortical thinning, tend to have lower cognitive scores than older adults who maintain a thicker cortex (Fjell et al., 2006).

1.1.3 Factors Affecting Variability in Brain Age

Ageing is a highly heterogeneous process, and the extent to which an individual exhibits anatomical and functional age-related changes is dependent on a variety of genetic and environmental variables (Raz & Rodrigue, 2006). While the genetic contributions are not yet fully understood, there are several candidate genes that are thought to have potential roles in the ageing process. The apolipoprotein E (APOE) gene is involved in repair, growth, and maintenance of myelin, and possibly plays a role in plasticity and amyloid clearance (Deary et al., 2004; Fjell & Walhovd, 2010). There are 3 major alleles of the APOE gene: ε2, ε3, and ε4. While the ε3 allele is the most common, the ε4 allele is a major genetic risk factor for Alzheimer's disease (AD) (Fjell & Walhovd, 2010) and lower cognitive performance that becomes more pronounced with age (Esiri,

2007). The ε2 allele on the other hand, is over-expressed in centenarians, suggesting that it may play a role in healthy brain ageing (Esiri, 2007). Genetic variations in the brain-derived neurotrophic factor (BDNF) gene may also contribute to variability in ageing. Neurotrophins are a class of proteins involved in brain plasticity, neuronal survival, axonal growth, synaptogenesis, and neutrotransmission, and BDNF gene variations have been linked to differences in age-related reductions of pre-frontal cortical and amygdala volume (Fjell & Walhovd, 2010). Various proinflammatory genes may also be implicated in ageing due to their role in apoptotic and neurodegenerative processes (Fjell & Walhovd, 2010). Finally, the prion protein gene PRNP may play a role in protecting neurons from the effects of cellular stress (Esiri, 2007), which is thought to be one of the leading mechanisms driving age-related cellular changes. Individuals who were homozygous for the methionine allele of the gene had better cognitive performance in old age than those who were heterozygous, suggesting a relationship between the mechanistic role of PRNP and resulting cognitive effects (Kachiwala et al., 2005).

Along with genetic factors, lifestyle factors including diet, physical activity level, extended years of education, and cognitive stimulation can all contribute to variability in the effects of ageing. Diet in particular can have a pronounced effect on the ageing brain. A healthy diet, including the intake of fatty acids, B-vitamins, and folate can have a protective effect for cognitive abilities, while excess calorie intake can result in elevated cholesterol and blood pressure which increase the risk for the development of cerebrovascular disease or dementia with age (Esiri, 2007; Murman, 2015). Exposure to certain pesticides or herbicides through food may also increase the risk of brain disease with age (Esiri, 2007). Other environmental factors such as incidence of head trauma, substance abuse, or excessive stress can accelerate the cognitive effects of ageing (Murman, 2015), and incidence of other diseases such as cardiovascular disease or diabetes can also contribute to increased risk for advanced or pathological ageing (Murman, 2015). Managing lifestyle factors contributing to unhealthy brain ageing by maintaining a healthy diet, exercising regularly, and managing stress, can increase signal pathways involved in plasticity and decrease cognitive decline and neural atrophy with age (Murman, 2015).

Finally, the study of anatomical and functional changes with age is complicated by the blurry distinction between healthy ageing processes and the emergence of age-related neuropathology. For example, neuron populations that are particularly sensitive to deterioration with normal ageing, such as cortical pyramidal cells and pigmented dopaminergic neurons, also show degeneration with the progression of Alzheimer's disease and Parkinson's disease, respectively (Esiri, 2007). Similarly, the neurometabolite changes that occur with normal ageing closely resemble what is reported in AD (Cleeland et al., 2019), and the memory loss and cortical thinning in the temporal regions that is observed in healthy ageing, is also considered to be a hallmark of AD (Fjell & Walhovd, 2010). Because of theses similarities, the precise distinction between healthy and unhealthy ageing is unclear and heavily debated in the literature. As such, when studying the ageing brain, we must consider these pathologies to be yet another factor that affects the heterogeneity of the ageing process.

Evidently, there are a wide variety of mechanisms underlying the non-uniform neuroanatomical and cognitive changes observed with age. Cardiovascular, hormonal, cellular, molecular, and biochemical factors all contribute to changes in individual brains over the lifespan as well as differences between individuals' brains. Before we can begin to understand the complex interactions between these various mechanisms in human ageing, we must first gain insight into the neurophysiological mechanisms of ageing. In particular, how does the behaviour of neurons and neuronal networks change across the lifespan and how does this relate to the hallmark functional changes observed with age?

1.2 Cortical Rhythms and Transient Events

1.2.1 Cellular Basis of Cortical Rhythms

Neurons in the brain communicate primarily through chemical synapses, where pre-synaptic neurons release chemical neurotransmitters that activate receptors on the dendrites of post-synaptic neurons. This post-synaptic receptor activation results in alterations to the neuronal membrane permeability that allow either the influx or efflux of ions across the membrane. At rest, the intracellular space is characterised by a high concentration of positively charged potassium ions and the extracellular space is characterized by a high concentration of positively charged sodium ions and negatively charged chloride ions, resulting in strong ion concentration gradients. Therefore, when

alterations to the post-synaptic neuron cause sodium channels to open, current flows into the cell resulting in an excitatory post-synaptic potential, and when potassium or chloride channels open, current flows out of the cell resulting in an inhibitory post-synaptic potential. When post-synaptic potentials occur synchronously across a sufficiently large population of neurons, it results in a measurable change in voltage that can be recorded locally in the cortex using local field potential (LFP) recordings or non-invasively from outside the head using electroencephalography (EEG). Similarly, the synchronous current flow into or out of a large population of similarly oriented neurons generates a magnetic field that can be recorded externally with magnetoencephalography (MEG). Rhythmic oscillations (i.e., spontaneous rhythmic fluctuations of electrical activity) in the cortex arise from frequency-specific synchronous neural activity across many neurons (Lopes Da Silva, 1991), with the size of the synchronous neuronal population dictating the power of the resulting oscillation (Murthy & Fetz, 1996).

The cellular mechanisms underlying these cortical rhythms have been extensively studied since the first characterisation of alpha waves by Hans Berger in 1929 (Berger, 1929). Researchers in the field have since employed various experimental techniques including EEG, MEG, and LFP recordings to understand large-scale oscillations, single-unit recordings to examine spike-timing, *in vivo* and *in vitro* imaging to understand circuit mechanisms, optogenetic manipulation to selectively investigate nerve cell activation, and computational modelling to explore dynamic network behaviour (Wang, 2010). From this body of literature, it is evident that the emergence of synchronous rhythmic activity is dependent on a complex system of cellular and network level mechanisms. At the cellular level, rhythmic activity of a particular frequency arises based on the intrinsic oscillatory properties of neurons (Wang, 2010; Buskila et al., 2019), modulated by ion concentrations and currents (Kadala et al., 2015), and modulatory inputs from astrocytes (Bellot-Saez et al., 2017; Buskila et al., 2019). At the network level, the synchronization of a sufficiently large population of neurons is dependent on electrical and chemical communication between neurons (Wang, 2010; Timofeev et al., 2012) and recurrent thalamocortical connections that facilitate the organization of local and long-range neural networks (Steriade, 2004). Finally, different types of rhythmic activity can influence one another through cross-frequency coupling mechanisms (Buzsáki & Wang, 2012; Buskila

et al., 2019). Figure 1.1 provides a summary of some of the key mechanisms involved in the generation of cortical rhythms.

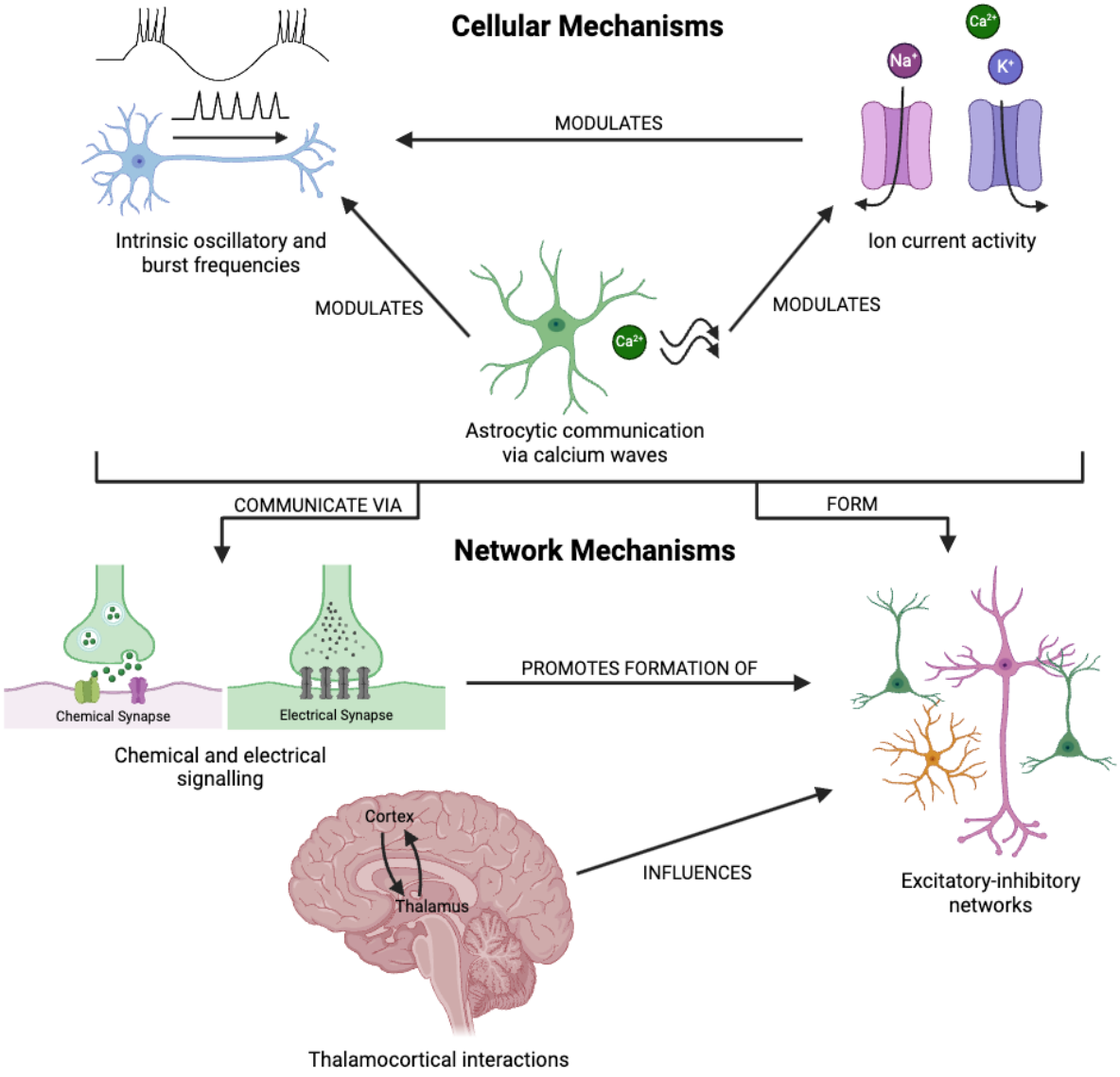

Figure 1.1 Cellular and network mechanisms involved in the generation of cortical rhythms. Created with BioRender.com.

1.2.2 Functional Role of Cortical Rhythms

Power spectral density analyses of cortical oscillations have revealed the presence of a set of functionally relevant frequency bands ranging from <0.1 Hz to >1000 Hz (Penttonen & Buzsáki, 2003). In the healthy brain, there are at least 10 different types

of cortical oscillations, each associated with a particular frequency band and contributing to different cognitive and perceptual functions (Buskila et al., 2019).

During sleep and periods of inattentiveness or drowsiness, cortical oscillations are dominated by low-frequency rhythms including delta waves (1-4 Hz) which predominantly occur during deep sleep (Steriade & Timofeev, 2003; Timofeev et al., 2012), and theta waves (4-8 Hz) which occur most often during drowsiness or early sleep (Hughes & Crunelli, 2005). Both delta and theta waves have also been implicated in the process of sleep consolidation of memory (Hasselmo, 2005; Steriade & Timofeev, 2003; Timofeev et al., 2012). The transition to wakefulness is associated with suppression of low frequency rhythms and an increase in higher frequency rhythms (McCormick et al., 2015). During wakeful resting, alpha (8-15 Hz) is the dominant cortical rhythm, occurring primarily in the posterior (e.g., occipital) cortex (Hughes & Crunelli, 2005; Lozano-Soldevilla, 2018). Posterior alpha is a reliable cortical rhythm found in almost all healthy individuals and is thought to play a functional inhibitory role during wakefulness, inhibiting brain regions or cognitive processes when they are not needed (Foxe & Snyder, 2011; Jensen & Mazaheri, 2010; Klimesch et al., 2007). Rolandic mu, which spans the same frequency range as posterior alpha, is also present during quiet wakefulness but differs from alpha in that it occurs over the central cortical regions and plays a specialized role in the inhibition of sensorimotor processes (Pfurtscheller et al., 1997). The beta rhythm (15-30 Hz) is similarly involved in inhibitory motor control during wakefulness, but it has also been suggested to play a more general role in sensorimotor integration and top-down control (Wang, 2010). Finally, active and attentive states of wakefulness are characterised by gamma frequency oscillations (>30 Hz) that are highly variable in frequency and occur throughout the cerebral cortex as well as subcortical brain regions (Buzsáki & Wang, 2012; McCormick et al., 2015). Gamma activity is involved in exploratory behaviour and perceptual tasks (Bragin et al., 1995; Gray et al., 1989) and is thought to play a role in the integration of sensory information (Gray, 1994).

1.2.3 Cortical Rhythms as Transient Events

While some cortical rhythms may reflect a sustained oscillation at a particular frequency that is modulated only by a change in task or brain state, many cortical rhythms are not sustained. Instead, these cortical rhythms arise as brief, high-power

bursts of rhythmic activity termed “transient events” (Jones, 2016). The first realisation of transient events in electrophysiological data dates back to the identification of sleep spindles (spontaneous 12-14 Hz transient activity) in human EEG data in the 1930s (Berger, 1929; Loomis et al., 1935). Since then, transient events of various frequencies have been identified in electrophysiological recordings from humans and animal models, and have been linked to physiological and cognitive functions including attention, working memory, arousal and relaxation, and voluntary movement (Errington et al., 2020; Feingold et al., 2015; He et al., 2020; Hebert and Lehmann, 1977; Lakatos et al., 2004; Little et al., 2019; Lundqvist et al., 2016; Shin et al., 2017; Wessel, 2020).

Historically, electrophysiological data has been analysed by averaging across many repetitions of a task or aggregating over time, resulting in an easily interpretable signal, with high signal to noise ratio. This method, however, is a simplification that results in a loss of important information about the transient dynamics in the raw signal. As shown in Figure 1.2, traditional average power analysis tends to result in the appearance of a sustained signal of a particular frequency that changes in power in response to a task. However, when we instead consider power in the individual trials, it is evident that the underlying neural activity is not sustained, but rather transient in nature. Identifying these transient events and their characteristics (e.g., peak frequency, peak power, duration, rate of occurrence, etc.) in the unaveraged signal allows us to gain insight into the potential neural mechanisms underlying electrophysiological signals. For example, higher power events are suggestive of a larger population of synchronous neurons (Murthy & Fetz, 1996), while a higher rate of bursting suggests that the neuronal network is becoming active more frequently. In the average, these features would be indistinguishable, and thus the study of transient event characteristics provides important mechanistic insight that has traditionally been overlooked.

This thesis explores two types of transient events, sensorimotor beta bursts and paroxysmal slow wave events, and their role in the process of healthy ageing. The following sections provide an overview of our current understanding of each of these types of transient events.

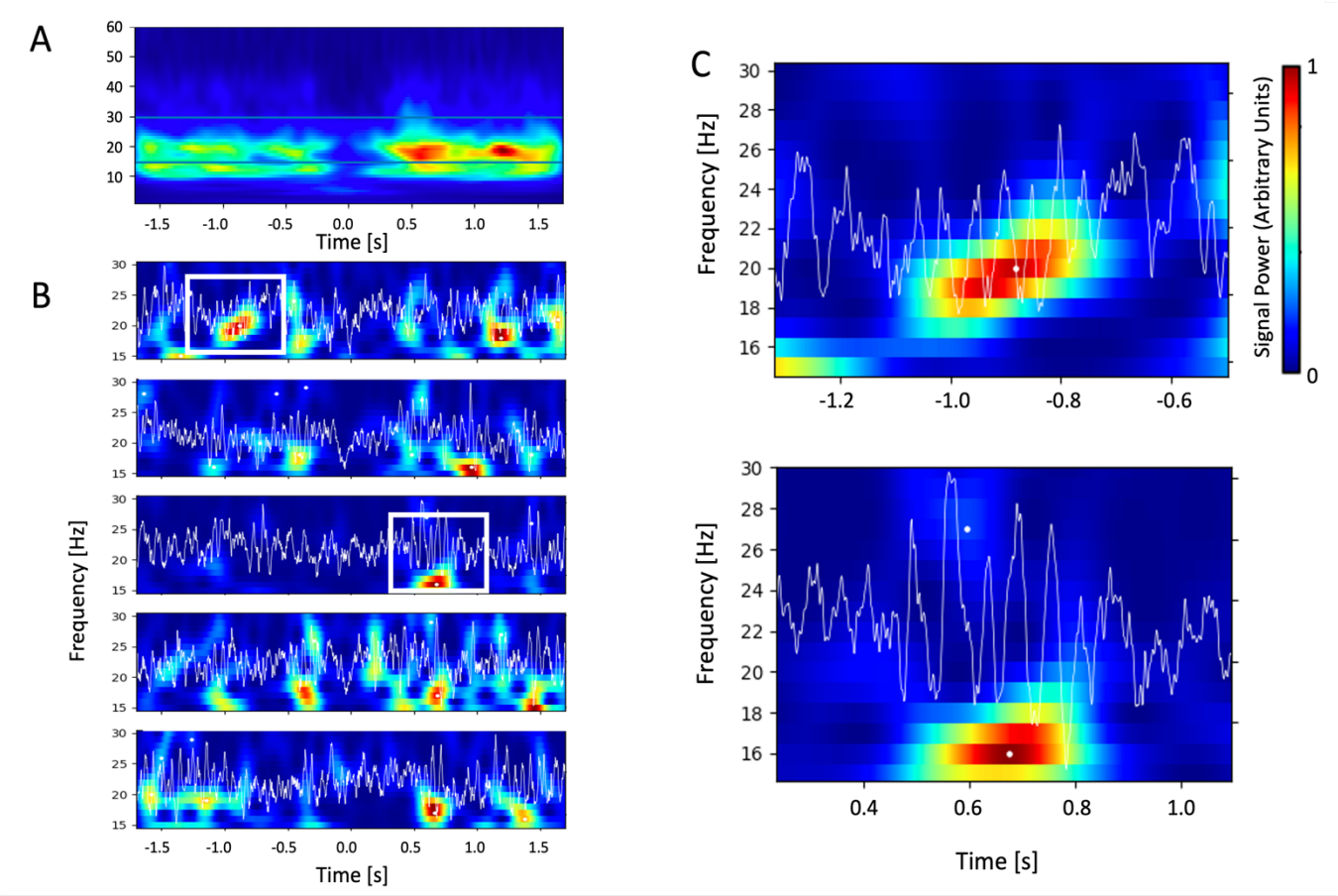

Figure 1.2 Time-frequency representations showing examples of transient events at a single MEG sensor (MEG 0221). Data is shown for a representative subject (CC110056) from the CamCAN dataset. (A) The average time-frequency representation across 63 trials of a unilateral button press (sensorimotor) task. In the average, the signal appears sustained prior to and following the button press event at time=0. (B) The time-frequency representations (colour) and overlaid time courses (white line) for 5 sample trials from the same button press task. The individual trials show sporadic, high-power (red) transient bursts of activity rather than a sustained signal as is seen in the average. (C) The time-frequency representations and overlaid time courses for 2 transient bursts identified in the individual trials (indicated by the white boxes in B). Variability in the duration, power and frequency span of the bursts can be noted.

1.3 Sensorimotor Beta Bursts

1.3.1 Sensorimotor Beta Bursts in Health and Disease

The resting brain is characterised by high-power rhythmic electrophysiological signals (Pfurtscheller & Lopes Da Silva, 1999). Voluntary movement elicits a distinct pattern of frequency and region-specific changes in cortical rhythms (Hari & Salmelin,

1997) including changes in power of mu (8-12 Hz), beta (15-30 Hz) and gamma (30-90 Hz) oscillations in the sensorimotor cortices. Movement onset is accompanied by a bilateral reduction in sensorimotor beta activity (beta suppression) that persists throughout the duration of sustained movement. Approximately 200ms following movement offset, strong increases in beta band activity (beta rebound) occur that surpass pre-movement levels before ultimately returning to baseline approximately 1-2 seconds post-movement (Bardouille & Bailey, 2019; Jurkiewicz et al., 2006; Neuper et al., 2006; Pfurtscheller & Lopes Da Silva, 1999).

Underlying the movement-related changes in average beta power are short (150-200 ms) bursts of 15-30 Hz rhythmic neural activity termed "sensorimotor beta bursts" (Brady et al., 2020; Shin et al., 2017). In 2015, Feingold et al. first demonstrated that brief bursts of beta oscillations in the motor and pre-motor cortices could account for virtually all cortical beta-band activity in monkeys. These findings were later replicated in a multi-modal, multi-species study by Shin et al. (2017). Further, the work by Shin and colleagues also demonstrated that beta burst timing was predictive of behaviour such that beta bursts occurring close in time to the onset of a barely perceptible stimulus inhibited the participant's ability to detect the stimulus (Shin et al., 2017). Recently, Brady et al. (2020) demonstrated that task-related reductions in the inter-trial average beta-band power (i.e., beta suppression) in humans could be explained primarily by a reduction in the rate of occurrence of beta bursts with movement onset. Transient beta and mu bursts have since been shown to play a functional role in movement initiation and cancellation (Errington et al., 2020; Wessel, 2020), and response accuracy and reaction time (He et al., 2020; Little et al., 2019; Wessel, 2020).

Sensorimotor beta bursts have also been shown to change in an age-dependent manner. Work by Bardouille & Bailey (2019) demonstrated that, in a large dataset of healthy adults, there were marked changes in average movement-related beta power with age. In particular, there was a significant increase in the magnitude of beta suppression with age, and a significant decrease in the magnitude of beta rebound with age. In other words, on average, older adults exhibited a larger drop in beta power with the onset of a movement and a smaller rebound in beta power following movement offset (Bardouille & Bailey, 2019). Subsequent work by Brady et al. (2020) using the same dataset, showed

that the reported age-related changes in average spectral power in the beta band (Bardouille & Bailey, 2019) could be explained by specific changes in the underlying power, frequency, and rate of occurrence of transient beta bursts. As shown in Figure 1.3, significant age-related changes in burst rate, peak power, peak frequency, and frequency span were identified in resting state data and across multiple phases of a motor task. Of these effects, burst rate was determined to be the predominant factor influencing modulations in average beta power. The age-related increase in burst rate prior to movement could explain age-related increases in the magnitude of beta suppression, while the age-related decrease in burst rate in the post-movement interval could explain the decrease in beta rebound magnitude (Bardouille & Bailey, 2019; Brady et al., 2020).

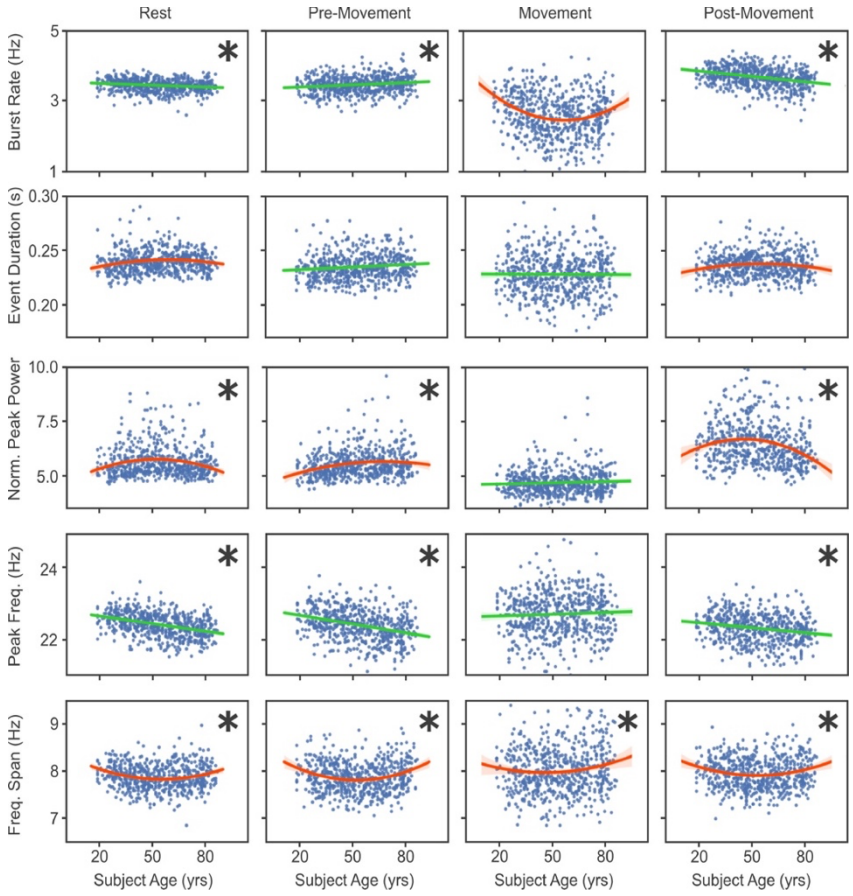

Figure 1.3 Relationships between age and beta burst characteristics detected during resting state, pre-movement, movement, and post-movement intervals. Each relationship is fit with either a linear (green) or quadratic (red) model, depending on which model was deemed the best fit for the data with a chi-square comparison. The shaded region around the best fit line indicates the 95% confidence interval. Asterisks indicate significant effects. Figure reproduced from Brady et al., 2020.

In addition to healthy ageing, sensorimotor beta bursts are also implicated in movement disorders including Parkinson's Disease (PD). Beta oscillations are thought to be generated in a reciprocal basal ganglia-cortical circuit (Levy et al., 2002; Kühn et al., 2004; Lipski et al., 2017; Shimamoto et al., 2013). The reduced dopaminergic activity associated with PD results in disruptions to this circuit that lead to hyper-synchronous beta oscillations in the basal ganglia (Jenkinson & Brown, 2011) as well as a reduction in resting beta power in the motor cortex (Heinrichs-Graham et al., 2014). Recent work by Vinding et al. (2020) demonstrated that the characteristic reduction in motor cortical beta could be explained by a reduction in sensorimotor beta burst rate in unmedicated PD patients. This finding suggests that sensorimotor beta bursts have important implications in age-related neuropathology in addition to healthy ageing.

1.3.2 Cellular Basis of Beta Bursts

Over the years, a considerable amount of work has been conducted to investigate the anatomical underpinnings of beta rhythms, but there is still some debate as to the specific mechanisms at play and how the proposed mechanisms translate to individual transient beta bursts. Research into the cortical sources of beta rhythms suggests that sensorimotor beta rhythms are generated in a medium range cortical network involving the motor cortex, supplementary motor areas, and contralateral supramarginal gyrus (Brovelli et al., 2002) with potential driving inputs from the somatosensory cortex (Brovelli et al., 2004). Further, there is also evidence to suggest that a number of sub-cortical structures, including the subthalamic nucleus, globus pallidus, and striatum are involved in beta rhythm generation (Mirzaei et al., 2017; West et al., 2018). In particular, recordings from the subthalamic nucleus have revealed movement-related beta frequency oscillations that have high coherence with cortical beta oscillations suggesting a common network (Blenkinsop et al., 2017; Kramer et al., 2008; Lipski et al., 2017; Marsden et al., 2001; Roopun et al., 2006; Shimamoto et al., 2013; Yamawaki et al., 2008). In addition, research into the role of neurotransmitter activity in beta rhythm generation has revealed that gamma aminobutyric acid (GABA) (Gaetz et al., 2011; Muthukumaraswamy et al., 2013), and dopamine (Levy et al., 2002; McCarthy et al., 2011) concentrations have modulatory effects on beta power. When taken together, this research suggests the

existence of a complex GABA- and dopamine-dependent corticothalamic network underlying beta rhythm generation.

With these various neural mechanisms in mind, researchers have begun to use computational modelling to construct holistic models of the underlying circuitry contributing to the sensorimotor beta response. One such model proposed by Sherman et al. (2016) used simulated trains of action potentials to imitate proximal and distal drives to a local network to re-create the stereotypical temporal waveform shape of human beta bursts. The authors found that a weak, 100 ms proximal drive from the lemniscal thalamus (i.e., a feedforward drive) combined with a stronger, 50 ms distal drive from the non-lemniscal thalamus or higher-order cortex (i.e., a feedback drive) resulted in a reliable reproduction of the transient beta burst waveform (Sherman et al., 2016). The proposed mechanism was subsequently validated and shown to be in concordance with human neuromagnetic data as well as primate LFP data (Sherman et al., 2016, Neymotin et al., 2020). Despite the recent advances in our understanding of the generative mechanism of transient beta bursts, the changes in these mechanisms that occur with ageing and disease are not yet understood.

1.4 Paroxysmal Slow Wave Events

1.4.1 PSWEs in Health and Disease

Electrocortical slowing is a commonly observed phenomenon in neurological diseases including epilepsy (Milikovsky et al., 2017, 2019; Zelig et al., 2022) and Alzheimer's disease (AD) (Benwell et al., 2020; Brenner et al., 1986; Hier et al., 1991; Jeong, 2004; Meghdadi et al., 2021; Milikovsky et al., 2019; Musaeus et al., 2018; Özbek et al., 2021; Penttilä et al., 1985; Weiner and Schuster, 1956; Wiesman et al., 2022). Patients with epilepsy tend to show higher amplitude delta (0.5-4 Hz) and theta (4-8 Hz) oscillations and lower amplitude beta (15-30 Hz) and gamma (30-100 Hz) oscillations compared to healthy controls (Milikovsky et al., 2017; Zelig et al., 2022). Similarly, patients with AD have increased spectral power and coherence at lower frequencies (e.g., delta and theta) and decreased spectral power at higher frequencies (e.g., alpha and beta) (Benwell et al., 2020; Meghdadi et al., 2021; Özbek et al., 2021), suggesting a shift towards slower oscillatory activity in the disease state.

Recently, Milikovsky and colleagues (2019) observed that this pathological slowing is associated with transient (5-10 second) patterns of slow-wave activity, rather than a persistent slowing of the sustained signal. The authors termed these transient shifts in network activity "paroxysmal slow-wave events" (PSWEs) and showed that the duration and number of PSWEs were underlying the slowing effects observed in the average spectral power analysis (Milikovsky et al., 2019). They also detected PSWEs at a higher rate in both epilepsy and AD populations compared to healthy controls and replicated these findings in rodent models of epilepsy (Senatorov et al., 2019; Milikovsky et al., 2019; Zelig et al., 2022). In addition, PSWEs were found to be related to cognitive impairment and blood-brain barrier disruption (BBBd) in animals and patient populations (Milikovsky et al., 2019). A negative relationship was observed between cognitive performance and PSWE occurrence in patients with AD suggesting that PSWEs could be a marker for cognitive impairment in patient populations. This observation supported previous findings that low frequency (e.g., delta and theta) oscillations are related to cognitive impairment in older adult populations (Adler et al., 1999; Benwell et al., 2020). In addition, it was found that patients with a high rate of PSWEs were more likely to have a higher percentage of blood-brain barrier disruption (BBBd) than patients with fewer PSWEs and that PSWEs and BBBd tended to be spatially co-localized in patients with epilepsy (Milikovsky et al., 2019).

Synthesizing the above work provides evidence for the existence and disease-dependent modulation of PSWEs in humans and animal models, and a fundamental relationship between PSWEs, cognitive impairment, and BBBd. However, there has been little research into the presence of PSWEs in healthy populations. It is known that non-pathological (i.e., healthy) ageing is associated with declines in cognitive functions including memory, executive function, processing speed and reasoning that occur from middle age onwards (Deary et al., 2009). In addition, alterations to blood-brain barrier integrity occur with age as a result of physiological factors including the accumulation of iron in astrocytes and decreased activity of transporters involved in the extrusion of toxins from the brain (Popescu et al., 2009). The relationships between ageing, cognitive performance, and BBBd therefore suggest that PSWEs may be related to normal ageing and associated cognitive decline in humans. Electrophysiological studies of non-

pathological ageing, however, have provided mixed results. In animal models of ageing, older mice were found to have increased low-frequency activity in EEG (Senatorov et al., 2019) and a higher number of PSWEs compared to younger mice (Milikovsky et al., 2019; Senatorov et al., 2019). Human electrophysiological studies, however, have either found no significant changes in low-frequency oscillatory activity with age (Caplan et al., 2015; Cesnaite et al., 2023), or have found reduced low-frequency activity in healthy older adults (Emek-Savas et al., 2016; Leirer et al., 2011; Meghdadi et al., 2021; Vlahou et al., 2015). It is clear from these contradictory findings that further investigations into the role of PSWEs in healthy ageing are required.

1.4.2 Cellular Basis of PSWEs

The phenomenon of cortical slowing that is often reported in patients with AD and cognitively impaired older adults tends to be quite generalized, affecting widespread brain regions (Benwell et al., 2020; Gómez et al., 2013). This generalized slowing could be the result of subtle shifts in the mechanisms underlying generalized alpha rhythms, which are the dominant resting frequency in healthy adults. Alpha (8-15 Hz) and theta (4-8 Hz) oscillations have been found to be generated by a similar thalamic mechanism, whereby strong depolarization in thalamocortical cells causes strong activation of glutamate receptors leading to alpha waves, while weaker depolarization and reduced glutamate receptor activation in the same thalamocortical cells leads to theta waves (Hughes & Crunelli, 2005). In a healthy brain, reduced arousal is associated with a decrease in thalamic glutamate receptor activity resulting in a shift from alpha to theta waves (Hughes & Crunelli, 2005). In a pathological brain, dysregulation of this thalamocortical circuit could result in atypical periods of slow wave activity in the theta frequency range. It has been demonstrated that sufficient glutamate and acetylcholine concentrations are required to generate reliable 10-12 Hz oscillations in the thalamus, and that reduced activity of these neurotransmitters leads to reductions in the oscillatory frequency (Hughes & Crunelli, 2005). In patients with AD, reductions in acetylcholine activity have been reported (Soininen et al., 1992), providing a potential neurochemical mechanism of slowing in AD. This mechanism, however, has not been investigated in the context of PSWEs.

Research into the specific cortical and cellular underpinnings of PSWEs is limited due to the recency of their discovery. Studies with patient populations and animal models suggest that PSWEs tend to localize to temporal (e.g., hippocampal) brain regions where high blood-brain barrier permeability is detected (Milikovsky et al., 2019; Senatorov et al., 2019). In rodent models of ageing, Senatorov and colleagues (2019) demonstrated that degradation of the blood-brain barrier triggers hyperactivation of the transforming growth factor-beta (TGF-beta) signalling pathway (Senatorov, 2019). The result of the TGF-beta signalling cascade is neuronal hyperexcitability and an increased incidence of hippocampal PSWEs (Senatorov, 2019), suggesting a relationship between TGF-beta signalling and PSWE generation. However, the precise causal mechanism underlying this relationship is not fully understood.

Our current understanding of PSWEs suggests multiple possible cellular mechanisms that could result in either focal or widespread PSWEs. In order to elucidate the role of these mechanisms in healthy ageing, further investigation into the prevalence and characteristics of PSWEs in healthy ageing is required.

1.5 Technical Considerations

1.5.1 Magnetoencephalography

Magnetoencephalography (MEG) is a powerful non-invasive functional neuroimaging technique that has been instrumental in advancing our understanding of human brain function over the past few decades. MEG is sensitive to small (e.g., 5-100 fT) fluctuations in magnetic fields induced by electric currents in the brain (Baillet, 2017; Cohen, 1968, 1972). As described in Section 1.2.1, these currents arise from synchronous activity across populations of neurons in the cerebral cortex (Hansen et al., 2010), and therefore provide a direct measure of underlying neural activity. Despite the knowledge that the source of neuromagnetic activity is a set of synchronous post-synaptic potentials across a population of similarly oriented dendrites that may span several centimetres of cortex, it has been observed that from a distance (e.g., outside the head), this post-synaptic activity can be approximated by a current dipole oriented along the dendrites (Hämäläinen et al., 1993). Modelling the cortex as a spherical, homogeneous conductor, we can describe the current density by two components: the primary current, which describes the current flow in the vicinity of the cell, and the volume current, which flows

passively everywhere in the medium. A current dipole is essentially a concentration of the primary current density to a single point. A current dipole $\vec{Q}$ with position $\overrightarrow{r_Q}$ within a spherically symmetric conductor produces a magnetic field B at a distant sensor with position r and orientation z, according to Equation 1.1 (Williamson & Kaufman, 1981; Hämäläinen et al., 1993):

Equation 1.1

$$B_z = \frac{\mu_0}{4\pi} \frac{\vec{Q} \times (\vec{r} - \overrightarrow{r_Q}) \cdot \overrightarrow{e_z}}{|\vec{r} - \overrightarrow{r_Q}|^3}$$

This simplified model illustrates the general principles of neuromagnetic source and can be used to reasonably estimate the magnetic fields generated by a post-synaptic potential at a given source. However, more complex methods that use more realistic conductor shapes are also common (Hämäläinen et al., 1993). Equation 1.1 demonstrates that distant sensors are sensitive to the tangential component of primary currents. In other words, MEG is specifically sensitive to dendrites that are oriented tangentially to the surface of the head (i.e., those that line the banks of sulci in the cortex). In simple terms, this is because the neuromagnetic field wraps around the dendrites such that tangentially oriented dendrites create a field that propagates out of (and then back into) the head, allowing the field to be measured externally (see Figure 1.4A).

The current MEG landscape consists of two main types of MEG systems: cryogenic systems, and optically pumped magnetometer (OPM) systems. Cryogenic MEG systems detect neuromagnetic fields using sensitive detector coils that are made of materials that have superconducting properties (i.e., near zero resistance to current flow) at low temperatures (e.g., less than 10 Kelvin). The current on the superconducting coil wire is then transformed into a measurable voltage via a superconducting quantum interference device (SQUID). In order to maintain a sufficiently low temperature for the superconducting components, cryogenic MEG sensors are typically housed in a dewar of liquid helium. OPM systems on the other hand are a more recent advancement in MEG technology that allow sensitive magnetic recordings to be performed at room temperature (Knappe et al., 2014; Boto et al., 2017; Tierney et al., 2019). This advancement has several advantages over cryogenic technology including reduced operating costs and an

increased signal to noise ratio, because without the cryogenic dewar, sensors can be in closer proximity to the head. Despite these advantages, OPM is relatively new and rapidly changing and thus is not as widely used as cryogenic MEG. For the remainder of this thesis, I will focus primarily on cryogenic MEG as the data analysed in this work was acquired using a cryogenic system.

There are three main types of detector coils used in cryogenic MEG: magnetometers, axial gradiometers, and planar gradiometers (see Figure 4B). Magnetometers consist of a single coil loop oriented with the flat surface of the loop parallel to the surface of the head. Any magnetic field passing through the loop, either from the head or the surrounding environment, will induce a current in the magnetometer. Gradiometers on the other hand consist of two coils, wound in opposite directions, and are sensitive to gradients in magnetic fields along the spatial dimension. In axial gradiometers, the second coil is located approximately 5 cm above the first, allowing for sensitivity to magnetic fields that demonstrate a large change as one moves away from the scalp. Planar gradiometers consist of two coils in the same plane, equidistant from the head, making them sensitive to magnetic fields that change as one moves tangentially to the scalp. The benefit of gradiometers is that changing magnetic fields can be captured close to the source (i.e., near-field sources) but not far from the source (i.e., far-field sources). Therefore, gradiometers are sensitive to changing fields coming from inside the head but not to changes in fields from distant sources in the surrounding environment. In this work, data was collected using a 306-channel Vectorview system (Elekta Neuromag, Helsinki, Finland) which has a sensor array comprised of 102 triple-sensor element chips. Each chip consists of a single magnetometer and a pair of planar gradiometers oriented 90 degrees to one another (see Figure 4C), to allow signals of all orientations to be detected.

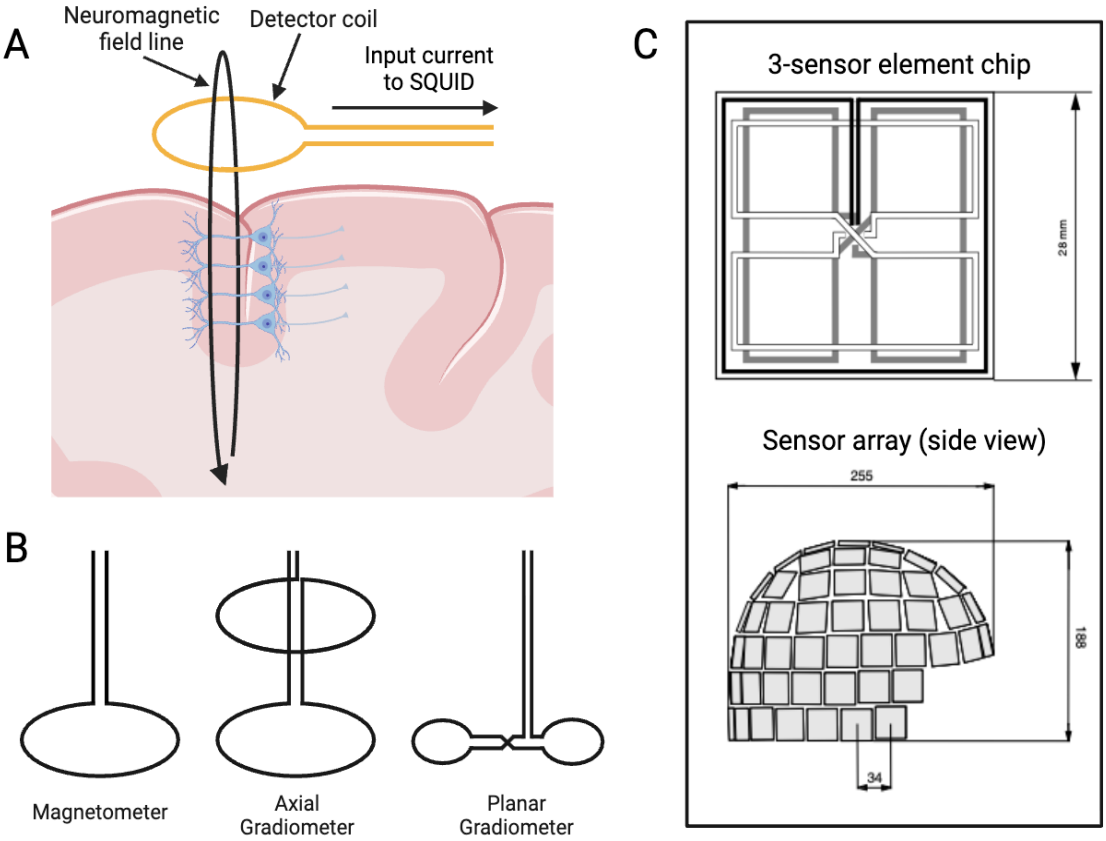

Figure 1.4 MEG sensor specifications. (A) An illustration demonstrating how neuromagnetic fields are produced and detected using MEG sensors. Neurons oriented tangentially to the surface of the head generate a magnetic field that propagates out of the head and is detected by detector coils in the MEG helmet. (B) Schematics of the 3 types of detector coils commonly used in MEG systems. (C) The arrangement of magnetometers and gradiometers in the Elekta Neuromag 306-channel Vectorview system used in this work. The sensor array is comprised of 102 triple sensor element chips that consist of 1 magnetometer (black) and 2 planar gradiometers that are oriented at 90 degrees with respect to one another (white and grey). Elekta chip schematics are taken from the Elekta Neuromag System Hardware Technical Manual (Revision F, 2005). Figure created with BioRender.com.

MEG is capable of measuring neural activity on a millisecond timescale providing high temporal resolution that is limited only by the sampling rate of the system (up to 12 kHz) (Hall et al., 2014). Further, unlike the electrical signals recorded in EEG, magnetic fields are not susceptible to distortion by the skull and scalp and have a consistent attenuation rate through all media in the head, allowing for an accurate (i.e., centimetre resolution) estimation of source (Baillet, 2017; Hansen et al., 2010). The high spatiotemporal resolution afforded by MEG has allowed us to advance research into

human brain activity underlying sensory processing, motor control, and cognition (Logothetis, 2008), and has provided a useful clinical tool for diagnosis and pre-surgical planning in patients with neurological diseases such as epilepsy (Barth et al., 1982; Bowyer et al., 2005; Hansen et al., 2010; Papanicolaou et al., 2005).

1.5.2 Source Localization

Cryogenic MEG provides a set of signals that characterizes the pattern of radial magnetic activity a few centimetres above the surface of the head. The challenge we are then faced with is identifying the set of neural sources responsible for generating the observed pattern of activity. This problem is typically referred to as the "inverse problem" because it involves starting with the effect (i.e., the sensor activity) and working backwards to identify the cause (i.e., the neural generators). Unfortunately, this problem is mathematically ill-posed, meaning that there are an infinite number of solutions that can result in the same pattern. While Maxwell's equations can be used to compute forward solutions (i.e., estimates of surface activity for known generators) as described in Section 1.5.1, the inverse problem has no unique solution (Williamson & Kaufman, 1981). Therefore, source localization methods typically compute forward solutions at one or more points in the source space and use iterative methods along with physiological constraints and regularization techniques to identify the most plausible source or combination of sources to explain the observed pattern of sensor activity (Halder et al., 2019).

The simplest method of source localization attempts to explain sensor activity with a single equivalent current dipole. A dipole is a point source, meaning that it is an infinitely small point at a particular location, that has negative and positive poles of equivalent strength (Newman, 2019). Focal electrical brain activity can be readily modelled by a current dipole which represents the movement of a localized charge over a short distance (i.e., the product of current and distance) (Williamson & Kaufman, 1981; Hämäläinen et al., 1993). While it is not true that neural activity is generated by infinitely small point sources, this simplification is reasonable for focal cortical sources. Post-synaptic potentials over a $1mm^2$-$1cm^2$ cortical patch generate a complex magnetic pattern close to the source, but when recorded from a distance (i.e., from outside the body), much of this complexity is lost, such that a single equivalent current dipole is a reasonable

representation (Williamson & Kaufman, 1981). Dipole modelling involves an iterative process that begins by placing a dipole with a random position, orientation, and strength, and computing the forward solution for that dipole. The forward solution is then compared to the observed data and small adjustments are made to traverse the parameter space until the best fit (i.e., least squared difference between observed and modelled patterns) is found (Newman, 2019). This procedure can also be performed with more than one dipole if multiple focal sources are expected. While this method is suitable for interpreting the simplest magnetic field patterns (Williamson & Kaufman, 1981), it has several associated limitations. Most notably, dipole fitting requires the user to define the number of dipole sources, and the chosen number of dipoles can drastically change the results, making the method susceptible to high inter-rater variability. Further, some a priori knowledge of the expected source distribution is required for accurate dipole modelling, but this expectation of source can lead to confirmation bias.

When minimal a priori information about the source is available, or a distributed source is anticipated, distributed source modelling is often used (Hämäläinen & Ilmoieni, 1994). The procedure for distributed source modelling involves simultaneously fitting a dipole at every vertex on a tesselated cortical surface (typically 10,000-20,000 vertices) and then determining the optimal primary current density at each point to best match the observed data (Newman, 2019). One of the most common distributed source models is minimum norm estimation (MNE). MNE constrains the source model by assuming that the best estimate of the true primary current density explains the measured signals while minimizing the length of the current vector (Hämäläinen & Ilmonieni, 1994). This method, however, has the inadvertent effect of being biased towards superficial sources. Therefore, modern versions of MNE tend to apply additional constraints to penalize superficial sources in favour of deeper ones. Some variants of MNE also apply additional regularization methods to normalize noise. Examples of noise normalization methods include dynamic statistical parametric mapping (DSPM; Dale et al., 2000), and standardized low-resolution brain electromagnetic tomography (sLORETA; Pascal-Marqui, 2002).

An alternative method for localizing widespread sources of MEG activity is a beamformer spatial filter. Beamformers operate by computing a forward solution at every

point in the source space, and then for each point, building a spatial filter (i.e., a set of weights applied to the data from each MEG sensor) that suppresses signal from every location other than the point of interest (Newman, 2019). Some beamformers operate on signals in the time domain (e.g., synthetic aperture magnetometry (SAM; Robinson & Vrba, 1991) and linearly constrained minimum variance (LCMV; VanVeen et al., 1997)), while others operate on signals in the frequency domain (e.g., dynamic imaging of coherent sources (DICS; Gross et al., 2001). DICS, which is of interest for the study of frequency-specific cortical oscillations, operates by calculating the cross spectral density for each point over a frequency range of interest, in addition to calculating the forward solution at each point (Gross et al., 2001). Given these values, power and coherence to a given reference point can be calculated for each point in the source space, and one of these measures can then be used to visualize source contributions on a co-registered anatomical MRI.

Distributed source models and beamformers both provide plausible explanations of source, but also have associated limitations. On one hand, MNE tends to have low resolution and is likely to overestimate the spatial extent of the source, while beamformers tend to null highly correlated sources due to the nature of the spatial filtering technique, resulting in a possible underestimation of source (Newman, 2019). Given the complexity of the inverse problem, it is unknown which of these methods provides a more accurate estimate of source, and the choice of method is highly dependent on the research question at hand.

1.5.3 Transient Event Detection

In recent years there has been an increasing interest in transient burst-based analyses and with this interest has come a surge in development of analysis methods for detecting and characterising bursts. At present, there is no gold-standard method for detecting and characterising transient bursts in electrophysiological data, and each proposed method comes with associated advantages and limitations.

The simplest, and most commonly used burst detection method uses amplitude thresholding to detect bursts of high-power activity within a pre-defined frequency range of interest. This method, popularized by Shin et al. (2017) defines bursts as local maxima in the time-frequency representation that exceed a pre-set power threshold (multiple of

the median power) and fall within a pre-defined frequency range (Brady et al., 2020; Shin et al., 2017). While this method has been widely used to detect mu, beta, and gamma bursts in human and animal models (Errington et al., 2020; Feingold et al., 2015; He et al., 2020; Hebert and Lehmann, 1977; Lakatos et al., 2004; Little et al., 2019; Lundqvist et al., 2016; Shin et al., 2017; Wessel, 2020), it is limited in its applications due to its imposition of assumptions about the frequency, waveform shape, and linearity of the signal of interest. In addition, the method does not effectively account for the aperiodic background activity when applying thresholding. Further, this method operates on a single signal (e.g., channel or source reconstructed time course), and does not take into consideration multi-channel interactions or signal spread, making it difficult to compare spatiotemporal characteristics between subjects. To address these limitations, a number of alternative burst detection methods have been proposed.

The Better Oscillation Detection (BOSC) and Periodic/Aperiodic Parameterization of Transient Oscillations (PAPTO) methods are alternative amplitude thresholding methods that have been designed to account for aperiodic background activity in the signal and have been shown to increase sensitivity to bursts (Brady & Bardouille, 2022; Caplan et al., 2015; 2001; Kosciessa et al., 2020; Rayson et al., 2022; Whitten et al., 2011). These methods, however, still rely on several fundamental assumptions about the approximate frequency, waveform shape, and spatial location of the signal of interest. To reduce these assumptions, many have moved towards data-driven methods of burst detection. Examples of this include Empirical Mode Decomposition (EMD) and cycle- by-cycle analyses which automatically detect approximately sinusoidal waveforms in nonlinear or nonstationary data (Cole & Voytek, 2019; Fabus et al., 2021; Huang et al., 1998), and Brief Amplitude Undulation (BAU) detection which automatically detects stereotypical waveforms based on their shape in the temporal domain (Abeles, 2014; Tal and Abeles, 2016; 2018). Several types of dictionary learning algorithms including MoTIF (Brockmeier and Principe, 2016; Jost et al., 2006), Sliding Window Matching (Gips et al., 2017), and Adaptive Waveform Learning (Hitziger et al., 2017) have also been applied to the burst detection problem. These algorithms, which were largely developed for other applications such as image processing, and audio signal segmentation, have shown promise as burst detection

methods due to their ability to learn repeating temporal motifs in the signal. While the data-driven nature of all of these methods provides an improvement over traditional amplitude thresholding methods, these methods are still limited in scope as they operate on a single time course and fail to consider the multi-channel dynamics that are critical to understanding electrophysiological signals, and how they change across a population.

Analysis methods that account for multi-channel interactions, such as Hidden Markov Modelling (HMM) and EEG Microstates have been used to detect transient states of brain activity during task-performance and in disease (Baker et al., 2014; Becker et al., 2020; Coquelet et al., 2022; Michel & Koenig, 2018; Quinn et al., 2018; Seedat et al., 2020; Vidaurre et al., 2016). HMM identifies full graphical networks that exist for 100-200ms at a time and exhibit rapid shifts between states, while the EEG Microstates method identifies short periods of stable scalp potentials that reflect sharp events of neural synchronization (Coquelet et al., 2022). A strength of these data-driven approaches is that they can identify repeating transient states across the whole head. However, the assumption that multiple states cannot coexist in time is a limitation as it is not uncommon to observe independent electrophysiological processes (e.g., occipital alpha and sensorimotor beta) co-occurring in time.

Another method that has been proposed for use in the multi-channel detection of transient bursts is the well-known Independent Component Analysis (ICA) algorithm (Briley et al., 2021; Himberg et al., 2004; Hyvärinen & Oja, 2000; Oja & Zhijian, 2006; Vigário et al., 1998). ICA has been a widely successful workhorse for extracting spatiotemporal components in electrophysiological data. However, assuming the independence of sources may not be realistic when working with highly correlated task-related brain oscillations such as sensorimotor mu and beta. In addition, ICA considers long time course states of brain activity and does not break the signal into short repeating temporal motifs that are characteristic of transient bursts.

Finally, multivariate convolutional sparse coding (CSC), which is a specification of the broader class of convolutional dictionary learning (CDL) algorithms is a potentially promising multi-channel, data-driven event detection method. CDL represents the multivariate neural signals as a set of spatiotemporal patterns, called *atoms*, with their respective onset times and magnitudes, called *activations*. CDL operates similarly to

classical Independent Component Analysis (ICA), decomposing the signals as a sum of topographies and sources (Dupré la Tour et al., 2018). However, CDL does so not by assuming that the sources are independent, but by assuming that the source time courses are formed by repeated waveforms. In this work, we explore the use of CDL for large-scale burst detection applications.

1.6 Thesis Overview

This thesis investigates the characteristics and neural sources of transient patterns of human brain activity in a large cohort of healthy participants. The objectives of the thesis are a) to develop and validate novel tools for detecting transient events and identifying their generative sources in the brain, and b) to provide insight into the neurophysiological changes that occur in healthy ageing. In each chapter of the thesis, a transient event framework is applied to explore the relationship between oscillatory neural activity and normal ageing. Chapters 2 and 3 implement novel methods to investigate the sources and spatiotemporal characteristics of typically occurring transient events related to a sensorimotor task and reveal insights into mechanistic changes that occur with healthy ageing. Chapter 4 then explores the prevalence and characteristics of atypical slow wave transients in the same cohort of healthy adults and relates the findings to ageing and cognitive performance. Each chapter of this thesis consists of a peer-reviewed publication containing original research that addresses the above objectives. Together, the chapters of this thesis provide validation for new methods of transient event detection and localization as well as insights into the neural mechanisms of ageing.

Project 1 (Chapter 2) aims to a) implement existing source localization algorithms for use in the detection of the cortical sources of transient beta bursts and b) uncover age-related trends in the source localization pattern of transient beta bursts. In this work, minimum norm estimation and beamformer methods are implemented for this novel application allowing the precise cortical sources of transient beta bursts to be identified for the first time. Further, distinct changes in the source patterns of beta bursts with age are revealed, providing insight into the cortical mechanisms underlying changes in sensorimotor beta activity with age. Project 1 is published as follows:

Power, L., & Bardouille, T. (2021). Age-related trends in the cortical sources of transient beta bursts during a sensorimotor task and rest. *NeuroImage*, *245*, 118670. https://doi.org/10.1016/j.neuroimage.2021.118670

Project 2 (Chapter 3) uses a data-driven transient event detection approach (convolutional dictionary learning) to naively detect and characterise ageing trends in task-related transient bursts at the group level. This project provides validation of a data-driven framework for identifying functionally relevant bursting activity in neurophysiological recordings. The work reveals the presence of several types of task-related transient events including sensorimotor beta and mu bursts, and occipital and temporal alpha bursts. Age-related changes in the rate of occurrence of all types of events are also observed. Project 2 is published as follows:
Power, L., Allain, C., Moreau, T., Gramfort, A., & Bardouille, T. (2023). Using convolutional dictionary learning to detect task-related neuromagnetic transients and ageing trends in a large open-access dataset. *NeuroImage*, *267*, 119809. https://doi.org/10.1016/j.neuroimage.2022.119809

Finally, project 3 (Chapter 4) aims to determine the prevalence of PSWEs in healthy populations and to identify the relationships between age, cognitive performance, and PSWE characteristics. The work quantifies the prevalence of atypical PSWEs in healthy participants for the first time and demonstrates a relationship between PSWEs and participant age. These findings have important clinical implications as PSWEs were previously thought to be a marker of neuropathology. Project 3 is published as follows:
Power, L., Friedman, A., & Bardouille, T. (2024). Atypical slow paroxysmal activity in healthy adults: Relationship to age and cognitive performance. *Neurobiology of Aging*, *136*, 44-57. https://doi.org/10.1016/j.neurobiolaging.2024.01.009

The data used in this thesis comes from a large open-access dataset collected by the Cambridge Centre for Ageing and Neuroscience (CamCAN). The dataset consists of imaging and behavioural data from over 600 healthy participants with a uniform age distribution between 18-88 years (Shafto et al., 2014; Taylor et al., 2017). This dataset is ideal for studying cross-sectional ageing trends in a healthy population. However, it is important to note that given the cross-sectional nature of the data, we can only infer age-related trends, and cannot confirm that the effects are present across the lifespan of an

individual. Cross-sectional ageing studies are inherently limited because there are environmental and lifestyle factors that vary between age groups that may be unrelated to ageing. For example, medicine, nutrition, and hygiene practices have all changed significantly in the past 60-70 years, and differences in any of these variables could confound the age-related effects observed in this work. Therefore, the inferences made throughout this thesis should be interpreted with this limitation in mind.

Chapter 2

Age-Related Trends in the Cortical Sources of Transient Beta Bursts During a Sensorimotor Task and Rest

2.1 Preamble

Previous work by our group detected transient beta bursts during a sensorimotor task and rest in a large dataset collected by the Cambridge Centre for Ageing and Neuroscience (CamCAN) (Brady et al., 2020). As described in Section 1.3.1, this work revealed significant age-related changes in the burst rate, peak power, peak frequency, and frequency span of the beta bursts. The findings of this work provided significant evidence that the *temporal characteristics* of individual beta bursts changed throughout the lifespan. It further demonstrated that these temporal burst features could explain changes in average beta power observed in previous works (Bardouille & Bailey, 2019), providing insight into the neural population mechanisms involved in age-related changes in average power. However, this work did not consider the *spatial characteristics* or cortical sources of the bursts. This was due in part to a lack of established methods to identify the sources of individual transient events. Thus, this chapter aims to expand on this prior work by presenting a method to localize transient beta burst sources, and applying that method to the same (i.e., CamCAN) dataset to explore changes in the cortical generators of beta bursts across the lifespan.

Chapter 2 of the thesis contains peer-reviewed work published in *NeuroImage* in December, 2021. Text in the introduction and discussion has been modified to reduce redundancies in the thesis, but all other sections appear as published. The reference for the publication is provided below.

Power, L., & Bardouille, T. (2021). Age-related trends in the cortical sources of transient beta bursts during a sensorimotor task and rest. *NeuroImage*, *245*, 118670. https://doi.org/10.1016/j.neuroimage.2021.118670

2.2 Abstract

Interpreting neurophysiology recordings as a series of transient bursts with varying temporal and spectral characteristics provides meaningful insight into mechanisms underlying neural networks. Previous research has revealed age-related changes in the time-frequency dynamics of sensorimotor beta bursts, but to date, there has been little focus on the spatial localization of these beta bursts or how the localization patterns change with normal healthy ageing. The objective of the current study is to implement existing source localization algorithms for use in the detection of the cortical sources of transient beta bursts, and to uncover age-related trends in the resulting source localization patterns. Two well-established source localization algorithms (minimum-norm estimation and beamformer) were applied to localize beta bursts detected over the sensorimotor cortices in a cohort of 561 healthy participants between the ages of 18 and 88 (CamCAN open access dataset). Age-related trends were then investigated by applying regression analysis between participant age and average source power within several cortical regions of interest. This analysis revealed that beta bursts localized primarily to the sensorimotor cortex ipsilateral to the side of the sensor used for their detection. Region of interest analysis revealed that there were age-related changes in the beta burst localization pattern, with most substantial changes evidenced in frontal brain regions. In addition, regression analysis revealed a tendency of age-related trends to peak around 60 years of age suggesting that 60 is a potential critical age in this population. These results show for the first time that source localization techniques can be implemented for the identification of the sources of transient beta bursts. The exploration of these sources provides us with insight into the anatomical generators of transient beta activity and how they change across the lifespan.

2.3 Introduction

Movement-dependent transient beta bursts are thought to emerge in the neocortex with synaptic drive from proximal and distal sources in the cortex, basal ganglia and thalamus (Bonaiuto et al., 2021; Sherman et al., 2016; Whittington et al., 2000). However, the specific cortical sources that are involved in beta burst generation during each phase of movement are not yet fully understood. To identify the underlying cortical sources responsible for generating transient beta bursts using MEG, we must solve the

inverse problem (Hämäläinen & Ilmoniemi, 1994; Sarvas, 1987). Several different algorithms have been developed to tackle this ill-posed problem including non-adaptive spatial filters, such as minimum norm estimation (MNE) and its variants (e.g. dynamic statistical parametric mapping (dSPM), standardized low-resolution brain electromagnetic tomography (sLORETA), etc.) and adaptive spatial filters, such as beamformer algorithms (e.g. dynamic imaging of coherent sources (DICS), linearly constrained minimum variance (LCMV)) (Gross et al., 2001; Halder et al., 2019; Newman, 2019). Both algorithm types tesselate the brain into a large number of segments (on the order of 10,000) and compute a forward solution (i.e., lead field generated by an equivalent current dipole) at each vertex. The goal is then to re-create the measured data by varying the magnitude (and sometimes orientation) of each current dipole (Newman, 2019).

In the present study, we combine the use of these source localization algorithms with recent developments to detect transient burst onsets to determine the cortical generators of beta activity on a burst-by-burst basis. Previous work has successfully detected changes in average spectral power between movement intervals (e.g., pre-versus post-movement, movement versus baseline), which we know to be dependent on the underlying transient burst characteristics (Brady et al., 2020; Shin et al., 2017). However, source maps based on these comparative approaches confound power change due to transient bursts in each interval and fail to localize sources of transient bursts directly. To date, source localization of transient beta bursts on a burst-by-burst basis, performed independently for each interval/condition within a recording has not yet been implemented. Such an approach would prove valuable for improving our understanding of the generator of these transient bursts. Here, we will be attempting to localize the cortical sources of transient beta bursts using two well-established source localization algorithms: MNE, and DICS beamformer. Each method has a different set of regularization procedures in place to constrain the number of possible solutions to the inverse problem, each with their associated strengths and weaknesses. It is unclear which of these algorithms will be more beneficial for the novel problem of localizing transient beta sources. Therefore, both methods will be employed, and concordance between methods will be evaluated.

Previous source localization studies focused on changes in average spectral power have demonstrated that the sensorimotor beta band response involves somewhat diffuse activation of the bilateral primary motor, primary somatosensory and supplementary motor cortices, and contralateral activation of the pre-motor cortex (Cheyne, 2013; Gaetz et al., 2011; Wilson et al., 2010). The beta suppression that occurs during and immediately prior to movement tends to localize bilaterally in the primary somatosensory cortex (Jurkiewicz et al., 2006). Beta suppression can primarily be explained by a reduction in the number of beta bursts during movement, compared to the pre-movement interval (Brady et al., 2020). Therefore, we expect to find prominent beta burst activity in both the contralateral and ipsilateral hemispheres during the pre-movement interval. It is unclear, however, whether the bilateral source pattern observed in average spectral power data is due to simultaneous reductions in beta bursts that occur independently in each hemisphere, or a primary reduction in bursts in the contralateral hemisphere that has widespread source contributions. Identifying the sources of the individual beta bursts in the pre-movement interval will provide insight into the contributions of each hemisphere. Beta rebound, on the other hand, tends to localize more contralaterally in the primary motor cortex (Jurkiewicz et al., 2006). Beta rebound is the result of an increase in the both the number and peak power of beta bursts in the post-movement interval compared to the movement and baseline intervals (Brady et al., 2020). We would therefore expect to find significant beta bursting activity localizing to the contralateral hemisphere during the post-movement interval. It is unknown however, whether the high-power nature of the post-movement bursts is due to high power activity at few focal sources or the coordinated activity of a large number of contributing sources. It is therefore necessary to localize the individual beta bursts themselves, rather than changes in average spectral power with respect to the pre-movement interval, in order to elucidate the underlying sources contributing to the movement-related beta response.

In addition, there is reason to believe that the beta burst localization patterns will show changes across the lifespan that could have functional and/or clinical relevance. In addition to the findings that average spectral power and transient beta bursts have age-related properties (Bardouille & Bailey, 2019; Brady et al., 2020), a number of functional neuroimaging studies have noted changes in the spatial representation of motor activity

with age. A series of fMRI studies show that older participants tend to have activation across a broader range of motor and non-motor regions than their younger counterparts when performing repetitive motor tasks (Hutchinson, 2002; Mattay et al., 2002). Older participants show bilateral activation of the sensorimotor cortex and putamen and contralateral activation of the cerebellum that are not consistently observed in younger participants (Mattay et al., 2002; Vallesi et al., 2010). It has been proposed that this change in activation pattern is related to the recruitment of compensatory mechanisms that are required to account for age-related structural and chemical changes in the brain. These previously reported age-related changes in movement-related brain activation, combined with the findings that transient beta bursts demonstrate age-related changes, suggest that the cortical sources of transient beta bursts may change with normal healthy ageing.

The objective of the current study is thus two-fold. First, we aim to implement existing source localization algorithms for use in the detection of the cortical sources of transient beta bursts. Based on studies using average spectral power data, we hypothesise that bursts identified in the pre-movement interval will localize primarily to the primary somatosensory cortices and have bilateral sources, and those identified in the post-movement interval will localize primarily to the contralateral primary motor cortex. Secondly, we aim to uncover age-related trends in the source localization pattern of transient beta bursts. Based on previous studies of movement-related brain activation, we predict that older participants will tend to show a more widespread pattern of activation than their younger counterparts. Particularly, it is expected that older participants will show increased activation in the pre-motor and supplementary motor areas and will recruit ipsilateral sensorimotor regions in addition to the contralateral sources expected in the younger participants.

To our knowledge, the present study is the first to implement source localization algorithms for the identification of the sources of transient beta bursts. Success of this work could therefore provide the framework for future studies to explore the cortical sources of a variety of transient event types. In addition, the work will provide insight into age-related changes in the sources of transient beta bursts. The exploration of these sources and how they change across the lifespan could have functional or clinical

implications as the results could provide anatomical justification for previously observed electrophysiological and behavioural changes in motor function with age.

2.4 Methods

Text in Sections 2.4.1-2.4.4 was adapted from Bardouille and Bailey (2019) and Brady et al. (2020). Work described in these sections was completed previously, except where specified.

2.4.1 Participants and Experimental Paradigm

MEG data was collected from 650 participants in Phase 2 of the Cam-CAN examination of healthy cognitive ageing. Participant ages ranged from 18 to 88 years of age, with an equal distribution in age per decile and equal proportions of males and females. All participants provided written, informed consent prior to participating in each phase of the study. The study was conducted in compliance with the declaration of Helsinki and data collection was approved by local ethics boards (see Shafto et al., 2014). In the current work, we report findings from 561 participants (86.3% of the original 650 datasets) who had sufficient MEG and anatomical MRI data required for localization. Each participant performed the 'Sensorimotor task' and a 'Resting state' scan (CamCAN et al., 2014). In the sensorimotor task, participants responded with a right index finger button press to unimodal or bimodal audio/visual stimuli. The order of bimodal and unimodal trials was randomized, and the inter-trial interval varied between 2 and 26 s. The button press task did not include specific imperatives related to performance (e.g., fast responses). Thus, brain-behaviour interactions focused on response time were not investigated in this report. In the resting state scan, data were acquired for 8 minutes and 40 seconds while participants rested with their eyes closed. The first 20 seconds of the resting data were discarded.

2.4.2 Data Acquisition

Data were obtained from the CamCAN repository (available at http://www.mrc-cbu.cam.ac.uk/datasets/camcan/ (Shafto et al., 2014; Taylor et al., 2017)). MEG data were acquired at 1000 Hz with inline band-pass filtering between 0.03 and 330 Hz using a 306-channel Vectorview system with continuous head position monitoring (Elekta Neuromag, Helsinki, Finland). Digitization of anatomical landmarks (i.e., fiducial points; nasion and left/right preauricular point) as well as additional points on the scalp was also performed

for co-registration of MEG and MRI coordinate systems. Electrooculogram (EOG) and electrocardiogram (ECG) were recorded concurrently. T1-weighted magnetic resonance images (MRI) were acquired using a 3T Siemens Tim Trio system with a 32-channel head coil.

2.4.3 MRI Data Processing

Each participant's MRI was reconstructed using the FreeSurfer recon-all algorithm (Dale et al., 1999; Desikan et al., 2006; Fischl et al., 1999a, 1999b, 2001, 2002, 2004). The reconstruction process provided a digitization of the cortical surface for source estimation, a transformation to the average (i.e., fsaverage) brain for spatial normalization and group statistics, and a boundary element model of the brain to provide more accurate calculation of the forward solution (Hamalainen & Sarvas, 1989). Locations for source estimation were defined covering the entire cortical surface with 5 mm spacing. Finally, each participant's MRI data was registered to the MEG data based on the alignment of anatomical landmarks (i.e., fiducials) in MEG and MRI, and MEG head digitization with the scalp was visualized on the MRI (MNE python coreg, v.0.14) using a semi-automated process (Bardouille & Bailey, 2019). Coregistration data are available at https://github.com/tbardouille/camcan_coreg. Participants missing MRI data were excluded from further analyses.

2.4.4 MEG Data Processing

Data were pre-processed by the CamCAN group using temporal signal space separation to perform environmental noise reduction, reconstruction of missing or corrupted MEG channels, continuous head motion correction, and a transform of each dataset to a common head position (Taulu & Simola, 2006). All subsequent MEG processing was completed in the Python programming environment (v.2.7.13), using the MNE-python library (v.0.18.1) (Gramfort et al., 2014). Python code for all subsequent analysis is available at https://github.com/lindseypower/CamCAN_BetaSourceLocalization. Raw MEG data were lowpass filtered at 125 Hz and notch filtered at 50 Hz and 100 Hz to remove signals related to power lines. The task data was then parsed into trials synchronized to each button press, with a duration of 3.4 s, including a 1.7 s pre-movement interval. The 3.4 s window length was selected to ensure a sufficient post-movement interval to capture the

entire beta rebound response. Trials were excluded if the button press occurred more than 1 s after the cue (indicating poor task performance) or if the button press occurred within 3 s of the previous button press (which provided insufficient baseline for subsequent analysis). Participants with less than 55 trials after these exclusions were excluded from further analysis due to insufficient data. The rest data were cropped to a single 210 s trial including 105 s prior to and following the midpoint of the resting data. The length of this trial was chosen to be approximately equal in length to the sum of all task trials. Independent component analysis was performed on the task and rest data using the FASTICA algorithm (Hyvärinen & Oja, 2000; Delorme et al., 2007) to remove artifacts using a fully automated process. This process resulted in cleaned MEG task data (i.e., channels x time x trials) and cleaned rest data, which were used for burst detection and localization.

As part of the current localization work, empty room noise data for each participant was also processed using similar methods. The head transformation and digitization info for the empty room noise data was matched to that of the task data to ensure equivalent processing. The empty room noise data was then filtered to remove environmental noise and bad channels (MNE python maxwell_filter function). Additional processing steps including filtering and ICA were then carried out as described above for the task data.

Beta bursts were detected in task and rest data at two peak MEG sensors using methods described by Shin et al. (2017). Sensors MEG0221 (left central sensor, contralateral to the hand used in the task) and MEG1311 (right central sensor, ipsilateral to the hand used in the task) were selected as the peak sensors. These sensors overlay the left and right sensorimotor areas, are most sensitive to task-related changes in average beta power (predicted to originate in the sensorimotor cortex), are far away from the midline (to ensure sensitivity to a single hemisphere) and are in mirrored positions on the sensor array (Brady et al., 2020). Single-trial time-frequency representations (TFRs) were generated using a Morlet wavelet for frequencies between 1 and 100Hz, with a 1Hz resolution. Local maxima in spectral power were then identified in the TFRs. Beta bursts were defined as local maxima that exceeded a spectral power of 6x the median power (as defined by Shin et al., 2017) and had a peak frequency between 15-30Hz. To facilitate

localizing bursts occurring in different task states, bursts were detected in two intervals of the Task data (pre-movement and post-movement), and throughout the Resting State data for each participant in the CamCAN dataset. Pre-movement bursts were defined as beta bursts with a peak time between -1.25 to -0.25 s relative to movement onset and post-movement bursts were defined as having a peak time between 0.25 to 1.25 s relative to movement onset. In the current work, the 55 highest power beta bursts were selected for each condition (pre-movement, post-movement, and rest) and sensor (left and right) to be used in the localization procedure.

2.4.5 Burst Localization Algorithm

In order to isolate data segments associated with transient bursts, we re-epoched the MEG data for each participant based on the onset times of the detected bursts to create "beta burst epochs". As per prior work in transient burst characterization, the burst onset time for each local maximum in the TFR was determined using the full width at half-maximum along the time axis. Each beta burst epoch was 1.15 s in length, centered on the burst onset time. An epoch length of 1.15 s was selected as this was the average inter-burst interval for the data. Figure 2.1 shows an example of bursts detected in a single trial TFR and a resulting beta burst epoch. Two source localization methods: dynamic imaging of coherent sources (DICS) beamformer and minimum norm estimation (MNE) were then applied to each set of epoched data to localize spectral power change associated with beta bursts.

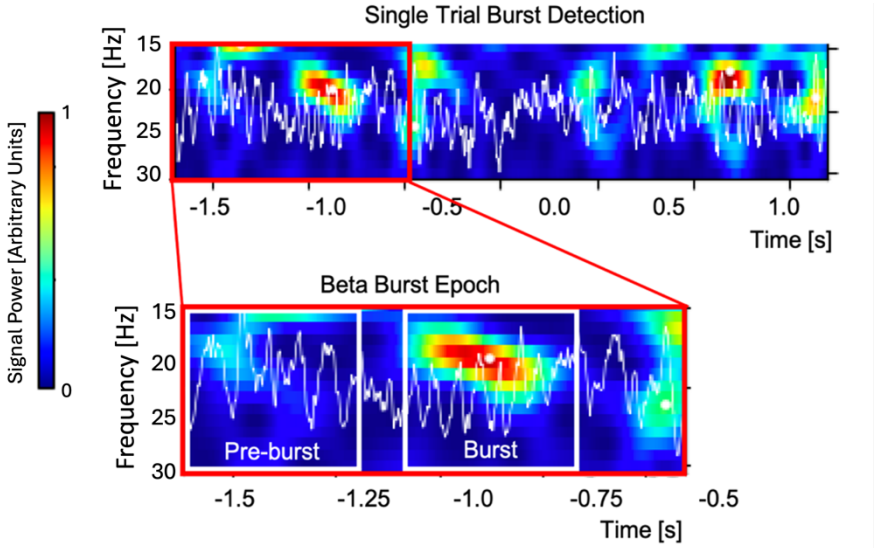

Figure 2.1 An example of a time frequency representation for a single task epoch (top) and a single beta burst epoch (bottom). The MEG time course is overlaid on the TFR as a

white line and transient beta bursts are identified by white dots. The beta burst epoch is indicated in the task epoch as a red box. The 400 ms burst and pre-burst intervals used in the source localization algorithms for this beta burst epoch are shown by white boxes.

DICS Beamformer:

For each participant in the CamCAN dataset, and for each condition (pre-movement, post-movement, and rest), the beta burst epochs were used to compute a forward solution. Cross-spectral density was then computed using the epoched MEG data and the noise cross-spectral density was computed using the empty room noise data collected prior to the participant's MEG session. The DICS beamformer was then applied to pre-burst (-0.575 to -0.175s relative to burst onset) and burst (0 to 0.400s relative to burst onset) intervals of each beta burst epoch across a 15-30Hz frequency range. The 400 ms burst and pre-burst interval length was selected in order to capture the entirety of the longest burst events while ensuring maximal separation between intervals. The difference between burst and pre-burst source power estimates was then calculated using the following equation:

Equation 2.1 $$\Delta P(f) = log_2\left(\frac{P_{burst}(f)}{P_{pre-burst}(f)}\right)$$

The resulting source estimate was then averaged across all frequencies of interest and morphed to the fsaverage brain to allow source estimates to be compared across participants.

Minimum Norm Estimation:

For the minimum norm estimation procedure, beta burst epochs were used to compute a forward solution and an inverse operator for each participant in the CamCAN dataset, and for each condition. A noise covariance matrix was also computed using the empty room noise data collected prior to the participant's MEG session. A source estimate was then computed in the 15-30Hz frequency band using the minimum norm method of estimation. The resulting estimate was parsed into pre-burst (-0.575 to -0.175s) and burst (0 to 0.400s) intervals, and the difference in spectral power between intervals was calculated using Equation 2.1. The resulting source estimate was then morphed to the fsaverage brain to allow comparison to other participants.

Note that while variants of the original MNE method (e.g. dSPM, sLORETA, etc.) are widely used and often considered superior to MNE, these methods do not provide a benefit over original MNE for the current application. dSPM and sLORETA methods are both derived from MNE by multiplying the estimation result by a normalization matrix (Hauk et al., 2011). Because the current methodology involves the voxel-wise division of the active by the baseline interval, any multiplication factor is cancelled out during this process, rendering these advanced methods equivalent to the original MNE. For that reason, this work employing the original MNE is generalizable to the aforementioned MNE variants.

Each source localization method yielded a 20484-vertex map that represented the mean difference in power between the beta burst and an interval prior at each vertex. These "beta burst power" values were unitless and directly comparable between participants and localization methods.

2.4.6 Data Analysis

The beta burst localization algorithm described above was applied to each participant in the CamCAN dataset using bursts detected by the left (contralateral) and right (ipsilateral) sensors in the pre-movement, post-movement and resting state conditions. Grand average source estimations were then created for each estimation method and condition by averaging the 20484-vertex beta burst power estimates across all participants (N=561). To assess whether sources detected by the left (contralateral) and right (ipsilateral) sensors were independent, coherence analysis was employed for the pre-movement and post-movement intervals. For all participants, the MEG time course data from each sensor was extracted during each time interval. The coherence spectrum between left and right sensor time courses during each interval was then calculated and plotted for all frequencies between 0 and 100 Hz. Low coherence (<0.1) indicates that the sources detected by the two sensors are independent, while high coherence indicates correlated sources between the left and right hemisphere. We expected that there would be low coherence (i.e., no synchrony) between left and right hemisphere bursts given that beta rhythms are generally understood to be independently generated in each hemisphere via thalamocortical loops.

To provide a measure of similarity between the two methods, the correlation coefficient between the grand average source estimations generated by the MNE and DICS beamformer methods was then calculated for each condition. In addition, difference maps were created comparing the two estimation methods for each condition to visually assess areas with varying source power between methods. Difference maps were created by subtracting the DICS beamformer source estimation from the MNE source estimation for each participant and conducting t-tests at each vertex comparing the difference across participants to a null hypothesis of 0 (indicating no difference between estimation methods). The T statistics for each vertex were then plotted on a 3-dimesional average head model and examined qualitatively to assess regions of significant difference between methods. Using a Bonferroni corrected alpha of 2.44e-6 (0.05/20484 vertices) and 560 degrees of freedom, T statistics with a magnitude greater than 4.61 are considered significant.

To facilitate visualization of age-related changes, average source estimations were created for participants in each of 5 coarse age bins: 18-32 years (N=83), 33-46 years (N=129), 47-60 years (N=132), 61-74 years (N=119) and 75-88 years (N=98). The source estimates were then plotted on a 3-dimensional head model and examined qualitatively to assess for any gross age-related trends and identify potential regions of interest. Based on this preliminary analysis, 12 regions of interest (6 per hemisphere) were selected from a standard set of anatomical parcellations defined by Destrieux and colleagues (Destrieux et al., 2010). Regions corresponding to the middle frontal gyrus (region 15), superior frontal gyrus (16), supramarginal gyrus (26), superior parietal lobule (27), postcentral gyrus (28) and precentral gyrus (29) were selected for further investigation. Within each region of interest, the beta burst power was averaged across the constituent vertices. Figure 2.2 shows the regions of interest used for this analysis and their associated abbreviations.

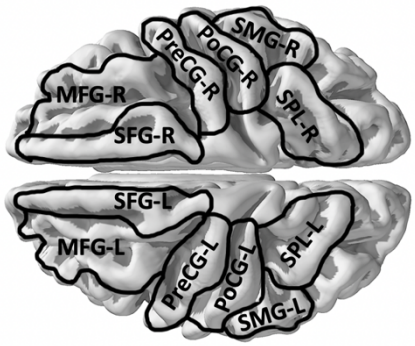

MFG	Middle Frontal Gyrus
SFG	Superior Frontal Gyrus
SMG	Supramarginal Gyrus
SPL	Superior Parietal Lobule
PoCG	Post-Central Gyrus
PreCG	Pre-Central Gyrus

Figure 2.2 The regions of interest used for the age-related analysis. Regional abbreviations will be used in the results figures to identify relevant brain regions.

Age-related trends in beta burst power were then investigated by conducting linear and quadratic regression between average regional beta burst power and age across all participants. The goodness of fit of each model (linear and quadratic) to the data was assessed using a chi-square test. An F-test was then employed to decide the more appropriate model for each region of interest. A quadratic model was selected if $F > 4$, indicating 95% confidence. Otherwise, a linear model was deemed most appropriate. The T statistic associated with the chosen model was then plotted on the 3-dimensional head model to visually represent the anatomical regions associated with significant age-related changes. Regressions were computed for each region of interest (12), condition (3), localization method (2) and sensor (2) with alpha = 0.05. Due to the large number of t-tests, a Bonferroni correction was applied to yield a corrected alpha value of 0.000174 (0.05/288 tests).

In addition to the region of interest-based analysis, the age-related change in the peak location of the beta burst spatial map was also assessed. The goal was to assess if there was a shift in the focal source of the beta burst generator with age, motivated by a visual inspection of the average source estimations for coarse age bins (Figure 2.5). For each participant, the vertex in their source estimation with the greatest relative source power was identified and the associated x, y, and z coordinates were used to represent the peak location. The x, y, and z coordinates were then regressed against age across participants for each condition (3), sensor (2), and localization method (2) in order to evaluate any age-related shifts in peak localization. A Bonferroni corrected p-value of 0.00139 (0.05/ 36 tests) was used to assess significance. To provide a qualitative

depiction of the position and variability of peak locations with age, the peak vertex for each participant was also plotted on a 3-dimensional average brain model, with coloured markers representing participant age.

Finally, in order to visualize the points throughout the lifespan that are associated with the largest changes in brain activity, the data was binned into fine, 2-year age bins (35 bins in total), and average source estimates were calculated for each group. To compute the average source maps per group, the 20484-vertex beta burst power maps computed for each participant were averaged across all participants in the 2-year age bin (approximately 16 participants per group). Paired-sample T-tests were then conducted comparing the 20484-vertex average source power map for each age group to every other age group in the sample. In this context, the T statistic quantifies the difference in source power maps between the two age groups. The resulting T statistics were plotted as a 2-dimensional colourmap, similar to a correlation matrix. Age groups that have the particularly dissimilar localization patterns have high T statistics (shown as yellow pixels in the colour map). Clusters of high T statistics in the 2-dimensional colormap (shown as large yellow regions) can provide an indication of the age groups where large shifts in brain activity occur. A total of 1225 t-tests (35x35 groups) were conducted for each condition (3), localization method (2) and sensor (2). Therefore, a Bonferroni correction was applied to yield a corrected alpha value of 3.4e-6 (0.05/14700 tests). Using an alpha of 3.4e-6 and 16 degrees of freedom (16 people per bin on average), T statistics with a magnitude greater than 6.54 are considered significant.

2.5 Results

2.5.1 Grand Average Localization

Grand average source estimates created using the MNE source estimation method are shown for each condition in Figure 2.3. All estimates have been morphed to an average 3-dimensional headspace for direct comparison between groups. Overall, we found high concordance in the spatial localization of beta bursts between the DICS beamformer and MNE methods. However, the DICS beamformer method yielded consistently lower relative activation values across all conditions (see Appendix A for DICS beamformer estimates). Transient beta bursts detected in the resting state mainly localize ipsilateral to the sensor used for their detection. Bursts detected at the left

(contralateral) sensor localized primarily to the left sensorimotor cortex, pre-motor, and supramarginal regions, with very little right hemisphere contribution. Bursts detected at the right (ipsilateral) sensor during resting state had a similar pattern of localization over the right sensorimotor cortex with minimal left hemisphere activation. Bursts detected in the pre-movement interval also strictly localized to the side of the sensor used for their detection, with a localization pattern centred over the somatosensory cortex and supramarginal gyrus. This lateralization suggests that both the resting state and pre-movement bursts have independent cortical generators in the left and right hemispheres. This was confirmed through coherence analysis which revealed that MEG data recorded from the left and right hemisphere sensors during the pre-movement interval had coherence < 0.01 for all frequencies between 0 and 100 Hz. Compared to the resting state bursts, pre-movement bursts had a more focal localization pattern with lower peak magnitude. This discrepancy in the spatial distribution of beta burst activity between the resting state and pre-movement interval suggests that there may be a shift in the cortical generators of beta bursts in preparation for motor performance.

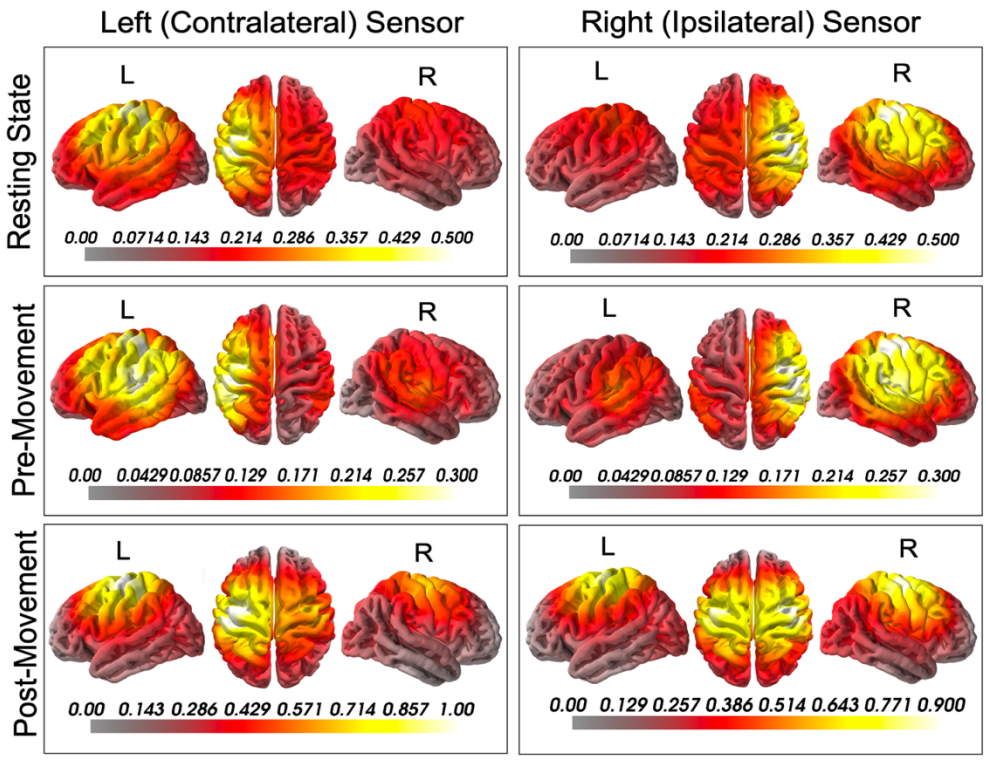

Figure 2.3 Average source estimation patterns for 561 healthy participants as estimated by the MNE source estimation method. Source estimation patterns are shown during

resting state (top) pre-movement (middle), and post-movement (bottom) conditions, for bursts detected at left (contralateral) and right (ipsilateral) sensors. The left, dorsal and right views of the 3-dimensional head model are shown for each condition. The colour bar values represent the relative power between the active and baseline intervals as calculated in Equation 2.1. Note that the scales are different for each condition to reflect the full range of relative power values for each condition.

Bursts detected in the post-movement interval showed a much broader pattern of localization compared to rest and pre-movement, with bilateral sources detected at both sensors of interest. Bursts detected at the left (contralateral) sensor localized to the bilateral sensorimotor sources, as well as left hemisphere pre-motor and superior parietal sources. Bursts detected at the right (ipsilateral) sensor localized approximately bilaterally to the sensorimotor cortices, pre-motor, and superior parietal sources. It was unclear from this result whether left and right hemispheric bursts during the post-movement interval had a common neural source or if they emerged through independent generators. A coherence analysis between the MEG data recorded at left and right hemisphere sensors during the post-movement interval revealed coherence values of < 0.0002 for all frequencies between 0 and 100 Hz. This suggests that the bursts localized in each hemisphere had independent generators but concurrent timing.

2.5.2 Comparison of MNE and Beamformer Methods

As indicated by the grand averages (Figure 2.3, Supplementary Figure A.1), MNE and DICS beamformer methods showed high concordance in their spatial localization of transient beta bursts. The correlation coefficients between the localization maps produced by each method were 0.778 and 0.806 for the resting state condition (left and right sensors, respectively), 0.695 and 0.626 for the pre-movement condition (left, right), and 0.899 and 0.885 for the post-movement condition (left, right). These values indicate a high degree of similarity between the two localization methods. From this analysis, it can be concluded that the similarity between estimations is sufficient to proceed with a single analysis method in the main body of this manuscript. Difference maps comparing the MNE and DICS beamformer estimation methods for each condition are shown in Figure 2.4. Across all conditions, the MNE method has higher relative source power near the focal source (i.e., the sensorimotor cortices), as shown by the positive values in Figure 2.4. Alternatively, the DICS beamformer method has higher source power in the

surrounding (non-focal) brain regions across all conditions. These results together suggest that MNE and DICS beamformer estimation methods have similar patterns of localization, but that the MNE method results in a more focal localization compared to the DICS beamformer method for beta burst localization. For that reason, only the results from the MNE analysis will be shown herein. The results for the DICS beamformer analysis can be found in Appendix A.

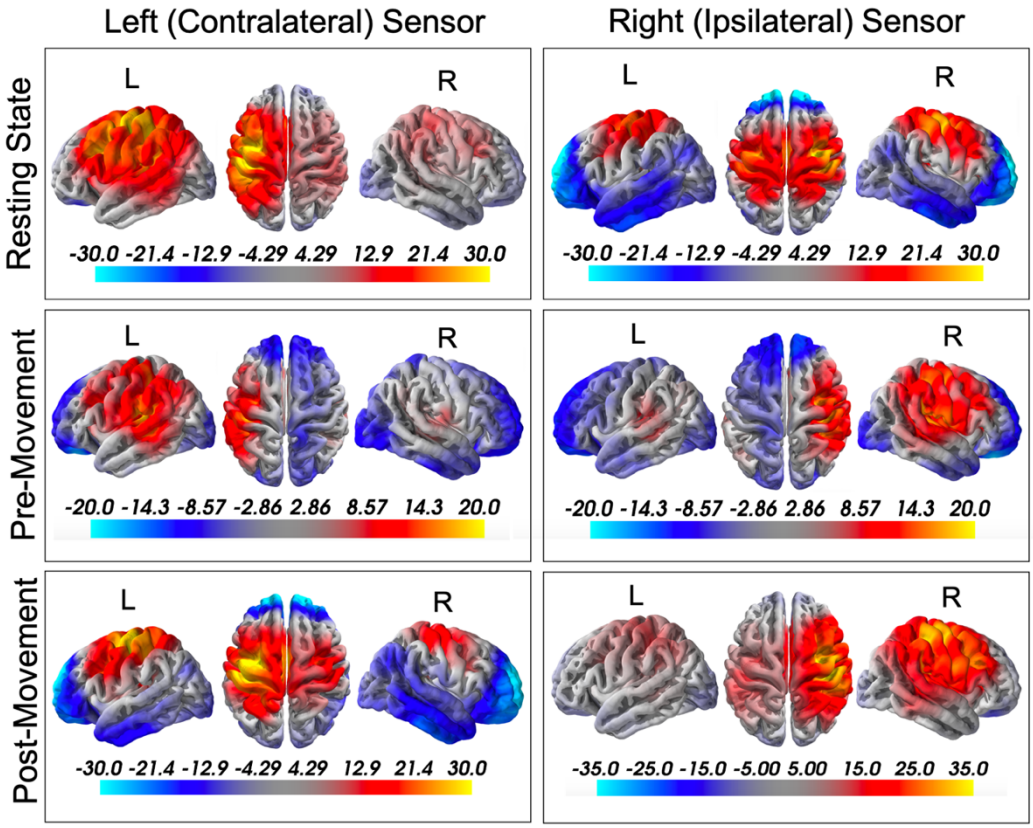

Figure 2.4 Difference maps comparing the MNE and DICS beamformer localization methods (MNE - DICS beamformer). Differences in localization during the resting state (top), pre-movement (middle) and post-movement (bottom) conditions are shown for the left and right sensors, respectively. Left hemisphere, dorsal, and right hemisphere views are shown for each condition and sensor. The colour bar values represent t-statistics for the t-test between the MNE - DICS beamformer difference and a null hypothesis of zero difference at each vertex. Positive values therefore indicate vertices where the MNE localization algorithm had greater relative source power and negative values indicate vertices where the DICS beamformer algorithm had greater relative source power.

2.5.3 Source Patterns by Age

In order to evaluate the presence of age-related trends in source estimation patterns, the data was binned into 5 coarse age bins as shown in Figure 2.5. As in Figure 2.4, the average relative power for each condition is plotted on a 3-dimensional head model. Within the resting state and pre-movement conditions, the regions of interest in the source estimation remain relatively constant across groups, with only small age-related changes in magnitude being noted in the contralateral and/or ipsilateral frontal and sensorimotor cortices. In the post-movement condition, however, there are some notable differences in both location and magnitude between age groups. In particular, the 18-32-year group shows a much more focal source pattern compared to the older groups. For bursts detected by the left (contralateral) sensor, the 18-32-year group has high-power sources confined to the left sensorimotor and superior parietal cortices, while the subsequent age groups show a broadening of the spatial extent of high-power sources to include the right sensorimotor cortex and the bilateral premotor cortices. For bursts detected by the right (ipsilateral) sensor, the localization pattern is bilateral even in the 18-32-year age group but is restricted to the left and right sensorimotor cortices. As with the left sensor, this pattern expands to include surrounding cortical regions in the older age groups. In both cases, this pattern appears to reach maximum spatial distribution in the 47-60- year age group before levelling off, and possibly reducing spatial extent in the oldest age bins. While it was initially hypothesised that age-related changes would present as linear trends in source pattern, this preliminary investigation suggested the possibility of quadratic trends, particularly in the post-movement condition.

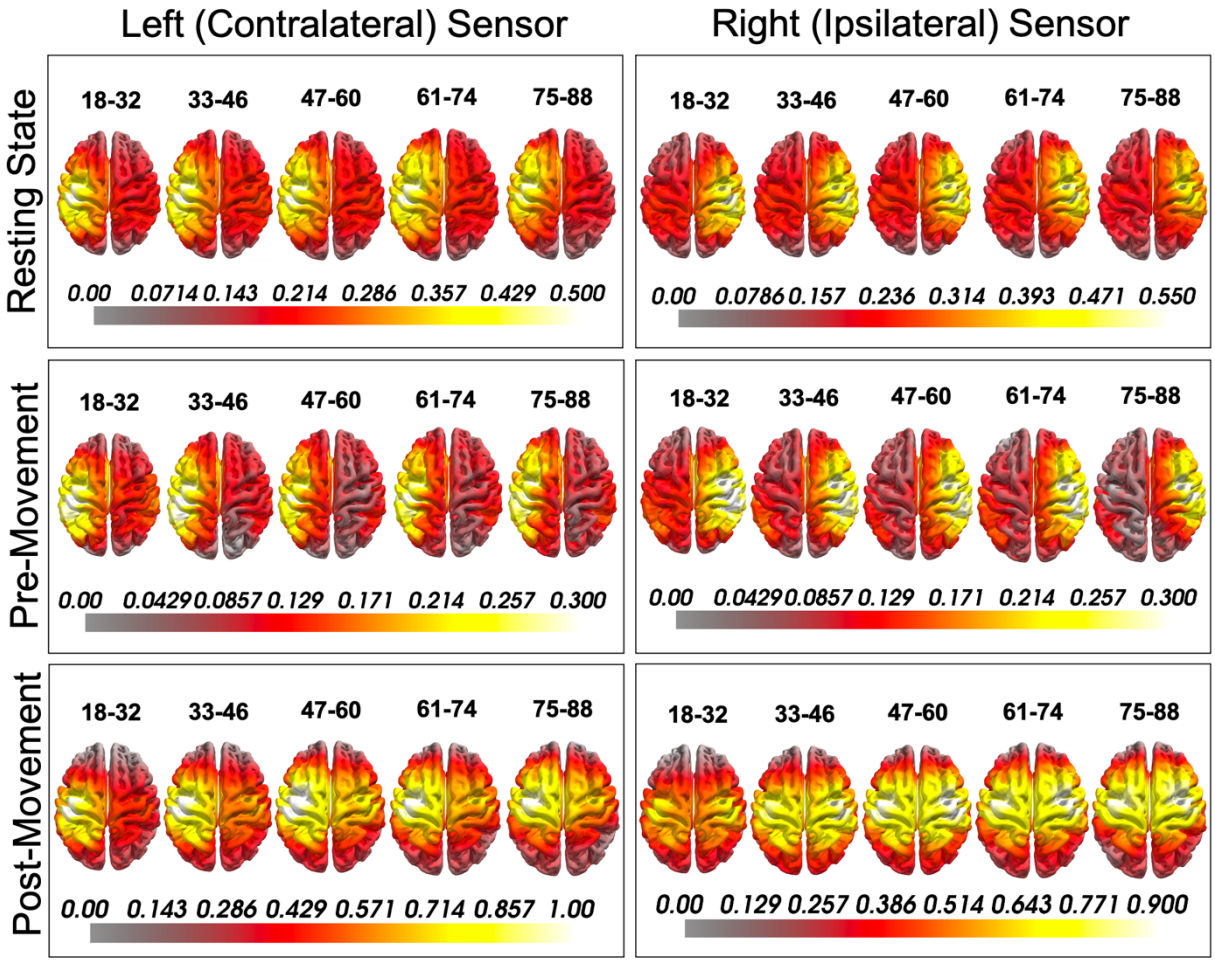

Figure 2.5 Average source estimation patterns for 5, 14-year spanning age groups of healthy participants during resting state (top), pre-movement (middle) and post-movement (bottom) conditions, for bursts detected at left (contralateral) and right (ipsilateral) sensors. Dorsal views are shown for each age group, condition, and sensor. The colour bar values represent the relative power between the active and baseline intervals as calculated in Equation 2.1. Note that the scales are different between conditions in order to maximize the contrast but are kept consistent across age groups within the same condition to allow for direct comparison between ages.

2.5.4 Region of Interest-Based Ageing Trends

Age-related trends in relative source power and the results of the best-fit model for each region of interest are shown in Figure 2.6. A Bonferroni-corrected significance level of 0.000174 is used to evaluate all models. Results are only shown for the post-movement condition as the resting state and pre-movement conditions had primarily null

results. Significant results for the resting state and pre-movement conditions are discussed briefly in text and figures are presented in Appendix A.

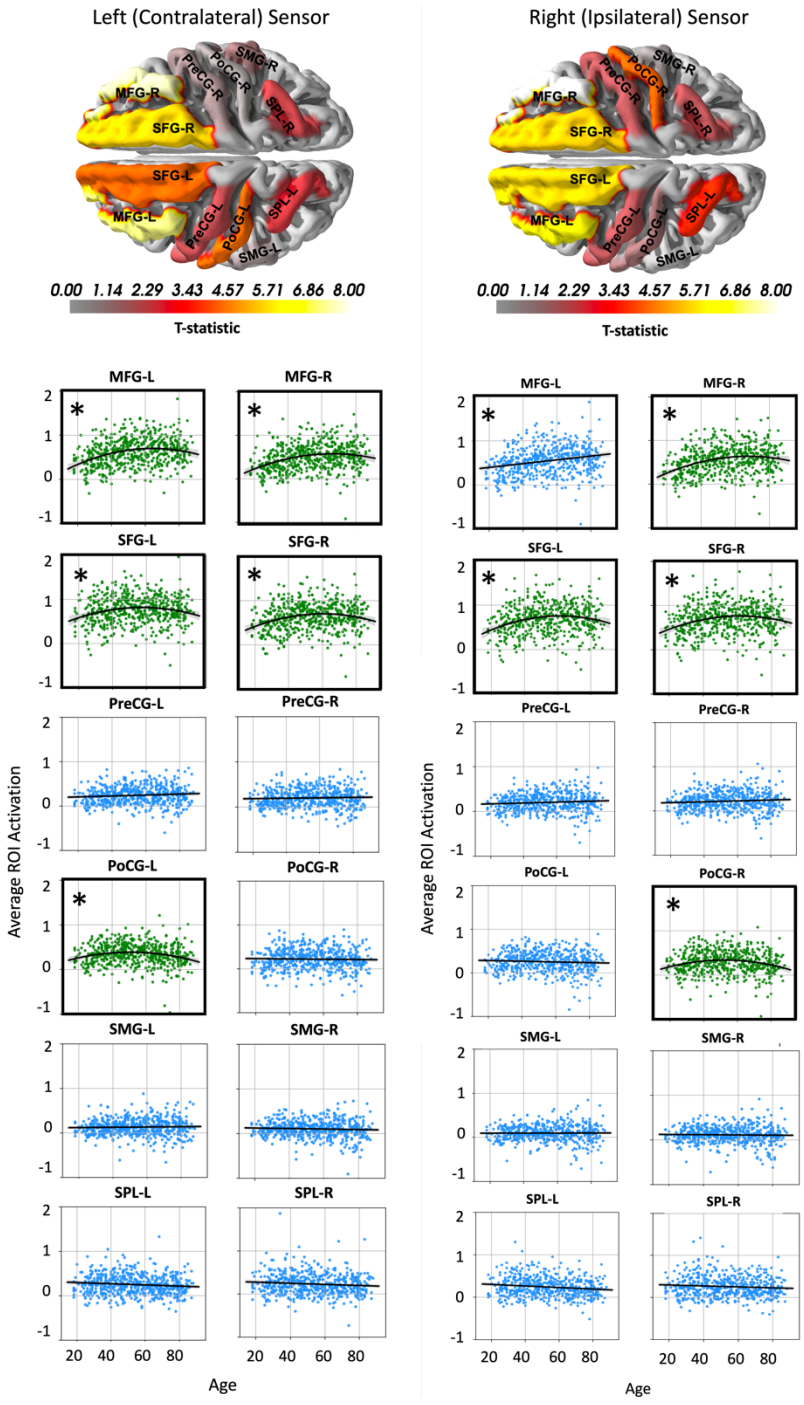

Figure 2.6 The best-fit regression models for each of 12 anatomical regions of interest. The average beta burst source power values during the post-movement condition for each region of interest are plotted against age along with the best-fit regression model (linear: blue; quadratic: green). The T statistics associated with the chosen models are plotted

using a colour bar on the dorsal view of the 3-dimensional head model. Data is shown from 561 healthy participants from the left and right sensors. Resting state and pre-movement data is shown in Appendix A.

For bursts detected by the left (contralateral) sensor during the resting state condition, all regions of interest had linear changes in relative power with age, but the majority of the fits were non-significant. A significant positive linear trend was observed only in the left middle frontal gyrus ($p = 5.46e-5$). For bursts detected by the right (ipsilateral) sensor during the resting state condition, all of the of the regions of interest also showed non-significant linear trends with age. For bursts detected by the left (contralateral) sensor during the pre-movement interval, all regions of interest had linear changes in relative power with age, but all fits were non-significant. For bursts detected by the right (ipsilateral) sensor during the pre-movement interval, all regions also showed non-significant linear trends. The lack of significance of these results suggests that there is little support for age-related changes in beta burst source localization during the resting and pre-movement interval using the methods described.

In the post-movement interval, there was a mix of quadratic and linear age-related trends that were observed, with many regions of interest having significant trends. For bursts detected by the left (contralateral) sensor, these regions include the right middle frontal gyrus ($p = 1.86e-13$) and superior frontal gyrus ($p = 4.81e-8$) and the left middle frontal gyrus ($p = 2.70e-12$), superior frontal gyrus ($p = 1.72e-5$) and post-central gyrus ($p = 1.06e-5$). Each of these regions had a positive slope in younger participants followed by a significant negative quadratic trend with a peak at approximately 60 years of age. For bursts detected by the right (ipsilateral) sensor, the right middle frontal gyrus ($p = 6.90e-15$), superior frontal gyrus ($p = 7.43e-8$), and post-central gyrus ($p = 1.89e-5$), and the left middle frontal gyrus ($p = 5.70e-9$) and superior frontal gyrus ($p = 3.10e-8$) had significant age-related trends. The majority of these trends followed the same quadratic trend described in the left sensor data, with the exception of the left middle frontal gyrus which showed a positive linear trend with age. The statistical significance of these trends indicates that these anatomical regions may play an important role in age-related changes in the network that generates beta bursts.

It can be noted from Figure 2.6 that all significant quadratic trends in the post-movement interval reach their peak amplitude (vertex) at approximately 60 years of age. For bursts detected by the left (contralateral) sensor in the post-movement interval, the average peak age for significant quadratic fits was 59 + /- 6 years (mean + /- standard deviation). For bursts detected by the right (ipsilateral) sensor in the post-movement interval, the average peak age for significant quadratic fits was 60 + /- 6 years. This provides evidence for the presence of a critical age at approximately 60 years. Prior to this age, relative source power increases across many regions of interest, however, after this point, relative source power begins to level off and, in some cases, decreases with increasing age.

2.5.5 Peak Location Ageing Trends

Figure 2.7 indicates that there were also shifts in the peak source location with increasing age. For bursts detected at the left (contralateral) sensor, there were significant anterior shifts in peak source location with age found in the resting state (p = 8.263e-05) and post-movement (p = 8.221e-10) conditions. This trend can be appreciated qualitatively in Figure 2.7 and suggests an age-related shift in the main generator of beta bursts in these conditions. There were no significant relationships between the medial/lateral or inferior/superior coordinates and participant age. For bursts detected at the right (ipsilateral) sensor, there were no significant relationships between peak coordinate and participant age detected in any of the conditions.

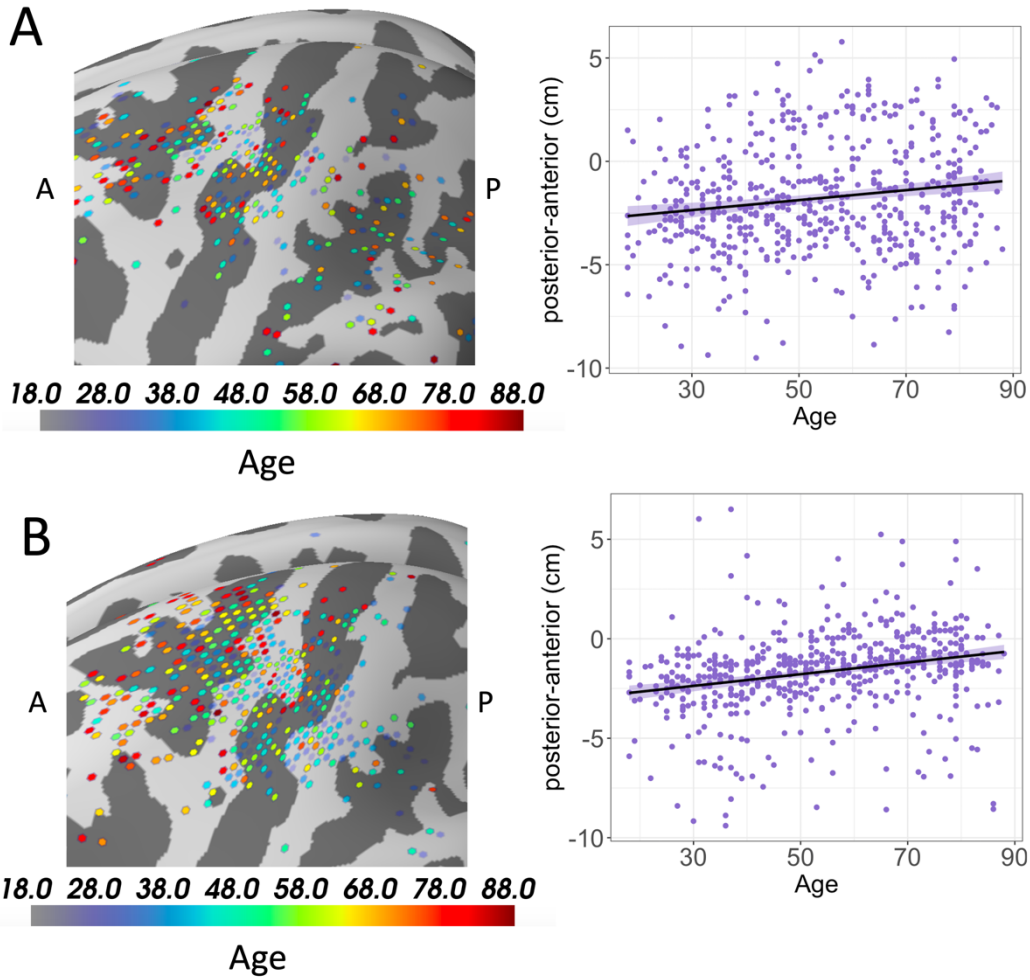

Figure 2.7 Significant trends in peak location with age. Peak location of transient beta bursts detected at the left (contralateral) sensor during the (A) resting state and (B) post-movement conditions. Points on the 3-dimensional average brain model (left) show the peak location for each participant, with colour representing the age of the participant. Pictured here is a section of the left central brain region, enlarged to show the shift in peak position in this region. "A "and "P "labels indicate the anterior and posterior ends of the section. Both conditions show an anterior shift with age indicated by the positive trends in the y-coordinate with age (right). Non-significant conditions are not shown in this figure.

2.5.6 Source Map Ageing Trends

Because there was evidence of both linear and quadratic age-related trends in Figures 2.5, 2.6, and 2.7 we implemented a post-hoc analysis to further investigate the difference in source maps between age groups, quantified as a T statistic. The data was binned into fine, 2-year age groups and an average relative power map was calculated for each age group. Paired sample T-tests were then conducted between each pair of maps

and the resulting T statistics are plotted using a colour bar in Figure 2.8 . Here, a high T statistic indicates that the beta burst source map is very different between participants in age groups X and Y. Yellow and green regions of the figure represent comparisons that had the highest T statistics. Looking at the age groups associated with these comparisons can give us an indication of ages at which the beta burst source pattern undergoes significant changes.

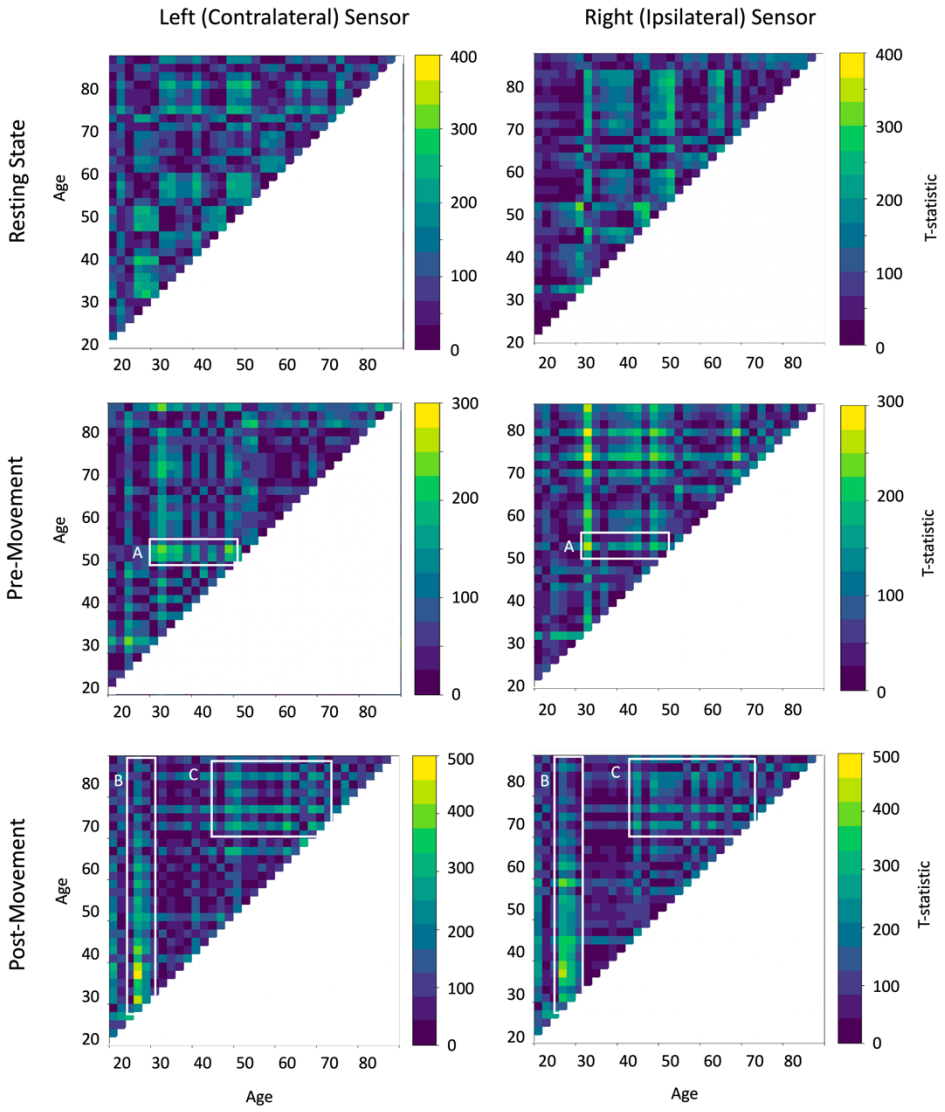

Figure 2.8 T statistics computed by conducting paired-samples T-tests between the average source estimations of all 2-year age groups. The colour bar represents the magnitude of the T statistic with purple representing low values (similar source maps) and yellow representing high values (dissimilar source maps). Note the differences in scale between conditions. Data is shown for resting state (top), pre-movement (middle) and post-movement (bottom) conditions. Attention should be drawn to yellow and green regions, which represent comparisons between groups that had the highest T statistics and

therefore the most dissimilar source estimations. Boxes A, B, and C highlight some of these regions of this plot that show the highest T statistics. Notably, box A highlights a large difference in source estimation pattern between individuals in their 30s-40s and those in their 50s-60s, box B highlights a difference between individuals in their mid-20s and all other ages, and box C highlights a difference between individuals in their 40s and those over 70.

The T statistics were the highest in the post-movement condition (left sensor: 170 + /- 132; right sensor 181 + /- 137 (mean + /- standard deviation)), indicating the highest variability between age groups, followed by the resting state condition (left sensor: 111 + /- 85; right sensor: 141 + /- 104) and then the pre-movement condition (left sensor: 87 + /- 64; right sensor: 94 + /- 69). The majority of tests were highly significant with a critical T statistic of 6.54.

In the pre-movement condition, the pairs that showed the highest T statistics, and were therefore the most dissimilar, were those in their 30 s and 40 s paired with those in their 50 s and 60 s (see Figure 2.8 , box A). The mean T statistic for groups aged 30–50 compared to groups 52+ was 101 + /- 71 for the left sensor and 123 + /- 81 for the right sensor. These values are higher than the overall sensor means for the pre-movement condition indicating that there may be a critical age around 50 years after which the pattern of source localization is dissimilar to the pattern that was present in the preceding years.

In the post-movement interval, the highest T statistics appear when comparing those in their mid-20s to any other age group (see Figure 2.8 , box B). The mean T statistic when comparing groups aged 22–28 to all other groups was 314 + /- 140 for the left sensor and 331 + /- 153 for the right sensor. This indicates that there is a fundamental difference in the source localization present in the youngest age group that could signify a shift in brain activity beyond a critical age. This finding is in line with the observation that the 18-32-year age group had an average spatial localization map that was dissimilar from older age groups in the post-movement interval (Figure 2.5). Other pairings that exhibited high T statistics were those comparing individuals in their late 40s to individuals in their 70s and above (see Figure 2.8 , box C). When comparing groups age 46–50 to those aged 70+, the mean T statistic was 221 + /- 134 for the left sensor and 203 + /- 110 for the right sensor. This indicates that there could be an additional shift in brain

activity in this dataset that occurs later in life (between 50 and 70 years of age). This is in line with the finding that all significant quadratic trends peaked around this critical age (Figure 2.6) .

In the resting state data, the pairings with the highest T statistics were concordant with those pairings identified in the post-movement interval. Particularly, the resting state condition had the highest T statistics when comparing individuals in their late 40s to individuals above 70. The mean T statistic for these groups was 197 + /- 110 for the left sensor and 217 + /- 76 for the right sensor. This provides further support for the existence of critical ages at which the pattern of brain activity shifts.

2.6 Discussion

2.6.1 Summary of Findings

The present work investigated the efficacy of two well-known source localization algorithms (MNE and DICS beamformer) for use in the localization of the cortical sources associated with transient beta bursts. Movement-related beta bursts were detected at two MEG sensors located in the contralateral and ipsilateral sensorimotor cortices. Bursts localized primarily to the primary motor and somatosensory cortices, as expected, but also showed variable localization in the premotor, superior parietal and supramarginal regions depending on the movement condition. The pattern of beta burst localization was highly concordant between localization methods for the majority of conditions, but the MNE method consistently showed higher relative activation values, and more focal source estimation patterns compared to the DICS beamformer method. This suggests that while both methods are capable of reliably identifying the sources of beta bursts, the MNE localization algorithm has greater amplification of differences between baseline and active bursting intervals and more focal estimation of source. Age-related analysis revealed significant quadratic trends in relative activity in the middle and superior frontal brain regions during the post-movement interval, suggesting an increase in frontal bursting activity with age that peaks at approximately 60 years of age. Further analysis revealed potentially critical ages at 25–30 years and 60 years, during which the spatial pattern of beta burst activity undergoes a significant shift. The results of this study provide support for the use of existing source localization methods for localizing transient

bursting activity and reveal significant age-related trends in the spatial pattern of beta bursts that increase our understanding of age-dependent changes in neuronal activity.

2.6.2 Significance

Bursts detected in the pre-movement interval had a focal, unilateral pattern of localization that was centred on the post-central (somatosensory) gyrus ipsilateral to the sensor used for their detection. Bursts detected in the post-movement interval, on the other hand, were centred on the pre-central (motor) gyrus and had a more widespread, bilateral localization pattern, with slightly stronger activation in the hemisphere contralateral to movement (left). The tendency of pre-movement events to localize posterior to post-movement events is in line with previous findings that beta suppression (prior to and during movement) localizes post-centrally while beta rebound (post-movement) localizes pre-centrally (Jurkiewicz et al., 2006). The finding that pre-movement sources were more focal and lateralized than post-movement sources, however, appears to contradict previous literature that indicates that beta suppression has more diffuse and bilateral representation compared to beta rebound (Jurkiewicz et al., 2006). A possible explanation for this apparent discrepancy is that the documented bilateral movement-related beta suppression, as compared to a pre-movement baseline, is associated with a reduction in independent sources of bursting activity in both the left and right sensorimotor regions. Our findings that the left and right motor cortical sensors (MEG0221 and MEG1311, respectively) detected different unilateral sources of the beta bursts suggests that the two hemispheres independently contribute to the bilateral peaks in average spectral power typically observed in the beta band during the pre-movement interval.

In the post-movement interval on the other hand, our results suggest roughly synchronous timing of beta bursts in the left and right hemispheres. However, further investigation into the coherence of the MEG time courses at MEG0221 and MEG1311 during the post-movement interval revealed that there was very low coherence between hemispheres, suggesting that bursts occurring during this time are generated by independent left and right cortical sources. Given this, a likely explanation for the apparent synchronicity between hemispheres is that the transient beta burst rate increases substantially in both hemispheres during the post-movement interval (Brady et al., 2020).

This movement-related facilitation following movement-related inhibition likely generates a period of time during which beta bursts are more likely to occur in each hemisphere. This would result in rough co-occurrence of beta bursts across hemispheres and spatial maps with bilateral activation irrespective of which sensor was used for event detection. As such, we posit that the bilateral patterns observed are considered to be a statistical anomaly that is an artefact of the analysis rather than the result of a common generator between hemispheres. Regardless, the finding that left hemisphere activity was greater than right hemisphere activity overall suggests that there is more bursting detectable in the hemisphere contralateral to movement compared to ipsilaterally, which provides a potential explanation for the documented lateralization of post-movement beta rebound. The high level of concordance in the location of contributing sources between DICS and MNE methods provides support for the validity of these novel findings.

When examining age-related trends in the patterns of beta event localization, one noteworthy finding was that younger participants, particularly the 18–32-year age group, showed a localization pattern that was highly discordant with older participants. Comparing 2-year averaged maps to one another further supported the uniqueness of this age group as groups in their twenties tended to be highly dissimilar ($T > 300$) from all other age groups. This finding suggests that there are critical differences in the sources of beta generation in young adults compared to middle age and older adults. The most likely explanation for this finding is that the brains of many of the young adults (age < 32) in this study were not fully developed at the time of study. Previous neuroimaging work has indicated that the human brain continues to develop well into a person's twenties (Giedd et al., 1999 ; Sowell et al., 1999 ; Sowell, 2001). This means that the neuroanatomy and physiology of young adults is still changing, and this is likely why we observed discordance in beta event localization between young adults and their older counterparts. This finding has far-reaching implications for the neuroimaging community. Often, studies involving human participants, including neuroimaging studies, recruit healthy participants from an undergraduate and/or graduate student population, resulting in many studies having an average participant age that is skewed towards young adults (e.g., < 25 years). The results of the present study show that the sources of brain activity of participants in this age group are dissimilar from the sources used by older participants,

suggesting that source localization results obtained in young adults may not be generalizable to older adults. We should therefore use caution when interpreting neuroimaging studies for which the sample of participants is restricted to young adults, as these findings may not be reflective of the general population.

When assessing relative source power in various anatomical regions of interest, the most significant continuous age-related trends that emerged were the quadratic trends observed in the post-movement data. It was initially hypothesised that relative source power would vary linearly with age, such that sources surrounding the sensorimotor cortex, including the premotor and supplementary motor areas, would show an increase in relative activation with increasing age. This hypothesis was based on previous fMRI studies that indicated that older participants tend to recruit more widespread compensatory mechanisms when performing a motor task (Hutchinson, 2002 ; Mattay et al., 2002 ; Vallesi et al., 2010). There was relatively good agreement between the compensatory areas suggested in the previous work and the regions of interest that showed the most significant age-related changes in the present work. Particularly, the superior and middle frontal regions (premotor areas) had highly significant age-related trends in the post-movement data across both localization methods. However, these regions exhibited an increase in magnitude with age that ceased around 60 years of age, rather than a linear increase over all ages.

While quadratic trends were not hypothesised, they are also not unfounded. In a previous paper published by our group using the same dataset, we examined age-related trends in beta event characteristics (event rate, peak frequency, duration, peak power, etc.) and found that many of these characteristics exhibited quadratic trends with age. Particularly, the peak power of the events showed an initial positive correlation with age followed by a negative quadratic age-related trend in the rest, pre-movement and post-movement conditions (Brady et al., 2020). The relative source power computed in the current work showed a similar quadratic age-related trend across a number of frontal and central regions of interest. In addition, the vertex of the quadratic trends observed in the previous work tended to fall around 60 years, which matches the approximate vertex of the parabolas observed here. The consistency of this relationship along with the concordance to the previous event characteristic findings (Brady et al., 2020) suggests

that there may be a critical shift in brain activity at approximately 60 years of age. Prior to this age, relative source power steadily increases across bilateral frontal and central brain regions. After this point, however, there is a change in the trajectory of the trend and relative source power begins to fall off in these regions. This pattern could be indicative of a functional shift in activity that occurs later in life and could signify a critical age in the normal ageing process for the sensorimotor neural network.

2.6.3 Limitations and Future Directions

This study demonstrated the successful implementation of source localization algorithms for use in localizing transient beta bursts detected at single sensors centred over the right and left sensorimotor cortices. While this has provided us with valuable information, the use of individual sensors for beta burst localization is a limitation of this method because each sensor is sensitive to activity at a number of sources in the brain. For that reason, it would be beneficial for future studies to investigate the possibility of identifying beta bursts of interest by a combination of spatial and temporal characteristics, rather than their presence at a single sensor. This would allow for more accurate identification of bursts associated specifically with the sensorimotor network. Such analysis could be implemented with an iterative learning algorithm such as convolutional sparse coding (Dupré La Tour et al., 2018). However, this method requires further validation before it can be implemented for use in beta burst localization.

2.7 Conclusion

In the present work, two source localization algorithms were successfully implemented to localize the cortical sources of transient beta bursts during pre-movement, post-movement and resting state conditions. Beta bursts detected during the pre-movement and post-movement intervals had approximately concordant localization patterns to those observed in beta suppression and rebound providing support for the validity of the current methods. This work also revealed several age-related phenomena including a unique localization pattern in young adults compared to older adults that is likely due to ongoing brain development, and the presence of a critical shift in the sources of beta bursts at age 60. The results of this work have provided validation for the use of existing source localization methods for identifying the cortical sources of transient beta

bursts and have advanced our understanding of the relationship between beta bursts and normal healthy ageing.

Chapter 3

Using Convolutional Dictionary Learning to Detect Task-Related Neuromagnetic Transients and Ageing Trends in a Large Open-Access Dataset

3.1 Preamble

The work presented in Chapter 2 provided important insights into the generative sources of transient beta bursts during a sensorimotor task and rest. However, a key methodological limitation was identified in this work. In Chapter 2, and in other work by our group (Brady et al., 2020), transient bursts were detected using a simple amplitude thresholding method to identify high power bursts of activity within a pre-defined frequency range of interest (see Section 1.5.3). While this is one of the most commonly used burst detection approaches, it is limited in its applications due to its imposition of assumptions about the frequency, waveform shape, and linearity of the signal of interest. Further, this method operates on a single signal (e.g., channel or source reconstructed time course), and does not take into consideration multi-channel interactions or signal spread, making it difficult to compare spatiotemporal characteristics between subjects. For these reasons, we wished to develop and validate a multi-channel, data-driven approach to investigating transient bursts that would improve upon the burst detection methods employed in Chapter 2. Therefore, Chapter 3 applies a data-driven convolutional dictionary learning approach to naively detect task-related neuromagnetic transients in the large CamCAN dataset and introduces a novel clustering method to evaluate age-related changes in transient event characteristics across the group.

Chapter 3 of the thesis contains peer-reviewed work published in *NeuroImage* in February, 2023. Text in the introduction and discussion has been modified to reduce redundancies in the thesis, but the methods and results sections appear as published. The reference for the publication is provided below.

Power, L., Allain, C., Moreau, T., Gramfort, A., & Bardouille, T. (2023). Using convolutional dictionary learning to detect task-related neuromagnetic transients and ageing trends in a large open-access dataset. *NeuroImage*, *267*, 119809. https://doi.org/10.1016/j.neuroimage.2022.119809

3.2 Abstract

Human neuromagnetic activity is characterised by a complex combination of transient bursts with varying spatial and temporal characteristics. The characteristics of these transient bursts change during task performance and normal ageing in ways that can inform about underlying cortical sources. Many methods have been proposed to detect transient bursts, with the most successful ones being those that employ multi-channel, data-driven approaches to minimize bias in the detection procedure. There has been little research, however, into the application of these data-driven methods to large datasets for group-level analyses. In the current work, we apply a data-driven convolutional dictionary learning (CDL) approach to detect neuromagnetic transient bursts in a large group of healthy participants from the CamCAN dataset. CDL was used to extract repeating spatiotemporal motifs in 538 participants between the ages of 18–88 during a sensorimotor task. Motifs were then clustered across participants based on similarity, and relevant task-related clusters were analysed for age-related trends in their spatiotemporal characteristics. Seven task-related motifs resembling known transient burst types were identified through this analysis, including beta, mu, and alpha type bursts. All burst types showed positive trends in their activation levels with age that could be explained by increasing burst rate with age. This work validated the data-driven CDL approach for transient burst detection on a large dataset and identified robust information about the complex characteristics of human brain signals and how they change with age.

3.3 Introduction

Recent work has shown that sensorimotor beta burst characteristics change with normal healthy ageing. Particularly, it has been demonstrated that transient beta burst characteristics (e.g., burst rate, peak frequency, peak power) show age-related changes (Brady and Bardouille, 2022; Brady et al., 2020) that can explain the previously observed age-related increase in sensorimotor beta suppression in the average (Bardouille et al., 2019; Rossini et al., 2007). Furthermore, it has also been shown (in Chapter 2) that the spatial localization of transient beta bursts changes with age, expanding to recruit additional areas, and exhibiting an anterior shift in peak localization with increasing age (Power and Bardouille, 2021).

With increasing interest in transient burst-based analyses developing in recent years, has come a surge in development of analysis methods for detecting and characterising bursts. At present, there is no gold-standard method for detecting and characterising transient bursts in electrophysiological data, and the various proposed methods come with associated advantages and limitations (as described in Section 1.5.3). In addition, there is no obvious framework to complete a group-level analysis of the combined spatial and temporal characteristics of identified bursts and most techniques have not been optimized for use with large datasets.

This work aims to address these gaps by applying multivariate convolutional sparse coding (CSC) which is a specification of the broader class of convolutional dictionary learning (CDL) algorithms, to detect transient bursts in a large open-access dataset. CDL represents the multivariate neural signals as a set of spatiotemporal patterns, called *atoms*, with their respective onset times and magnitudes, called *activations*. CDL has emerged as a convenient and efficient tool to extract patterns, in particular due to its ability to easily include physical priors for the patterns to recover. For example, for M/EEG data, Dupré la Tour et al. (2018) have proposed a CDL method which extracts atoms that relate to the current dipoles used to model brain activity by imposing a rank-1 structure to better account for the linear spread of the signal across channels. Each atom is associated with an activation vector that provides a record of time points throughout the signal at which the atom is present, and the associated magnitude of the atom at those time points (Dupré la Tour et al., 2018; Jas et al., 2017; Moreau and Gramfort, 2020). CDL operates similarly to classical Independent Component Analysis (ICA; Winkler et al., 2015), decomposing the signals as a sum of topographies and sources (Dupré la Tour et al., 2018). However, CDL does so not by assuming that the sources are independent, but by assuming that the source time courses are formed by repeated waveforms. CDL has been previously validated on single subject datasets to recover biological artifacts, non-sinusoidal mu patterns with sensorimotor topography, occipital alpha bursts, and evoked-type responses (Allain et al., 2021; Dupré la Tour et al., 2018).

Despite the success of CDL and other data-driven methods on single subject studies, the validity of multi-channel, data-driven methods for use in between-subject comparisons and group-level analyses has been largely unexplored. Some work has

employed HMM extended to a multi-subject setting by concatenating data across participants to identify common repeating states (Baker et al., 2014; Becker et al., 2020; Quinn et al., 2018; Seedat et al., 2020; Vidaurre et al., 2016), and few studies have demonstrated that ICA and EEG Microstates yield consistent patterns across participants (Himberg et al., 2004; Michel and Koenig, 2018). However, none of these studies explored variability between subjects, and group-level differences and trends, highlighting the need for methods to explore group-level trends in transient bursts detected by a robust data-driven method. The favourable characteristics and promising preliminary results of the CDL method make it a logical candidate for group-level investigations of transient bursts.

The objective of the current work is thus to use the CDL method to detect and characterise ageing trends in task-related transient bursts at the group level in a large, open-access dataset. Here, we detect (in single subjects) repeating spatiotemporal atoms in sensorimotor MEG data from the CamCAN dataset (Shafto et al., 2014; Taylor et al., 2017), and cluster similar atoms across participants to allow for group-level analysis. We then assess clusters for age-related trends in atom characteristics. It is hypothesised that CDL will successfully extract task-related atoms that are biologically plausible, including those that resemble sensorimotor beta and mu transient bursts. This hypothesis is based on the findings of previous literature that demonstrate a functional role of beta and mu transient bursts in sensorimotor tasks (Errington et al., 2020; Feingold et al., 2015; He et al., 2020; Hebert and Lehmann, 1977; Lakatos et al., 2004; Little et al., 2019; Lundqvist et al., 2016; Shin et al., 2017; Wessel, 2020). It is further hypothesised that within task-related atom clusters, atoms will show age-related changes in their spatiotemporal characteristics, in line with previous findings. Specifically, it is predicted that for sensorimotor beta-type bursts, burst frequency will decrease with age, spatial position will shift anteriorly with age, and pre-movement activation will increase with age as a result of increasing burst rate with age (Bardouille et al., 2019; Brady et al., 2020).

This work presents, for the first time, the detection of group-level trends in transient bursts using a flexible, multi-channel, data-driven CDL method. By combining this powerful detection algorithm with the big data available in the CamCAN dataset, we can increase our understanding of the role of neuromagnetic transients in normal healthy

ageing and provide an improved framework for analysing transient bursts at the group level in future work.

3.4 Methods

This work uses the same dataset as described in Chapter 2. Refer to Chapter 2 for descriptions of the participants and experimental paradigm (2.4.1), data acquisition (2.4.2) and MRI data processing (2.4.3).

See Figure 3.1 for a workflow diagram describing the analysis procedure for this work.

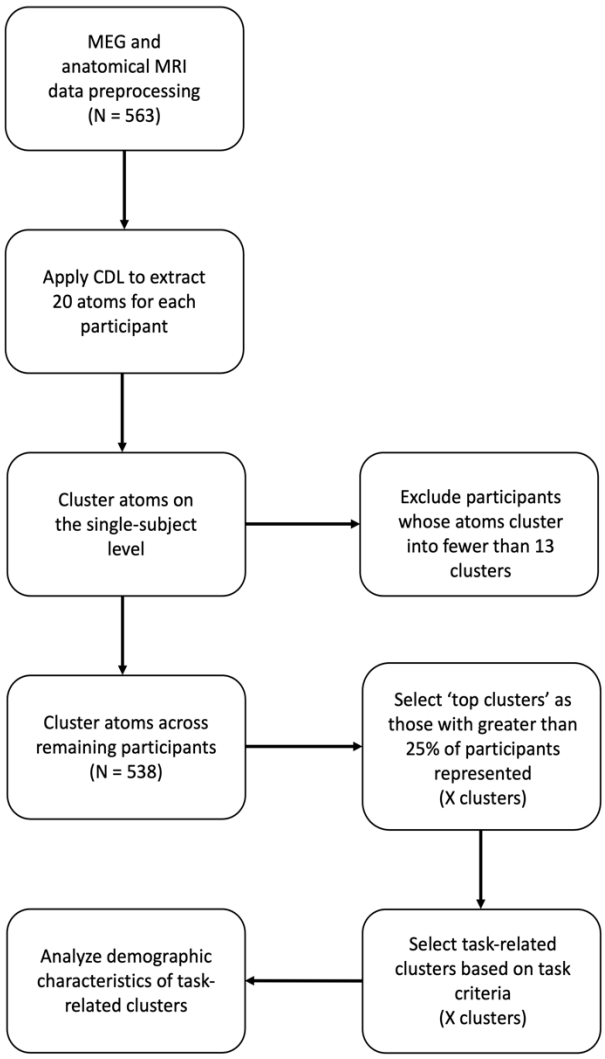

Figure 3.1 Workflow diagram.

3.4.1 MEG Data Processing

All MEG processing was completed in the Python programming environment (v.3.7.7), using the MNE-Python library (v.0.23.0) (Gramfort et al., 2013; 2014). Python code for this analysis is available at https://github.com/tbardouille/camcan_CSC_beta. Data were pre-processed using temporal signal space separation (tSSS) to perform environmental noise reduction, and reconstruction of missing or corrupted MEG channels (Taulu and Simola, 2006). The task data was then parsed into trials synchronized to each button press, with a duration of 3.4s, including a 1.7s pre-movement interval. The 3.4s window length was selected to ensure a sufficient post-movement interval to capture the entire beta rebound response. Trials were excluded if the button press occurred more than 1s after the cue (indicating poor task performance) or if the button press occurred within 3s of the previous button press (which provided insufficient baseline for subsequent analysis). Data were bandpass filtered between 2 Hz and 45 Hz and resampled with a sample rate of 150 Hz.

3.4.2 Convolutional Dictionary Learning

Convolutional Dictionary Learning (CDL) was applied to each subject to extract 20 spatiotemporal atoms of duration 500ms from the multivariate MEG recording (see Figure 3.2). The objective of CDL is to decompose a signal into the convolution between a few translationally invariant recurring patterns, called atoms, and their sparse activation vectors. This is done by minimizing an objective function (see supplementary Equation B.1) that represents the residuals of the signal after the dictionary of atoms has been removed, plus a sparsity promoting regularization that pushes the activation vector to be as sparse as possible. In the application to M/EEG signals, a rank-1 constraint is added to the dictionary to take into account the physics of the signals (i.e., the instantaneous linear spread of the signals across channels; see supplementary Equation B.2). This extra constraint decomposes the atoms with a spatial and a temporal component, which can easily be interpreted by neuroscientists. The optimization is done in an alternating way: the dictionary is fixed and the activation vectors are learned, then vice versa, and the operation is repeated until convergence. The result of the optimization is a set of instantaneous spatiotemporal signals and associated sparse activation vectors.

In the current work, we relied on the alphacsc Python package (Dupré la Tour et al., 2018) for CDL with rank-1 constraint. The hyperparameters used in this work are based on those established by Dupré la Tour et al. (2018) and used in the alphacsc tutorials. These hyperparameters were used because they have given satisfying results for detecting similar types of induced responses (e.g., somatosensory mu waves) in previous work. For each considered subject, CDL outputs 20 spatiotemporal atoms alongside their respective sparse activation vector z that corresponds to the onsets of the waveforms. For each atom, CDL with rank-1 constraint provides the topography, later referred to as u of size number of MEG sensors, and the temporal waveform v of duration 500ms.

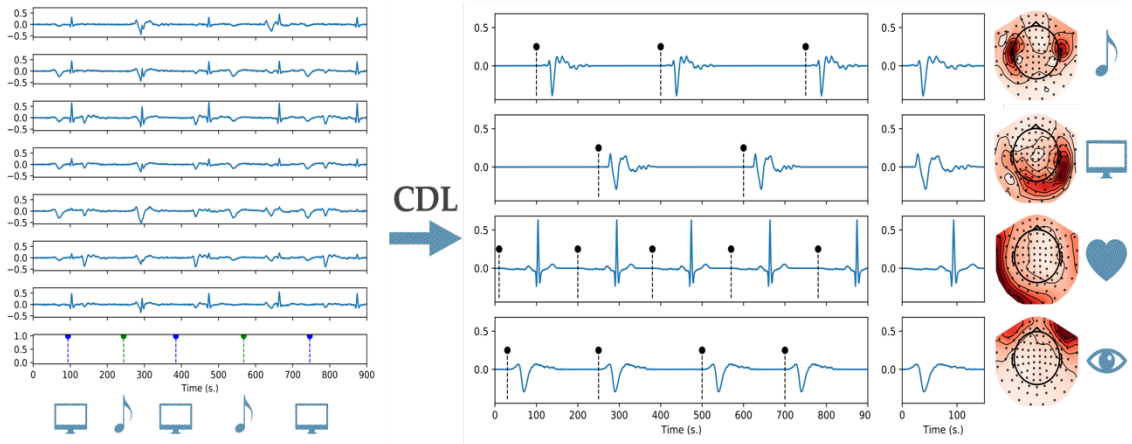

Figure 3.2 CDL decomposes raw signals (left) as the convolution between the sparse activation signal (black stem on the right) and the pattern obtained as the product of a spatial map and a temporal pattern. The bottom row on the left corresponds to stimuli events (visual or auditory). Each atom on the right can be associated with a response type (auditory, visual, heartbeat and eye blinks).

3.4.3 Atom Clustering

After applying CDL to each individual participant, atoms from all participants were clustered into groups, based on their spatiotemporal similarity. The approach of detecting atoms in individuals and then clustering across participants was employed to ensure that individual variability in atoms was preserved to allow for between-subject comparisons of atom characteristics. A correlation-based clustering approach taking into consideration both the u (spatial) and v (temporal) vectors was applied to the atoms. The clustering relies on a simple iterative approach that groups atoms together on the basis of high correlation without prior specification of the number of clusters. This method is similar to that described by Bansal et al. (2004) and has been widely used for biomedical

clustering applications in the past (Bhattacharya and De, 2008; 2010; Miljkovic et al., 2010). This method was selected over other traditional clustering methods because it allowed for simultaneous consideration of multiple clustering metrics (i.e., both spatial and temporal vectors), which is not possible with other "out of the box" clustering methods.

To compare two atoms ($u1$, $v1$) and ($u2$, $v2$), we used the Pearson correlation coefficient of the u vectors R_u and the maximum cross-correlation coefficients of the v vectors R_v. Cross-correlation was used for the v vector to account for phase differences in otherwise similar waveforms. The algorithm then stepped through each atom of interest sequentially (in no particular order), and clustered atoms with one another based on the magnitude of their correlation coefficients (R values). Each atom was compared to pre-existing clusters by calculating R_u and R_v values between the current atom and each atom in the cluster, and then averaging across all R values (for u and v separately) obtained from the cluster. If, for a given cluster, both (R_u and R_v) average values exceeded a pre-determined threshold ρ, the atom was considered highly correlated to the cluster. For atoms that were highly correlated to more than one pre-existing cluster, the atom was added to the cluster to which it had the highest cumulative correlation (average R_u + average R_v) . If the atom was not highly correlated (i.e., the average R_u and R_v values did not exceed the threshold) to any of the pre-existing clusters, then a new cluster was created. The algorithm proceeded through all atoms of interest, yielding a number of clusters not defined a priori.

Preliminary correlation-based analysis of single participants' atoms revealed that a few participants had numerous highly correlated atoms (i.e., little variability in the spatiotemporal features of their atoms) as presented in Figure 3.3. Visual inspection of the atom data revealed that these participants tended to have atom profiles dominated by artefacts (i.e., eyeblink and other global artifacts, see Figure B.1 compared to Figure B.2) or by a persistent slow (alpha frequency) rhythm with variable topographic representation. This observation suggested that these participants have abnormal and/or artefactual data that should be excluded from further analysis to avoid skewing effects in the whole-group clustering process. This prompted the development of an exclusion

process based on the correlation-based clustering methods described above, by which participants with low atom variability were identified and excluded from further analysis.

Here, the 20 atoms computed for a given participant were compared to one another and clusters of highly similar atoms were created within participants. In order to select the optimal *R* value threshold ρ for clustering, the threshold was varied from $\rho = 0.2$ to $\rho = 0.9$ and clustering was performed for each value of ρ. Histograms illustrating the number of clusters yielded per participant were then created and examined for each value of ρ (see Figure B.3). The goal of the analysis was to select a threshold that yielded maximum separation between participants with few groups (high degree of similarity between atoms) and those with many groups (dissimilar atoms). Therefore, histograms were examined for a bimodal distribution with maximal separation between peaks. On this basis, a *R* value threshold of $\rho = 0.8$ was selected. All participants with less than 13 distinct groups of atoms were excluded from subsequent analyses. The value of 13 clusters was selected as the point that best separated the first and second peaks of the distribution. Based on these criteria, 25 participants were excluded at this step, resulting in a total of 538 participants who were used for the remaining analyses.

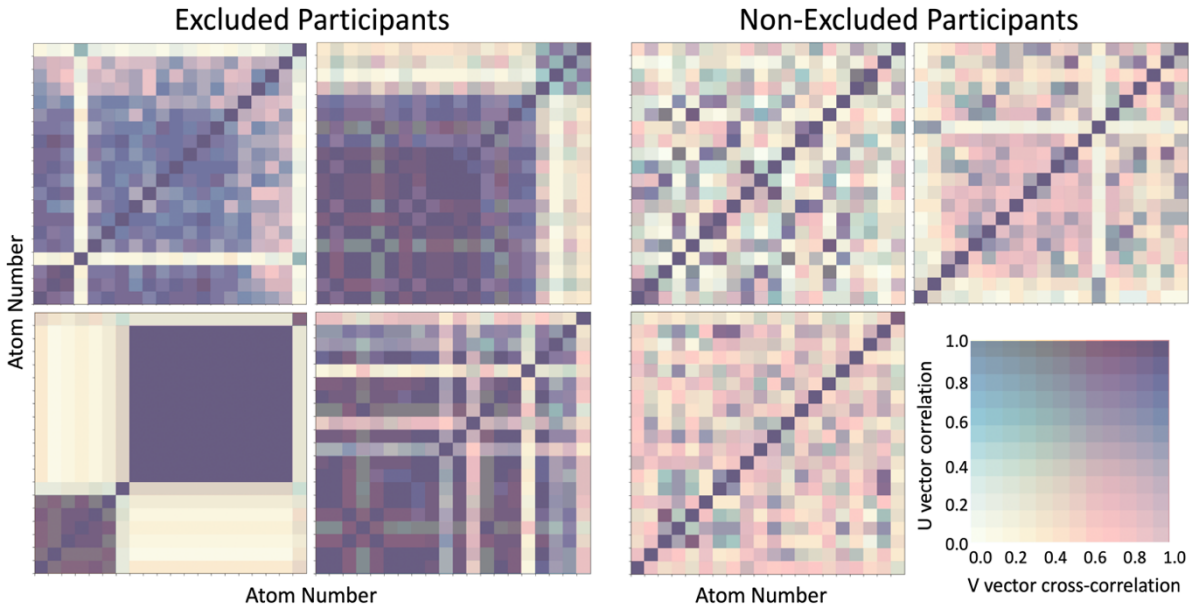

Figure 3.3 Two-variable correlation matrices from a representative sample of participants who were excluded (left) or not excluded (right) from the dataset. Each 20 ×20 cell correlation matrix shows data from a single participant, comparing each of the participant's 20 atoms to each other. The colour of the cells represents the magnitude of

the spatiotemporal correlation between each pair of atoms. As indicated in the legend on the bottom right, *u* vector correlation is represented by a white to blue colour bar (low to high correlation), and the *v* vector cross-correlation is represented by a yellow to red colour bar. Atom pairs with a high correlation in both the *u* and *v* vector are thus indicated by dark purple colouration in the correlation matrices. It can be observed from the examples given here that excluded participants have numerous highly correlated atoms presenting as many dark purple cells in their matrices. This is highly dissimilar from other non-excluded participants, for whom the correlation matrices have few highly correlated atoms.

The correlation-based clustering methods described above were then applied on the whole-group level to create clusters of atoms of the same type across participants, which would facilitate atom comparisons between participants. The selection of an *R* value threshold ρ for the global clustering was conducted separately from the single subject clustering due to the differing objectives of the two analyses. While the single subject clustering aimed to exclude participants with an abnormally high degree of similarity between atoms, the global clustering aimed to create clusters of atoms between participants that had a lower level of similarity but could be presumed to be representative of similar neural processes. Therefore, it was predicted that the ρ used for the global clustering would be lower than that of the subject level clustering.

To select the optimal ρ for the global clustering, the threshold was once again varied from $\rho = 0.2$ to $\rho = 0.9$ and clustering was performed for each threshold. Because of the high computational time associated with clustering on a 538-person dataset, threshold selection was performed using 10 randomly selected 50-person datasets. The *R* value threshold ρ was selected based on the analysis of both qualitative and quantitative metrics. Firstly, the *u* and *v* vectors of a selection of atoms in each cluster were manually inspected to qualitatively assess the success of the clustering. Functional labels (e.g., “occipital alpha ”, “left central beta ”, “eyeblink artefact ”, etc.) were assigned to atoms in each cluster to assess whether similar types of atoms were being appropriately clustered together for various *R* thresholds. This qualitative analysis suggested that $\rho = 0.4$ yielded the most appropriately grouped atom clusters. This selection was supported by quantitative metrics comparing the number of clusters detected at each *R* threshold to the number of “top clusters ”(i.e., common clusters, defined as clusters for which a minimum of 25% of participants had atoms present in the cluster; see Figure 3.5). Figure 3.4 shows

that $\rho = 0.4$ yielded the highest number of top clusters relative to the overall number of clusters, suggesting that the top clusters were most representative of the group. These findings were consistent across 10 random selections of data, suggesting that the choice of threshold was stable, and that the selection and ordering of subjects did not have a large effect on the overall results. $\rho = 0.4$ was thus selected as the optimal clustering threshold for the global analysis and was used in subsequent analysis of the entire dataset.

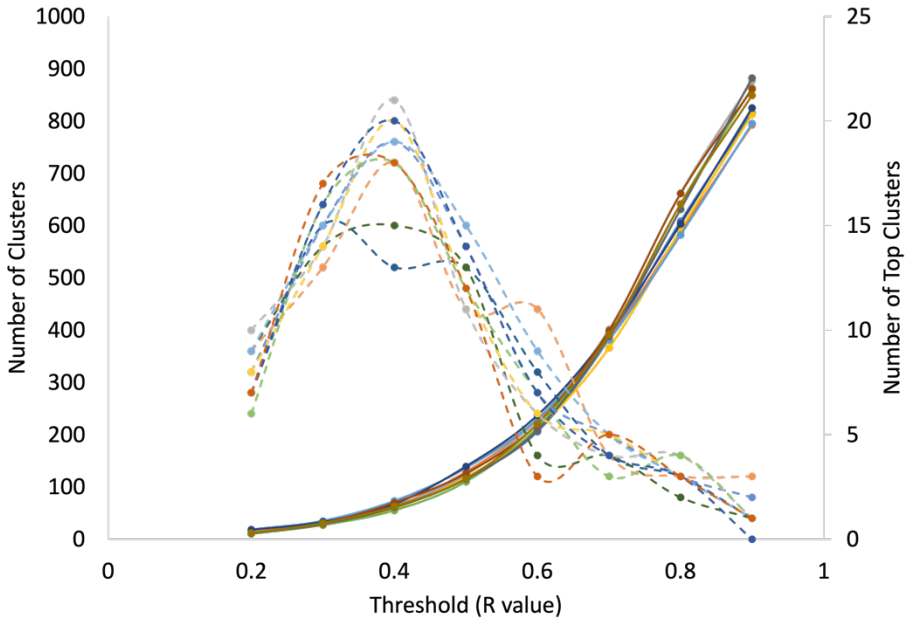

Figure 3.4 Plot showing the total number of clusters (solid lines) and the number of top clusters (dashed lines) identified with varying *R* value thresholds. Each colour of line is a different random sample of 50 participants from the CamCAN dataset. For all samples, the total number of clusters increases as the threshold increases, while the number of top clusters shows a clear peak at approximately $\rho = 0.4$.

Global clustering on the entire dataset yielded 226 clusters of atoms, 11 of which were considered "top clusters" by the criteria that a minimum of 25% of participants had atoms present in the cluster. The 25% value was selected as a reasonable trade-off between maximizing the number of participants in the top clusters and ensuring that movement-related atoms of interest were being captured. Figure 3.5 shows representative atoms for each of the top clusters identified when the minimum percentage was varied to values of 50, 35, 25, 20, and 15%. Minimum percentages above 25% primarily captured eyeblink artifacts as these were the most stereotypical atoms in the population. The 25%

cut-off was the greatest cut-off that provided insight into movement-related atoms of interest (e.g., contralateral sensorimotor beta) and was therefore selected as an appropriate threshold to define top clusters. To ensure adequate sample sizes for assessing cross-sectional ageing trends, only these top clusters are analysed in subsequent sections. However, additional analysis of other smaller clusters can be found in the supplementary material Figure B.7.

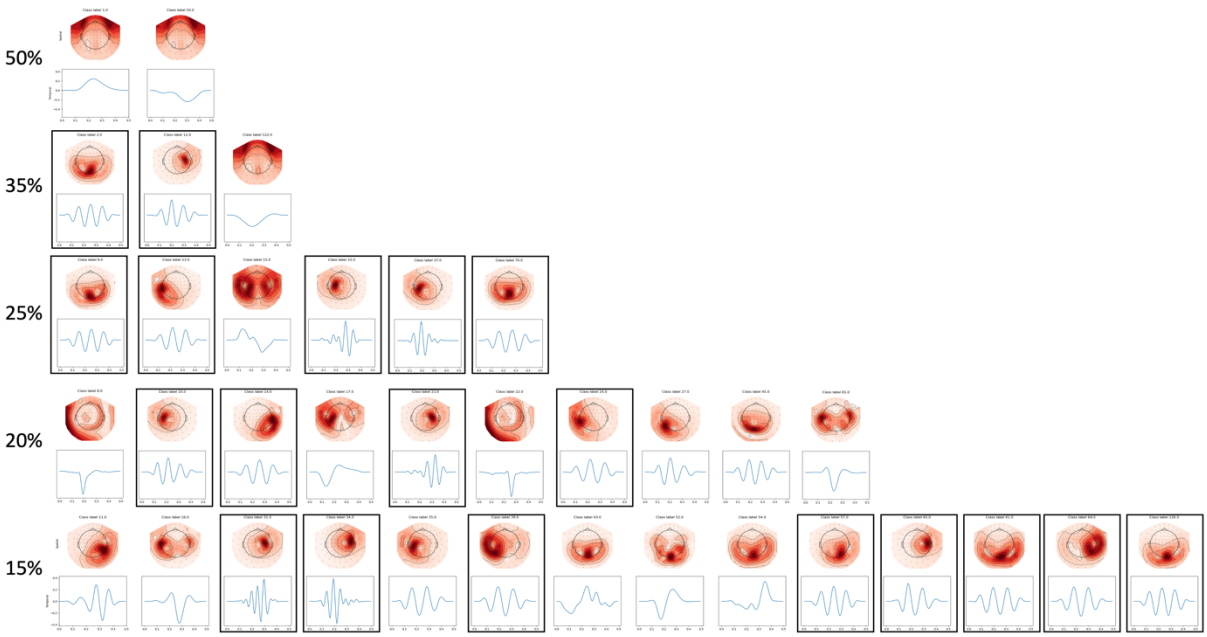

Figure 3.5 Representative atoms (spatial topographies and temporal waveforms) for the top clusters that are returned when the top cluster cut-off is varied. The top clusters identified at values of 50, 35, 25, 20, and 15% are shown. Note that each percentage captures all the clusters in its row, as well as all of the above clusters. Black boxes - indicate the clusters that were determined to be "task-related" (as defined in Section 3.4.4). It can be observed that task-related clusters resemble common induced responses (e.g., occipital alpha, and sensorimotor beta and mu), while non-task-related clusters resemble common artefacts (e.g., eyeblinks and heartbeats), and evoked responses (e.g., auditory and visual).

3.4.4 Selection of Task-Related Atom Clusters

Each of the top clusters were then analysed to reveal which were "task-related". Clusters were classified as task-related based on criteria related to the average characteristics of their component atoms (i.e., the individual atoms that make up the cluster). In particular, atoms in a cluster had to have, on average, a focal source and a task-related reduction in activation. These criteria are based on previous findings that

task-related transients, particularly the movement-related beta transients hypothesized to be present in this work, have a focal localization pattern (Power and Bardouille, 2021) and a marked reduction and rebound in their rate of occurrence with the onset and offset of task performance (Brady et al., 2020). The focality of source was determined for each atom by calculating an equivalent current dipole (ECD) from the spatial representation of *u.* The dipole was then projected onto the participant's MRI to determine the anatomical position and orientation of the source. If the average goodness of fit for atoms in a given cluster exceeded 90%, then the cluster source was considered to be focal. The task-related reduction in activity criteria was assessed by segmenting the activation *z* vector into pre-task, task, and post-task intervals (where the task was a unimanual button press) and calculating the percent change in activation between intervals. The pre-movement, movement, and post-movement intervals were set to -1.25s to -0.25s, -0.25s to 0.25s, and 0.25s to 1.25s relative to movement onset, respectively. Percent changes were then calculated between the movement and pre-movement, movement and post-movement, and post-movement and pre-movement intervals. More specifically, the percent change between period A and period B corresponds to the sum of the activations during period A divided by the sum of activations during period B, subtracted by 1. A positive value for this metric corresponds to a relative increase in the average number of activations in A compared to B while a negative value corresponds to a decrease.

If, on average, activations for an atom in a given cluster had a decrease from the pre-movement to movement interval that exceeded 10% and an increase from the movement to post-movement interval that exceeded 10%, the cluster was considered to meet the criteria for a task-related change in activity. Clusters were also assessed for an additional "rebound "criteria, to determine whether clusters exhibited an increase in activity above pre-movement levels, characteristic of movement-related beta transients (Brady et al., 2020). If, on average, atoms in the cluster had a difference between post-movement and pre-movement that exceeded 10%, the cluster was also considered to have a rebound component. The 10% threshold used to compare task intervals was selected based on the magnitude of task-related changes in beta activity reported in previous analyses of the CamCAN dataset (Bardouille et al., 2019; Brady et al., 2020). Using both average power (Bardouille et al., 2019), and burst-based (Brady et al., 2020) analyses of

beta activity, task-related changes on the order of 10-30% were observed. Therefore, to capture beta events along with other task-related event types for which the magnitude of this change is not defined, the threshold was set to the lower end of this range.

Of the 11 clusters included in this analysis, seven met the criteria for both focality and activity changes and were therefore classified as task-related. Of these, only one did not meet the additional rebound criteria.

3.4.5 Representative Atom Generation

For each of the task-related clusters identified in previous steps, a representative atom was generated using a modified version of the CDL process described in Section 3.4.2. The creation of a representative atom allowed the cluster to be characterised and visualised, and provided a basis of comparison for atoms within and between clusters. For each atom in a given cluster, representative MEG data for the atom was recreated by convolving the activation vector with the outer product of the u and v vectors to yield MEG time course data (channels x time). The MEG data from all component atoms in the cluster was then concatenated to create a single representative signal for the cluster. CDL was then applied to the concatenated signal to learn a single, 500ms atom that would be representative of the most highly repetitive spatiotemporal signal in the cluster. An ECD was also computed for each representative atom using spatial representation of the u vector projected onto an average template brain.

The concatenated signal for each cluster was also used to generate a time-frequency representation (TFR) to show each atom clusters' frequency-specific behaviour relative to the movement task, averaged over tasks and participants. The concatenated signal was epoched based on stimulus onset as described in Section 3.4.1. TFRs were then generated using a Morlet wavelet transform with a 500ms wavelet, and were used as a basis of comparison between the atom types detected in this work and traditional band-limited power analyses.

3.4.6 Demographic Analysis

The demographic characteristics of each task-related cluster were first investigated by creating histograms depicting the age and sex distribution of the participants whose atoms were included in the cluster. Participants were only counted once per cluster, regardless of how many atoms the participant had assigned to a given

cluster. The demographic distributions for each cluster were then compared to the demographic distribution of the overall dataset (538 participants). The cluster and overall distributions were then quantitatively compared by conducting a Chi-squared test with a Bonferroni-corrected $\alpha = 0.007$ (as the result of 0.05 divided by 7 clusters) to determine whether the real cluster demographics were significantly different from what would be expected if clusters were created by random sampling. The results of the Chi-squared test provided information on the presence of age- or sex-related biases within clusters.

To further investigate demographic trends within each cluster, a series of regression analyses were conducted relating the component atoms' spatiotemporal characteristics to participant age. Atom characteristics including peak frequency of the power spectrum, activation sum (in the pre-movement and post-movement intervals described in Section 3.4.4), and dipole position and orientation were regressed with age using both linear and quadratic models. To determine the best fit model type, goodness of fit of each model (linear and quadratic) to the data was assessed using a Chi-squared test. An F-test was then employed to decide the more appropriate model for each regression. A quadratic model was selected if $F>6.635$, indicating 99% confidence. Otherwise, a linear model was deemed most appropriate. The appropriate model was then plotted, and significant trends were assessed using Bonferroni-corrected $\alpha=0.007$.

Additional regression analyses were also implemented to disambiguate the effects of burst rate and burst power on changes in the activation sum for each task interval and cluster. The distinction between these underlying factors is important because they are related to fundamentally different activity of the neural network (e.g., burst rate is related to neural firing rates while burst power is related to neural network size). Therefore, the independent analysis of burst rate and burst power was performed to determine whether burst rate or burst power underlies age-related changes in atom activation sum, for each cluster. Burst rate was defined as the number of non-zero activation values in the interval of interest divided by the length of the interval. This was calculated for each component atom during each task interval (pre-movement and post-movement) and regressed against age using the linear and quadratic models as described above. Burst power was defined as the magnitude of the non-zero activations and was assessed as a distribution of values for each atom in each task interval. The role of burst power in the activation sum trends was

investigated by calculating the distribution of activation values for each atom and assessing the shift in the distribution with age. A Gaussian function was fit to the distribution of activation values for each atom, and the μ (mean) and σ (standard deviation) values for each distribution were regressed against age to assess for age-related changes in the distribution.

In addition to the atoms' characteristics, the relationship between participant age and the correlation of their atoms to the cluster's representative atom was also assessed. A significant age-related change in correlation would indicate that similarity to the representative atom changed with age and would provide particular insight into whether atom characteristics may be converging towards or deviating from the mean with age. The correlation of the *u* vectors and the maximum cross-correlation of the *v* vectors were calculated between each atom in a given cluster and the cluster's representative atom to provide a measure of atom similarity to the representative atom for the group. As above, linear and quadratic regression analyses relating the correlation values of each atom to the age of the participant to whom the atom belonged were conducted. All linear and quadratic regression analyses were assessed for significance with a Bonferroni-corrected $\alpha = 0.007$. All results are reported to two decimal places.

3.5 Results

3.5.1 Spatiotemporal Characteristics of Task-Related Atoms

The global clustering methods described above resulted in seven task-related clusters of atoms across participants. Figure 3.6 shows the spatial topographies and temporal waveforms for each of the representative atoms for the task-related clusters. Of the seven representative atoms, four had waveforms resembling alpha waves (i.e., 8 to 12 Hz sinusoid), one had a waveform resembling a mu wave (i.e., complex waveform with a peak frequency of 8 to 12Hz), and two had waveforms resembling beta waves (i.e., complex waveform with a peak frequency of 15 to 30Hz). Three of the clusters characterized by alpha-type waveforms had topographies resembling occipital activation. These clusters were distinguished spatially by their tendency to activate sensors either in the left occipital lobe (LO_alpha), right occipital lobe (RO_alpha) or more anteriorly and medially in the medial occipitoparietal region (MOP_alpha). The fourth alpha-type waveform had an associated spatial topography resembling left temporal lobe activity

(LT_alpha). The cluster characterised by a mu waveform had a spatial topography resembling right central (sensorimotor) activation (RC_mu). Finally, both clusters characterised by beta waveforms had topographies suggesting left central (sensorimotor) activity. One such cluster showed peak activity just anterior to the center of the topography, near the primary motor area (LPreC_beta), and the other showed peak activity just posterior to the center of the topography, near the primary somatosensory area (LPostC_beta).

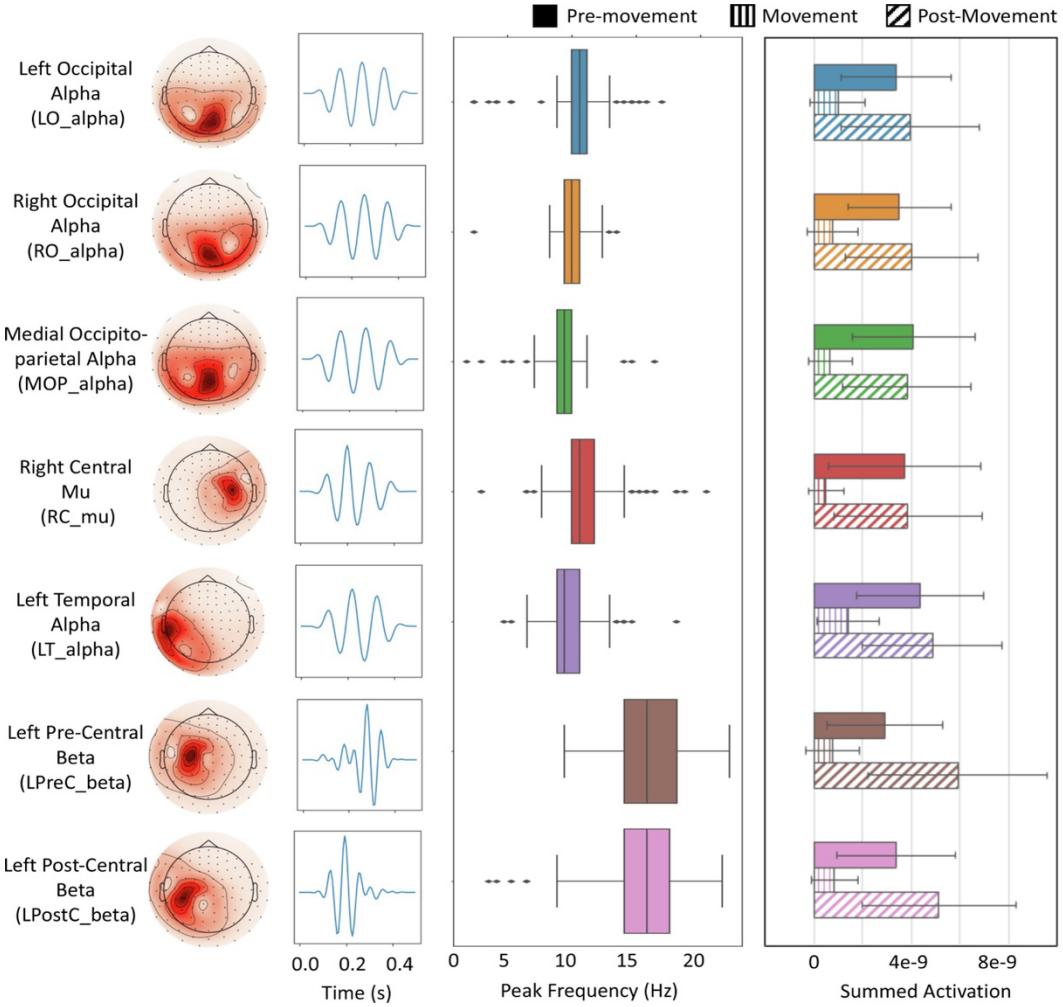

Figure 3.6 The seven task-related clusters identified in this work. (Left) The shift-invariant spatial and temporal vectors of the representative atoms created for each of the seven clusters identified. Clusters are given a functional label based on the spatial and temporal representation of the atom. (Center) Box plots depicting the distribution of peak frequencies of the component atoms for each cluster. (Right) The mean and standard deviation (error bars) of the summed activation during the pre-movement (solid bar),

movement (vertical striped bar), and post-movement (diagonal striped bar) intervals for the component atoms of each of the seven clusters.

The distributions of the peak frequencies and activation sums of the component atoms are shown in Figure 3.6. In general, the alpha-type clusters (LO_alpha, RO_alpha, MOP_alpha, and LT_alpha) have relatively narrow frequency distributions, with few outliers. The mean peak frequencies of the component atoms for the alpha-type clusters are 10.36 +/- 1.56 Hz, 9.98 +/- 0.80 Hz, 9.23 +/- 1.08 Hz, and 9.72 +/- 1.61 Hz (mean +/- standard deviation), for LO_alpha, RO_alpha, MOP_alpha, and LT_alpha, respectively. The mu-type cluster has a slightly wider frequency distribution with a mean of 11.10 +/- 1.99 Hz, and the beta-type clusters have the widest frequency distributions with means of 16.03 +/- 2.81 Hz and 15.50 +/- 3.02 Hz, respectively. This suggests that there is more variability in the frequency content of the atoms making up the beta-type clusters than the mu- or alpha-type clusters. In terms of activation sums, all task-related clusters had, on average, a decrease in activation from the pre-movement to movement time intervals, and a subsequent increase in activation from movement to post-movement, as this was one of the criteria required to classify the cluster as “task-related”. However, it should be noted that for all clusters, there was a large amount of variability in the level of activation of the component clusters during each task interval, as indicated by the error bars in Figure 3.6. In addition, 6 of the task-related clusters (LO_alpha, RO_alpha, RC_mu, LT_alpha, LPreC_beta, and LPostC_beta) also had a rebound component, meaning that there was an increase in activation from pre-movement to post-movement intervals. Notably, the beta-type clusters (LPreC_beta and LPostC_beta), on average, have the largest difference between post-movement and pre-movement activation. This characteristic “rebound” of activation is in line with existing literature that notes a post-movement rebound of beta power, surpassing baseline (i.e., pre-movement) levels, in primary sensorimotor areas contralateral to the movement.

For each component atom, and each representative atom, an ECD was calculated to infer the approximate source of the atom. The representative atom dipoles (fit to an average template brain) are shown in Figure 3.7. In general, the ECDs for the representative atoms localize to the expected regions based on their spatial topographies. Representative atoms for LO_alpha and RO_alpha both localized to very similar

positions near the midline of the occipital lobe. Despite hemispheric differences in the topographies of these two atom clusters, their exact dipole localization was relatively indistinguishable. The representative atom for MOP_alpha localized near the midline at the boundary of the occipital and parietal lobes (slightly anterior and superior to the other occipital alpha clusters). The representative atom for LT_alpha localized to the left temporal lobe just posterior to the center of the head. The representative atom for RC_mu localized anterior to the pre-central sulcus in the right hemisphere, and the representative atom for LPreC_beta localized to a similar location in the left hemisphere. The representative atom for LPostC_beta localized slightly posterior to the LPreC_beta atom in the left post-central gyrus. Table B.2 (Appendix B) presents the positions, orientations, and goodness of fit values for each of the representative atom ECDs.

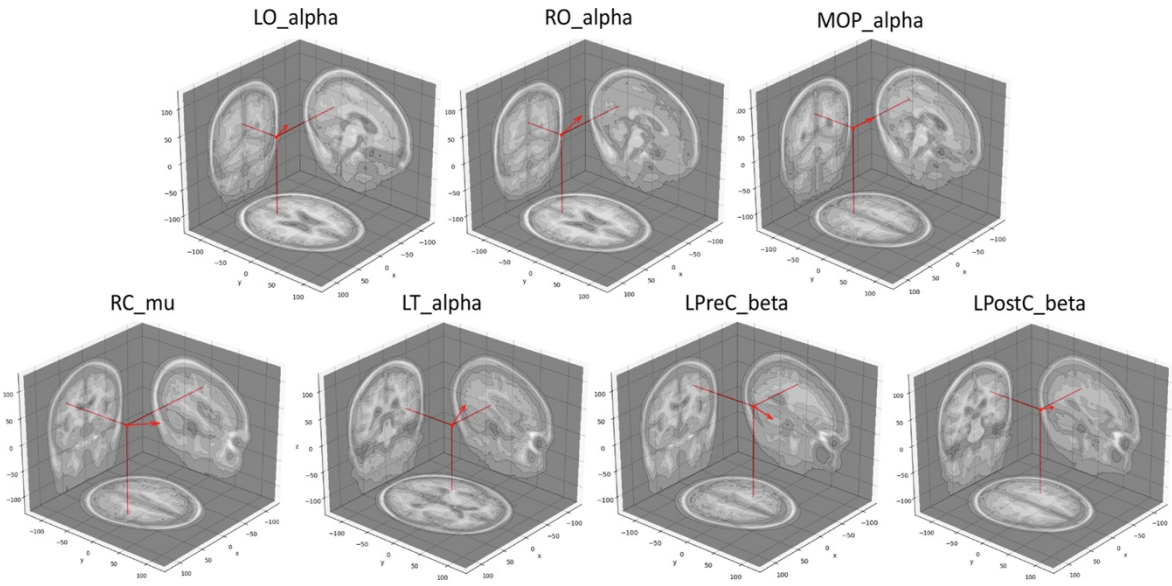

Figure 3.7 The dipole fits for each of the seven representative atoms. Axial, sagittal, and coronal slices are shown for each fit, with the thin lines indicating the position of the dipole in each plane and red arrows indicating the orientation of the dipole. Representative atom dipoles were fit to an average template brain.

Average TFRs were created for each atom cluster to allow the atoms' behaviour to be compared to traditional average spectral power analysis (see Figure 3.8). In an average power analysis of an audio-visual cued simple movement task, we would expect to see suppression of occipital alpha and sensorimotor mu and beta activity, and a rebound in sensorimotor beta activity. As shown in Figure 3.8, each atom type shows a distinct

reduction in activity near the onset of the movement (at time = 0 s) and an increase to baseline activity following the task. In addition, clear rebound behaviour is evident in the beta-type atoms, reflecting the post-movement beta rebound seen in traditional analyses (for example, Bardouille et al., 2019). This suggests that CDL reconstructs the expected brain responses. Finally, the right central mu atoms show a frequency profile that is distinctly different from the occipital and temporal alpha atoms, providing further confidence in the relationship between the CDL-detected waveforms and traditional analyses.

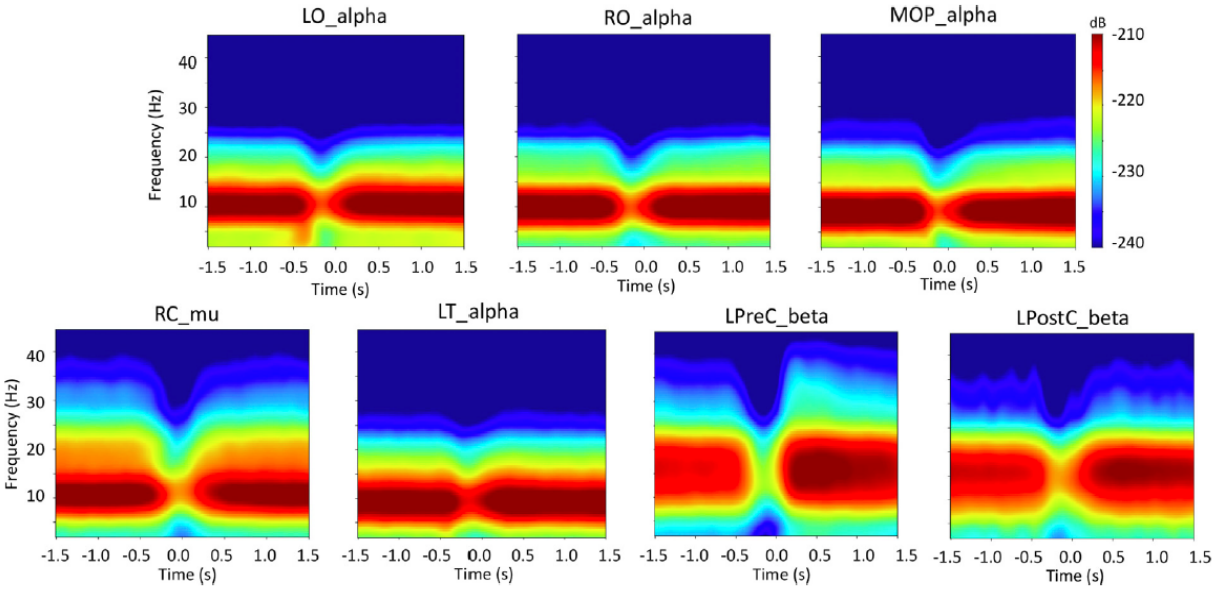

Figure 3.8 Time-frequency representations generated from the concatenated signal for each of the 7 task-related atom clusters. The signal is averaged across epochs and atoms, and activity is shown relative to movement onset (time = 0s). Color represents the magnitude of the activity in dB.

3.5.2 Demographic Distributions

The demographic composition of each cluster was assessed by comparing the age and sex distributions of the cluster to the distribution generated from the overall dataset using a Chi-squared test. Clusters LT_alpha and LPostC_beta were found to have an age distribution that was significantly different from that of the overall dataset, with Chi-squared values of 27.47 ($p = 0.0012$) and 36.29 ($p = 0.000035$), respectively. Both clusters had age distributions that were skewed towards older participants. Histograms showing the distributions of the two significant clusters compared to the overall dataset

are presented in Figure 3.9. No other clusters had age or sex distributions that were significantly different from that of the overall dataset.

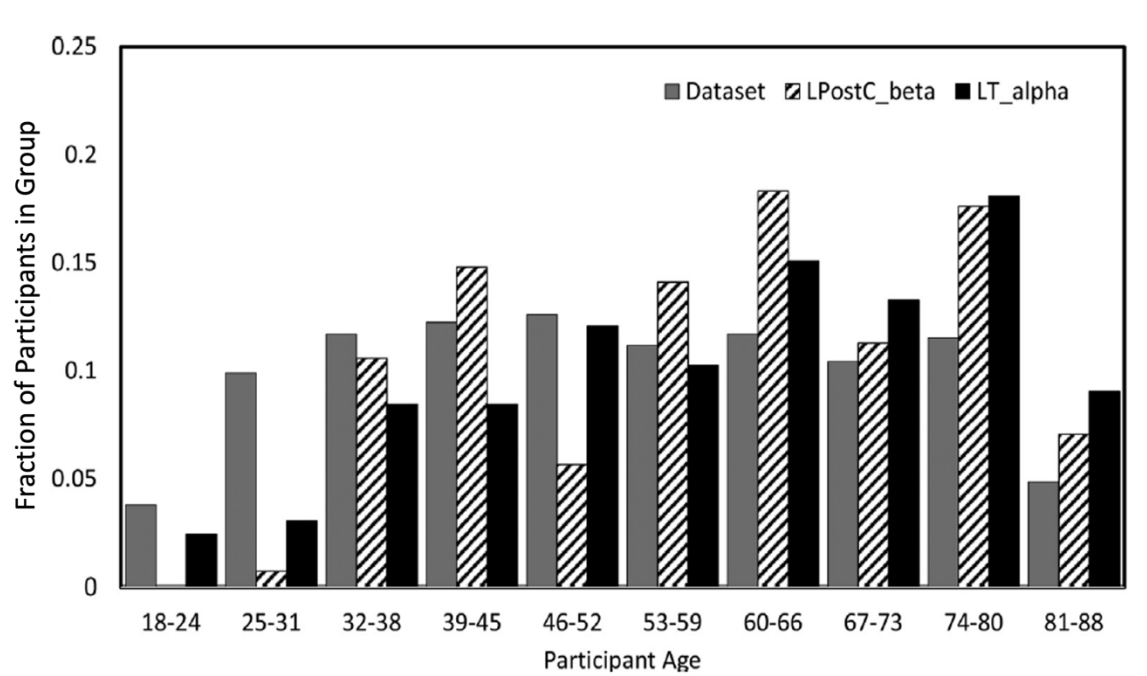

Figure 3.9 The age distribution of participants in the LPostC_beta (striped) and LT_alpha (black) clusters compared to the age distribution of the overall dataset (grey).

3.5.3 Age-Related Trends in Atom Characteristics

All clusters were examined for age-related changes in their component atom characteristics including peak frequency, activation sum (in the pre-movement and post-movement intervals), dipole position and orientation, and correlation of the *u* and *v* vectors to the mean atoms' vectors. Of these, activation sum showed significant age-related changes across the most clusters. Age-related trends in activation sum for each cluster are shown in Figure 3.10 for the pre-movement and post-movement intervals. In the pre-movement interval, clusters LO_alpha, RO_alpha, MOP_alpha, LPreC_beta, and LPostC_beta showed significant positive linear trends with increasing age. In the post-movement interval, clusters LO_alpha and RO_alpha showed positive quadratic trends with a vertex around 40 years, clusters MOP_alpha, RC_mu, and LT_alpha showed significant positive linear trends with age, and cluster LPreC_beta showed a negative quadratic trend with a vertex at approximately 60 years. The corrected p-values and RMSE values for all trends can be found in Table 3.1.

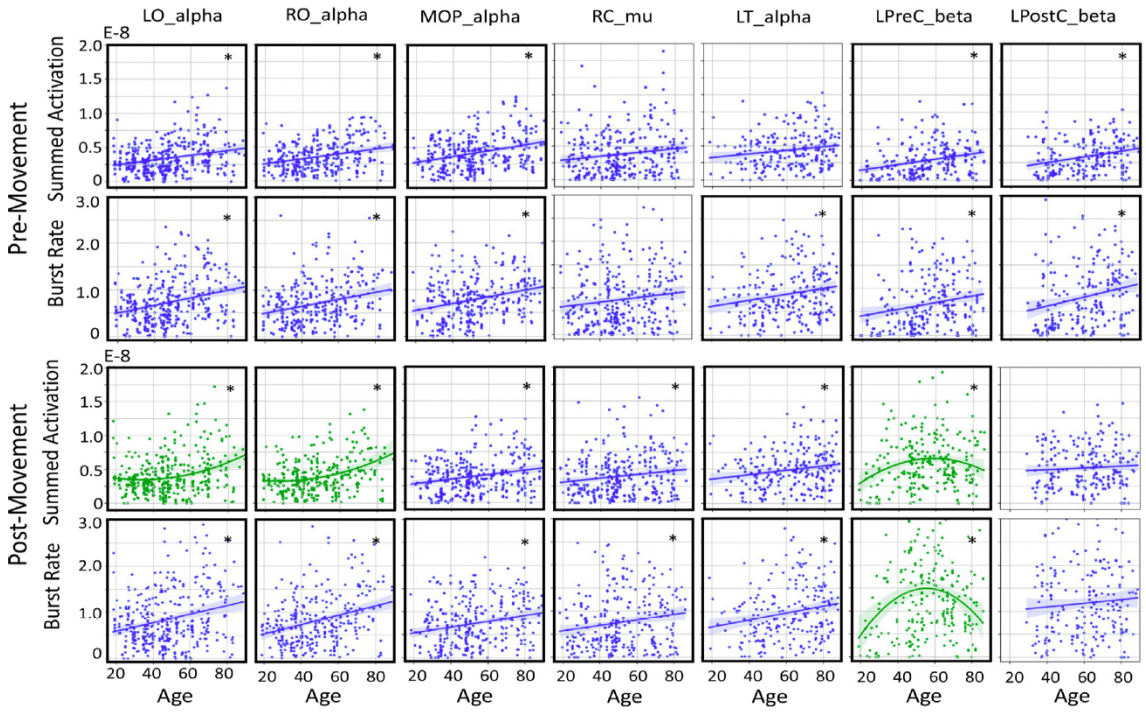

Figure 3.10 Results of linear and quadratic regression of summed activation and burst rate with age during pre-movement and post-movement. Summed activation and burst rate during each interval are plotted against participant age for the component atoms of each cluster. Blue plots represent those that were modelled by a linear fit, and green plots were modelled by a quadratic fit. Asterisks indicate clusters and intervals for which the best fit regression was significant (Bonferroni corrected alpha < 0.007).

To investigate the roles of burst rate in the activation sum trends, linear and quadratic regression were also conducted between burst rate and age. The results are displayed alongside the activation sum regression results in Figure 3.10. P-values and RMSE values associated with this analysis can be found in Table 3.1. The results of the burst rate regression in the pre-movement interval were similar to those of the activation sum regression with positive linear trends evident in most clusters. As with activation sum, clusters LO_alpha, RO_alpha, MOP_alpha, LPreC_beta, and LPostC_beta showed significant positive linear trends with increasing age, but in addition, cluster LT_alpha also showed a significant positive increasing trend in burst rate which was not present in the activation sum regression. Similarly, the results of the burst rate regression in the post-movement interval also showed high concordance to the activation sum regression results. All significant effects in the post-movement interval matched those found in the

activation sum regression except for clusters LO_alpha and RO_alpha which were better fit with a positive linear model in the burst rate regression rather than the positive quadratic model fit in the activation sum regression. Despite the discrepancy in the best model fit, LO_alpha, and RO_alpha show similar increasing trajectories for both activation sum and burst rate. These results suggest that burst rate can account for the majority of the trends that were observed in activation sum with age.

Table 3.1

p-values and RMSE values for age-related regression of the summed activation vector, activation burst rate, and mu and sigma of the activation distribution. Data is shown for the pre-movement and post-movement activation intervals. Significant p-values are indicated by an asterisk.

Cluster	Pre-Movement							
	Sum		Rate		Mu		Sigma	
	p-value	RMSE	p-value	RMSE	p-value	RMSE	p-value	RMSE
LO_alpha	5.1e-7*	2.2e-9	2.8e-8*	4.6e-1	2.7e-2	2.9e-11	7.6e-2	1.6e-11
RO_alpha	2.8e-7*	2.0e-9	2.1e-6*	4.5e-1	8.4e-2	3.1e-11	1.6e-1	1.6e-11
MOP_alpha	1.1e-8*	2.4e-9	2.5e-7*	4.5e-1	4.3e-1	3.4e-11	6.1e-2	1.8e-11
RC_mu	8.6e-3	3.1e-9	2.2e-2	6.1e-1	9.6e-1	3.8e-11	8.4e-1	1.7e-11
LT_alpha	9.1e-3	2.6e-9	2.4e-3*	5.3e-1	3.9e-1	2.8e-11	4.8e-1	1.4e-11
LPreC_beta	2.5e-5*	2.3e-9	1.4e-3*	5.4e-1	8.9e-3	4.1e-11	4.1e-5*	1.4e-11
LPostC_beta	4.8e-5*	2.3e-9	4.8e-4*	6.2e-1	7.0e-1	3.4e-11	5.7e-1	1.3e-11
	Post-Movement							
	Sum		Rate		Mu		Sigma	
	p-value	RMSE	p-value	RMSE	p-value	RMSE	p-value	RMSE
LO_alpha	1.7e-7*	2.7e-9	8.3e-7*	5.9e-1	2.2e-1	3.0e-11	1.7e-1	1.6e-11
RO_alpha	1.1e-9*	2.6e-9	6.1e-8*	5.4e-1	5.6e-1	3.2e-11	3.3e-1	1.6e-11
MOP_alpha	4.4e-5*	2.6e-9	4.0e-5*	4.8e-1	7.9e-1	3.3e-11	5.1e-1	1.8e-11
RC_mu	6.2e-3*	3.0e-9	3.9e-3*	6.1e-1	6.0e-1	3.7e-11	4.6e-1	1.6e-11
LT_alpha	3.4e-3*	2.8e-9	1.5e-3*	6.0e-1	2.3e-2	2.8e-11	8.1e-1	1.3e-11
LPreC_beta	9.9e-4*	3.6e-9	3.3e-5*	8.7e-1	1.4e-3*	4.4e-11	2.3e-1	1.5e-11
LPostC_beta	3.3e-1	3.2e-9	2.6e-1	8.1e-1	3.2e-2	3.2e-11	1.6e-1	1.3e-11

The role of burst power in the activation sum trends was then investigated by calculating the distribution of activation values for each atom and assessing the shift in the distribution with age. Relevant p-values are given in Table 3.1. In the pre-movement interval, no significant age-related changes in the distribution mean were found, and only one significant effect of the distribution standard deviation was found (LPreC_beta). For cluster LPreC_beta, the standard deviation increased linearly with age suggesting that older participants had more variable burst power values than younger participants. The lack of effects in the mean value, however, suggested that the magnitude of burst power does not change significantly with age. In the post-movement interval, there was a single

significant age-related quadratic effect in the mean of the distribution for cluster LPreC_beta. The effect was such that the atoms from the youngest and oldest participants had a distribution that was shifted towards larger activation values, while those atoms belonging to middle-aged participants tended to come from a distribution with a lower mean activation value. This suggests that, for cluster LPreC_beta, burst power is highest in young and old participants. This contrasts the results of the activation sum regression for cluster LPreC_beta which showed that young and old participants had a reduced activation sum compared to their middle-aged counterparts. These results suggest that burst power plays a lesser role in the overall activation sum trends, and in some cases may even contradict the overall effects driven by burst rate. Supporting figures can be found in Appendix B, Figure B.4.

In addition to the dominant age-related effects demonstrated in activation sum, several spurious age-related trends in other atom characteristics were found. Figure B.5 shows plots of the age-related linear and quadratic effects of peak frequency, y position of the dipole, and correlation of the *u* and *v* vector to the mean atom, and highlights the clusters for which these effects were significant. There were no significant age-related effects found in the x or z position or x, y, or z orientation of the dipole for any cluster. The correlation of the *u* vector (spatial topography) to the mean atom showed a significant negative linear trend with age for cluster LO_alpha ($p = 0.0035$). This indicates that the spatial topography for cluster LO_alpha becomes increasingly variable, or dissimilar to the mean atom with age. The correlation of the *v* vector (temporal waveform) to the mean atom showed a significant positive linear trend with age for clusters LPreC_beta ($p = 0.0029$) and LPostC_beta ($p = 0.0021$) indicating that these clusters showed a convergence in their temporal waveform with age. In addition, peak frequency of the component atoms showed a significant negative linear trend in cluster RO_alpha with age ($p = 0.0016$) and a significant positive linear trend in cluster RC_mu with age ($p = 0.0014$). Finally, the y position of the dipole showed a significant negative linear trend with age in cluster LT_alpha ($p = 0.0018$), indicating that there may be a posterior shift in the dipole position of cluster LT_alpha with age.

A summary of all age-related effects observed in each cluster is shown in Table 3.2. The variability in the effects observed in different clusters suggests that all clusters are distinct and have unique individual relationships to the ageing process.

Table 3.2

Summary of the age-related effects for each cluster.

Cluster	Age-Related Effects
LO_alpha	Linear increase in pre-movement activation Positive quadratic effect in post-movement activation Linear increase in pre-movement and post-movement burst rate Linear decrease in *u* vector correlation to mean atom
RO_alpha	Linear increase in pre-movement activation Positive quadratic effect in movement and post-movement activation Linear increase in pre-movement, movement, and post-movement burst rate Linear decrease in peak frequency
MOP_alpha	Linear increase in pre-movement and post-movement activation Positive quadratic effect in movement activation Linear increase in pre-movement and post-movement burst rate
RC_mu	Linear increase in movement and post-movement activation Linear increase in post-movement burst rate Linear increase in peak frequency
LT_alpha	Age distribution skewed towards older adults Linear increase in post-movement activation Linear increase in pre-movement and post-movement burst rate Linear increase in y position of dipole (posterior shift)
LPreC_beta	Linear increase in pre-movement activation Negative quadratic effect in post-movement activation Linear increase in pre-movement burst rate Negative quadratic effect in post-movement burst rate Linear increase in pre-movement sigma property of activation distribution Positive quadratic effect in post-movement mu property of activation distribution Linear increase in *v* vector correlation to mean atom
LPostC_beta	Age distribution skewed towards older adults Linear increase in pre-movement activation Linear increase in pre-movement burst rate Linear increase in *v* vector correlation to mean atom

3.6 Discussion

3.6.1 Summary of Findings

In this work, a multi-channel data-driven CDL approach and unsupervised clustering method were successfully applied to the large open-access CamCAN dataset to detect a set of prototypical, transient task-related atoms that occurred across many participants. The atom clusters that were generated had stereotypical patterns resembling known task-related brain activity, including occipital alpha and sensorimotor beta and mu. The spatial and temporal characteristics of each type of atom showed various age-related changes, with activation sum (driven by burst rate) showing the most prominent age-related effects across atom types. The results of this work suggest that several distinct types of sensorimotor and occipital transients are present in human MEG data, and that these transient bursts change in their rate of occurrence during task performance and throughout the normal ageing process. The use of the data-driven CDL approach combined with simple correlation clustering across participants allowed for these bursts to be detected and characterised at the group level through a data-driven approach that generated rich information about the complex types of transients underlying human brain activity.

3.6.2 Significance

It was hypothesised that some of the task-related atoms identified in this work would resemble sensorimotor beta and mu transients as these have been shown in previous literature to have a marked (mu and beta) reduction and (beta) rebound in occurrence with the onset and offset of a voluntary movement (Errington et al., 2020; Feingold et al., 2015; He et al., 2020; Hebert and Lehmann, 1977; Lakatos et al., 2004; Little et al., 2019; Lundqvist et al., 2016; Shin et al., 2017; Wessel, 2020). In line with this hypothesis, two of the identified atom clusters resembled left sensorimotor beta transients, and one atom cluster resembled a right sensorimotor mu transient. The frequency bands and movement-related temporal behaviour associated with each of these atoms coincided with the features associated with sensorimotor beta and mu activity identified in classical average power analysis (as shown in Figure 3.8). Given that the sensorimotor task used in this dataset was a right-handed unimanual button press, it was expected that contralateral (left) sensorimotor beta transients would be a dominant task-

related atom type across many participants. An interesting finding of this analysis, however, was that two distinct clusters of contralateral sensorimotor beta transients emerged with slightly different representative waveforms and spatial topographies. Upon fitting an ECD for the representative atom for each cluster, it was found that one atom localized slightly pre-centrally, while the other localized slightly post-centrally. This finding suggests that these two atom clusters may represent two distinct types of beta transients that come from different (primary motor and primary somatosensory) sources and may have different physiological properties. Further, post-hoc analysis revealed that in the pre-movement interval there was higher activation of the LPostC_beta atoms compared to the LPreC_beta atoms ($p = 0.034$) and in the post-movement interval there was higher activation of the LPreC_beta atoms compared to the LPostC_beta atoms ($p = 0.018$), suggesting that these two types of beta bursts were related to different phases of movement. The finding of differentiable beta bursts for two separate generators is a novel contribution of the CDL method. Other thresholding-based transient burst detection methods rely on specifying an approximate burst frequency and spatial location prior to detection. Therefore, previous methods have been largely insensitive to the subtle waveform and spatial differences between pre- and post-central bursts.

Despite the identification of multiple contralateral central beta burst clusters, no contralateral central mu burst clusters or ipsilateral central beta burst clusters were identified in this analysis. This apparent gap is not due to an inability of the CDL method to detect such atoms but is rather a result of the “top cluster” cut-off selected in this work. The objective of this work was to assess cross-sectional ageing trends in highly stereotypical atom types, and as such, only the largest (i.e., most common) atom clusters were investigated. The result of this, however, is that some atom types were not included if they had high between-subject variability resulting in the formation of several, smaller clusters rather than a single larger cluster. As shown in Figure 3.5, this was the case for clusters of contralateral central mu and ipsilateral central beta atoms, which formed clusters identifiable by CDL, but whose cluster sizes did not meet the required “top cluster” threshold. To address the limitation imposed by the top cluster framework, an alternative analysis method has been provided in the supplementary material (see Figure B.7) that provides more insight into the diversity of atom clusters. While the selection of

top clusters was necessary for the current work to ensure adequate sample sizes for studying cross-sectional ageing trends, future work using CDL and atom clustering should consider which analysis strategy is best suited for the research question at hand.

In addition to sensorimotor beta and mu atoms, three of the seven task-related atom clusters identified in this work resembled occipital alpha transients, and one resembled a temporal alpha transient. The presence of these atoms was not explicitly hypothesised in this work, as most sensorimotor literature does not focus on the occipital (or temporal) alpha signal. However, the task-related nature of this signal is not surprising. It is well-established that occipital alpha is primarily a resting-state signal, and that its amplitude decreases relative to baseline with increased alertness or attention to stimuli (Britton et al., 2016). Task-related atoms were identified in this work as those that showed a decrease in activation relative to pre-movement levels with the onset of a sensorimotor task, and an increase in activation relative to movement levels following the offset. Because the occipital alpha signal is inversely related to alertness, it is unsurprising that engagement in a sensorimotor task resulted in a reduction and rebound of these occipital alpha atoms' activation values. Similarly to the left sensorimotor beta atoms, the analysis also identified multiple distinct occipital alpha patterns. In this case, the temporal waveform of the alpha atoms was quite consistent across the three clusters, but the spatial representation varied between clusters. This suggests that there may be several distinct generators of occipital alpha in the left and right occipital and posterior occipitoparietal regions, as well as potentially related alpha generators in the temporal regions. While occipital alpha atoms were not the intended target of this analysis, the data-driven nature of the CDL method allowed for their identification. As a result, we were afforded a unique opportunity to assess age-related trends in transient bursts of occipital alpha in the context of a motor task, which otherwise would not have been a focus.

Each of the atom clusters identified in this work showed trends in some of their spatiotemporal characteristics with age, with all atoms showing a significant trend in activation sum during at least one of the task intervals. Interestingly, occipital alpha-type clusters tended to show consistent increasing trends in activation with age across both pre-movement and post-movement intervals, whereas beta- and mu-type clusters tended

to have differential age-related effects depending on the phase of movement. This suggests that occipital alpha transients show an overall increase in activation with age that is independent of the phase of movement, while beta/mu transient activation trends are dependent on the movement phase. The overall increase in occipital alpha activity with age, while not hypothesised, is in line with previous findings that show that ageing is associated with a reduced frequency of brain activity and that older participants tend to have dominant alpha peaks in their spectrograms (Chiang et al., 2011). Further investigation into the underlying properties of the activation showed that for all occipital alpha clusters, the increasing trends observed in activation sum with age could be explained by similar trends in burst rate with age. Burst power, however, did not play a significant role. This finding suggests that increasing occipital alpha activity with age is related to an increase in the number of activations of the underlying neural networks (i.e., the neuronal firing rate), rather than the magnitude of the individual activations (i.e., the size of the activated neuronal population).

Similarly, for beta atoms, burst rate was also the primary driver behind age-related changes in activation sum. In the pre-movement interval, both beta atoms showed a linear increase in activation sum with age that could be explained by an associated increase in burst rate with age. This pre-movement increase in sensorimotor beta burst rate is in line with our hypothesis and previous findings that burst rate is the primary factor influencing increases in pre-movement sensorimotor beta with age (Brady et al., 2020). In the post-movement interval, the age-related trends were less consistent. The left pre-central beta cluster showed a negative quadratic trend in activation sum with a peak around 60 years of age that was mirrored by a similar negative quadratic trend in burst rate with age. In addition, there was also a significant positive quadratic trend in both the mean and standard deviation of the activation distribution for the left pre-central beta cluster during post-movement that contrasted the negative quadratic trend observed in the activation sum and burst rate. This suggests that young and old participants exhibit a larger number of lower power sensorimotor bursts than middle-aged participants, but that the increased burst rate is the primary factor driving an overall increased activation sum in young and old participants. Interestingly, the quadratic activation trends in the post-movement interval for the left pre-central beta cluster were not present in the left post-central beta

cluster. This further demonstrates that the two beta clusters are distinct from one another and vary differently with age. Overall, these results provide strong evidence that age-related changes in transient bursts are primarily driven by changes in the firing rate of the underlying neural networks.

Surprisingly, the hypotheses that beta and mu sensorimotor atoms would show a decrease in burst frequency and an anterior shift in dipole position with age were largely unsupported by our results. In fact, the right central mu cluster showed an increase in burst frequency with age, while the left central beta clusters did not show any significant change in frequency with age. A possible explanation for this apparent discrepancy is that if central mu bursts increase in frequency with age such that their peak frequency approaches 15 Hz (as is observed in the right central mu cluster), these bursts may begin to be considered as beta bursts instead of mu bursts if the signals are dichotomized based on classic frequency band limits. The misrepresentation of these high-frequency mu bursts as low-frequency beta bursts could then result in the appearance of a reduction in frequency of beta bursts. This effect could also contribute to an exaggerated increasing trend in burst rate with age in other analyses, as more mu bursts may be counted as beta in older participants. The anterior shift in the source of beta bursts that was noted previously using minimum norm source estimation (Power and Bardouille, 2021) was not present for either of the sensorimotor beta clusters in this work. This may be due in part to the discrepancy in source localization methods and a reduced sensitivity of the ECD fit compared to the minimum norm estimation method.

3.6.3 Limitations and Future Directions

As a result of the success of CDL for detecting group-level, task-related transient events, several new avenues for future research have emerged. One such direction for future research is to use this approach to create a data-driven set of representative atoms that could be used as a standard dictionary of transient bursts. Previous research has discussed the value of creating such a dictionary (Tal et al., 2020), and applying the methods described here to a large dataset of resting state data, such as that offered in the CamCAN dataset, would allow for such a set of transients to be realised. While CDL and the associated clustering methods presented here could be applied to any dataset regardless of size, the relatively small cluster sizes (i.e., 25–40% of participants per

cluster) reported here suggest that a top cluster analysis of a much smaller dataset would not yield particularly representative results. However, with access to a standard dictionary derived from a large dataset, template matching could be used to search small datasets for signals that have high similarity to the standard transients. This would provide an opportunity for fast and efficient identification of a variety of transient bursts, regardless of the dataset size.

The CDL approach described here also lends itself well to applications where an external synchronisation signal (i.e., a task) is not present in the data. In the current work, we were interested in detecting task-related transients that were comparable to those detected by existing methods to help validate the efficacy of our methods. However, CDL is also well-suited for detecting transient signals that are not related to a task, because it can detect transient signals throughout electrophysiological data without reliance on task-related timestamps. This makes CDL an ideal tool for resting-state applications and burst-based neurofeedback applications (see Karvat et al., 2020; Ossadtchi et al., 2017) where we cannot rely on the concatenation of task-based trials for our analysis.

Despite the overall success and promising areas for future work based on these results, there are some limitations of the current work that should be addressed. One such limitation is that in the current analysis, the data was bandpass filtered between 2 and 45 Hz to target the mu and beta frequency activity upon which the hypotheses were based. The limitation of this is that higher frequency activity (e.g., gamma bursts) were not identifiable in this work. Therefore, future work may wish to expand the frequency band of interest to detect a wider range of bursts than were targeted in this work. In addition, future work could improve upon the clustering methods used in this work. While the correlation-based clustering method was successful for clustering atoms based on the simultaneous consideration of spatial and temporal metrics, it may not be desirable for all applications as it relies on a number of user-defined hyperparameters tuned by manual data inspection. To improve upon this and increase the ease of use of our methods, future developments could be made to existing “out of the box” clustering methods to formalize an algorithm that could simultaneously consider multiple clustering metrics. Finally, a limitation of the CDL algorithm is that it imposes a particular duration on the atoms that are being detected. This could result in the exclusion of some types of transient bursts

that have a duration that is much longer or much shorter than the pre-defined atom window. This limitation demonstrates that while CDL imposes fewer assumptions than previous methods and employs a data-driven approach, it is not entirely without restrictions.

Prior to using CDL for transient burst detection applications, researchers should consider the applicability of the method to the research question at hand and should consider the advantages and disadvantages of CDL compared to other burst detection methods. In some cases, a simpler amplitude-thresholding method may be sufficient, or potentially more appropriate than CDL. For example, if a researcher is interested in investigating the transient bursts that specifically underlie a sustained signal in the spectral power, a spectral power thresholding approach may be preferred because the bursts can be directly related to the average spectral power. However, this method should only be used if the researcher has a hypothesis about the approximate location and frequency of interest, and if the bursts can be assumed to have a Morlet wavelet shape (and the researcher is not interested in variations in waveform shape). If any of these conditions are not met, then CDL could be a beneficial alternative to investigate the research question.

3.7 Conclusion

The CDL methods employed in this work have provided us with an opportunity to investigate transient bursts at the group level using a data-driven approach that makes minimal assumptions about the spatial and temporal dynamics of the signal. This has allowed us to identify multiple, distinct types of transient bursts that have similar temporal and/or spatial patterns and may co-occur in time and space. In particular, we were able to identify 2 distinct types of contralateral sensorimotor beta bursts and 3 distinct types of occipital alpha bursts. Due to the constraints of other methods, the detection of these types of similar, but distinct, atoms was not previously possible. In addition, the data-driven nature of this work allowed us to gain important insight into the spatiotemporal dynamics of occipital alpha bursts in the context of a motor task, even though hypotheses about these bursts were not made. This insight would have been lost had a different method that required a-priori specification of frequency bands been used. The clustering methods applied in this work allowed us to investigate data-driven

transient bursts at the group level for the first time, which opened up the possibility of studying age-related trends in a large dataset. This work therefore afforded us with the unique opportunity to gain rich information about the age-related changes in these various transient burst types, and provided convincing evidence that burst rate was the primary factor driving these age-related changes. The methods developed in the current work provide a framework that other researchers can use in the future to detect transient bursts at the group level and further our collective understanding of human neuromagnetic transients.

Chapter 4

Atypical Slow Paroxysmal Activity in Healthy Adults: Relationship to Age and Cognitive Performance

4.1 Preamble

Transient beta bursts are detectable in all healthy participants and have been widely accepted as a reliable movement-dependent phenomenon. Therefore, beta bursts were ideal for validating novel analysis methods such as those presented in Chapters 2 and 3. Explorations of beta bursts in the prior chapters provided rich information about the neural mechanisms of sensorimotor processes and how those mechanisms change across the lifespan. While this is useful information for our understanding of healthy ageing, the clinical applicability of the work is less clear. Given this, an interesting progression of this work is to expand some of the concepts and methods used to analyse beta bursts into other frequency bands, particularly those that could have important clinical implications. Slow wave brain activity has been associated with a number of age-related neuropathologies and its study has the potential to provide insight into the ageing brain. However, studying slow wave activity in healthy ageing using a transient event framework has never been done. Therefore, Chapter 4 explores transient (i.e., paroxysmal) slow wave events in the large CamCAN dataset and characterises the relationship between slow wave event features and healthy ageing and cognition.

Chapter 4 of the thesis contains peer-reviewed work published in *Neurobiology of Aging* in April, 2024. Text in the introduction and discussion has been modified to reduce redundancies in the thesis, but the methods and results sections appear as published. The reference for the publication is provided below.

Power, L., Friedman, A., & Bardouille, T. (2024). Atypical slow paroxysmal activity in healthy adults: Relationship to age and cognitive performance. *Neurobiology of Aging*, *136*, 44-57. https://doi.org/10.1016/j.neurobiolaging.2024.01.009

4.2 Abstract

Paroxysmal patterns of slow cortical activity have been detected in EEG recordings from individuals with age-related neuropathology and have been shown to be correlated with cognitive dysfunction and blood-brain barrier disruption in these participants. The prevalence of these events in healthy participants, however, has not been studied. In this work, we inspect MEG recordings from 623 healthy participants from the CamCAN dataset for the presence of paroxysmal slow wave events (PSWEs). PSWEs were detected in approximately 20% of healthy participants in the dataset, and participants with PSWEs tended to be older and have lower cognitive performance than those without PSWEs. In addition, event features changed linearly with age and cognitive performance, resulting in longer and slower events in older adults, and more widespread events in those with low cognitive performance. These findings provide the first evidence of PSWEs in a subset of purportedly healthy adults. Going forward, these events may have utility as a diagnostic biomarker for atypical brain activity in older adults.

4.3 Introduction

Paroxysmal slow wave events (PSWEs) are a clinically relevant transient event type that were first described by Milikovsky and colleagues in 2019. The group reported the presence of PSWEs in patients with Alzheimer's disease (AD) and epilepsy as well as in animal models of AD, epilepsy, and normal ageing (Milikovsky et al., 2019). Importantly, this work revealed that the frequency of occurrence of PSWEs had a strong relationship with the extent of blood-brain barrier disruption and level of cognitive impairment of patients with AD and epilepsy.

The established relationship between PSWEs, cognitive impairment, and BBBd suggests that PSWEs may be a signal of interest in other neurological processes that are associated with cognitive impairment and BBBd. One such process for which the presence of PSWEs has not yet been investigated, is the process of normal (i.e., non-pathological) ageing. Non-pathological ageing is associated with a decline in cognitive functions including memory, executive function, processing speed and reasoning that occurs from middle age onwards (Deary et al., 2009a; Hedden and Gabrieli, 2004; Park and Reuter-Lorenz, 2009). This cognitive decline is thought to be related to subtle and widespread changes that lead to atrophy of neural tissue and overall reduction in brain

volume (Deary et al., 2009a). The extent of cognitive ageing varies significantly between individuals and depends on a variety of factors including genetic (Deary et al., 2004; Deary et al., 2009b), cardiovascular (Hochstenbach et al., 1998; Rafnsson et al., 2009, 2007), dietary (e.g., lack of B-vitamins, antioxidants, omega-3 fatty acids, etc.) (Deary et al., 2009a), and lifestyle (e.g., smoking, alcohol consumption, physical activity levels, etc.) (Fratiglioni et al., 2004; Ganguli et al., 2005; Nooyens et al., 2008). In addition, non-pathological ageing is associated with BBBd which may further contribute to cognitive decline (Senatorov et al., 2019). A combination of physiological factors including the accumulation of iron in astrocytes (Connor et al., 1990) and decreased activity of transporters involved in the extrusion of toxins from the brain (Toornvliet et al., 2006) can participate in alterations to the blood-brain barrier that are seen with age (Popescu et al., 2009). Other conditions that increase in prevalence with age such as hypertension and type-2 diabetes are risk factors for BBBd and vascular dementia (Popescu et al., 2009). The evidence for cognitive decline and BBBd with normal ageing and age-related pathology (Montagne et al., 2015; Sweeney et al., 2018; van de Haar et al., 2016) raise the hypothesis that PSWEs may also be found in non-pathological ageing and be associated with cognitive decline.

Electrophysiological studies of non-pathological ageing, however, have provided mixed results. In animal models of ageing, older mice were found to have increased low-frequency activity in EEG (Senatorov et al., 2019) and a higher number of PSWEs compared to younger mice (Milikovsky et al., 2019; Senatorov et al., 2019). Human electrophysiological studies, however, have either found no significant changes in low-frequency oscillatory activity with age (Caplan et al., 2015; Cesnaite et al., 2023), or have found reduced low-frequency activity in healthy older adults (Emek-Savaş et al., 2016; Leirer et al., 2011; Meghdadi et al., 2021; Vlahou et al., 2015). To our knowledge, the presence of PSWEs in non-pathological ageing has not been investigated in humans, and all other studies of low-frequency activity in healthy ageing have used average spectral power approaches and relatively small datasets.

The limitation of previous average spectral power analyses is that changes in spectral power can be caused by various rhythmic signal characteristics including power, frequency, duration, or number of high-power events in the signal. Luckily, this limitation

can be overcome by detecting and characterising individual transient bursts in the raw data. A large body of literature has explored the presence and characteristics of high-power transient bursts in the mu, beta, and gamma frequency bands (Brady et al., 2020; Milikovsky et al., 2019; Sherman et al., 2016; Shin et al., 2017; van Ede et al., 2018) and has demonstrated the diverse relationships between burst characteristics and spectral power. The success of previous literature suggests that the investigation of the characteristics of individual PSWEs in a large dataset of healthy individuals will allow us to extract more specific information about event characteristics and relate these to age-related effects previously observed using spectral power analyses. The limitations of previous spectral power analyses along with the discrepancy between electrophysiological studies of healthy ageing and studies of pathological populations and animal models, suggests a need for further detailed investigation of slow-wave activity in a large cohort of healthy participants.

The objectives of the current work are to determine the prevalence of PSWEs in healthy populations and to identify the relationship between age, cognitive performance, and PSWE characteristics. We used a large open-access dataset of healthy human MEG data collected by the Cambridge Centre for Ageing and Neuroscience (CamCAN; Shafto et al., 2014; Taylor et al., 2017) for the detection of PSWEs. We hypothesised that PSWEs increase in prevalence with participant age and are associated with lower cognitive performance. The current work provides complementary insight into the functional impact of slow-wave activity in healthy ageing, improves our understanding of age-related functional brain changes, and may promote the use of EEG/MEG for the early diagnosis of age-related cognitive decline.

4.4 Methods

4.4.1 Participants and Experimental Paradigm

MEG data was collected by the Cambridge Centre for Ageing and Neuroscience (CamCAN) in Phase 2 of the CamCAN examination of healthy cognitive ageing. A key characteristic of this large open access dataset is the uniform age distribution between 18 and 88 years. The current work uses MEG data acquired during the “resting state” component of the study. In this component, approximately 9.5 minutes of data were obtained from 623 healthy participants while they rested with their eyes closed.

Participants also completed a series of 14 domain-specific cognitive tasks as part of the CamCAN examination, spanning several cognitive domains including emotion, language, memory, and executive function (Shafto et al., 2014; Taylor et al., 2017). Six of these tasks were excluded from the current analysis due to subjectivity of their scoring metrics. The remaining 8 tasks included 2 language tasks, 3 memory tasks, 2 executive function tasks, and 1 emotion recognition task. Descriptions of all included tasks are provided in Table 4.1. Of the 623 participants included in the MEG data analysis, 500 had available data for all 8 cognitive tasks.

Table 4.1

Cognitive task descriptions.

Task Name	Cognitive Domain	Description	Scoring Metric
Tip-of-Tongue Task (TOT)*	Language	View faces of famous people and respond with (a) the person's name, (b) "don't know", or (c) "tip-of-tongue" (i.e., know but temporarily unable to retrieve)	Tip of Tongue ratio = (# of tip of tongue)/ (# of tip of tongue + # of correct known)
Picture-Picture Priming	Language	Name picture when picture is presented alone or preceded by a phonologically or semantically related image	Overall number of correct responses
Visual Short-Term Memory Task (VSTM)	Memory	View 1-4 coloured discs and then report the colour at a cued location after a delay	Average number of discs remembered for 4-disc condition
Familiar Face Recognition	Memory	View faces of famous people and judge whether they are familiar and what they are known for, and attempt to provide their name	Accuracy = # correctly named/ # recognized

Task Name	Cognitive Domain	Description	Scoring Metric
Unfamiliar Face Recognition	Memory	View a target image of an unfamiliar face, then identify the same individual in an array of 6 unfamiliar faces	Overall accuracy
Fluid Intelligence Task	Executive Function	Complete 4 subsets of nonverbal puzzles involving series completion, classification, matrices, and conditions	Overall accuracy across all 4 tasks
Hotel Task*	Executive Function	Allocate time equally between several hotel-related tasks including writing bills, sorting money, proofreading, sorting cards, and alphabetizing a list	Deviation from optimal time allocation
Emotional Expression Recognition	Emotion	View expressive face and label the emotion expressed	Overall accuracy

*Lower scores indicate better performance

To assess differences in cognition related to PSWE characteristics, an average Z-score was calculated to represent the overall cognitive ability for each participant. Z-scores were calculated relative to all participants (i.e., 500 participants with available cognitive data) for each of the 8 cognitive tasks individually and were then averaged across all tasks to generate an overall cognitive score. In the case of the tip-of-tongue and hotel tasks, lower scores were indicative of better cognitive performance and therefore the signs of the raw scores were flipped prior to calculating the Z-scores. For all other tasks, the raw scores were not modified.

In addition, participants completed Addenbrooke's Cognitive Examination-Revised (ACE-R) which is a brief cognitive assessment that is useful for detecting dementia and mild cognitive impairment. This assessment was used as part of the CamCAN screening procedure to exclude participants with neuropathology, but it also provides an overall standardized cognitive score that is a useful addition to our analysis. The ACE-R score is therefore included in our cognitive analysis. However, ACE-R scores are strongly skewed towards high values in this relatively cognitively intact population.

Thus, the ACE-R scores are analysed separately from the aggregate Z-scores described above.

4.4.2 MEG Data Acquisition

Data were obtained from the CamCAN repository (available at http://www.mrc-cbu.cam.ac.uk/datasets/camcan/ (Shafto et al., 2014; Taylor et al., 2017). MEG data were acquired at 1000 Hz with inline band-pass filtering between 0.03 and 330 Hz using a 306-channel Vectorview system with continuous head position monitoring (Elekta Neuromag, Helsinki, Finland). Digitization of anatomical landmarks (i.e., fiducial points; nasion and left/right preauricular point) as well as additional points on the scalp was also performed for registration of MEG and MRI coordinate systems. Electrooculogram (EOG) and electrocardiogram (ECG) were recorded concurrently.

4.4.3 MEG Data Processing

Data were pre-processed by the CamCAN group using temporal signal space separation to perform environmental noise reduction, reconstruction of missing or corrupted MEG channels, continuous head motion correction, and a transform of each dataset to a common head position (Taulu and Simola, 2006). All subsequent MEG processing was completed in the Python programming environment (v.2.7.13), using the MNE-python library (v.0.18.1) (Gramfort et al., 2014). Data analysis scripts used in this work are available at https://github.com/lindseypower/CamCAN_detectPSWEs. Raw MEG data were bandpass filtered between 1 and 50 Hz. The data was then cropped into a single 9-minute epoch beginning 15 seconds after the onset of the recording. Independent component analysis was performed on the cropped data using the FASTICA algorithm (Delorme et al., 2007) to remove artefacts using a fully automated process. Epochs with signals that exceeded 5 pT (magnetometers) or 400 pT/cm (gradiometers) were not included when calculating the deconstruction. Following this, components were excluded if the amplitude and phase of the component was similar to that of the EOG or ECG (Bardouille et al., 2019). An average of 4 +/- 1 (mean +/- standard deviation) independent components were removed from each subject's data. This process resulted in cleaned MEG data (i.e., channels x time) which was used for subsequent analysis.

4.4.4 Paroxysmal Slow Wave Event Detection

Paroxysmal slow wave events (PSWEs) were detected at each MEG channel (102 magnetometers and 204 gradiometers) in each participant. Briefly, MEG data was windowed into 2 second windows with a 1 second overlap. The power spectrum was then calculated for each time window and the median power frequency (MPF) was selected for that window. The algorithm then found all windows that had an MPF between 1-6 Hz, and if more than 4 consecutive windows (i.e., at least 5 seconds of data) met this low-frequency criteria, then this segment of data was considered a PSWE. The low frequency threshold of 6 Hz was defined based on ROC (receiver operating characteristic) analysis to determine the frequency that best separated patients with AD from healthy age-matched controls in prior work. Thresholds of 2,4,6, and 8 Hz were compared, and it was found that 6 Hz resulted in the greatest area under the curve in the ROC analysis and was therefore selected as the frequency threshold that would characterize PSWEs (Milikovsky et al., 2019). Following PSWE detection, characteristics of each PSWE, including the onset and offset times (s), duration (s), and mean frequency (Hz) were calculated (see Figure 4.1).

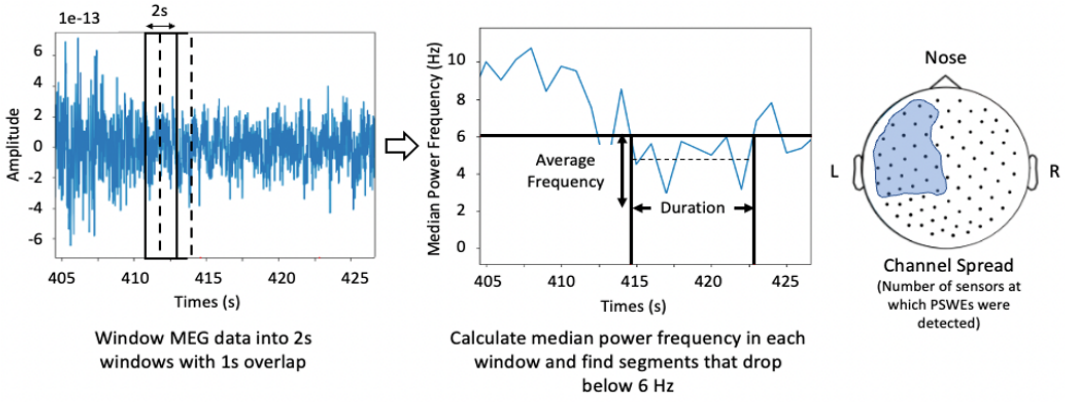

Figure 4.1 Methods for detecting PSWEs in MEG data. PSWEs are characterised by their frequency, duration and channel spread.

The events detected in this work are considered paroxysmal, rather than continuous, because they are characterised by a sudden drop in the MPF of the signal. Figure 4.2 shows the MPF and spectrogram over time for a representative participant with PSWEs and an age-matched participant without PSWEs. It is clear from this representation that the typical 10-15 Hz MPF exhibits sudden drops at irregular intervals

throughout the signal. These drops in MPF are associated with transient increases in low frequency power evident in the participant's spectrogram. The behaviour of this signal is strikingly different from an age-matched control who shows a stable MPF of approximately 10 Hz over time and consistently high power in the canonical alpha frequency band. To further illustrate the paroxysmal nature of the signals of interest, enlarged views of 3 sample PSWEs are presented in Figure 4.3. Here, the sudden decrease in MPF and sudden increase in low-frequency power can be observed on a shorter timescale. Following a 5-10 second period of low frequency activity, a similarly sudden return to baseline behaviour is observed in all cases. The synchronous behaviour of all participating channels is also apparent in Figure 4.3.

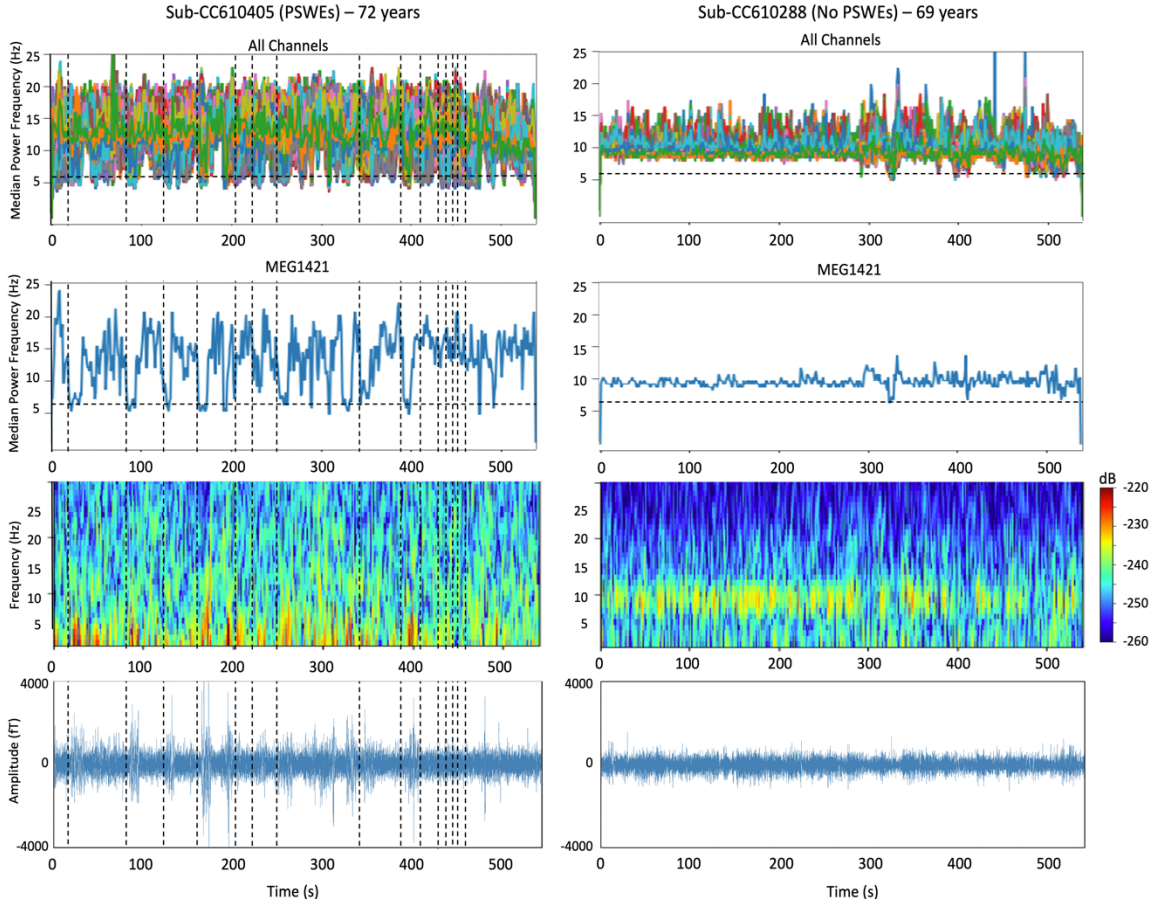

Figure 4.2 Median power frequency plots, spectrograms, and raw data traces for a representative participant with PSWEs (left) and an age-matched participant with no PSWEs (right). The top panels show the MPF for all channels over time, the second-row panels show the MPF for a single channel (MEG1421) over time, the third-row panels show the spectrograms for channel MEG1421 where colour represents the magnitude of activity in dB, and the bottom panels show the raw data for channel MEG1421. The horizontal dashed lines show the 6 Hz frequency cut-off, and the vertical dashed lines

indicate the onset of each detected PSWE. Note that not all indicated PSWEs were captured by MEG1421.

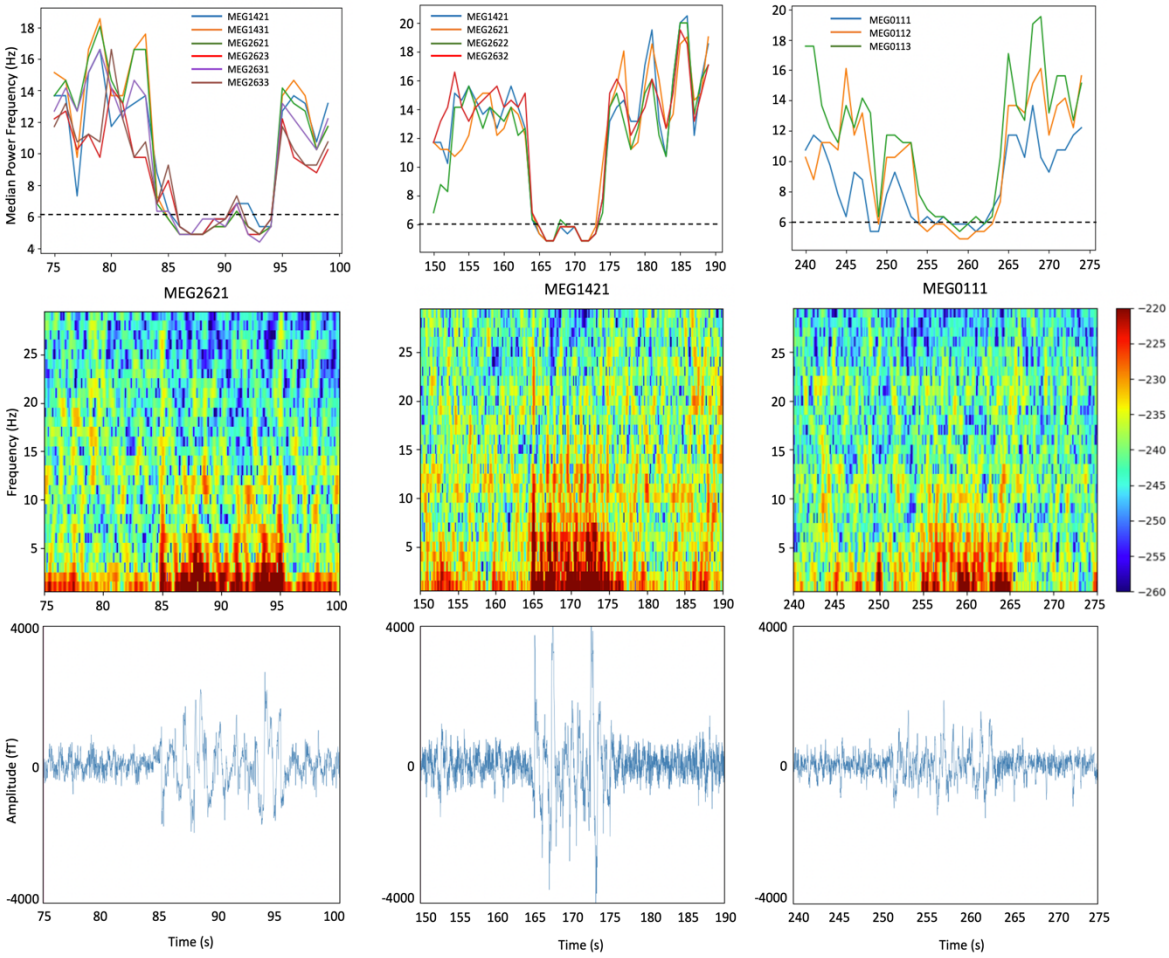

Figure 4.3 Median power frequency plots, spectrograms, and raw data traces for 3 sample PSWEs from a representative participant (sub-CC610405). The top panels show the MPF over time where each coloured line represents one of the channels identified as contributing to the event. The horizontal dashed lines show the 6 Hz low-frequency cut-off for classifying an event as a PSWE. The middle panels show the spectrograms associated with each event for a single channel where colour represents the magnitude of activity in dB.. The bottom panels show the raw data for the same single channel

For each participant, events were collapsed across channels such that any events that occurred at different channels but had overlapping onset and offset times were averaged together to create a single event. Specifically, events were ordered based on their onset times, and for each event, if the offset time was later than the onset time of an event from another channel, then the events were pooled. The characteristics of the overlapping individual channel events were averaged to obtain an average event duration

and frequency that would characterise the multi-channel event. The number of channels involved in the multi-channel event was also recorded as an event characteristic. After pooling events across channels, events with only 1 active channel were excluded because activity generated within brain tissue is generally captured by multiple sensors and single-channel effects are often artefactual. In addition, due to the low-frequency nature of the signal of interest, events were excluded from the analysis if they occurred during significant head movements. Specifically, 1-sample t-tests were used to determine whether the head position velocities during an event were significantly different from the mean head position velocity during the entire scan. Those events that had velocities that were significantly different ($p<0.05$/number of events) from the mean were excluded from further analysis.

PSWEs were further characterised based on their spatial distribution in the MEG sensor array. MEG channels were divided into 8 regions based on their lobe (frontal, parietal, temporal, occipital) and hemisphere (left, right) placement (see supplemental Figure C.1 for illustration of channels by region). For each PSWE, the number of contributing channels from each of the 8 regions was counted and recorded as an indicator of spatial distribution.

4.4.5 Demographic Analysis

Following the detection of PSWEs in all datasets, participants were split into groups based on PSWE presence (i.e., "PSWEs" and "No PSWEs"). Chi-squared tests were performed for characteristics of age, sex, ACE-R scores, and aggregate cognitive scores using a significance threshold of alpha=0.05. Effect size was measured using Cramer's V.

4.4.6 Statistical Analysis

Spectral power in canonical frequency bands including delta (0-4 Hz), theta (4-8 Hz), alpha (8-12 Hz) and beta (12-30 Hz) bands were compared between participants with and without PSWEs using t-tests. Spectral power was calculated for gradiometers and magnetometers separately and a Bonferroni-corrected significance threshold of 0.00625 (0.05/8 tests) was used for all t-tests. Effect size was measured using Cohen's D.

For those participants who had detectable PSWEs (N=127), statistical analyses were conducted assessing the relationship between PSWE characteristics and participant

age/cognitive performance using the R statistical software packages (R Core Team, 2021). Characteristics including event duration, event frequency, number of channels, and number of regions were calculated for each PSWE. In addition, an overall indicator of event prevalence (i.e., time in events) was calculated for each participant. Time in events was calculated as the sum of the durations of all detected PSWEs (in seconds) for a given participant. For each characteristic, the distribution of values was plotted and Kolmogorov-Smirnov tests with alpha=0.05 were used to assess the normality of the distribution as well as the normality of the residuals for a linear model. In cases where the relevant distribution was significantly different from normal (e.g., right skewed), a logarithmic transform was applied to the data to improve normality.

For each characteristic, simple linear regression models were used to assess the relationship between the characteristic and participant age, and between the characteristic and cognitive score. A forward stepwise approach was then used to add cognitive score as an additional predictor to the linear model with age, and to add age as an additional predictor to the linear model with cognitive score. Akaike information criterion (AIC) was used to compare models with and without the additional predictors to assess the contribution of the additional predictors to the model.

For time in events, the relationship with age and cognitive score were relatively weak (see Figure 4.6). However, when inspecting the distribution of log-transformed time in events values across all participants, it was found to be approximately bimodal with an excess mass of 0.0871 (p=0.016). Based on this, a bimodal curve was fit to the distribution and the data were split into “less” and “more” time in events groups based on a splitting point that was defined as the local minimum between the two modes. Differences in participant age between groups with more, less, and no PSWEs were then assessed using a Kruskal-Wallis test (i.e., non-parametric ANOVA), followed by pairwise Wilcoxon rank sum tests in cases where the Kruskal-Wallis was significant with alpha=0.05. Similar statistical analysis was used to assess differences in cognitive score between groups. To evaluate the association between PSWE prevalence and particular cognitive domains, Kruskal-Wallis tests were also conducted comparing Z-scores for individual cognitive tasks between participants with more time in events, less time in events, and no events. A Bonferroni-corrected alpha of 0.00625 (0.05/8 cognitive tests)

was used to assess significance. Effect sizes for Kruskal-Wallis tests were measured using eta^2.

To contextualize the PSWE findings in relation to traditional metrics, model comparisons between linear models of 1-6 Hz average power, 1-6 Hz root mean square (RMS), and time in events with age were conducted. Linear models were constructed using the entire CamCAN cohort (N=623). Average power and RMS were calculated and analysed separately for magnetometers and gradiometers. In addition, previous literature investigating the relationship between low-frequency spectral power and age has reported decreases in low-frequency power with age in healthy populations and increases in low-frequency power in age-related neuropathology. To contextualize the differences between PSWE prevalence groups in relation to these previous findings, the interaction effect of age and PSWE group on power in the 1-6 Hz band was tested using a multiple linear regression model. Similarly, the interaction effect of cognitive score and PSWE group was also investigated. Average power was calculated and analysed separately for magnetometers and gradiometers.

4.4.7 Spatial Analysis

To assess the spatial distribution of PSWEs, the number of active channels in each of 8 spatial regions were compared. Statistical analyses were conducted for gradiometers and magnetometers separately. For each set of events, a Kruskal-Wallis test with alpha = 0.05 was used to determine whether there were significant differences in the number of active channels in the different spatial regions during PSWEs. When significant differences were found, multiple pairwise comparisons were subsequently used to determine which regions were significantly different from one another. A Bonferroni-corrected alpha of 0.00179 (0.05/28 pairs) was used to assess significance of the pairwise comparisons.

Spatial maps were also created to provide a visual representation of PSWE distribution across channels. The total number of PSWEs detected at each channel (across all participants) was calculated and plotted on a spatial topography. Separate plots were created for magnetometer and gradiometer arrays.

4.5 Results

4.5.1 PSWEs and Power Spectral Density

Of the 623 participants included in the PSWE analysis, 127 (~20%) had any detectable PSWEs. The onsets of the detected PSWEs were uniformly distributed across the recording time. The presence of PSWEs was found to be associated with power spectral density such that participants with PSWEs had increased power at low frequencies including delta (gradiometers: T(df=172) = 8.75, p=1.89e-15, effect size=0.978; magnetometers: T(df=164) = 10.1, p<2.2e-16, effect size=1.19) and theta (gradiometers: T(df=199) = 2.96, p=3.46e-3, effect size=0.290; magnetometers: T(df=199) = 3.64, p=3.51e-4, effect size=0.357) frequency bands. At higher frequencies (i.e., alpha and beta), power spectral density values were not significantly different between participants with and without PSWEs (see Figure 4.4). Further exploration of canonical frequency band power in relation to this work is included in the supplemental material (Figures C.2-C.3).

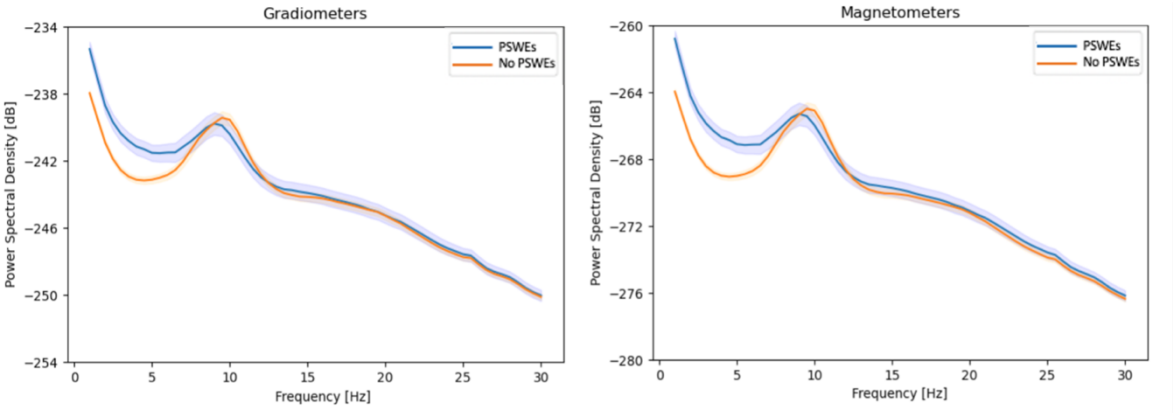

Figure 4.4 Power spectral density plots in dB for all gradiometers (left) and magnetometers (right) averaged across groups of participants with PSWEs (blue), and no PSWES (orange). The solid lines represent the group mean and the shaded region represents the 95% confidence interval.

4.5.2 Demographic Differences

Significant differences in demographic characteristics were also found between participants with and without PSWEs (see Figure 4.5, Table 4.2). Chi-squared tests comparing the distributions of each group revealed that participants with PSWEs have a significantly different age distribution than those without PSWEs (X^2(df=9) = 87.2, p=5.96e-15, effect size=0.265) such that there is a higher proportion of older participants

with PSWEs compared to those without. In addition, there was a higher proportion of females with PSWEs compared to those without PSWEs (X^2(df=1) = 4.62, p=0.0316, effect size=0.0609). Cognitive performance was also skewed to lower values for participants with PSWEs compared to those without PSWEs for both aggregate cognitive scores (X^2(df=8) = 16.5, p=0.0361, effect size=0.115) and ACE-R scores (X^2(df=9) = 36.5, p=3.19e-5, effect size=0.265).

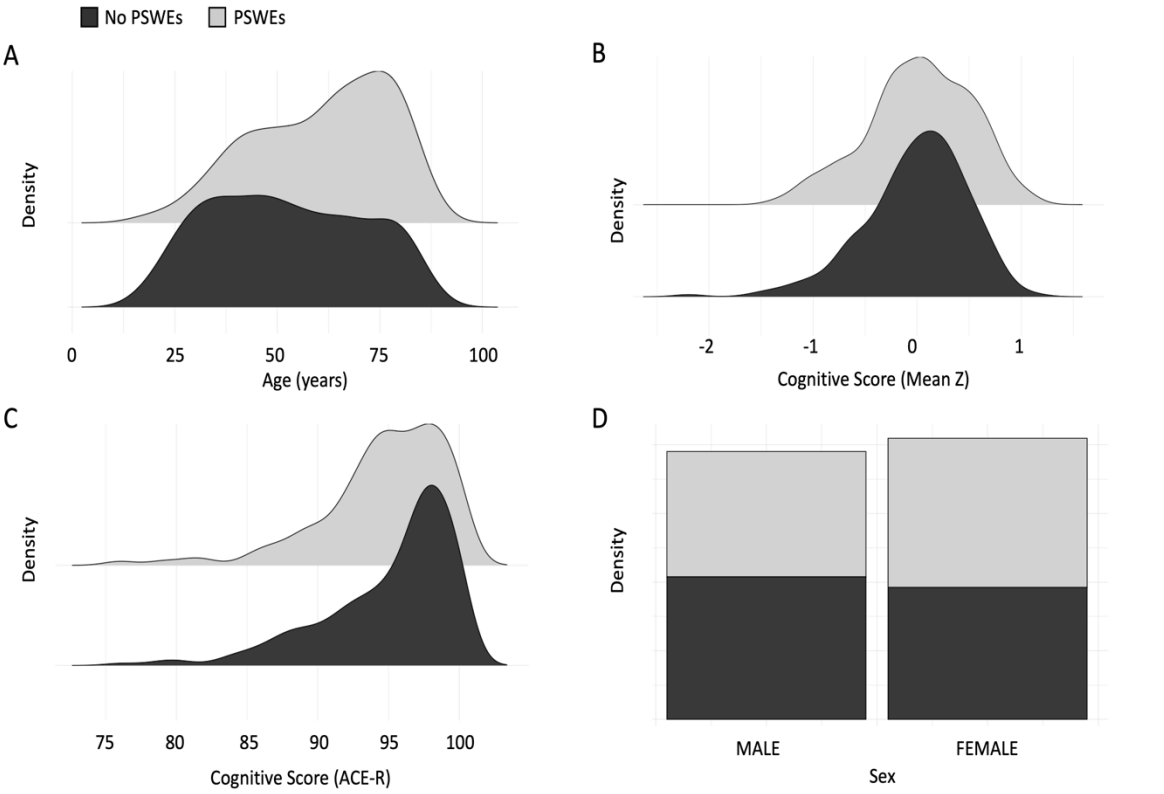

Figure 4.5 Distributions comparing participants with PSWEs (light grey) and those with no PSWEs (dark grey) Groups are scaled to the same total density for comparison. Ridge plots show the distributions of participant age (A), aggregate Z scores of cognitive performance (B), and ACE-R scores of cognitive performance (C). A stacked bar plot is used to compare the distributions of males and females in the two groups (D).

Table 4.2

Summary demographics for participants with and without PSWEs and for the overall group. Means and standard deviations are given for continuous metrics.

Variable	PSWEs	No PSWEs	Overall
Age	61 +/- 16	52 +/- 19	54 +/- 18
Sex	69 F, 58 M	238 F, 257 M	307 F, 315 M
Mean Z Score	-0.15 +/- 0.68	0.03 +/- 0.64	-0.007 +/- 0.65
ACE-R Score	94 +/- 5	95 +/- 5	95 +/- 5

4.5.3 PSWE Prevalence with Age and Cognitive Performance

For participants with PSWEs, the PSWE prevalence (i.e., time in events) was further investigated for trends related to age and aggregate (mean Z) cognitive score. The aggregate cognitive scores were chosen over ACE-R scores for further investigation because the values were more normally distributed.

Within the group of participants with PSWEs (N=127), log-transformed time in events values were regressed against age and cognitive score using simple linear regression. A significant increasing trend was found with age ($F(df=1,125) = 4.46$, $p=0.0366$, $R=0.164$), but no significant effect was found with cognitive score (see Figure 4.6). Stepwise addition of age to the linear model of cognitive score resulted in a significant improvement in the model AIC, but stepwise addition of cognitive score to the model of age did not improve AIC. Based on a comparison of AIC between all models, the model containing age as the only predictor was the best fit for the data.

In addition to the regression analysis, it was determined based on an excess mass test, that the distribution of the log-transformed time in events values were approximately bimodal (excess mass = 0.0871, $p=0.016$). Participants who had detectable events were therefore split into two groups based on the log-transform of their time in events. Fitting a bimodal curve to the distribution revealed modes at 0.8 and 2.1 and a splitting point at 1.6. “Less PSWE” participants were thus defined as participants with a log-transformed time in events value less than 1.6 (approximately 40 seconds; N=76), and “more PSWE” participants were defined as those with a log-transformed time in events value greater than or equal to 1.6 (N=51). Note that the total recording time for each participant was

540 seconds, therefore, participants with more time in PSWEs spent at least ~7% of the recording in PSWEs. Kruskal-Wallis tests comparing the ages of participants with more PSWEs, less PSWEs, and no PSWEs found significant differences between groups ($H(df=2) = 26.6$, $p=1.65e-6$, effect size = 0.0397). Pairwise Wilcoxon rank sum tests revealed that those with more PSWEs were significantly older than those with less PSWEs ($p=0.019$) and those with no PSWEs ($p=7.7e-6$), and that those with less PSWEs were significantly older than those with no PSWEs ($p=0.015$). The mean (+/- standard error) participant age was 52 +/- 1 for participants with no PSWEs, 58 +/- 2 for participants with less PSWEs, and 65 +/- 2 for participants with more PSWEs. Kruskal-Wallis tests comparing the cognitive scores of participants with more, less, and no PSWEs revealed significant differences between groups ($H(df=2) = 15.1$, $p=5.25e-4$, effect size=0.0211). Pairwise Wilcoxon rank sum tests revealed that participants with more PSWEs had significantly lower cognitive scores than those with less PSWEs ($p=0.014$) and those with no PSWEs ($p=3.2e-4$). No significant differences in cognitive scores were found between those with less and no PSWEs. The mean (+/- standard error) cognitive score was 0.030 +/ 0.029 for participants with no PSWEs, -0.060 +/- 0.084 for participants with less PSWEs, and -0.29 +/- 0.079 for participants with more PSWEs.

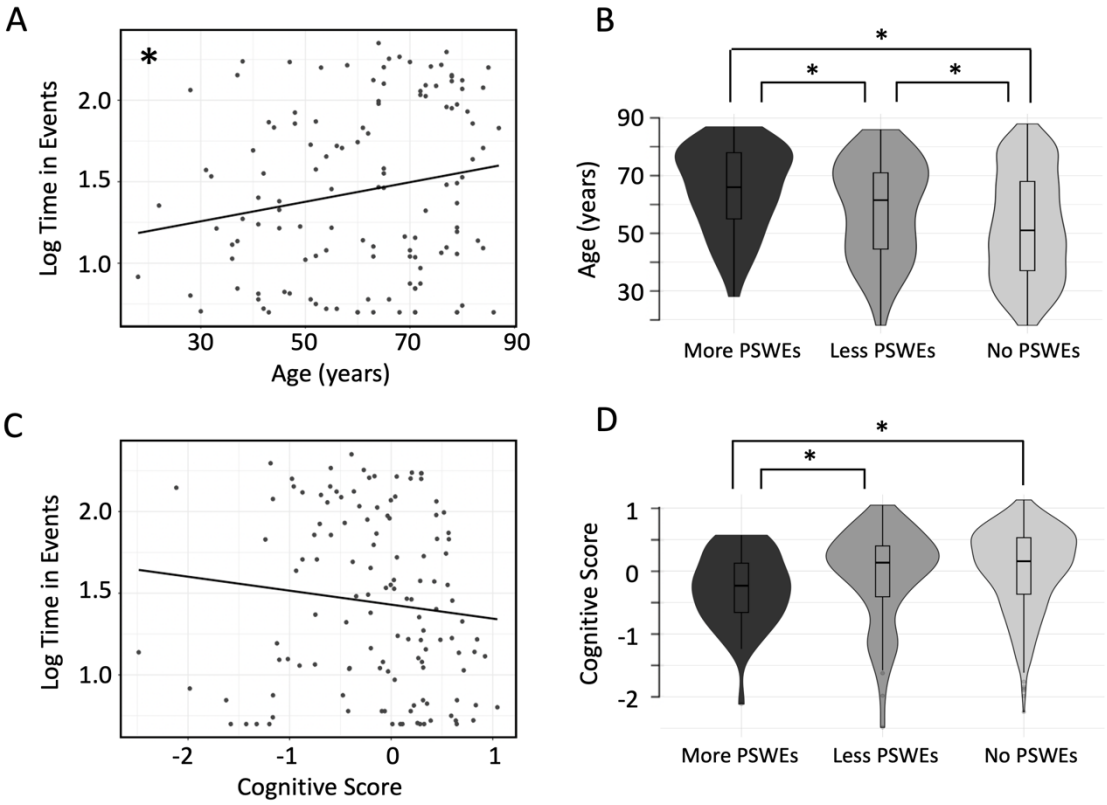

Figure 4.6 The relationship between PSWE prevalence and participant age/aggregate cognitive score. (A) Linear regression relating age to log-transformed time in events values. The solid black line is the best fit regression for this data. (B) Violin plots showing the age distribution of participants with no PSWEs (light grey), less PSWEs (medium grey), and more PSWEs (dark grey). (C) Linear regression relating cognitive score to log-transformed time in events values. (D) Cognitive scores for participants in each PSWE prevalence group. Asterisks indicate a significant effect between groups.

Analysis of individual cognitive task data revealed that participants with more time in PSWEs had lower mean Z-scores than those with less or no time in PSWEs for all cognitive tasks (see Figure 4.7). However, the only cognitive tasks for which this difference was statistically significant with Bonferroni-corrected alpha=0.00625 were the fluid intelligence task (H(df=2) = 14.5, p=7.20e-4, effect size=0.0201), and the hotel task (H(df=2) = 11.2, p=3.74e-3, effect size=0.0148). In both cases, the more PSWEs group had significantly lower Z scores than the no PSWEs group (fluid intelligence p=0.0015; hotel p=0.004).

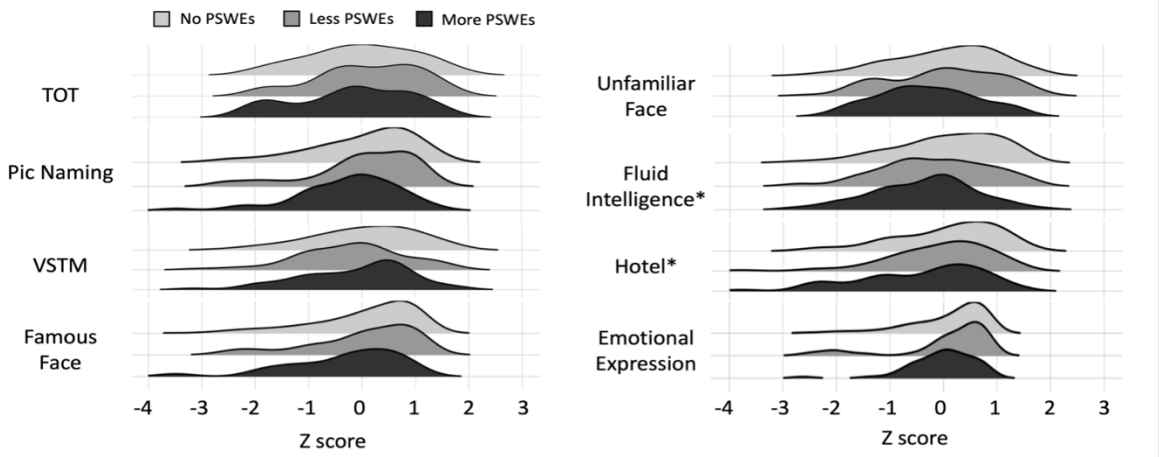

Figure 4.7 Relationship between individual cognitive task scores and PSWE prevalence. Distributions of mean Z-scores for each of 8 cognitive tasks are shown for participants with no PSWEs (light grey), less PSWEs (medium grey) and more PSWEs (dark grey). Significant differences are indicated by asterisks.

4.5.4 Comparison to Common Metrics

Linear model comparisons between 1-6 Hz average power, 1-6 Hz RMS, and time in PSWEs with age revealed that time in PSWEs explained the most variance in age (see Figure C.4, Table C.1). This finding suggests that the time in PSWEs metric is more sensitive to age-related effects than other traditional metrics, and thus provides novel and valuable information about age-related brain activity. A complete breakdown of this analysis, including figures and statistical results is included in the supplemental material (Figure C.4, Table C.1).

Multiple linear regression assessing the effects of age and PSWE prevalence on low-frequency band power revealed significant effects (gradiometers: $F(df=5,617) = 12.7$, $p=9.40e-12$, $R=0.293$; magnetometers: $F(df=5,617) = 18.4$, $p<2.2e-16$, $R=0.351$; see Figure 4.8). Particularly, an interaction effect was found whereby participants in the less and no PSWE groups showed a decreasing trend in 1-6 Hz band power with age, in line with previous findings of healthy ageing (Emek-Savaş et al., 2016; Leirer et al., 2011; Meghdadi et al., 2021; Vlahou et al., 2015), while participants in the more PSWEs group showed an increasing trend in 1-6 Hz band power with age. This interaction effect was significant for magnetometer power values (age by more-less: $p=0.0496$; age by more-none: $p=0.0429$) but did not reach significance for gradiometers (age by more-less: $p=0.0563$, age by more-none: $p=0.0517$). Multiple linear regression assessing the effects

of cognitive score and PSWE prevalence on low-frequency band power also revealed significant effects (gradiometers: F(df=5,617) = 11.3, p=2.09e-10, R=0.276; magnetometers: F(df=5,617) = 16.6, p=2.38e-15, R=0.333). In this case however, there was a significant effect of group (high-none) for gradiometers (p=9.60e-5) and magnetometers (p=1.03e-7), but no significant interaction effect of cognitive score and PSWE prevalence.

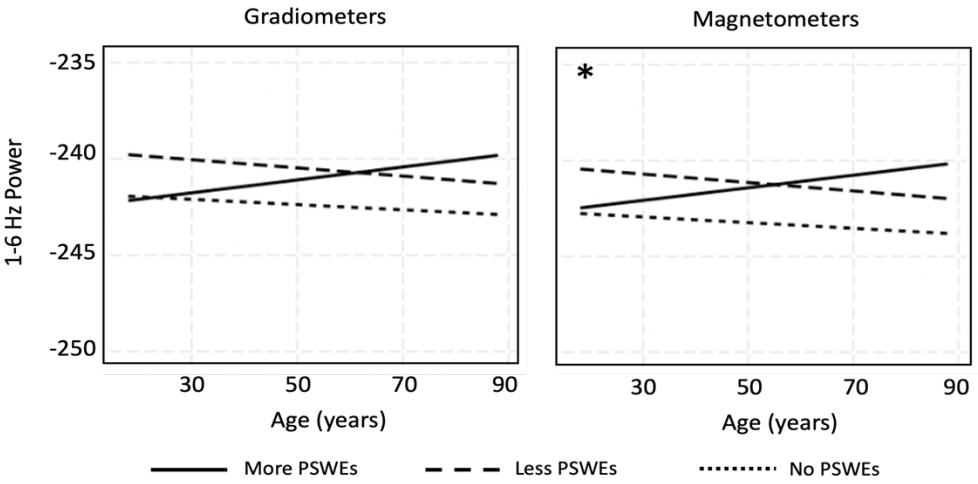

Figure 4.8 Interaction effect of age and PSWE prevalence on 1-6Hz band power for gradiometers (left) and magnetometers (right). Significance is indicated by asterisks.

4.5.5 Burst Characteristics of PSWEs

In addition to PSWE prevalence, PSWE characteristics including event duration, event frequency, number of channels, and number of regions were regressed against age and cognitive score (see Figure 4.9). For event duration, there was a significant increase in log-transformed event duration with age (F(df=1,916) = 23.6, p=1.40e-6, R=0.155) and a decrease with cognitive score (F(df=1,916) = 7.63, p=5.84e-3, R=0.0847). The stepwise addition of age to the linear model of cognitive score improved the model AIC, but the addition of cognitive score to the model of age did not. The model of age alone was the best model to explain the effects related to event duration. Log-transformed mean frequency was found to decrease with age (F(1,916)=25.1, p=6.66e-7, R=0.160), but no significant effect of cognitive score was found. However, both the addition of age to the cognitive score model and cognitive score to the age model resulted in an improved model AIC, and the model containing both predictors was found to be the best fit for the mean frequency data. Log-transformed number of channels and log-transformed number

of regions both showed decreases with cognitive score (channels: F(df=1,916) = 32.4, p=1.68e-8, R=0.182; regions: F(df=1,916) = 23.2, p=1.68e-6, R=0.154), but no significant changes with age. In both cases, the addition of age to the cognitive score model and the addition of cognitive score to the age model resulted in an improved model AIC, and the model containing both predictors was the best fit for the data. The relationship between event spread and age and cognitive performance is further explored in supplemental Figure C.5.

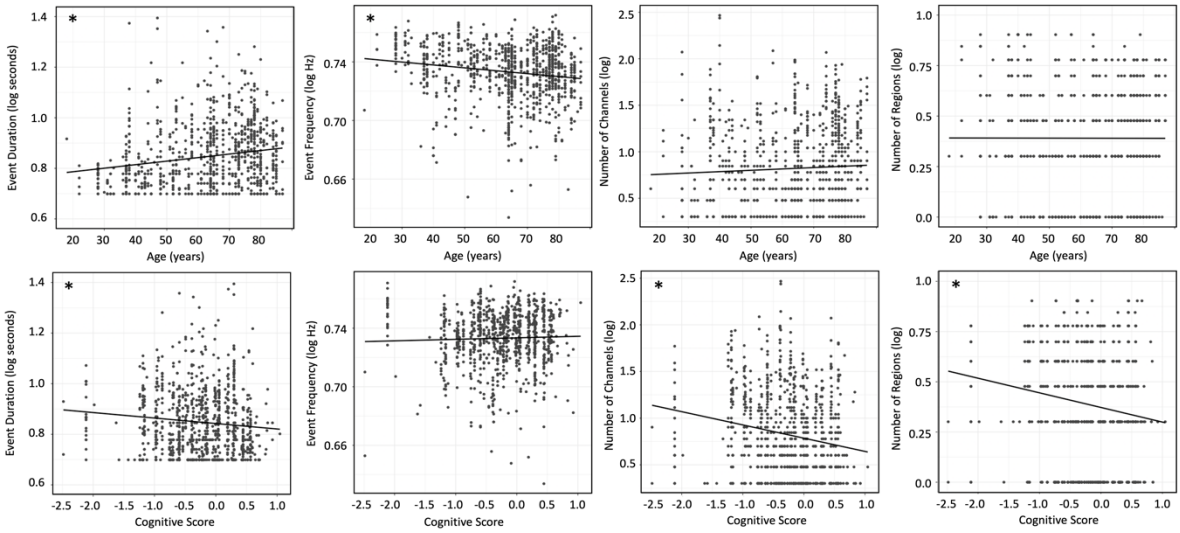

Figure 4.9 Results of regression between PSWE characteristics and age/cognitive score. Each point represents the characteristic associated with a single PSWE and black lines show the best fit result of the regression. Significance is indicated by asterisks.

4.5.6 Spatial Distribution of PSWEs

The spatial distribution of PSWEs is shown in Figure 4.10. A Kruskal-Wallis test comparing the number of channels affected by PSWEs in each spatial region revealed that, for both gradiometers and magnetometers, there were significant differences between regions (gradiometers: H(df=7) = 949, p<2.2e-16, effect size=0.128; magnetometers: H(df=7) = 727, p<2.2e-16, effect size=0.0981). A diagrammatic representation of the significant differences between brain regions is shown in Figure 4.10C. In particular, for gradiometer events, the number of affected channels in the temporal regions (left and right) were significantly higher than all other regions, and the number of affected channels in the parietal regions (left and right) were significantly lower than all other regions. The number of affected channels in the frontal regions were

significantly greater than in the occipital regions. There were no significant differences between the left and right hemispheres with the exception of the occipital region where the right hemisphere had a greater number of affected channels than the left hemisphere. For magnetometer events, the results were quite similar with a few exceptions. Firstly, for magnetometers, there were no significant differences between the number of channels affected in the frontal and occipital regions. And secondly, while there was no significant difference between left and right occipital regions, there was a significant difference between left and right frontal regions.

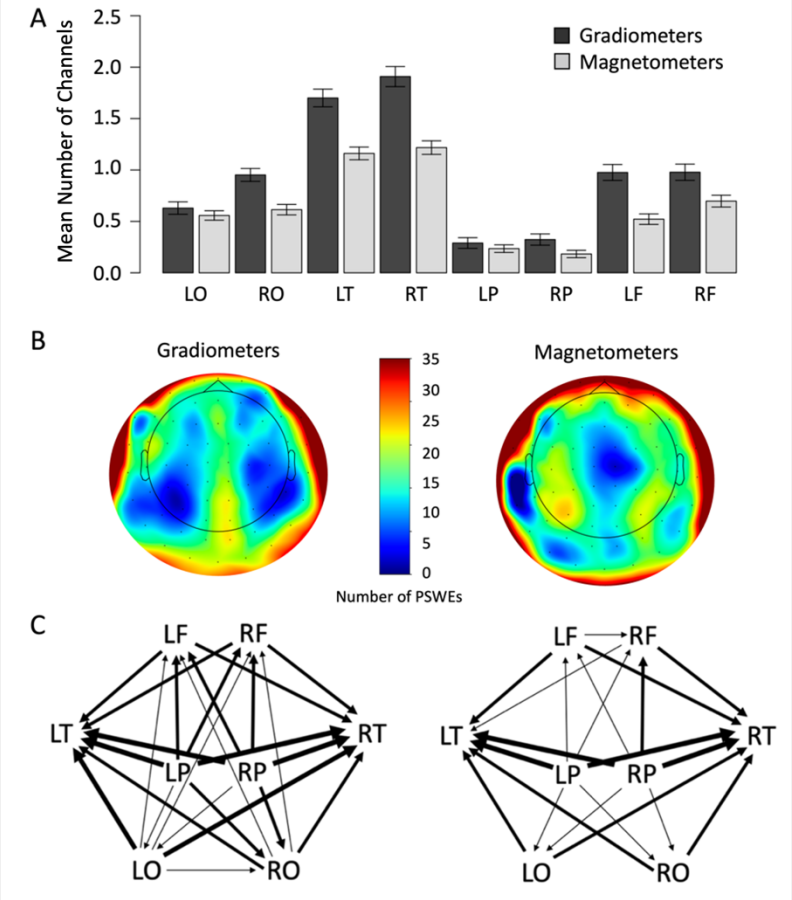

Figure 4.10 Spatial distribution of gradiometer and magnetometer PSWEs. (A) Mean number of channels in each spatial region for magnetometer (light grey) and gradiometer (dark grey) PSWEs. Error bars represent standard error. The 8 spatial regions indicated are left occipital (LO), right occipital (RO), left temporal (LT), right temporal (RT), left parietal (LP), right parietal (RP), left frontal (LF), and right frontal (RF). The diagram of the sensors included in each region is provided in the supplemental material (Figure C.1). (B) Spatial topographies showing the total number of PSWEs across all participants that were detected at each channel. Plots are shown for magnetometers and gradiometers separately. (C) Visual representation of the difference in the number of active channels

between spatial regions, averaged across participants. Significant differences between brain regions are indicated by arrows. Arrows point in the direction of the brain region with a greater number of active channels. Line width represents the magnitude of the difference.

4.6 Discussion

4.6.1 Summary of Findings

This work provides the first characterisation of the presence and prevalence of PSWEs in a healthy human population. In this work, PSWEs were identified in MEG recordings from a subset (~20%) of healthy participants. This finding demonstrates for the first time, that PSWEs can be found in some individuals in the absence of a known neuropathological diagnosis and that the prevalence of this purportedly pathological activity in persons without a diagnosis is as high as 1 in 5. The presence and prevalence of PSWEs in healthy participants was found to be related to the age and cognitive performance of participants such that older participants and those with lower cognitive scores tend to have more time spent in a PSWE state. In addition, it was found that PSWE characteristics including event duration and event frequency changed linearly with age, resulting in longer, and slower events in older adults. On the other hand, lower cognitive performance was found to be related to more widespread events (i.e., higher number of channels and regions affected). This work provides unique insight into the transient nature of low-frequency brain activity. While the debate regarding whether a transient or continuous analysis of neurophysiological data is most appropriate is still unresolved, this work provides a novel, complementary perspective on slow wave activity in a healthy cohort by highlighting the characteristics of transient events that are most relevant to the age and cognitive score. Finally, this work provides the first sensor-level evidence for potential sources of PSWEs in healthy ageing.

4.6.2 Significance

The findings of this work have several implications for our understanding of changes in cortical network activity during ageing. Importantly, the findings suggest that there may be a meaningful difference in the neurophysiology of a subset of participants leading to the emergence of atypical brain activity. Participants with PSWEs tend to be older and have lower cognitive performance than those without PSWEs, but it remains unclear whether the presence of these events can be attributed to normal variability in

non-pathological ageing, or if the presence of PSWEs suggests underlying undiagnosed pathology in this subset. Previous studies suggest that increased low-frequency brain activity is more indicative of pathology than healthy ageing. While increased low-frequency activity is commonly observed in age-related pathology such as dementia and AD (Brenner et al., 1986; Hier et al., 1991; Jeong, 2004; Musaeus et al., 2018; Penttilä et al., 1985; Weiner and Schuster, 1956), studies of healthy older adult populations have often observed an opposite effect whereby low-frequency activity actually decreases with age (Emek-Savaş et al., 2016; Leirer et al., 2011; Meghdadi et al., 2021; Vlahou et al., 2015). Interestingly, when relating our PSWE prevalence findings to average band power, we found an interaction effect between PSWE prevalence and age whereby participants with more PSWEs showed an increasing trend in band power with age, while participants with low or no PSWEs showed a decreasing trend in band power with age. In the context of previous age-related band power findings, this suggests that prevalent PSWEs are likely not characteristic of a healthy ageing brain and rather may be indicative of underlying cortical dysfunction. This observation suggests that PSWEs may have utility as a biomarker for atypical brain ageing. However, further work is required to elucidate the clinical applicability of this marker.

This work provides the first evidence for an association between PSWEs and cognitive processes in healthy adults. Particularly, cognitive performance was found to be related to the spatial spread of PSWEs such that those with lower cognitive scores had events that were captured on a large number of sensors and spatial regions. The relationship between overall cognitive score and PSWE prevalence was found to be primarily driven by age-related effects, however, we made an interesting observation whereby some cognitive tasks (e.g., fluid intelligence and hotel tasks) showed more prominent changes with PSWE prevalence than others. While the origin of this effect cannot be fully disentangled from the effect of age, this suggests that some cognitive processes, particularly higher order fluid intelligence and executive function processes have a stronger relationship to PSWE prevalence compared to other cognitive processes such as memory, language, and emotion recognition. Fluid intelligence tasks are typically cognitively demanding and require the integration of sensory, language, working memory, and higher-order reasoning and decision-making processes that require

activation of broadly distributed brain networks (Barbey et al., 2014). Therefore, the relationship between PSWEs and cognitive performance seems to depend on the cognitive demands of the task. This, together with the high occurrence of PSWEs in patients with AD (Milikovsky et al., 2019), suggests the need for future studies to test whether PSWE analysis can be used as a sensitive biomarker for early diagnosis of neurodegenerative brain disorders associated with cognitive decline.

The current work also provides insight into the mechanisms underlying PSWE generation using sensor-level regional analyses. Spatial topographies suggested widespread activation of large cortical networks during PSWEs, with particularly high activation of temporal sensors compared to other regions. These regional findings are in line with cognitive performance findings that showed a strong association between fluid intelligence and executive function and PSWE occurrence, since widespread sources are involved in these functions (Barbey et al., 2014). This evidence, taken together, provides some clues as to the functional relevance of PSWEs. In particular, it suggests temporal regions (i.e., temporal cortex or subcortical temporal structures such as the hippocampus), or widely distributed sources as potential sources of PSWE generation.

4.6.3 Limitations and Future Directions

It should be noted that there are limitations associated with the sensor-based spatial analysis conducted in this work. In particular, a region-based approach was used to index spatial spread, which provides only a rough estimate of underlying source activity. The sensor/region-based approach is limited due to variability in the position of the sensors relative to different participants' heads, and the complexity of the inverse problem. While we generally expect that sensors strongly activated by an event are close to the source of the event, it is impossible to confirm this without source estimation. Therefore, further studies using source localization approaches and/or intraoperative recordings are required to test the spatial hypotheses formed in this work. One logical approach to investigating PSWEs at the source level is to apply a transient burst localization method as previously proposed (Power and Bardouille, 2021). This method was attempted by our group and the results are included in the supplemental material (see Figure C.6). However, the source estimation resulted in high activity primarily in ventral regions of the cortex. Because MEG source estimation generally has low accuracy for

ventral and/or deep sources, we were not confident in the accuracy of these activation maps. In addition, MEG source localization is limited for this application because the PSWEs are widely distributed across cortical regions, as is evident from Figure 4.10. The MEG imaging modality is unreliable in its detection of deep and diffuse cortical sources because most source localization methods model a source as a focal (i.e., $<10mm^2$) cortical patch (Hansen et al., 2010). Due to these limitations, future work is required before definitive conclusions about PSWE sources can be made. To mitigate these limitations, future work could consider resting-state fMRI or multimodal imaging (e.g., simultaneous EEG-fMRI) results from participants known to have PSWEs. The differences between resting-state brain activity of participants with and without PSWEs could be investigated to identify the presence of any neurophysiological correlates of the PSWE signal.

While this work has provided promising results towards the identification of a potentially relevant marker of atypical brain function, there are some potential confounds of the work that should be addressed. Firstly, the significant correlation between age and cognitive score ($p<2.2e-16$, $R=0.524$) is a confound to our interpretation of the age and cognitive performance-related effects. We attempted to investigate the relative contributions of age and cognitive score to the model using stepwise regression. This suggested that age was the primary predictor of most of the PSWE effects, with the exception of spatial spread metrics which showed primary effects with cognitive performance. Despite our attempts, it is difficult to fully disentangle these highly related predictors, and this should be acknowledged when interpreting the results of this work.

In addition, given the high power, transient nature of the signal of interest, it is possible that some relevant signal was excluded during pre-processing steps. In particular, the exclusion of independent components and the removal of data segments corresponding to head movements may have inadvertently resulted in the loss of PSWE segments which could have confounded our results. The potential effects of these exclusions were investigated by comparing the age and cognitive performance values between the clean data and excluded components and it was found that there were no significant differences in effects between included and excluded data. Therefore, we can conclude that while some PSWEs were excluded from analysis, these exclusions did not

affect the overall findings of the work. In the future, large data projects that use artefact rejection with methods such as ICA should employ cautious investigation of excluded data. As we have done, excluded components should be interrogated carefully in order to obtain fulsome and balanced insight into their relationship to identified trends.

In addition, there are some avenues for future research that could further improve our understanding of the presence and prevalence of PSWEs. Firstly, while previous research examining PSWE prevalence used EEG data, our work detected PSWEs in MEG data. Due to differing sensitivity and channel numbers between technologies it is difficult to directly compare our findings to previous work. Therefore, future research should consider comparing PSWE detection in EEG and MEG from the same cohort of participants to provide insight into the sensitivity of each to PSWE activity. Another limitation of this work is that the temporal characteristics of the PSWE signal studied in this work were pre-defined based on previous observations of low frequency transient signals in pathological populations (Milikovsky et al., 2019). The PSWEs were detected in this work using identical methods to those described in the original characterisation of PSWEs by Milikovsky and colleagues (2019) to allow for comparison to previous results. However, it is possible that the constraints applied to the PSWE signal are not capturing the entire nature of the relevant signal in this cohort of healthy adults. For this reason, future studies should consider alternative methods of transient signal detection that make fewer a-priori assumptions about the temporal features of the signal of interest. For example, a method such as convolutional dictionary learning (Dupré la Tour et al., 2018; Power et al., 2023) could be used on this dataset to naively detect transient electrophysiological markers of ageing.

4.7 Conclusion

This work provides unique insight into electrophysiological characteristics of the ageing brain by utilizing a large open-access dataset and a transient event framework. We suggest that PSWEs could become a biomarker for the detection of atypical brain activity associated with reduced cognitive abilities in older adults. The identification of such a biomarker that is easily detectable through fast, non-invasive measurements is particularly desirable for rapid assessment of cognitive dysfunction which would normally require significant time and human resources to complete. These findings have

important implications for the future of the field of cognitive ageing research as they provide new information on pathophysiological mechanisms underlying the ageing brain and a promising target for therapy.

Chapter 5

Discussion

5.1 Summary of Findings

This thesis explores the relationship between age and transient patterns of brain activity in a healthy adult population. Novel analysis methods were employed to probe the temporal and spatial characteristics of typical and atypical transient events in neuromagnetic recordings, providing insight into the neurophysiological mechanisms involved in healthy ageing and task performance. The thesis is comprised of 3 projects.

In project 1, we investigated age-related trends in the cortical sources of transient beta bursts during a sensorimotor task and rest. It was found that beta bursts localized primarily to the sensorimotor cortex under the sensor used for their detection and had slight variations in their location depending on the movement condition. In addition, age-related changes in source were observed including an anterior shift in peak position with age, and an increase in frontal activation with age that peaked around age 60. These results showed for the first time that source localization techniques can be implemented for the identification of the sources of transient beta bursts, and provided insight into the anatomical generators of transient beta activity and how they change across the lifespan.

In project 2, we applied a convolutional dictionary learning algorithm to naively detect task-related neuromagnetic transients and assessed their relationship to age. A set of 7 task-related spatiotemporal patterns were identified including patterns that resembled beta, mu, and alpha type transients. All burst types showed positive trends in their activation levels with age that could be explained by increasing burst rate with age. This work validated the data-driven CDL approach for transient burst detection on a large dataset and identified robust information about the complex characteristics of human brain signals and how they change with age.

Finally, in project 3, we detected and characterised atypical slow wave transients (i.e., PSWEs) in a purportedly healthy population and investigated their relationship to age and cognitive performance. PSWEs were detected in approximately 20% of healthy participants in the dataset, and participants with PSWEs tended to be older and have

lower cognitive performance than those without PSWEs. In addition, event features changed linearly with age and cognitive performance, resulting in longer and slower events in older adults, and more widespread events in those with low cognitive performance. These findings provided the first evidence of PSWEs in a subset of purportedly healthy adults, which has implications for our understanding of their clinical relevance.

5.2 Neural Mechanisms of Transient Events

One of the main advantages of analysing neurophysiological signals using a transient event framework is that the results can provide greater mechanistic insight than can be derived from traditional average power measures. Studying the temporal and spatial characteristics of transient events and how those characteristics change with task performance, disease, and normal ageing, provides a window into the network-level mechanisms underlying these processes. Together, the chapters of this thesis provide significant insights into the mechanisms of typically occurring sensorimotor beta bursts as well as atypical PSWEs. This section provides a big picture overview of the mechanistic insights provided by this thesis, along with promising directions for further exploration. In the subsequent sections, specific hypotheses are explored in greater detail.

5.2.1 Mechanisms of Beta Bursts

The sources and network mechanisms underlying beta bursts were investigated in Chapters 2 and 3. Chapter 2 provided insight into the generative location of beta bursting, suggesting the presence of multiple cortical generators in the pre-central and post-central gyri that are differentially involved in different phases of a motor task. The work further revealed marked age-related changes in beta source, particularly in the post-movement interval, suggesting that with age, the coordinated beta bursting involved in the termination of voluntary movement expands from a relatively focal synchronous population in the primary motor cortex to a coordinated effort of a much more widespread cortical area. A potential functional explanation for this expansion of source is that the activation of a wider population of neurons is protective against loss of function if regional neurodegeneration occurs with age. As described in the introduction (Section 1.1), there are many factors that contribute to the degradation of grey and white matter with age. Because functions confined to a focal region would be more vulnerable

to the effects of this degradation, older adults may shift to a more spatially distributed network to protect against functional losses, or to compensate for neurodegeneration that has already occurred. In Chapter 3, the changes observed in activation sum, burst rate, and burst power with age provided additional insight into the network-level mechanisms underlying age-related effects. For beta-type atoms, burst rate was found to be the primary driver behind age-related changes in atom activation, with the age-related trends in beta burst rate in the pre- and post-movement intervals mirroring trends in beta activation. Burst power, however, did not play a significant role. This finding suggests that changing beta activity with age is related to changes in the number of activations of the underlying neural networks (i.e., the firing rate of the neuronal population), rather than the magnitude of the individual activations (i.e., the number of neurons contributing to the signal). Taken together, these findings suggest that while the network involved in beta generation becomes more widely distributed with age, the number of contributing neurons in the brain areas common across the population does not necessarily increase, and that the rate of occurrence of population bursting changes throughout the lifespan.

While the current thesis provides some hypotheses regarding the neural networks involved in beta bursts and their age-related dynamics, further investigations are required to validate these hypotheses, and to begin to understand the specific cellular and molecular underpinnings of the network-level changes. Computational modelling provides a promising avenue for investigating these mechanisms. In particular, the open-source Human Neocortical Neurosolver (HNN) software package (Neymotin et al., 2020) provides a useful framework for investigating changes in beta burst dynamics with age. The foundation of the HNN model is a scalable local network of pyramidal neurons and inhibitory interneurons in the supragranular (layers 2 and 3) and infragranular (layer 5) layers. Activity in the local network is driven by exogenous driving input through two pathways. The first is a proximal (i.e., feedforward) drive that originates in the lemniscal thalamus and contacts the basal dendrites of pyramidal cells, propagating upwards to the superficial cortical layers. The second is a distal (i.e., feedback) drive that originates in the higher-order cortex or non-specific thalamic nuclei and contacts the apical dendrites of the pyramidal neurons, propagating downwards to the infragranular layers. The HNN uses this basic model to simulate electrophysiological signals comparable to those

recorded experimentally by MEG or EEG (i.e., equivalent current dipole time courses). Work by Sherman et al. (2016) demonstrated that this model could be used to simulate the temporal waveform of transient beta bursts by combining a strong distal drive in-phase with a weaker proximal drive. The authors were then able to validate this mechanism in animal models (Sherman et al., 2016). Using this model as a starting point, age-related trends in beta burst mechanisms could be investigated by modifying the parameters of the model to induce changes in the simulated beta bursts that are reflective of the age-related changes observed empirically. For example, parameters of the model such as the firing rate and relative timing of the input drives, and the post-synaptic receptor weights, could be modified and related to the beta burst characteristics of the resulting simulated signals to provide insight into the relationship between neural parameters and burst characteristics. This information could then be used to form and test hypotheses about the relationship between neural parameters and age.

5.2.2 Mechanisms of PSWEs

The mechanisms of PSWE generation are more elusive, but the results of Chapter 4 provide some insights that will allow us to form more targeted hypotheses going forward. For beta transients, burst rate emerged as the clear driver of age-related changes in beta activation. However, for PSWEs, the number (i.e., rate) of PSWEs, as well as the duration and frequency all changed significantly with age, making it difficult to pinpoint the network mechanism driving the age-related trends. Interestingly, however, different relationships were observed for age and cognitive performance such that age was primarily related to the prevalence (i.e., number and duration) of events, and cognition was more strongly associated with the spatial spread of events (i.e., the number of channels and regions affected). This suggests that different network mechanisms may be involved in the PSWEs that appear in healthy ageing compared to those that appear in the progression to cognitive decline. In other words, the appearance and increased prevalence of focal PSWEs with age may be a normal feature of ageing, while the emergence of widespread events could be indicative of cognitive impairment or a pathological process. The mechanistic distinction between focal and widespread events is not clear from the current work. For example, focal and widespread events could emerge from independent mechanisms, or they could be inherently focal but have a tendency to co-occur resulting

in the appearance of widespread events. A third potential mechanism is that PSWEs could have a focal generator that eventually triggers the global spread of events, similar to the mechanism of secondary generalized seizures in epilepsy. This mechanism would be in line with previous speculation that PSWEs reflect sub-clinical seizures in patients with epilepsy or AD (Milikovsky et al., 2019).

In order to elucidate which of these mechanisms are involved in focal and widespread PSWEs, careful inspection of individual events and their source progression over time is required. In the current work, PSWE source localization was completed across events and subjects, and throughout the entire duration of the events, which resulted in the appearance of a distributed source pattern in the ventral regions of the brain. While this was a logical first step in estimating source, this averaging approach may not have been appropriate if the PSWE sources are heterogenous within or between events. In future work, PSWEs could be localized individually in order to get a sense of the variability in source between events. Additionally, if there is fairly low source variability between events, dynamic modelling (e.g., time resolved MNE or beamformer) could be performed on the PSWEs for each participant to provide insight into the generative source of the PSWEs (i.e., the source at onset) as well as their spatial progression over time. While these methods would likely provide rich information about the spatial dynamics of PSWEs in individual participants, the potential inter-subject variability may pose a challenge when attempting to interpret group-level effects. Therefore, applying these methods to the participants in the CamCAN dataset would likely require the development of methods to quantify and compare time-varying sources across large groups of participants. Despite these challenges, improving our understanding of the source progression of PSWEs is a necessary future direction towards understanding their clinical significance.

In addition to time-resolved source estimations of individual events, computational modelling approaches would also be beneficial to further elucidate the mechanisms of PSWE generation. Potential candidate models for recreating PSWEs include models used to simulate paroxysmal patterns of seizure activity (e.g., neural mass models, neural field models, formal mathematical models, etc.) (Wendling et al., 2016; Jafarian et al., 2021), and models that have been used to simulate changes in low

frequency power in the transition from sleep to wake (e.g., Robinson et al., 2001). Attempting to model PSWE characteristics using these types of models would provide insight into whether the PSWE phenomena observed in this work are mechanistically similar to seizure activity or the low frequency patterns present during sleep. These insights would guide our understanding of the implications of such phenomena in healthy ageing. Further, validating the hypotheses formed through computational modelling with animal models would also be a beneficial next step. Assuming one or both of the proposed model types provide a reasonable hypothesis of PSWE generation, the hypothesis could then be tested by electrically or chemically inducing the proposed generative mechanisms in animal models and evaluating the presence of PSWEs in EEG or LFP recordings. The concordance between computational and animal model findings would provide strong evidence for a generative mechanism of PSWEs.

5.3 Multiple Cortical Generators of Beta Bursts

An interesting finding of Chapter 3 was that two distinct clusters of contralateral sensorimotor beta transients emerged with slightly different representative waveforms and spatial topographies. Upon fitting an ECD for the representative atom for each cluster, it was found that one atom localized slightly pre-centrally, while the other localized slightly post-centrally. This finding suggests that these two atom clusters may represent two distinct types of beta transients that come from different (primary motor and primary somatosensory) sources and may have different physiological properties. The concept of different pre-central and post-central beta generators was also suggested in Chapter 2 where post-central (i.e., somatosensory) sources were found to be associated with pre-movement beta bursts, and pre-central (i.e., primary motor and pre-motor) sources were found to be associated with post-movement beta bursts. In line with this, in Chapter 3 we found that in the pre-movement interval there was higher activation of the left post-central beta atoms compared to the left pre-central beta atoms ($p = 0.034$) and in the post-movement interval there was higher activation of the left pre-central beta atoms compared to the left post-central beta atoms ($p = 0.018$). This finding suggests that the left post-central beta atoms identified in Chapter 3 may be related to the post-central generators involved in pre-movement beta bursts described in Chapter 2, and the left pre-

central beta atoms in Chapter 3 may be related to the pre-central generators involved in post-movement beta activity described in Chapter 2.

The converging evidence of multiple cortical generators for pre-movement and post-movement transient beta bursts has interesting implications for the emergent field of travelling cortical waves (Hindriks et al., 2014; Muller et al., 2018). Previous research in non-human primates and tetraplegic human participants has demonstrated that beta waves propagate short distances in the motor cortex, along the anterior-posterior axis in the primary motor cortex and along the medial-lateral axis in the pre-motor cortex, at speeds between 10-35 cm/second (Rubino et al., 2006; Takahashi et al., 2011). However, the propagation between pre-central (motor) and post-central (somatosensory) sources was not investigated in these works. The findings of Chapters 2 and 3 suggest that beta waves likely either propagate across the central sulcus throughout the phases of movement, or that there are two independent beta generators that switch their dominance depending on the phase of movement. These two potential mechanisms are depicted in Figure 5.1.

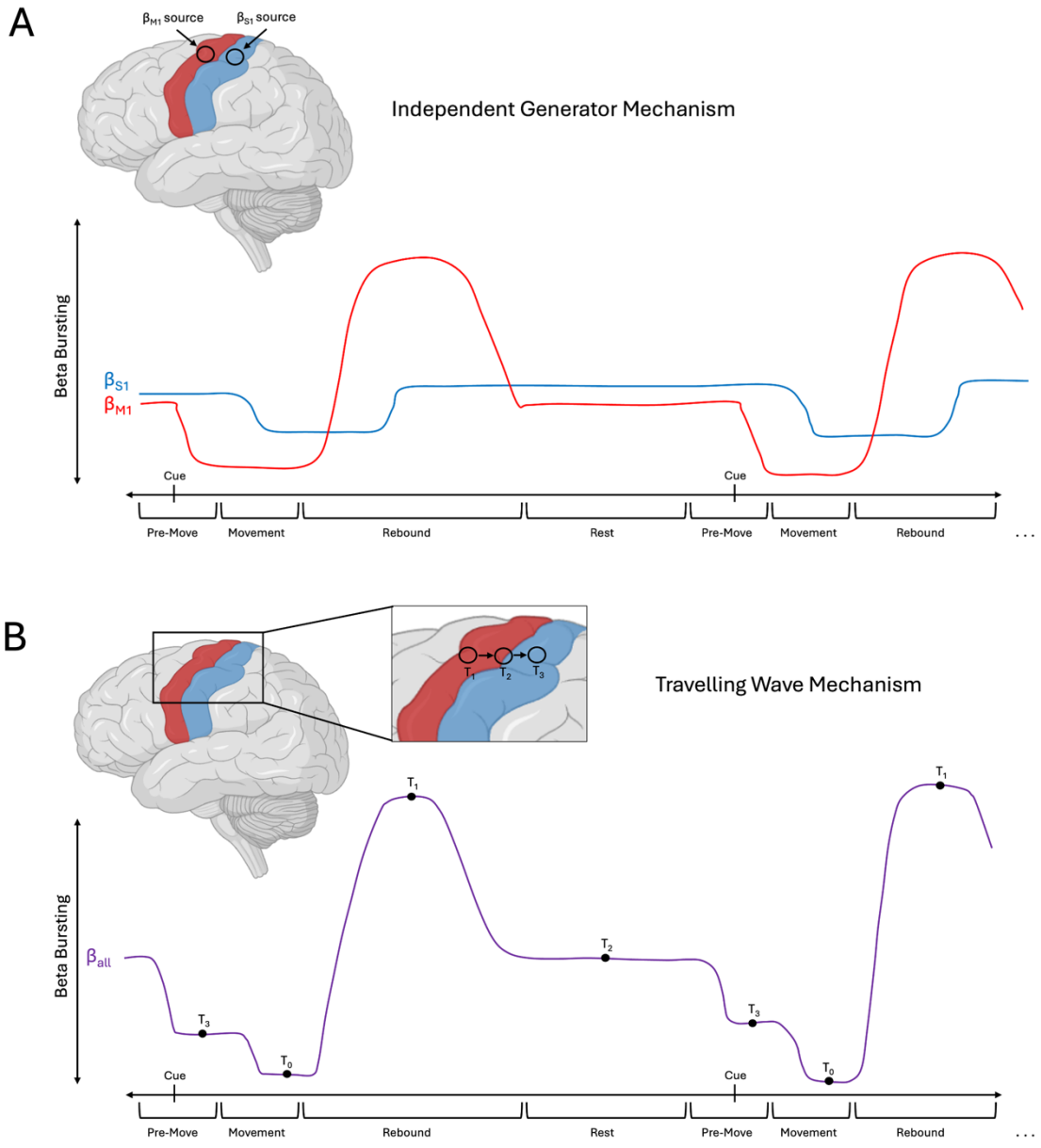

Figure 5.1 Potential mechanisms of sensorimotor beta burst generation. (A) Depicts the proposed independent generators mechanism whereby distinct sources in the primary motor (M1) and primary somatosensory (S1) cortices generate beta bursts independently. M1 beta (red) and S1 beta (blue) exhibit task-dependent fluctuations in bursting as depicted. (B) Depicts the alternative travelling wave mechanism whereby sensorimotor beta is generated by a single source, but that source propagates in space over time. This unified beta (beta-all; purple) shows task-dependent fluctuations over time that are an approximate summation of M1 and S1 beta depicted in A. At T0 beta bursting resets, then at different time points throughout the ISI (e.g., T1, T2, T3), the center of the generative source shifts as depicted on the cortical surface. Figure created using icons from Biorender.com.

As shown in Figure 5.1A, the independent generator hypothesis posits that there are two primary sources of beta activity: one in the primary motor cortex (M1 beta), and one in the primary somatosensory cortex (S1 beta). In this hypothesis, M1 and S1 beta bursts respond independently to the motor and somatosensory components of the task, respectively. M1 beta bursting exhibits a distinct suppression prior to and during movement, then a large rebound immediately following movement, before returning to baseline several seconds after movement termination. S1 beta bursting also exhibits a task-related beta suppression but does so in response to the tactile feedback associated with the button press task and is therefore delayed compared to the M1 suppression response. The combination of these two independent beta responses would explain the source patterns observed in Chapter 2 in the pre- and post-movement conditions. In particular, during pre-movement, S1 beta bursting would be greater than M1 beta bursting, and during post-movement M1 beta bursting would be greater than S1 beta bursting. This switching of dominance of M1 and S1 beta throughout the task would result in the appearance of a pre-movement S1 beta source, and a post-movement M1 beta source in the average source maps. In support of the independent generator mechanism is the finding that pre-movement and post-movement beta bursts had distinctly different relationships with age. On average, post-movement beta bursts localized to the primary motor cortex. However, compared to beta bursts in other conditions, post-movement bursts showed the most substantial age-related changes, including an expansion of source with age. Pre-movement beta bursts on the other hand, localize primarily to the primary somatosensory cortex and broader sensory areas, and these sources are relatively stable with age. This discrepancy could be indicative that M1 and S1 beta circuits are distinct and have different responses to the neurophysiological effects of ageing. For example, M1 neurons may be more vulnerable to the effects of ageing than S1 neurons resulting in the recruitment of more compensatory brain regions with age.

The alternative travelling wave hypothesis depicted in Figure 5.1B posits that all sensorimotor beta activity is generated by a unified mechanism whose source propagates in space over time. In this hypothesis, I propose that beta bursts emerge in M1 with the offset of a voluntary movement (T1 in Figure 5.1B) and subsequently move in the

posterior direction as beta activity returns to baseline, ultimately settling in S1 in preparation for subsequent movement. During a voluntary movement, the beta bursting mechanism effectively "resets" and when the movement is terminated, bursts once again emerge in M1 and repeat the same pattern of propagation. This mechanism would also explain our findings of an S1 source during pre-movement and an M1 source during post-movement. Further, the travelling wave mechanism would provide a potential explanation for the observation that the localization pattern and ageing trends noted in resting state were somewhere in between what was seen for pre-movement and post-movement type bursts. This pattern would make sense in the context of the proposed mechanism as the source of resting state bursts would likely be between the M1 and S1 extremes (see T2 in Figure 5.1B), but likely closer to S1, in line with the activation patterns observed in Chapter 2.

In the context of existing hypotheses of the functional role of beta oscillations (e.g., Pfurtscheller et al., 1996; Engel & Fries, 2010), both the independent generator and travelling wave mechanisms are plausible. The independent generator mechanism is more in line with the "idling" hypothesis of beta function which suggests that beta synchronicity (or high beta burst rate) is characteristic of an idling or resting state, while desynchronization of beta reflects a switch to an active state (Pfurtscheller et al., 1996). In line with this, in the independent generator model, beta in M1 and S1 is simply suppressed when the corresponding functional region becomes active (and rebounds in M1 following the movement). On the other hand, the travelling wave mechanism is more in line with the hypothesis of an active inhibitory role of beta (Engel & Fries, 2010). In this model, post-movement beta bursting could reflect a strong inhibitory signal that is involved in the termination of movement and thus is strongest in M1 where movement signals are generated. As the time since movement termination progresses, motor inhibition becomes less important, and beta bursting returns to its default source in the somatosensory regions. In the context of this explanation, the expansion of source with age in the post-movement interval could suggest that the termination of movement becomes more difficult with age requiring the coordinated effort of a wider cortical area, while the lack of such expansion in pre-movement could be due to the more passive inhibitory role at that time. Future work investigating the correlations between the spatial

extent of activation and behavioural measures such as reaction time or perceived effort for movement termination would provide insight into the validity of this proposed explanation.

While we cannot make conclusions about the definitive mechanism from our current findings, further analysis of the CamCAN data and follow-up animal studies may help to elucidate the roles of the independent generator and travelling wave mechanisms. One approach using the CamCAN data would be to detect beta bursts in source localized time courses in M1 and S1 hand regions and compare how burst dynamics change over time in each region. Rather than assessing burst characteristics in coarse pre-movement and post-movement time intervals, bursts could be characterised in a continuous manner throughout the inter-stimulus interval (ISI) to allow time-varying burst dynamics to be investigated. For example, peak burst time could be plotted against other burst characteristics (e.g., burst power, burst frequency, probability of burst, etc.) for S1 and M1 bursts separately. If the independent generator hypothesis holds, we would expect that M1 burst power or burst probability would decrease throughout the ISI, while S1 bursting would remain relatively constant. On the other hand, if the travelling wave hypothesis holds, we would expect S1 bursting to increase as M1 bursting decreased throughout the ISI. In addition, employing the burst localization methods described in Chapter 2 in finer time intervals in the ISI may allow us to assess subtle spatial shifts in burst location over time. This work would hopefully provide more insight into sensorimotor beta bursting mechanisms; however, the spatial resolution of MEG may be insufficient to explore such subtle differences in spatial patterns in relatively short time periods. If this is the case, additional LFP studies in animal models may be required to further investigate the sensorimotor network dynamics.

5.4 A Critical Shift in Brain Activity

Quadratic age-related trends with a vertex around 60 years were observed repeatedly in Chapter 2 and Chapter 3 findings. In Chapter 2 it was found that, prior to age 60, relative source power steadily increases across bilateral frontal and central brain regions. After this point, however, there is a change in the trajectory of the trend and relative source power begins to fall off in these regions. Similarly, quadratic trends in activation sum and burst rate were also observed in the post-movement interval for the

left pre-central beta cluster in Chapter 3. These quadratic trends were not hypothesised for post-movement sensorimotor beta bursts but were also not unfounded given the general theme of quadratic trends in our previous analyses of the CamCAN dataset (Brady et al., 2020; Brady et al., 2022). Specifically, previous analysis of beta bursts in the CamCAN dataset revealed quadratic trends with age in transient event characteristics including burst rate, peak power, and frequency span that tended to peak around 60 years of age. The consistency of the quadratic relationship in Chapters 2 and 3, along with the concordance to these previous event characteristic findings (Brady et al., 2020; Brady et al., 2022), suggest that 60 may be a critical age in this population.

There are several potential explanations for this apparent shift in the trajectory of brain activity at age 60. Firstly, this consistent pattern could be indicative of a functional shift in activity that occurs later in life and could signify a critical age in the normal ageing process at which significant changes to the sensorimotor network occur. This notion is supported by evidence of similar quadratic effects in neuroanatomical structure with age. In particular, white matter volume shows an inverted u-shaped trajectory across the lifespan with a peak around middle age (Taki et al., 2009; Hedman et al., 2012), suggesting that these types of trajectories are not unfounded in the brain. This pattern of white matter volume with age could potentially explain some of the quadratic changes in beta burst source found in Chapter 2. White matter is involved in forming long-range network connections between different brain areas. As such, it is sensible that increases in the spatial extent of beta burst source in early adulthood could be related to increases in white matter during this time, and the subsequent reduction in the extent of beta sources later in life could be due to white matter atrophy that begins in middle age.

Such a critical anatomical and functional shift could be triggered by either genetic or environmental factors. A potential environmental factor that could feasibly trigger such a critical shift is retirement, as the age of the vertex in the observed quadratic trends aligns with the average age of retirement in the United Kingdom, where the CamCAN data was collected. Working requires significant cognitive stimulation particularly in the domain of fluid intelligence. Upon retirement, there is a drastic reduction in this type of stimulation, which could feasibly trigger synaptic pruning and advanced white matter degradation, which in turn could be responsible for the changes in source pattern and

burst rate observed in this work. Future work could investigate this mechanism by comparing brain activity of individuals of the same age who are working and retired, or by comparing those who retired at different ages.

Alternatively, however, this apparent peak at 60 years could be related to confounds of the sample rather than a true functional shift. For example, there could be biases in the demographics of the sample. A study by Green and colleagues (2018) investigated patterns of participation in the CamCAN dataset and found that the likelihood to participate in the study peaked between 58 and 67 years of age (Green et al., 2018), which is similar to the peak age observed in our work. The CamCAN dataset maintains an approximately even distribution of participants per decile, however, the work by Green et al. indicates the presence of a sampling bias as the sample of willing participants was broader for the 58–67-year age group. In addition, due to the nature of the ageing process and the increasing prevalence of disease with age, the oldest adults in this dataset are sampled from a limited pool of the healthiest adults (i.e., those who have lived long lives without disease), while there is likely more variability in the health of the younger and middle-aged adults. This is supported by results from Chapter 3 which showed that younger adults tended to have more variability in their burst types than older adults. Particularly, the age distributions of the top beta clusters were skewed towards older adults, while the less common beta-type clusters tended to have distributions skewed to younger adults (see Figure B.7). While it is not clear that these sampling biases directly affect our results, more work should be conducted to investigate the origin of the 60-year peak.

The findings of Chapter 4 also have implications for our understanding of the potential shift in cortical network activity during ageing. Importantly, the Chapter 4 findings revealed that approximately 20% of the purportedly healthy participants in the CamCAN dataset had PSWEs, suggesting that there may be a meaningful difference in the neurophysiology of this subset of participants leading to the emergence of abnormal brain activity. These unexpected findings suggest that some of the CamCAN participants may have been misclassified as “healthy”. Previous research has demonstrated that task performance in healthy older adults tends to be associated with widespread networks, while older adults with cognitive impairment tend to have a focal activation pattern that is

more similar to younger adults (Cabeza et al., 2002; McIntosh et al., 2014). It has been suggested that a failure to shift to a more globalized pattern results in cognitive impairment. In the context of the CamCAN dataset, where we likely have a mix of "healthy" and "unhealthy" older adults, it is possible that the observed quadratic effects in Chapter 2 are driven by the "unhealthy" older adults who have spatial patterns similar to the younger adults. Given this hypothesis, an interesting avenue for future research would be to investigate whether the existence of PSWEs affects participants' brain activity in other contexts. For example, we could compare the spatial and temporal pattern of beta bursting between those with PSWEs and a group of age-matched adults without PSWEs. Alternatively, we could remove the subset of participants with PSWEs from the data and assess whether the age-related beta trends are preserved when these presumed "unhealthy" participants are removed.

5.5 The Role of Alpha Bursts

This thesis explores transient signals in the low frequency range (PSWEs; 1-6 Hz) as well as higher frequency transient beta signals (15-30 Hz). Signals in the intermediate alpha frequency range (8-12Hz), however, were not a focus of this work. Despite this, the nature of the methods employed and the relationships between alpha and the other frequency bands investigated in this work allowed for some unexpected insights into the mechanisms of alpha signals. As discussed in Chapter 3, alpha-type transients were some of the most abundant task-related atoms identified by CDL. Among the top 7 task-related clusters, 3 clusters resembled spatial variations of occipital alpha, 1 resembled temporal alpha (i.e., tau), and 1 resembled central mu (which has a central frequency in the alpha range but a more complex frequency distribution than other alpha atoms). This suggests not only that alpha events are abundant, but also that there is a high degree of variability in the spatial pattern of alpha events, resulting in the emergence of several distinct alpha clusters that are common across participants. The sensorimotor task used in this work involved the presentation of a visual and/or auditory cue that prompted the participant to perform a unimanual button press. As such, multiple functional regions (i.e., visual, auditory, and sensorimotor) were involved in the task, and showed reductions in alpha power during task performance. Interestingly, CDL allowed the associated functionally distinct alpha events to be easily separated based on their unique spatial distributions. In

previous literature, auditory alpha (i.e., tau) signals have been obscured due to their proximity to other sources of alpha in the occipital and sensorimotor regions (Wisniewski et al., 2024). The results of Chapter 3, however, provide support for the notion that there are, at minimum, 3 functionally distinct generators of alpha in the occipital, sensorimotor, and temporal regions. Furthermore, CDL extracted 3 common subtypes of occipital alpha events (as well as several other less common subtypes; see Figure B.7) for which the spatial representation varied slightly between clusters. This suggests that the generator of occipital alpha is not constant and that there is variability in the source of occipital alpha within and between participants. While these findings are not necessarily surprising, the ability to identify these features using a data-driven approach is a novel contribution of this thesis.

Chapter 3 also provided novel insight into age-related changes in alpha-type transients. Interestingly, occipital and temporal alpha-type clusters tended to show consistent increasing trends in activation with age independent of the phase of movement. The overall increase in occipital alpha activity with age, while not hypothesised, is in line with previous findings that show that ageing is associated with a reduced frequency of brain activity and that older participants tend to have dominant alpha peaks in their spectrograms (Chiang et al., 2011). Further investigation into the underlying properties of the activation showed that for all occipital and temporal alpha clusters, the increasing trends observed in activation sum with age could be explained by similar trends in burst rate with age (see Figure 3.10, Table 3.1). Burst power, however, did not play a significant role (see Figure B.4, Table 3.1). This finding suggests that increasing occipital and temporal alpha activity with age is related to an increase in the number of activations of the underlying neural networks (i.e., the firing rate of the neuronal population), rather than the magnitude of the individual activations (i.e., the size of the activated neuronal population). These findings provide novel mechanistic insight into age-related changes in the generative mechanisms of alpha.

In addition to trends in activation sum and burst rate, several other significant age-related trends were revealed, particularly for temporal alpha atoms. For example, the age distribution of participants who had temporal alpha atoms was significantly different from the overall population such that older adults were more likely to have temporal

alpha atoms. Further, the temporal alpha cluster was the only top cluster for which a positional shift was observed, with a significant posterior shift in ECD position observed with increasing age. These findings suggest that temporal alpha may play an important role in the healthy ageing process - a feature that has likely been overlooked in previous literature due to its limited study.

Another area of this thesis from which insights into alpha activity can be inferred, is the study of PSWEs in Chapter 4. As described in the introduction (Section 1.4.2), alpha and theta (4-8 Hz) oscillations are thought to be generated by a common thalamic mechanism whereby strong depolarization in thalamocortical cells causes strong activation of glutamate receptors leading to alpha waves, while weaker depolarization and reduced glutamate receptor activation in the same thalamocortical cells leads to theta waves (Hughes & Crunelli, 2005). As such, the emergence of PSWEs, which typically have a peak frequency in the canonical theta frequency range (e.g., 4-6 Hz), could be the result of a modification to this mechanism resulting in the generation of theta waves in place of the typical alpha waves. In support of this, previous investigations of PSWEs in patients with AD have demonstrated that these patients exhibit an increase in spectral power in the PSWE frequency range along with a reduction in spectral power in the alpha frequency range (Milikovsky et al., 2019). In the current work, individuals with PSWEs had a significant increase in delta and theta band power, and a slight (non-significant) decrease in alpha band power. This suggests that some, but likely not all, of the PSWE activity may be associated with a reduction in alpha activity. Interestingly, the supplementary analysis conducted in Chapter 3 (e.g., Figure B.7) provides interesting insight into this potential shared mechanism as well. In panel C of Figure B.7, it can be observed that several of the occipital and temporal atom clusters identified in this work had contributing atoms with peak frequencies below 6 Hz, suggesting that some participants may have lower frequency variations of the average temporal and occipital "alpha" atoms. Some of the temporal atoms (e.g., the fourth atom cluster shown in Figure B.7C) have particularly low frequencies suggesting that there may be some overlap between the atoms identified in Chapter 3 and the PSWEs described in Chapter 4, which were detected at the highest rates at temporal sensors. Future work could investigate the feasibility of this shared alpha/theta mechanism for generating PSWEs by using

computational models of the thalamocortical circuit to simulate PSWEs characteristics as described in Section 5.2.2. In addition, alpha bursts could be detected in the resting state data and the relationship between alpha burst characteristics and PSWEs could be examined to identify correlations between event types.

5.6 Clinical Applications

While this thesis is primarily focused on changes in brain activity in healthy ageing, some of the findings have important clinical implications. Most notably, the PSWEs described in Chapter 4 have potential as a biomarker for the detection of atypical brain activity associated with reduced cognitive abilities in older adults. PSWEs were previously considered to be a pathological signal related to cognitive impairment and anatomical abnormalities in patient populations (Milikovsky et al., 2019). Therefore, their presence in 20% of this purportedly healthy population is striking and raises the question of whether their presence could be indicative of an underlying undiagnosed pathology. If PSWEs are inherently pathological, their presence in this dataset is evidence that they may be a more sensitive marker of neuropathology than other metrics used to screen these participants. The identification of such a sensitive biomarker that is easily detectable through fast, non-invasive measurements is particularly desirable for rapid assessment of cognitive dysfunction. However, it is not clear from the current work whether PSWEs are in fact a marker of pathology, or if they are a normal variant of brain activity associated with healthy ageing; and further work is required to elucidate the clinical relevance of our findings.

The delineation of age-related changes in average low frequency band power for the “more PSWEs” group (presented in Figure 4.8) provides evidence for a pathological origin of PSWEs. In the less and no PSWEs groups, low frequency power decreases with age in line with findings from healthy populations (Emek-Savaş et al., 2016; Leirer et al., 2011; Meghdadi et al., 2021; Vlahou et al., 2015), however in the more PSWEs group, low frequency power increases with age in line with findings from populations with dementia and AD (Brenner et al., 1986; Hier et al., 1991; Jeong, 2004; Musaeus et al., 2018). In addition, in many of the analyses performed in Chapter 4, (see Figs 4.6,4.7,4.8) the “more PSWEs” group differed significantly from the other groups, while the “no PSWEs” and “less PSWEs” groups had similar findings. Given this, perhaps the

existence of PSWEs is normal, but high prevalence of PSWEs is indicative of pathology. Alternatively, it could be that those with less PSWEs are just at an earlier stage of pathology that will later progress to a "more PSWEs" phenotype. One way to investigate these potential hypotheses and to gauge the clinical relevance of PSWEs is to conduct a longitudinal study examining changes in PSWE prevalence over time. This would allow us to determine whether participants in the less PSWEs group progress to the more PSWEs group over an extended period (e.g., 5-10 years), and importantly, would provide insight into whether PSWEs are predictive of clinical progression.

Assessing the relationship between the spatial localization of PSWEs and areas of clinically relevant anatomical features is another potential direction for future research that would increase our understanding of the clinical relevance of PSWEs. Focal increases in blood-brain barrier disruption (Milikovsky et al., 2019) and cortical thinning (Fjell & Walhovd, 2010) have been shown to be associated with AD. Therefore, the co-localization of PSWE sources and areas of BBBd or cortical thinning could provide evidence that PSWEs are markers of region-specific degradation, as suggested by previous work in patient populations (Milikovsky et al., 2019). The spatial findings in Chapter 4 show PSWE activity predominantly in the temporal regions (Figure 4.10), with potential sources in the temporal pole (Figure C.4). This is in line with findings that patients with AD have substantially more cortical thinning in the anterior temporal regions than healthy older adults (Fjell & Walhovd, 2010). This concordance provides preliminary evidence that PSWEs may be related to functionally relevant brain areas in AD, but further work is required to determine whether participants with PSWEs are displaying neuroanatomical signs of AD.

In addition to the apparent clinical implications of the PSWE findings, the advances in our understanding of beta burst mechanisms afforded by Chapters 2 and 3 may have clinical implications as well. Sensorimotor beta bursts have been implicated in motor disorders such as Parkinson's disease. It has been demonstrated in previous work that patients with PD have a reduced beta suppression response (Heinrichs-Graham et al., 2014) that can be explained by a decreased resting beta burst rate (Vinding et al., 2020). Interestingly, this mechanism is similar (although opposite) to what is observed in our current and previous (Bardouille & Bailey, 2019; Brady et al., 2020) work with the

CamCAN dataset whereby increases in pre-movement burst rate with age seem to be responsible for increased beta suppression magnitude with age. This suggests that there may be similar, potentially opposing, mechanisms at play in healthy ageing as in symptomatic PD. In addition, work by Heinrichs-Graham and colleagues (2014) observed a reduction in the post-movement beta rebound amplitude in patients with PD, particularly in the supplementary motor area. This is interesting in the context of the findings of Chapter 2 which suggest increased post-movement beta activity in this area in healthy older adults. Once again, the mechanisms in PD and healthy ageing seem to oppose one another. Together, the insights into beta burst mechanisms provided by this thesis may have implications in our understanding of PD. In particular, the opposing trends in PD and healthy ageing could be evidence in support of the hypothesis that a failure to shift to widespread beta generators with age results in vulnerability to neuropathology.

5.7 Limitations and Future Directions

Finally, there are a few methodological limitations and confounds of the current thesis that should be addressed. In this section, limitations and discrepancies in the various source localization and transient event detection methods are discussed, along with the inherent limitations of the CamCAN dataset, and suggestions for future improvements and supplementary analyses are provided.

The discrepancy in source localization methods used in Chapters 2 and 3 is a potential limitation of our interpretations across chapters. In Chapter 2, MNE and beamformer methods were used to identify the sources of transient beta bursts, while in Chapter 3, an ECD model was used to identify the primary source of beta atom generation. This discrepancy in methods makes it difficult to directly compare spatial findings between chapters. Distributed source models such as MNE and beamformer are generally considered to be more robust and more widely applicable than ECD models and therefore were a sensible choice for use in Chapter 2. The ECD method, however, was selected in Chapter 3 because it provided a simple measure of focality (e.g., goodness of fit) that we used in our analysis pipeline to differentiate focal brain activity from artefacts. There is no similar measure for beamformer or MNE. Therefore, to use one of these methods in Chapter 3, we would have had to invent a way to filter out non-focal

sources. A further challenge to implementing a distributed source model in Chapter 3 is that they identify the source of all brain activity that occurs at a particular time within a given frequency band. In Chapter 3, our aim was to disentangle distinct sources of multiple types of bursts of the same frequency band that may overlap in time. Thus, MNE and beamforming approaches were limited for this application. In the future, it would be worthwhile to explore alternative approaches to circumventing the issue of overlapping timing between burst types with the same frequency but distinct spatial patterns, to allow CDL-detected bursts to be modelled with an MNE or beamformer approach. For example, the burst timing of different subtypes of atoms could be compared and co-occurring atoms could be excluded or otherwise accounted for to ensure that only one subtype of atoms was being localized at a time. Further development is required to determine the feasibility of such an approach.

Another methodological inconsistency between chapters is that, despite the emphasis of the importance of data-driven detection methods in Chapter 3, a simple thresholding approach was used to detect PSWEs in Chapter 4. This decision was made because the signal of interest was relatively novel, and the events had never been characterized in a healthy population. The method of PSWE detection was developed by Milikovsky et al. (2019) to discriminate between healthy controls and patients with AD. The low median power frequency threshold of 6 Hz was defined based on ROC (receiver operating characteristic) analysis to determine the parameters that best separated patients with AD from healthy age-matched controls. In this thesis, we wanted to replicate previously established methods using this definition of pathological PSWEs before introducing a novel approach that would complicate the interpretation of our results. Given the success of the initial characterisation, however, developing a more robust data-driven method for detection of abnormal slow-wave events would be an advantageous next step.

One other potential methodological limitation of this work is that the inter-stimulus interval (ISI) for the sensorimotor task data may not have been sufficient to allow movement-related signals to return to baseline prior to the onset of the subsequent trial. The CamCAN sensorimotor task was designed with varying ISIs ranging from 2 to 26 seconds (Taylor et al., 2017). In the current work, trials with an ISI less than 3 seconds

were excluded to allow for a sufficient baseline. However, recent findings by Pakenham et al. (2020) suggest that post-movement beta rebound responses may take up to 10 seconds to return to baseline following movement offset. This recent work used a force grip task with movement durations of 2, 5, and 10 seconds - much longer than the movement durations for our simple button-pressing task. Therefore, it is unclear whether this long duration beta rebound is present in the current data. The work by Pakenham et al. (2020) also demonstrated that beta rebound characteristics were modulated by task duration. Therefore, the rebound is likely different for the short ballistic movement performed in our work compared to the longer force grip movement. If the post-movement rebound interval does extend into the following movement, however, this would have significant implications for our interpretation of the burst dynamics in the pre-movement interval. Thus, future work should examine the duration of the post-movement beta rebound response in the long (e.g., >10 seconds) inter-stimulus intervals of the CamCAN sensorimotor task to elucidate the dynamics of the entire response.

Finally, this work is limited by the confounds of the CamCAN dataset. All the data analysed in this work was exclusively collected as part of the CamCAN initiative, and therefore consisted of a limited population of participants from a limited geographic region. While the CamCAN dataset has ideal demographics for studying cross-sectional ageing trends, it is unclear how generalizable the results are to a wider population. Therefore, future work attempting to replicate the findings of this thesis in other datasets would be welcome. In addition, because the data used in this work is cross-sectional, we can only infer age-related trends but cannot confirm that the effects are present across the lifespan of an individual. Cross-sectional studies in general are inherently limited because there are environmental and lifestyle factors that vary between age groups that may be unrelated to ageing. For example, medicine, nutrition, and hygiene practices have all changed significantly in the past 60-70 years, and differences in any of these variables could confound the age-related effects observed in this work. For this reason, longitudinal studies to validate the effects observed in this work would also be a useful future direction. Finally, a potential limitation of the dataset, as suggested by the finding of PSWEs in a subset of these participants, is that pathological brains (i.e., participants) may not have been adequately excluded from the dataset. This would confound our

interpretations about what constitutes “healthy” ageing. The results of this thesis should be interpreted with these confounds in mind and care should be taken not to generalize the findings beyond their relevant scope.

5.8 Conclusion

The results of this thesis have important implications for the advancement of neuroimaging analysis methods as well as our understanding of the human brain. This work validates a set of novel analysis tools to detect and localize transient patterns of human brain activity that can be used by the broader neuroimaging community. These methods have been made publicly available through open-access publications and open-source software platforms, allowing them to be widely used by other researchers in the field. Therefore, the methods presented in this thesis have the potential to aid neuroimaging analysis and expand our breadth of understanding of the human brain. Further, the results of the thesis provide direct insights into the neural mechanisms underlying human brain function and how these mechanisms change throughout normal ageing. In particular, insights into the spatial and temporal characteristics of transient bursts provide evidence of the cortical and network mechanisms at play in ageing. Source localization results provide evidence for generative sources of beta bursts in the pre- and post-central gyri, and data-driven burst analysis suggests that the rate of population bursting underlies age-related changes in alpha and beta power. Future work can explore the specifics of these mechanisms in greater detail using computational modelling, and eventually invasive studies to validate hypotheses. Finally, the findings from both the beta and slow wave event studies have potential clinical implications. The advanced understanding of beta burst mechanisms has implications in our understanding of motor disorders such as Parkinson’s disease for which beta bursts are implicated. The PSWE findings have potential implications in diagnostics and our understanding of the divergence of healthy and unhealthy neural mechanisms with ageing. This thesis has answered several important questions about the nature of human brain activity, but it has also inspired many new and exciting questions and areas for further exploration in the field. Going forward, I am excited to continue to explore this research area myself and witness how our understanding of the ageing brain continues to develop.

References

Abeles, M. (2014). Revealing instances of coordination among multiple cortical areas. *Biological Cybernetics*, *108*(5), 665–675. https://doi.org/10.1007/s00422-013-0574-2

Adler, G., Bramesfeld, A., & Jajcevic, A. (1999). Mild Cognitive Impairment in Old-Age Depression Is Associated with Increased EEG Slow-Wave Power. *Neuropsychobiology*, *40*(4), 218–222. https://doi.org/10.1159/000026623

Allain, C., Gramfort, A., Moreau, T., & Preprint, A. (2021). DriPP: Driven Point Processes to Model Stimuli Induced Patterns in M/EEG Signals. *arXiv:2112.06652 [Cs, Eess, Math, Stat]*. http://arxiv.org/abs/2112.06652

Baillet, S. (2017). Magnetoencephalography for brain electrophysiology and imaging. *Nature Neuroscience*, *20*(3), 327–339. https://doi.org/10.1038/nn.4504

Baker, A. P., Brookes, M. J., Rezek, I. A., Smith, S. M., Behrens, T., Probert Smith, P. J., & Woolrich, M. (2014). Fast transient networks in spontaneous human brain activity. *eLife*, *3*, e01867. https://doi.org/10.7554/eLife.01867

Bansal, N., Blum, A., & Chawla, S. (2004). Correlation Clustering. *Machine Learning*, *56*(1–3), 89–113. https://doi.org/10.1023/B:MACH.0000033116.57574.95

Barbey, A. K., Colom, R., Paul, E. J., & Grafman, J. (2014). Architecture of fluid intelligence and working memory revealed by lesion mapping. *Brain Structure and Function*, *219*(2), 485–494. https://doi.org/10.1007/s00429-013-0512-z

Bardouille, T., & Bailey, L. (2019). Evidence for age-related changes in sensorimotor neuromagnetic responses during cued button pressing in a large open-access dataset. *NeuroImage*, *193*, 25–34. https://doi.org/10.1016/j.neuroimage.2019.02.065

Barth, D. S., Sutherling, W., Engel, J., & Beatty, J. (1982). Neuromagnetic Localization of Epileptiform Spike Activity in the Human Brain. *Science*, *218*(4575), 891–894. https://doi.org/10.1126/science.6813968

Becker, R., Vidaurre, D., Quinn, A. J., Abeysuriya, R. G., Parker Jones, O., Jbabdi, S., & Woolrich, M. W. (2020). Transient spectral events in resting state MEG predict individual task responses. *NeuroImage*, *215*, 116818. https://doi.org/10.1016/j.neuroimage.2020.116818

Bellot-Saez, A., Kékesi, O., Morley, J. W., & Buskila, Y. (2017). Astrocytic modulation of neuronal excitability through K + spatial buffering. *Neuroscience & Biobehavioral Reviews*, *77*, 87–97. https://doi.org/10.1016/j.neubiorev.2017.03.002

Benwell, C. S. Y., Davila-Pérez, P., Fried, P. J., Jones, R. N., Travison, T. G., Santarnecchi, E., Pascual-Leone, A., & Shafi, M. M. (2020). EEG spectral power abnormalities and their relationship with cognitive dysfunction in patients with Alzheimer's disease and type 2 diabetes. *Neurobiology of Aging*, *85*, 83–95. https://doi.org/10.1016/j.neurobiolaging.2019.10.004

Berger, H. (1929). *Über das elektroenkephalogramm des menschen*. *87*(527–70).

Bhattacharya, A., & De, R. K. (2008). Divisive Correlation Clustering Algorithm (DCCA) for grouping of genes: Detecting varying patterns in expression profiles. *Bioinformatics*, *24*(11), 1359–1366. https://doi.org/10.1093/bioinformatics/btn133

Bhattacharya, A., & De, R. K. (2010). Average correlation clustering algorithm (ACCA) for grouping of co-regulated genes with similar pattern of variation in their expression values. *Journal of Biomedical Informatics*, *43*(4), 560–568. https://doi.org/10.1016/j.jbi.2010.02.001

Blenkinsop, A., Anderson, S., & Gurney, K. (2017). Frequency and function in the basal ganglia: The origins of beta and gamma band activity: Frequency and function in the basal ganglia. *The Journal of Physiology*, *595*(13), 4525–4548. https://doi.org/10.1113/JP273760

Bonaiuto, J. J., Little, S., Neymotin, S. A., Jones, S. R., Barnes, G. R., & Bestmann, S. (2021). Laminar dynamics of high amplitude beta bursts in human motor cortex. *NeuroImage*, *242*, 118479. https://doi.org/10.1016/j.neuroimage.2021.118479

Boto, E., Meyer, S. S., Shah, V., Alem, O., Knappe, S., Kruger, P., Fromhold, T. M., Lim, M., Glover, P. M., Morris, P. G., Bowtell, R., Barnes, G. R., & Brookes, M. J. (2017). A new generation of magnetoencephalography: Room temperature measurements using optically-pumped magnetometers. *NeuroImage*, *149*, 404–414. https://doi.org/10.1016/j.neuroimage.2017.01.034

Bowyer, S. M., Moran, J. E., Weiland, B. J., Mason, K. M., Greenwald, M. L., Smith, B. J., Barkley, G. L., & Tepley, N. (2005). Language laterality determined by MEG mapping with MR-FOCUSS. *Epilepsy & Behavior*, *6*(2), 235–241. https://doi.org/10.1016/j.yebeh.2004.12.002

Brady, B., & Bardouille, T. (2022). Periodic/Aperiodic parameterization of transient oscillations (PAPTO)–Implications for healthy ageing. *NeuroImage*, *251*, 118974. https://doi.org/10.1016/j.neuroimage.2022.118974

Brady, B., Power, L., & Bardouille, T. (2020). Age-related trends in neuromagnetic transient beta burst characteristics during a sensorimotor task and rest in the Cam-CAN open-access dataset. *NeuroImage*, *222*, 117245. https://doi.org/10.1016/j.neuroimage.2020.117245

Bragin, A., Jando, G., Nadasdy, Z., Hetke, J., Wise, K., & Buzsáki, G. (1995). *Gamma (40-100 Hz) Oscillation in the Hippocampus of the Behaving Rat*. *15*(1), 47–60.

Brenner, R. P., Ulrich, R. F., Spiker, D. G., Sclabassi, R. J., Reynolds, C. F., Marin, R. S., & Boller, F. (1986). Computerized EEG spectral analysis in elderly normal, demented and depressed subjects. *Electroencephalography and Clinical Neurophysiology*, *64*(6), 483–492. https://doi.org/10.1016/0013-4694(86)90184-7

Briley, P. M., Liddle, E. B., Simmonite, M., Jansen, M., White, T. P., Balain, V., Palaniyappan, L., Bowtell, R., Mullinger, K. J., & Liddle, P. F. (2021). Regional Brain Correlates of Beta Bursts in Health and Psychosis: A Concurrent Electroencephalography and Functional Magnetic Resonance Imaging Study. *Biological Psychiatry: Cognitive Neuroscience and Neuroimaging*, *6*(12), 1145–1156. https://doi.org/10.1016/j.bpsc.2020.10.018

Britton, J., Frey, L., & Hopp, J. (2016). The normal EEG. In E. St Louis & L. Frey (Eds.), *Electroencephalography (EEG): An Introductory Text and Atlas of Normal and Abnormal Findings in Adults, Children, and Infants*. American Epilepsy Society.

Brockmeier, A. J., & Principe, J. C. (2016). Learning Recurrent Waveforms Within EEGs. *IEEE Transactions on Biomedical Engineering*, *63*(1), 43–54. https://doi.org/10.1109/TBME.2015.2499241

Brovelli, A., Battaglini, P. P., Naranjo, J. R., & Budai, R. (2002). Medium-Range Oscillatory Network and the 20-Hz Sensorimotor Induced Potential. *NeuroImage*, *16*(1), 130–141. https://doi.org/10.1006/nimg.2002.1058

Brovelli, A., Ding, M., Ledberg, A., Chen, Y., Nakamura, R., & Bressler, S. L. (2004). Beta oscillations in a large-scale sensorimotor cortical network: Directional influences revealed by Granger causality. *Proceedings of the National Academy of Sciences*, *101*(26), 9849–9854. https://doi.org/10.1073/pnas.0308538101

Buskila, Y., Bellot-Saez, A., & Morley, J. W. (2019). Generating Brain Waves, the Power of Astrocytes. *Frontiers in Neuroscience*, *13*, 1125. https://doi.org/10.3389/fnins.2019.01125

Buzsáki, G., & Wang, X.-J. (2012). Mechanisms of Gamma Oscillations. *Annual Review of Neuroscience*, *35*(1), 203–225. https://doi.org/10.1146/annurev-neuro-062111-150444

Cabeza, R., Anderson, N. D., Locantore, J. K., & McIntosh, A. R. (2002). Aging Gracefully: Compensatory Brain Activity in High-Performing Older Adults. *NeuroImage*, *17*(3), 1394–1402. https://doi.org/10.1006/nimg.2002.1280

Caplan, J. B., Bottomley, M., Kang, P., & Dixon, R. A. (2015). Distinguishing rhythmic from non-rhythmic brain activity during rest in healthy neurocognitive aging. *NeuroImage*, *112*, 341–352. https://doi.org/10.1016/j.neuroimage.2015.03.001

Caplan, J. B., Madsen, J. R., Raghavachari, S., & Kahana, M. J. (2001). Distinct Patterns of Brain Oscillations Underlie Two Basic Parameters of Human Maze Learning. *Journal of Neurophysiology*, *86*(1), 368–380. https://doi.org/10.1152/jn.2001.86.1.368

Cesnaite, E., Steinfath, P., Jamshidi Idaji, M., Stephani, T., Kumral, D., Haufe, S., Sander, C., Hensch, T., Hegerl, U., Riedel-Heller, S., Röhr, S., Schroeter, M. L., Witte, A., Villringer, A., & Nikulin, V. V. (2023). Alterations in rhythmic and non-rhythmic resting-state EEG activity and their link to cognition in older age. *NeuroImage*, *268*, 119810. https://doi.org/10.1016/j.neuroimage.2022.119810

Cheyne, D. O. (2013). MEG studies of sensorimotor rhythms: A review. *Experimental Neurology*, *245*, 27–39. https://doi.org/10.1016/j.expneurol.2012.08.030

Chiang, A. K. I., Rennie, C. J., Robinson, P. A., Van Albada, S. J., & Kerr, C. C. (2011). Age trends and sex differences of alpha rhythms including split alpha peaks. *Clinical Neurophysiology*, *122*(8), 1505–1517. https://doi.org/10.1016/j.clinph.2011.01.040

Cleeland, C., Pipingas, A., Scholey, A., & White, D. (2019). Neurochemical changes in the aging brain: A systematic review. *Neuroscience & Biobehavioral Reviews*, *98*, 306–319. https://doi.org/10.1016/j.neubiorev.2019.01.003

Cohen, D. (1968). Magnetoencephalography: Evidence of Magnetic Fields Produced by Alpha-Rhythm Currents. *Science*, *161*(3843), 784–786. https://doi.org/10.1126/science.161.3843.784

Cohen, D. (1972). Magnetoencephalography: Detection of the Brain's Electrical Activity with a Superconducting Magnetometer. *Science*, *175*(4022), 664–666. https://doi.org/10.1126/science.175.4022.664

Cole, S., & Voytek, B. (2019). Cycle-by-cycle analysis of neural oscillations. *Journal of Neurophysiology*, *122*(2), 849–861. https://doi.org/10.1152/jn.00273.2019

Connor, J. R., Menzies, S. L., Martin, S. M. St., & Mufson, E. J. (1990). Cellular distribution of transferrin, ferritin, and iron in normal and aged human brains. *Journal of Neuroscience Research*, *27*(4), 595–611. https://doi.org/10.1002/jnr.490270421

Coquelet, N., De Tiège, X., Roshchupkina, L., Peigneux, P., Goldman, S., Woolrich, M., & Wens, V. (2022). Microstates and power envelope hidden Markov modeling probe bursting brain activity at different timescales. *NeuroImage*, *247*, 118850. https://doi.org/10.1016/j.neuroimage.2021.118850

Dale, A. M., Fischl, B., & Sereno, M. I. (1999). Cortical Surface-Based Analysis: I. Segmentation and Surface Reconstruction. *NeuroImage*, *9*(2), 179–194. https://doi.org/10.1006/nimg. 1998.0395

Dale, A. M., Liu, A. K., Fischl, B. R., Buckner, R. L., Belliveau, J. W., Lewine, J. D., & Halgren, E. (2000). Dynamic Statistical Parametric Mapping. *Neuron*, *26*(1), 55–67. https://doi.org/10.1016/S0896-6273(00)81138-1

Deary, I. J., Corley, J., Gow, A. J., Harris, S. E., Houlihan, L. M., Marioni, R. E., Penke, L., Rafnsson, S. B., & Starr, J. M. (2009). Age-associated cognitive decline. *British Medical Bulletin*, *92*(1), 135–152. https://doi.org/10.1093/bmb/ldp033

Deary, I. J., Johnson, W., & Houlihan, L. M. (2009). Genetic foundations of human intelligence. *Human Genetics*, *126*(1), 215–232. https://doi.org/10.1007/s00439-009-0655-4

Deary, I. J., Wright, A. F., Harris, S. E., Whalley, L. J., & Starr, J. M. (2004). Searching for genetic influences on normal cognitive ageing. *Trends in Cognitive Sciences*, *8*(4), 178–184. https://doi.org/10.1016/j.tics.2004.02.008

Delorme, A., Sejnowski, T., & Makeig, S. (2007). Enhanced detection of artifacts in EEG data using higher-order statistics and independent component analysis. *NeuroImage*, *34*(4), 1443–1449. https://doi.org/10.1016/j.neuroimage.2006.11.004

Desikan, R. S., Ségonne, F., Fischl, B., Quinn, B. T., Dickerson, B. C., Blacker, D., Buckner, R. L., Dale, A. M., Maguire, R. P., Hyman, B. T., Albert, M. S., & Killiany, R. J. (2006). An automated labeling system for subdividing the human cerebral

cortex on MRI scans into gyral based regions of interest. *NeuroImage*, *31*(3), 968–980. https://doi.org/10.1016/j.neuroimage.2006.01.021

Destrieux, C., Fischl, B., Dale, A., & Halgren, E. (2010). Automatic parcellation of human cortical gyri and sulci using standard anatomical nomenclature. *NeuroImage*, *53*(1), 1–15. https://doi.org/10.1016/j.neuroimage.2010.06.010

Dupré la Tour, T., Moreau, T., Jas, M., & Gramfort, A. (2018). *Multivariate Convolutional Sparse Coding for Electromagnetic Brain Signals*. NeurIPS, Montréal, Canada.

Emek-Savaş, D. D., Güntekin, B., Yener, G. G., & Başar, E. (2016). Decrease of delta oscillatory responses is associated with increased age in healthy elderly. *International Journal of Psychophysiology*, *103*, 103–109. https://doi.org/10.1016/j.ijpsycho.2015.02.006

Engel, A. K., & Fries, P. (2010). Beta-band oscillations—Signalling the status quo? *Current Opinion in Neurobiology*, *20*(2), 156–165. https://doi.org/10.1016/j.conb.2010.02.015

Errington, S. P., Woodman, G. F., & Schall, J. D. (2020). Dissociation of Medial Frontal β-Bursts and Executive Control. *The Journal of Neuroscience*, *40*(48), 9272–9282. https://doi.org/10.1523/JNEUROSCI.2072-20.2020

Esiri, M. (2007). Ageing and the brain. *The Journal of Pathology*, *211*(2), 181–187. https://doi.org/10.1002/path.2089

Fabus, M. S., Quinn, A. J., Warnaby, C. E., & Woolrich, M. W. (2021). Automatic decomposition of electrophysiological data into distinct nonsinusoidal oscillatory modes. *Journal of Neurophysiology*, *126*(5), 1670–1684. https://doi.org/10.1152/jn.00315.2021

Feingold, J., Gibson, D. J., DePasquale, B., & Graybiel, A. M. (2015). Bursts of beta oscillation differentiate postperformance activity in the striatum and motor cortex of monkeys performing movement tasks. *Proceedings of the National Academy of Sciences*, *112*(44), 13687–13692. https://doi.org/10.1073/pnas.1517629112

Fischl, B., Liu, A., & Dale, A. M. (2001). Automated manifold surgery: Constructing geometrically accurate and topologically correct models of the human cerebral cortex. *IEEE Transactions on Medical Imaging*, *20*(1), 70–80. https://doi.org/10.1109/42.906426

Fischl, B., Salat, D. H., Busa, E., Albert, M., Dieterich, M., Haselgrove, C., Van Der Kouwe, A., Killiany, R., Kennedy, D., Klaveness, S., Montillo, A., Makris, N., Rosen, B., & Dale, A. M. (2002). Whole Brain Segmentation. *Neuron*, *33*(3), 341–355. https://doi.org/10.1016/S0896-6273(02)00569-X

Fischl, B., Sereno, M. I., & Dale, A. M. (1999). Cortical Surface-Based Analysis. *NeuroImage*, *9*(2), 195–207. https://doi.org/10.1006/nimg.1998.0396

Fischl, B., Sereno, M. I., Tootell, R. B. H., & Dale, A. M. (1999). High-resolution intersubject averaging and a coordinate system for the cortical surface. *Human Brain*

Mapping, *8*(4), 272–284. https://doi.org/10.1002/(SICI)1097-0193(1999)8:4<272::AID-HBM10>3.0.CO;2-4

Fischl, B., van der Kouwe, A., Destrieux, C., Halgren, E., Ségonne, F., Salat, D. H., Busa, E., Seidman, L. J., Goldstein, J., Kennedy, D., Caviness, V., Makris, N., Rosen, B., & Dale, A. M. (2004). Automatically Parcellating the Human Cerebral Cortex. *Cerebral Cortex*, *14*(1), 11–22. https://doi.org/10.1093/cercor/bhg087

Fjell, A. M., & Walhovd, K. B. (2010). Structural Brain Changes in Aging: Courses, Causes and Cognitive Consequences. *Reviews in the Neurosciences*, *21*(3). https://doi.org/10.1515/REVNEURO.2010.21.3.187

Fjell, A. M., Walhovd, K. B., Reinvang, I., Lundervold, A., Salat, D., Quinn, B. T., Fischl, B., & Dale, A. M. (2006). Selective increase of cortical thickness in high-performing elderly—Structural indices of optimal cognitive aging. *NeuroImage*, *29*(3), 984–994. https://doi.org/10.1016/j.neuroimage.2005.08.007

Foxe, J. J., & Snyder, A. C. (2011). The Role of Alpha-Band Brain Oscillations as a Sensory Suppression Mechanism during Selective Attention. *Frontiers in Psychology*, *2*. https://doi.org/10.3389/fpsyg.2011.00154

Fratiglioni, L., Paillard-Borg, S., & Winblad, B. (2004). An active and socially integrated lifestyle in late life might protect against dementia. *The Lancet Neurology*, *3*(6), 343–353. https://doi.org/10.1016/S1474-4422(04)00767-7

Gaetz, W., Edgar, J. C., Wang, D. J., & Roberts, T. P. L. (2011a). Relating MEG measured motor cortical oscillations to resting γ-Aminobutyric acid (GABA) concentration. *NeuroImage*, *55*(2), 616–621. https://doi.org/10.1016/j.neuroimage.2010.12.077

Gaetz, W., Edgar, J. C., Wang, D. J., & Roberts, T. P. L. (2011b). Relating MEG measured motor cortical oscillations to resting γ-Aminobutyric acid (GABA) concentration. *NeuroImage*, *55*(2), 616–621. https://doi.org/10.1016/j.neuroimage.2010.12.077

Ganguli, M., Bilt, J. V., Saxton, J. A., Shen, C., & Dodge, H. H. (2005). Alcohol consumption and cognitive function in late life: A longitudinal community study. *Neurology*, *65*(8), 1210–1217. https://doi.org/10.1212/01.wnl.0000180520.35181.24

Giedd, J. N., Blumenthal, J., Jeffries, N. O., Castellanos, F. X., Liu, H., Zijdenbos, A., Paus, T., Evans, A. C., & Rapoport, J. L. (1999). Brain development during childhood and adolescence: A longitudinal MRI study. *Nature Neuroscience*, *2*(10), 861–863. https://doi.org/10.1038/13158

Gips, B., Bahramisharif, A., Lowet, E., Roberts, M. J., de Weerd, P., Jensen, O., & van der Eerden, J. (2017). Discovering recurring patterns in electrophysiological recordings. *Journal of Neuroscience Methods*, *275*, 66–79. https://doi.org/10.1016/j.jneumeth.2016.11.001

Gómez, C., M Pérez-Macías, J., Poza, J., Fernández, A., & Hornero, R. (2013). Spectral changes in spontaneous MEG activity across the lifespan. *Journal of Neural Engineering*, *10*(6), 066006. https://doi.org/10.1088/1741-2560/10/6/066006

Gramfort, A. (2013). MEG and EEG data analysis with MNE-Python. *Frontiers in Neuroscience*, *7*. https://doi.org/10.3389/fnins.2013.00267

Gramfort, A., Luessi, M., Larson, E., Engemann, D. A., Strohmeier, D., Brodbeck, C., Parkkonen, L., & Hämäläinen, M. S. (2014). MNE software for processing MEG and EEG data. *NeuroImage*, *86*, 446–460. https://doi.org/10.1016/j.neuroimage.2013.10.027

Gray, C. M. (1994). *Synchronous oscillations in neuronal systems: Mechanisms and functions*. *1*, 11–38.

Gray, C. M., König, P., Engel, A. K., & Singer, W. (1989). Oscillatory responses in cat visual cortex exhibit inter-columnar synchronization which reflects global stimulus properties. *Nature*, *338*(6213), 334–337. https://doi.org/10.1038/338334a0

Green, E., Bennett, H., Brayne, C., & Matthews, F. E. (2018). Exploring patterns of response across the lifespan: The Cambridge Centre for Ageing and Neuroscience (Cam-CAN) study. *BMC Public Health*, *18*(1), 760. https://doi.org/10.1186/s12889-018-5663-7

Gross, J., Kujala, J., Hämäläinen, M., Timmermann, L., Schnitzler, A., & Salmelin, R. (2001). Dynamic imaging of coherent sources: Studying neural interactions in the human brain. *Proceedings of the National Academy of Sciences*, *98*(2), 694–699. https://doi.org/10.1073/pnas.98.2.694

Grosse, R., Raina, R., Kwong, H., & Ng, A. Y. (2007). *Shift-invariance sparse coding for audio classification*. 23rd Conference on Uncertainty in Artificial Intelligence.

Halder, T., Talwar, S., Jaiswal, A. K., & Banerjee, A. (2019). Quantitative Evaluation in Estimating Sources Underlying Brain Oscillations Using Current Source Density Methods and Beamformer Approaches. *Eneuro*, *6*(4), ENEURO.0170-19.2019. https://doi.org/10.1523/ENEURO.0170-19.2019

Hall, E. L., Robson, S. E., Morris, P. G., & Brookes, M. J. (2014). The relationship between MEG and fMRI. *NeuroImage*, *102*, 80–91. https://doi.org/10.1016/j.neuroimage.2013.11.005

Hämäläinen, M., Hari, R., Ilmoniemi, R. J., Knuutila, J., & Lounasmaa, O. V. (1993). Magnetoencephalography—Theory, instrumentation, and applications to noninvasive studies of the working human brain. *Reviews of Modern Physics*, *65*(2), 413–497. https://doi.org/10.1103/RevModPhys.65.413

Hämäläinen, M. S., & Ilmoniemi, R. J. (1994). Interpreting magnetic fields of the brain: Minimum norm estimates. *Medical & Biological Engineering & Computing*, *32*(1), 35–42. https://doi.org/10.1007/BF02512476

Hämäläinen, M. S., & Sarvas, J. (1989). Realistic conductivity geometry model of the human head for interpretation of neuromagnetic data. *IEEE Transactions on Biomedical Engineering*, *36*(2), 165–171. https://doi.org/10.1109/10.16463

Hansen, P. C., Kringelbach, M. L., & Salmelin, R. (Eds.). (2010). *MEG: An introduction to methods*. Oxford University Press.

Hari, R., & Salmelin, R. (1997). Human cortical oscillations: A neuromagnetic view through the skull. *Trends in Neurosciences*, *20*(1), 44–49. https://doi.org/10.1016/S0166-2236(96)10065-5

Hasselmo, M. E. (2005). What is the function of hippocampal theta rhythm?—Linking behavioral data to phasic properties of field potential and unit recording data. *Hippocampus*, *15*(7), 936–949. https://doi.org/10.1002/hipo.20116

Hauk, O., Wakeman, D. G., & Henson, R. (2011). Comparison of noise-normalized minimum norm estimates for MEG analysis using multiple resolution metrics. *NeuroImage*, *54*(3), 1966–1974. https://doi.org/10.1016/j.neuroimage.2010.09.053

He, S., Everest-Phillips, C., Clouter, A., Brown, P., & Tan, H. (2020). Neurofeedback-Linked Suppression of Cortical β Bursts Speeds Up Movement Initiation in Healthy Motor Control: A Double-Blind Sham-Controlled Study. *The Journal of Neuroscience*, *40*(20), 4021–4032. https://doi.org/10.1523/JNEUROSCI.0208-20.2020

Hebert, R., & Lehmann, D. (1977). Theta bursts: An EEG pattern in normal subjects practising the transcendental meditation technique. *Electroencephalography and Clinical Neurophysiology*, *42*(3), 397–405. https://doi.org/10.1016/0013-4694(77)90176-6

Hedden, T., & Gabrieli, J. D. E. (2004). Insights into the ageing mind: A view from cognitive neuroscience. *Nature Reviews Neuroscience*, *5*(2), 87–96. https://doi.org/10.1038/nrn1323

Hedman, A. M., Van Haren, N. E. M., Schnack, H. G., Kahn, R. S., & Hulshoff Pol, H. E. (2012). Human brain changes across the life span: A review of 56 longitudinal magnetic resonance imaging studies. *Human Brain Mapping*, *33*(8), 1987–2002. https://doi.org/10.1002/hbm.21334

Heinrichs-Graham, E., Kurz, M. J., Becker, K. M., Santamaria, P. M., Gendelman, H. E., & Wilson, T. W. (2014). Hypersynchrony despite pathologically reduced beta oscillations in patients with Parkinson's disease: A pharmaco-magnetoencephalography study. *Journal of Neurophysiology*, *112*(7), 1739–1747. https://doi.org/10.1152/jn.00383.2014

Hier, D. B., Mangone, C. A., Ganellen, R., Warach, J. D., Van Egeren, R., Perlik, S. J., & Gorelick, P. B. (1991). Quantitative Measurement of Delta Activity in Alzheimer's Disease. *Clinical Electroencephalography*, *22*(3), 178–182. https://doi.org/10.1177/155005949102200309

Himberg, J., Hyvärinen, A., & Esposito, F. (2004). Validating the independent components of neuroimaging time series via clustering and visualization. *NeuroImage*, *22*(3), 1214–1222. https://doi.org/10.1016/j.neuroimage.2004.03.027

Hindriks, R., Van Putten, M. J. A. M., & Deco, G. (2014). Intra-cortical propagation of EEG alpha oscillations. *NeuroImage*, *103*, 444–453. https://doi.org/10.1016/j.neuroimage.2014.08.027

Hitziger, S., Clerc, M., Saillet, S., Benar, C., & Papadopoulo, T. (2017). Adaptive Waveform Learning: A Framework for Modeling Variability in Neurophysiological Signals. *IEEE Transactions on Signal Processing*, *65*(16), 4324–4338. https://doi.org/10.1109/TSP.2017.2698415

Hochstenbach, J., Mulder, T., van Limbeek, J., Donders, R., & Schoonderwaldt, H. (1998). Cognitive Decline Following Stroke: A Comprehensive Study of Cognitive Decline Following Stroke*. *Journal of Clinical and Experimental Neuropsychology*, *20*(4), 503–517. https://doi.org/10.1076/jcen.20.4.503.1471

Huang, N. E., Shen, Z., Long, S. R., Wu, M. C., Shih, H. H., Zheng, Q., Yen, N.-C., Tung, C. C., & Liu, H. H. (1998). The empirical mode decomposition and the Hilbert spectrum for nonlinear and non-stationary time series analysis. *Proceedings of the Royal Society of London. Series A: Mathematical, Physical and Engineering Sciences*, *454*(1971), 903–995. https://doi.org/10.1098/rspa.1998.0193

Hughes, S. W., & Crunelli, V. (2005). Thalamic Mechanisms of EEG Alpha Rhythms and Their Pathological Implications. *The Neuroscientist*, *11*(4), 357–372. https://doi.org/10.1177/1073858405277450

Hutchinson, S. (2002). Age-Related Differences in Movement Representation. *NeuroImage*, *17*(4), 1720–1728. https://doi.org/10.1006/nimg.2002.1309

Hyvärinen, A., & Oja, E. (2000). Independent component analysis: Algorithms and applications. *Neural Networks*, *13*(4–5), 411–430. https://doi.org/10.1016/S0893-6080(00)00026-5

Jafarian, A., Zeidman, P., Wykes, Rob. C., Walker, M., & Friston, K. J. (2021). Adiabatic dynamic causal modelling. *NeuroImage*, *238*, 118243. https://doi.org/10.1016/j.neuroimage.2021.118243

Jas, M., La Tour, T. D., Şimşekli, U., & Gramfort, A. (2017). Learning the Morphology of Brain Signals Using Alpha-Stable Convolutional Sparse Coding. *arXiv:1705.08006 [q-Bio, Stat]*. http://arxiv.org/abs/1705.08006

Jenkinson, N., & Brown, P. (2011). New insights into the relationship between dopamine, beta oscillations and motor function. *Trends in Neurosciences*, *34*(12), 611–618. https://doi.org/10.1016/j.tins.2011.09.003

Jensen, O., & Mazaheri, A. (2010). Shaping Functional Architecture by Oscillatory Alpha Activity: Gating by Inhibition. *Frontiers in Human Neuroscience*, *4*. https://doi.org/10.3389/fnhum.2010.00186

Jeong, J. (2004). EEG dynamics in patients with Alzheimer's disease. *Clinical Neurophysiology*, *115*(7), 1490–1505. https://doi.org/10.1016/j.clinph.2004.01.001

Jones, S. R. (2016). When brain rhythms aren't 'rhythmic': Implication for their mechanisms and meaning. *Current Opinion in Neurobiology*, *40*, 72–80. https://doi.org/10.1016/j.conb.2016.06.010

Jost, P., Vandergheynst, P., Lesage, S., & Gribonval, R. (2006). MoTIF: An Efficient Algorithm for Learning Translation Invariant Dictionaries. *2006 IEEE International Conference on Acoustics Speed and Signal Processing Proceedings*, *5*, V-857-V–860. https://doi.org/10.1109/ICASSP.2006.1661411

Judd, C. M., & Kenny, D. A. (1981). Process Analysis: Estimating Mediation in Treatment Evaluations. *Evaluation Review*, *5*(5), 602–619. https://doi.org/10.1177/0193841X8100500502

Jurkiewicz, M. T., Gaetz, W. C., Bostan, A. C., & Cheyne, D. (2006). Post-movement beta rebound is generated in motor cortex: Evidence from neuromagnetic recordings. *NeuroImage*, *32*(3), 1281–1289. https://doi.org/10.1016/j.neuroimage.2006.06.005

Kachiwala, S. J., Harris, S. E., Wright, A. F., Hayward, C., Starr, J. M., Whalley, L. J., & Deary, I. J. (2005). Genetic influences on oxidative stress and their association with normal cognitive ageing. *Neuroscience Letters*, *386*(2), 116–120. https://doi.org/10.1016/j.neulet.2005.05.067

Kadala, A., Verdier, D., Morquette, P., & Kolta, A. (2015). Ion Homeostasis in Rhythmogenesis: The Interplay Between Neurons and Astroglia. *Physiology*, *30*(5), 371–388. https://doi.org/10.1152/physiol.00023.2014

Karvat, G., Schneider, A., Alyahyay, M., Steenbergen, F., Tangermann, M., & Diester, I. (2020). Real-time detection of neural oscillation bursts allows behaviourally relevant neurofeedback. *Communications Biology*, *3*(1), 72. https://doi.org/10.1038/s42003-020-0801-z

Klimesch, W., Sauseng, P., & Hanslmayr, S. (2007). EEG alpha oscillations: The inhibition–timing hypothesis. *Brain Research Reviews*, *53*(1), 63–88. https://doi.org/10.1016/j.brainresrev.2006.06.003

Knappe, S., Sander, T., & Trahms, L. (2014). Optically-Pumped Magnetometers for MEG. In S. Supek & C. J. Aine (Eds.), *Magnetoencephalography* (pp. 993–999). Springer Berlin Heidelberg. https://doi.org/10.1007/978-3-642-33045-2_49

Kosciessa, J. Q., Grandy, T. H., Garrett, D. D., & Werkle-Bergner, M. (2020). Single-trial characterization of neural rhythms: Potential and challenges. *NeuroImage*, *206*, 116331. https://doi.org/10.1016/j.neuroimage.2019.116331

Kramer, M. A., Roopun, A. K., Carracedo, L. M., Traub, R. D., Whittington, M. A., & Kopell, N. J. (2008). Rhythm Generation through Period Concatenation in Rat Somatosensory Cortex. *PLoS Computational Biology*, *4*(9), e1000169. https://doi.org/10.1371/journal.pcbi.1000169

Kühn, A. A., Williams, D., Kupsch, A., Limousin, P., Hariz, M., Schneider, G., Yarrow, K., & Brown, P. (2004). Event-related beta desynchronization in human subthalamic nucleus correlates with motor performance. *Brain*, *127*(4), 735–746. https://doi.org/10.1093/brain/awh106

Lakatos, P., Szilágyi, N., Pincze, Z., Rajkai, C., Ulbert, I., & Karmos, G. (2004). Attention and arousal related modulation of spontaneous gamma-activity in the auditory cortex of the cat. *Cognitive Brain Research*, *19*(1), 1–9. https://doi.org/10.1016/j.cogbrainres.2003.10.023

Leirer, V. M., Wienbruch, C., Kolassa, S., Schlee, W., Elbert, T., & Kolassa, I.-T. (2011). Changes in cortical slow wave activity in healthy aging. *Brain Imaging and Behavior*, *5*(3), 222–228. https://doi.org/10.1007/s11682-011-9126-3

Levy, R., Ashby, P., Hutchison, W. D., Lang, A. E., Lozano, A. M., & Dostrovsky, J. O. (2002). Dependence of subthalamic nucleus oscillations on movement and dopamine in Parkinson's disease. *Brain*, *125*(6), 1196–1209. https://doi.org/10.1093/brain/awf128

Lipski, W. J., Wozny, T. A., Alhourani, A., Kondylis, E. D., Turner, R. S., Crammond, D. J., & Richardson, R. M. (2017). Dynamics of human subthalamic neuron phase-locking to motor and sensory cortical oscillations during movement. *Journal of Neurophysiology*, *118*(3), 1472–1487. https://doi.org/10.1152/jn.00964.2016

Little, B., Bonaiuto, J., Barnes, G., & Bestmann, S. (2019). Human motor cortical beta bursts relate to movement planning and response errors. *PLOS Biology*, *17*(10), e3000479. https://doi.org/10.1371/journal.pbio.3000479

Logothetis, N. K. (2008). What we can do and what we cannot do with fMRI. *Nature*, *453*(7197), 869–878. https://doi.org/10.1038/nature06976

Loomis, A. L., Harvey, E. N., & Hobart, G. (1935). Potential Rhythms of the Cerebral Cortex During Sleep. *Science*, *81*(2111), 597–598. https://doi.org/10.1126/science.81.2111.597

Lopes Da Silva, F. (1991). Neural mechanisms underlying brain waves: From neural membranes to networks. *Electroencephalography and Clinical Neurophysiology*, *79*(2), 81–93. https://doi.org/10.1016/0013-4694(91)90044-5

Lozano-Soldevilla, D. (2018). On the Physiological Modulation and Potential Mechanisms Underlying Parieto-Occipital Alpha Oscillations. *Frontiers in Computational Neuroscience*, *12*, 23. https://doi.org/10.3389/fncom.2018.00023

Lundqvist, M., Rose, J., Herman, P., Brincat, S. L., Buschman, T. J., & Miller, E. K. (2016). Gamma and Beta Bursts Underlie Working Memory. *Neuron*, *90*(1), 152–164. https://doi.org/10.1016/j.neuron.2016.02.028

Marsden, J. F., Limousin-Dowsey, P., Ashby, P., Pollak, P., & Brown, P. (2001). Subthalamic nucleus, sensorimotor cortex and muscle interrelationships in Parkinson's disease. *Brain*, *124*(2), 378–388. https://doi.org/10.1093/brain/124.2.378

Mattay, V. S., Fera, F., Tessitore, A., Hariri, A. R., Das, S., Callicott, J. H., & Weinberger, D. R. (2002). Neurophysiological correlates of age-related changes in human motor function. *Neurology*, *58*(4), 630–635. https://doi.org/10.1212/WNL.58.4.630

McCarthy, M. M., Moore-Kochlacs, C., Gu, X., Boyden, E. S., Han, X., & Kopell, N. (2011). Striatal origin of the pathologic beta oscillations in Parkinson's disease. *Proceedings of the National Academy of Sciences*, *108*(28), 11620–11625. https://doi.org/10.1073/pnas.1107748108

McCormick, D. A., McGinley, M. J., & Salkoff, D. B. (2015). Brain state dependent activity in the cortex and thalamus. *Current Opinion in Neurobiology*, *31*, 133–140. https://doi.org/10.1016/j.conb.2014.10.003

McIntosh, A. R., Vakorin, V., Kovacevic, N., Wang, H., Diaconescu, A., & Protzner, A. B. (2014). Spatiotemporal Dependency of Age-Related Changes in Brain Signal Variability. *Cerebral Cortex*, *24*(7), 1806–1817. https://doi.org/10.1093/cercor/bht030

Meghdadi, A. H., Stevanović Karić, M., McConnell, M., Rupp, G., Richard, C., Hamilton, J., Salat, D., & Berka, C. (2021). Resting state EEG biomarkers of cognitive decline associated with Alzheimer's disease and mild cognitive

impairment. *PLOS ONE*, *16*(2), e0244180. https://doi.org/10.1371/journal.pone.0244180

Michel, C. M., & Koenig, T. (2018). EEG microstates as a tool for studying the temporal dynamics of whole-brain neuronal networks: A review. *NeuroImage*, *180*, 577–593. https://doi.org/10.1016/j.neuroimage.2017.11.062

Milikovsky, D. Z., Ofer, J., Senatorov, V. V., Friedman, A. R., Prager, O., Sheintuch, L., Elazari, N., Veksler, R., Zelig, D., Weissberg, I., Bar-Klein, G., Swissa, E., Hanael, E., Ben-Arie, G., Schefenbauer, O., Kamintsky, L., Saar-Ashkenazy, R., Shelef, I., Shamir, M. H., … Friedman, A. (2019). Paroxysmal slow cortical activity in Alzheimer's disease and epilepsy is associated with blood-brain barrier dysfunction. *Science Translational Medicine*, *11*(521), eaaw8954. https://doi.org/10.1126/scitranslmed.aaw8954

Milikovsky, D. Z., Weissberg, I., Kamintsky, L., Lippmann, K., Schefenbauer, O., Frigerio, F., Rizzi, M., Sheintuch, L., Zelig, D., Ofer, J., Vezzani, A., & Friedman, A. (2017). Electrocorticographic Dynamics as a Novel Biomarker in Five Models of Epileptogenesis. *The Journal of Neuroscience*, *37*(17), 4450–4461. https://doi.org/10.1523/JNEUROSCI.2446-16.2017

Miljković, M., Chernenko, T., Romeo, M. J., Bird, B., Matthäus, C., & Diem, M. (2010). Label-free imaging of human cells: Algorithms for image reconstruction of Raman hyperspectral datasets. *The Analyst*, *135*(8), 2002. https://doi.org/10.1039/c0an00042f

Mirzaei, A., Kumar, A., Leventhal, D., Mallet, N., Aertsen, A., Berke, J., & Schmidt, R. (2017). Sensorimotor Processing in the Basal Ganglia Leads to Transient Beta Oscillations during Behavior. *The Journal of Neuroscience*, *37*(46), 11220–11232. https://doi.org/10.1523/JNEUROSCI.1289-17.2017

Montagne, A., Barnes, S. R., Sweeney, M. D., Halliday, M. R., Sagare, A. P., Zhao, Z., Toga, A. W., Jacobs, R. E., Liu, C. Y., Amezcua, L., Harrington, M. G., Chui, H. C., Law, M., & Zlokovic, B. V. (2015). Blood-Brain Barrier Breakdown in the Aging Human Hippocampus. *Neuron*, *85*(2), 296–302. https://doi.org/10.1016/j.neuron.2014.12.032

Moreau, T., & Gramfort, A. (2022). DiCoDiLe: Distributed Convolutional Dictionary Learning. *IEEE Transactions on Pattern Analysis and Machine Intelligence*, *44*(5), 2426–2437. https://doi.org/10.1109/TPAMI.2020.3039215

Morrison, J. H., & Hof, P. R. (1997). Life and Death of Neurons in the Aging Brain. *Science*, *278*(5337), 412–419. https://doi.org/10.1126/science.278.5337.412

Muller, L., Chavane, F., Reynolds, J., & Sejnowski, T. J. (2018). Cortical travelling waves: Mechanisms and computational principles. *Nature Reviews Neuroscience*, *19*(5), 255–268. https://doi.org/10.1038/nrn.2018.20

Murman, D. (2015). The Impact of Age on Cognition. *Seminars in Hearing*, *36*(03), 111–121. https://doi.org/10.1055/s-0035-1555115

Murthy, V. N., & Fetz, E. E. (1996). Synchronization of neurons during local field potential oscillations in sensorimotor cortex of awake monkeys. *Journal of Neurophysiology*, *76*(6), 3968–3982. https://doi.org/10.1152/jn.1996.76.6.3968

Musaeus, C. S., Engedal, K., Høgh, P., Jelic, V., Mørup, M., Naik, M., Oeksengaard, A.-R., Snaedal, J., Wahlund, L.-O., Waldemar, G., & Andersen, B. B. (2018). EEG Theta Power Is an Early Marker of Cognitive Decline in Dementia due to Alzheimer's Disease. *Journal of Alzheimer's Disease*, *64*(4), 1359–1371. https://doi.org/10.3233/JAD-180300

Muthukumaraswamy, S. D., Myers, J. F. M., Wilson, S. J., Nutt, D. J., Lingford-Hughes, A., Singh, K. D., & Hamandi, K. (2013). The effects of elevated endogenous GABA levels on movement-related network oscillations. *NeuroImage*, *66*, 36–41. https://doi.org/10.1016/j.neuroimage.2012.10.054

Neuper, C., Wörtz, M., & Pfurtscheller, G. (2006). ERD/ERS patterns reflecting sensorimotor activation and deactivation. In *Progress in Brain Research* (Vol. 159, pp. 211–222). Elsevier. https://doi.org/10.1016/S0079-6123(06)59014-4

Newman, A. (2019). *Research Methods for Cognitive Neuroscience*.

Neymotin, S. A., Daniels, D. S., Caldwell, B., McDougal, R. A., Carnevale, N. T., Jas, M., Moore, C. I., Hines, M. L., Hämäläinen, M., & Jones, S. R. (2020). Human Neocortical Neurosolver (HNN), a new software tool for interpreting the cellular and network origin of human MEG/EEG data. *eLife*, *9*, e51214. https://doi.org/10.7554/eLife.51214

Nooyens, A. C. J., van Gelder, B. M., & Verschuren, W. M. M. (2008). Smoking and Cognitive Decline Among Middle-Aged Men and Women: The Doetinchem Cohort Study. *American Journal of Public Health*, *98*(12), 2244–2250. https://doi.org/10.2105/AJPH.2007.130294

Oja, E. & Zhijian Yuan. (2006). The FastICA Algorithm Revisited: Convergence Analysis. *IEEE Transactions on Neural Networks*, *17*(6), 1370–1381. https://doi.org/10.1109/TNN.2006.880980

Ossadtchi, A., Shamaeva, T., Okorokova, E., Moiseeva, V., & Lebedev, M. A. (2017). Neurofeedback learning modifies the incidence rate of alpha spindles, but not their duration and amplitude. *Scientific Reports*, *7*(1), 3772. https://doi.org/10.1038/s41598-017-04012-0

Özbek, Y., Fide, E., & Yener, G. G. (2021). Resting-state EEG alpha/theta power ratio discriminates early-onset Alzheimer's disease from healthy controls. *Clinical Neurophysiology*, *132*(9), 2019–2031. https://doi.org/10.1016/j.clinph.2021.05.012

Pakenham, D. O., Quinn, A. J., Fry, A., Francis, S. T., Woolrich, M. W., Brookes, M. J., & Mullinger, K. J. (2020). Post-stimulus beta responses are modulated by task duration. *NeuroImage*, *206*, 116288. https://doi.org/10.1016/j.neuroimage.2019.116288

Papanicolaou, A. C., Castillo, E. M., Billingsley-Marshall, R., Pataraia, E., & Simos, P. G. (2005). A Review of Clinical Applications of Magnetoencephalography. In *International Review of Neurobiology* (Vol. 68, pp. 223–247). Elsevier. https://doi.org/10.1016/S0074-7742(05)68009-9

Park, D. C., & Reuter-Lorenz, P. (2009). The Adaptive Brain: Aging and Neurocognitive Scaffolding. *Annual Review of Psychology*, *60*(1), 173–196. https://doi.org/10.1146/annurev.psych.59.103006.093656

Pascual-Marqui, R. D. (2002). Standardized low resolution brain electromagnetic tomography (sLORETA): Technical details. *Clinical Pharmacology*.

Penttilä, M., Partanen, J. V., Soininen, H., & Riekkinen, P. J. (1985). Quantitative analysis of occipital EEG in different stages of Alzheimer's disease. *Electroencephalography and Clinical Neurophysiology*, *60*(1), 1–6. https://doi.org/10.1016/0013-4694(85)90942-3

Penttonen, M., & Buzsáki, G. (2003). Natural logarithmic relationship between brain oscillators. *Thalamus and Related Systems*, *2*(02), 145. https://doi.org/10.1017/S1472928803000074

Pfurtscheller, G., & Lopes Da Silva, F. H. (1999). Event-related EEG/MEG synchronization and desynchronization: Basic principles. *Clinical Neurophysiology*, *110*(11), 1842–1857. https://doi.org/10.1016/S1388-2457(99)00141-8

Pfurtscheller, G., Neuper, C., Andrew, C., & Edlinger, G. (1997). Foot and hand area mu rhythms. *International Journal of Psychophysiology*, *26*(1–3), 121–135. https://doi.org/10.1016/S0167-8760(97)00760-5

Pfurtscheller, G., Stancák, A., & Neuper, C. (1996a). Post-movement beta synchronization. A correlate of an idling motor area? *Electroencephalography and Clinical Neurophysiology*, *98*(4), 281–293. https://doi.org/10.1016/0013-4694(95)00258-8

Pfurtscheller, G., Stancák, A., & Neuper, C. (1996b). Post-movement beta synchronization. A correlate of an idling motor area? *Electroencephalography and Clinical Neurophysiology*, *98*(4), 281–293. https://doi.org/10.1016/0013-4694(95)00258-8

Popescu, B. O., Toescu, E. C., Popescu, L. M., Bajenaru, O., Muresanu, D. F., Schultzberg, M., & Bogdanovic, N. (2009). Blood-brain barrier alterations in ageing and dementia. *Journal of the Neurological Sciences*, *283*(1–2), 99–106. https://doi.org/10.1016/j.jns.2009.02.321

Power, L., Allain, C., Moreau, T., Gramfort, A., & Bardouille, T. (2023). Using convolutional dictionary learning to detect task-related neuromagnetic transients and ageing trends in a large open-access dataset. *NeuroImage*, *267*, 119809. https://doi.org/10.1016/j.neuroimage.2022.119809

Power, L., & Bardouille, T. (2021). Age-related trends in the cortical sources of transient beta bursts during a sensorimotor task and rest. *NeuroImage*, *245*, 118670. https://doi.org/10.1016/j.neuroimage.2021.118670

Power, L., Friedman, A., & Bardouille, T. (2024). Atypical paroxysmal slow cortical activity in healthy adults: Relationship to age and cognitive performance. *Neurobiology of Aging*, *136*, 44–57. https://doi.org/10.1016/j.neurobiolaging.2024.01.009

Quinn, A. J., Lopes-dos-Santos, V., Huang, N., Liang, W.-K., Juan, C.-H., Yeh, J.-R., Nobre, A. C., Dupret, D., & Woolrich, M. W. (2021). Within-cycle instantaneous frequency profiles report oscillatory waveform dynamics. *Journal of Neurophysiology*, *126*(4), 1190–1208. https://doi.org/10.1152/jn.00201.2021

Quinn, A. J., Vidaurre, D., Abeysuriya, R., Becker, R., Nobre, A. C., & Woolrich, M. W. (2018). Task-Evoked Dynamic Network Analysis Through Hidden Markov Modeling. *Frontiers in Neuroscience*, *12*, 603. https://doi.org/10.3389/fnins.2018.00603

R Core Team. (2021). *R: A language and environment for statistical computing.* R Foundation for Statistical Computing. https://www.R-project.org/

Rafnsson, S. B., Deary, I. J., & Fowkes, F. (2009). Peripheral arterial disease and cognitive function. *Vascular Medicine*, *14*(1), 51–61. https://doi.org/10.1177/1358863X08095027

Rafnsson, S. B., Deary, I. J., Smith, F. B., Whiteman, M. C., & Fowkes, F. G. R. (2007). Cardiovascular Diseases and Decline in Cognitive Function in an Elderly Community Population: The Edinburgh Artery Study. *Psychosomatic Medicine*, *69*(5), 425–434. https://doi.org/10.1097/psy.0b013e318068fce4

Rayson, H., Debnath, R., Alavizadeh, S., Fox, N., Ferrari, P. F., & Bonaiuto, J. J. (2022). Detection and analysis of cortical beta bursts in developmental EEG data. *Developmental Cognitive Neuroscience*, *54*, 101069. https://doi.org/10.1016/j.dcn.2022.101069

Raz, N., & Rodrigue, K. M. (2006). Differential aging of the brain: Patterns, cognitive correlates and modifiers. *Neuroscience & Biobehavioral Reviews*, *30*(6), 730–748. https://doi.org/10.1016/j.neubiorev.2006.07.001

Robinson, P. A., Rennie, C. J., Wright, J. J., Bahramali, H., Gordon, E., & Rowe, D. L. (2001). Prediction of electroencephalographic spectra from neurophysiology. *Physical Review E*, *63*(2), 021903. https://doi.org/10.1103/PhysRevE.63.021903

Robinson, S. E., & Vrba, J. (1999). Functional neuroimaging by synthetic aperture tomography (SAM). *Recent Advances in Biomagnetism*, 302–305.

Roopun, A. K., Middleton, S. J., Cunningham, M. O., LeBeau, F. E. N., Bibbig, A., Whittington, M. A., & Traub, R. D. (2006). A beta2-frequency (20–30 Hz) oscillation in nonsynaptic networks of somatosensory cortex. *Proceedings of the National Academy of Sciences*, *103*(42), 15646–15650. https://doi.org/10.1073/pnas.0607443103

Rossini, P. M., Rossi, S., Babiloni, C., & Polich, J. (2007). Clinical neurophysiology of aging brain: From normal aging to neurodegeneration. *Progress in Neurobiology*, *83*(6), 375–400. https://doi.org/10.1016/j.pneurobio.2007.07.010

Rubino, D., Robbins, K. A., & Hatsopoulos, N. G. (2006). Propagating waves mediate information transfer in the motor cortex. *Nature Neuroscience*, *9*(12), 1549–1557. https://doi.org/10.1038/nn1802

Sarvas, J. (1987). Basic mathematical and electromagnetic concepts of the biomagnetic inverse problem. *Physics in Medicine and Biology*, *32*(1), 11–22. https://doi.org/10.1088/0031-9155/32/1/004

Seedat, Z. A., Quinn, A. J., Vidaurre, D., Liuzzi, L., Gascoyne, L. E., Hunt, B. A. E., O'Neill, G. C., Pakenham, D. O., Mullinger, K. J., Morris, P. G., Woolrich, M. W., & Brookes, M. J. (2020). The role of transient spectral 'bursts' in functional connectivity: A magnetoencephalography study. *NeuroImage*, *209*, 116537. https://doi.org/10.1016/j.neuroimage.2020.116537

Senatorov, V. V., Friedman, A. R., Milikovsky, D. Z., Ofer, J., Saar-Ashkenazy, R., Charbash, A., Jahan, N., Chin, G., MIhaly, E., Lin, J. M., Ramsay, H. J., Moghbel, A., Preininger, M. K., Eddings, C. R., Harrison, H. V., Patel, R., Shen, Y., Ghanim, H., Sheng, H., … Kaufer, D. (2019). Blood-brain barrier dysfunction in aging induces hyperactivation of TGF-beta signaling and chronic yet reversible neural dysfunction. *SCIENCE TRANSLATIONAL MEDICINE*, *11*, 15.

Shafto, M. A., Tyler, L. K., Dixon, M., Taylor, J. R., Rowe, J. B., Cusack, R., Calder, A. J., Marslen-Wilson, W. D., Duncan, J., Dalgleish, T., Henson, R. N., Brayne, C., Cam-CAN, & Matthews, F., E. (2014). The Cambridge Centre for Ageing and Neuroscience (Cam-CAN) study protocol: A cross-sectional, lifespan, multidisciplinary examination of healthy cognitive ageing. *BMC Neurology*, *14*(1), 204. https://doi.org/10.1186/s12883-014-0204-1

Sherman, M. A., Lee, S., Law, R., Haegens, S., Thorn, C. A., Hämäläinen, M. S., Moore, C. I., & Jones, S. R. (2016). Neural mechanisms of transient neocortical beta rhythms: Converging evidence from humans, computational modeling, monkeys, and mice. *Proceedings of the National Academy of Sciences*, *113*(33). https://doi.org/10.1073/pnas.1604135113

Shimamoto, S. A., Ryapolova-Webb, E. S., Ostrem, J. L., Galifianakis, N. B., Miller, K. J., & Starr, P. A. (2013). Subthalamic Nucleus Neurons Are Synchronized to Primary Motor Cortex Local Field Potentials in Parkinson's Disease. *The Journal of Neuroscience*, *33*(17), 7220–7233. https://doi.org/10.1523/JNEUROSCI.4676-12.2013

Shin, H., Law, R., Tsutsui, S., Moore, C. I., & Jones, S. R. (2017). The rate of transient beta frequency events predicts behavior across tasks and species. *eLife*, *6*, e29086. https://doi.org/10.7554/eLife.29086

Soininen, H., Reinikainen, K. J., Partanen, J., Helkala, E.-L., Paljärvi, L., & Riekkinen, P. J. (1992). Slowing of electroencephalogram and choline acetyltransferase activity in post mortem frontal cortex in definite Alzheimer's disease. *Neuroscience*, *49*(3), 529–535. https://doi.org/10.1016/0306-4522(92)90223-O

Sowell, E. R., Thompson, P. M., Holmes, C. J., Jernigan, T. L., & Toga, A. W. (1999). In vivo evidence for post-adolescent brain maturation in frontal and striatal regions. *Nature Neuroscience*, *2*(10), 859–861. https://doi.org/10.1038/13154

Sowell, E. R., Thompson, P. M., Tessner, K. D., & Toga, A. W. (2001). Mapping Continued Brain Growth and Gray Matter Density Reduction in Dorsal Frontal Cortex: Inverse Relationships during Postadolescent Brain Maturation. *The Journal*

of Neuroscience, *21*(22), 8819–8829. https://doi.org/10.1523/JNEUROSCI.21-22-08819.2001

Statistics Canada. (2021). *A portrait of Canada's growing population aged 85 and older from the 2021 Census*. *98*.

Statistics Canada. (2022). *In the midst of high job vacancies and historically low unemployment, Canada faces record retirements from an aging labour force: Number of seniors aged 65 and older grows six times faster than children 0-14*. *11*.

Steriade, M. (2004). Acetylcholine systems and rhythmic activities during the waking–sleep cycle. In *Progress in Brain Research* (Vol. 145, pp. 179–196). Elsevier. https://doi.org/10.1016/S0079-6123(03)45013-9

Steriade, M., & Timofeev, I. (2003). *Networks during Sleep and Waking Oscillations*. *37*(563–576).

Sweeney, M. D., Sagare, A. P., & Zlokovic, B. V. (2018). Blood–brain barrier breakdown in Alzheimer disease and other neurodegenerative disorders. *Nature Reviews Neurology*, *14*(3), 133–150. https://doi.org/10.1038/nrneurol.2017.188

Takahashi, K., Saleh, M., Penn, R. D., & Hatsopoulos, N. G. (2011). Propagating Waves in Human Motor Cortex. *Frontiers Human Neuroscience*, *5*. https://doi.org/10.3389/fnhum.2011.00040

Taki, Y., Kinomura, S., Sato, K., Goto, R., Kawashima, R., & Fukuda, H. (2011). A longitudinal study of gray matter volume decline with age and modifying factors. *Neurobiology of Aging*, *32*(5), 907–915. https://doi.org/10.1016/j.neurobiolaging.2009.05.003

Tal, I., & Abeles, M. (2016). Temporal accuracy of human cortico-cortical interactions. *Journal of Neurophysiology*, *115*(4), 1810–1820. https://doi.org/10.1152/jn.00956.2015

Tal, I., & Abeles, M. (2018). Imaging the Spatiotemporal Dynamics of Cognitive Processes at High Temporal Resolution. *Neural Computation*, *30*(3), 610–630. https://doi.org/10.1162/neco_a_01054

Tal, I., Neymotin, S., Bickel, S., Lakatos, P., & Schroeder, C. E. (2020). Oscillatory Bursting as a Mechanism for Temporal Coupling and Information Coding. *Frontiers in Computational Neuroscience*, *14*, 82. https://doi.org/10.3389/fncom.2020.00082

Taulu, S., & Simola, J. (2006). Spatiotemporal signal space separation method for rejecting nearby interference in MEG measurements. *Physics in Medicine and Biology*, *51*(7), 1759–1768. https://doi.org/10.1088/0031-9155/51/7/008

Taylor, J. R., Williams, N., Cusack, R., Auer, T., Shafto, M. A., Dixon, M., Tyler, L. K., Cam-CAN, & Henson, R. N. (2017). The Cambridge Centre for Ageing and Neuroscience (Cam-CAN) data repository: Structural and functional MRI, MEG, and cognitive data from a cross-sectional adult lifespan sample. *NeuroImage*, *144*, 262–269. https://doi.org/10.1016/j.neuroimage.2015.09.018

Tierney, T. M., Holmes, N., Mellor, S., López, J. D., Roberts, G., Hill, R. M., Boto, E., Leggett, J., Shah, V., Brookes, M. J., Bowtell, R., & Barnes, G. R. (2019). Optically

pumped magnetometers: From quantum origins to multi-channel magnetoencephalography. *NeuroImage*, *199*, 598–608. https://doi.org/10.1016/j.neuroimage.2019.05.063

Timofeev, I., Bazhenov, M., Seigneur, J., & Sejnowski, T. (2012). Neuronal Synchronization and Thalamocortical Rhythms in Sleep, Wake and Epilepsy. *Jasper's Basic Mechanisms of the Epilepsies*.

Toornvliet, R., Vanberckel, B., Luurtsema, G., Lubberink, M., Geldof, A., Bosch, T., Oerlemans, R., Lammertsma, A., & Franssen, E. (2006). Effect of age on functional P-glycoprotein in the blood-brain barrier measured by use of (R)-[11C]verapamil and positron emission tomography. *Clinical Pharmacology & Therapeutics*, *79*(6), 540–548. https://doi.org/10.1016/j.clpt.2006.02.004

Vallesi, A., McIntosh, A. R., Kovacevic, N., Chan, S. C. C., & Stuss, D. T. (2010). Age effects on the asymmetry of the motor system: Evidence from cortical oscillatory activity. *Biological Psychology*, *85*(2), 213–218. https://doi.org/10.1016/j.biopsycho.2010.07.003

van de Haar, H. J., Burgmans, S., Jansen, J. F. A., van Osch, M. J. P., van Buchem, M. A., Muller, M., Hofman, P. A. M., Verhey, F. R. J., & Backes, W. H. (2016). Blood-Brain Barrier Leakage in Patients with Early Alzheimer Disease. *Radiology*, *281*(2), 527–535. https://doi.org/10.1148/radiol.2016152244

van Ede, F., Quinn, A. J., Woolrich, M. W., & Nobre, A. C. (2018). Neural Oscillations: Sustained Rhythms or Transient Burst-Events? *Trends in Neurosciences*, *41*(7), 415–417. https://doi.org/10.1016/j.tins.2018.04.004

Van Veen, B. D., Van Drongelen, W., Yuchtman, M., & Suzuki, A. (1997). Localization of brain electrical activity via linearly constrained minimum variance spatial filtering. *IEEE Transactions on Biomedical Engineering*, *44*(9), 867–880. https://doi.org/10.1109/10.623056

Vidaurre, D., Quinn, A. J., Baker, A. P., Dupret, D., Tejero-Cantero, A., & Woolrich, M. W. (2016). Spectrally resolved fast transient brain states in electrophysiological data. *NeuroImage*, *126*, 81–95. https://doi.org/10.1016/j.neuroimage.2015.11.047

Vigário, R., Jousmäki, V., Hämäläinen, M., Hari, R., & Oja, E. (1998). *Independent Component Analysis for Identification of Artifacts in Magnetoencephalographic Recordings*. 7.

Vinding, M. C., Tsitsi, P., Waldthaler, J., Oostenveld, R., Ingvar, M., Svenningsson, P., & Lundqvist, D. (2020). Reduction of spontaneous cortical beta bursts in Parkinson's disease is linked to symptom severity. *Brain Communications*, *2*(1), fcaa052. https://doi.org/10.1093/braincomms/fcaa052

Vlahou, E. L., Thurm, F., Kolassa, I.-T., & Schlee, W. (2015). Resting-state slow wave power, healthy aging and cognitive performance. *Scientific Reports*, *4*(1), 5101. https://doi.org/10.1038/srep05101

Wang, X.-J. (2010). Neurophysiological and Computational Principles of Cortical Rhythms in Cognition. *Physiological Reviews*, *90*(3), 1195–1268. https://doi.org/10.1152/physrev.00035.2008

Weiner, H., & Schuster, D. B. (1956). The electroencephalogram in dementia. —Some preliminary observations and correlations. *Electroencephalography and Clinical Neurophysiology*, *8*(3), 479–488. https://doi.org/10.1016/0013-4694(56)90014-1

Wendling, F., Benquet, P., Bartolomei, F., & Jirsa, V. (2016). Computational models of epileptiform activity. *Journal of Neuroscience Methods*, *260*, 233–251. https://doi.org/10.1016/j.jneumeth.2015.03.027

Wessel, J. R. (2020). β-Bursts Reveal the Trial-to-Trial Dynamics of Movement Initiation and Cancellation. *The Journal of Neuroscience*, *40*(2), 411–423. https://doi.org/10.1523/JNEUROSCI.1887-19.2019

West, T. O., Berthouze, L., Halliday, D. M., Litvak, V., Sharott, A., Magill, P. J., & Farmer, S. F. (2018). Propagation of beta/gamma rhythms in the cortico-basal ganglia circuits of the parkinsonian rat. *Journal of Neurophysiology*, *119*(5), 1608–1628. https://doi.org/10.1152/jn.00629.2017

Whitten, T. A., Hughes, A. M., Dickson, C. T., & Caplan, J. B. (2011). A better oscillation detection method robustly extracts EEG rhythms across brain state changes: The human alpha rhythm as a test case. *NeuroImage*, *54*(2), 860–874. https://doi.org/10.1016/j.neuroimage.2010.08.064

Whittington, M. A., Traub, R. D., Kopell, N., Ermentrout, B., & Buhl, E. H. (2000). Inhibition-based rhythms: Experimental and mathematical observations on network dynamics. *International Journal of Psychophysiology*, *38*(3), 315–336. https://doi.org/10.1016/S0167-8760(00)00173-2

Wiesman, A. I., Murman, D. L., Losh, R. A., Schantell, M., Christopher-Hayes, N. J., Johnson, H. J., Willett, M. P., Wolfson, S. L., Losh, K. L., Johnson, C. M., May, P. E., & Wilson, T. W. (2022). Spatially resolved neural slowing predicts impairment and amyloid burden in Alzheimer's disease. *Brain*, *145*(6), 2177–2189. https://doi.org/10.1093/brain/awab430

Williamson, S. J., & Kaufman, L. (1981). Biomagnetism. *Journal of Magnetism and Magnetic Materials*, *22*(2), 129–201. https://doi.org/10.1016/0304-8853(81)90078-0

Wilson, T. W., Slason, E., Asherin, R., Kronberg, E., Reite, M. L., Teale, P. D., & Rojas, D. C. (2010). An extended motor network generates beta and gamma oscillatory perturbations during development. *Brain and Cognition*, *73*(2), 75–84. https://doi.org/10.1016/j.bandc.2010.03.001

Winkler, I., Debener, S., Muller, K.-R., & Tangermann, M. (2015). On the influence of high-pass filtering on ICA-based artifact reduction in EEG-ERP. *2015 37th Annual International Conference of the IEEE Engineering in Medicine and Biology Society (EMBC)*, 4101–4105. https://doi.org/10.1109/EMBC.2015.7319296

Wisniewski, M. G., Joyner, C. N., Zakrzewski, A. C., & Makeig, S. (2024). Finding tau rhythms in EEG: An independent component analysis approach. *Human Brain Mapping*, *45*(2), e26572. https://doi.org/10.1002/hbm.26572

Yamawaki, N., Stanford, I. M., Hall, S. D., & Woodhall, G. L. (2008). Pharmacologically induced and stimulus evoked rhythmic neuronal oscillatory activity in the primary

motor cortex in vitro. *Neuroscience*, *151*(2), 386–395. https://doi.org/10.1016/j.neuroscience.2007.10.021

Zelig, D., Goldberg, I., Shor, O., Ben Dor, S., Yaniv-Rosenfeld, A., Milikovsky, D. Z., Ofer, J., Imtiaz, H., Friedman, A., & Benninger, F. (2022). Paroxysmal slow wave events predict epilepsy following a first seizure. *Epilepsia*, *63*(1), 190–198. https://doi.org/10.1111/epi.17110

Appendices

Appendix A: Chapter 2 Supplementary Material

DICS Beamformer Analysis Figures

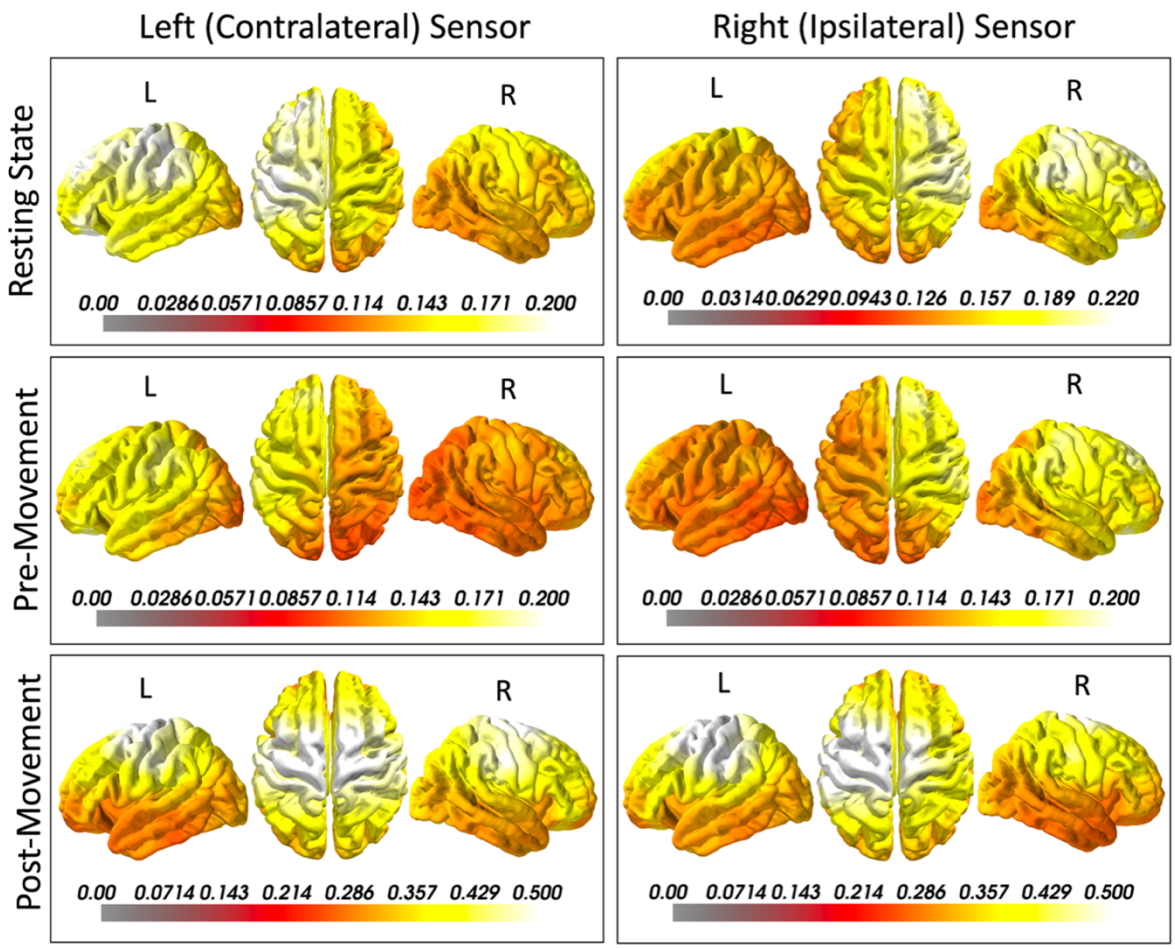

Figure A.1 Average source estimation patterns for 561 healthy participants as estimated by the DICS beamformer source estimation method. Source estimation patterns are shown during resting state (top) pre-movement (middle), and post-movement (bottom) conditions, for bursts detected at left (contralateral) and right (ipsilateral) sensors. The left, dorsal and right views of the 3-dimensional head model are shown for each condition. The colour bar values represent the relative power between the active and baseline intervals as calculated in equation 2.1. Note that the scales are different for each condition to reflect the full range of relative power values for each condition.

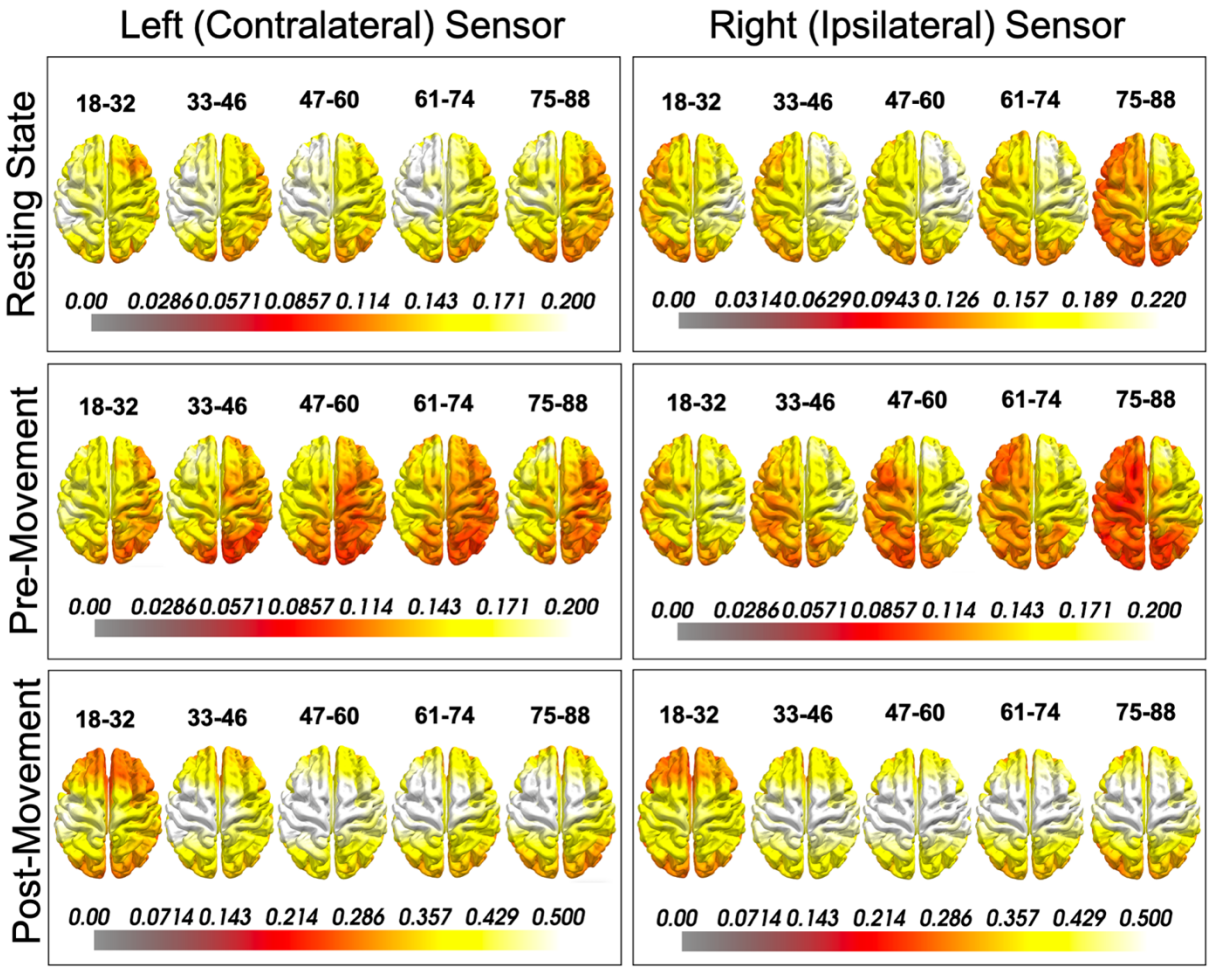

Figure A.2 Average source estimation patterns as estimated by the DICS beamformer estimation method for 5, 14-year spanning age groups of healthy participants during resting state (top), pre-movement (middle) and post-movement (bottom) conditions, for bursts detected at left (contralateral) and right (ipsilateral) sensors. Dorsal views are shown for each age group, condition, and sensor. The colour bar values represent the relative power between the active and baseline intervals as calculated in equation 2.1. Note that the scales are different between conditions in order to maximize the contrast but are kept consistent across age groups within the same condition to allow for direct comparison between ages.

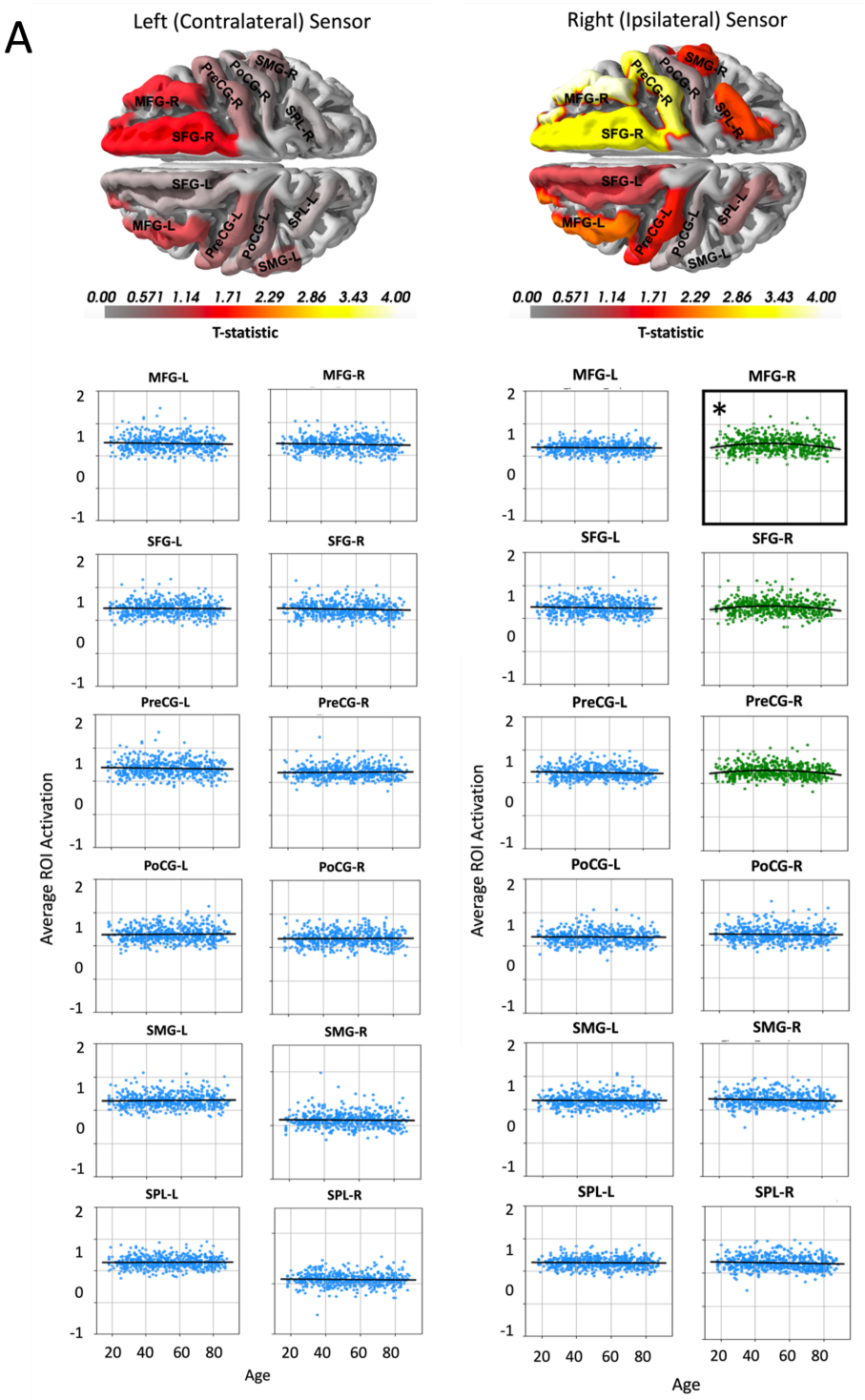
A
Left (Contralateral) Sensor
Right (Ipsilateral) Sensor
SMG-R
PreCG-R
PoCG-R
MFG-R
SPL-R
SFG-R
SFG-L
SPL-L
MFG-L
PreCG-L
PoCG-L
SMG-L
0.00 0.571 1.14 1.71 2.29 2.86 3.43 4.00
T-statistic
MFG-L
MFG-R
SFG-L
SFG-R
PreCG-L
PreCG-R
PoCG-L
PoCG-R
SMG-L
SMG-R
SPL-L
SPL-R
*
Average ROI Activation
2
1
0
-1
20 40 60 80
Age

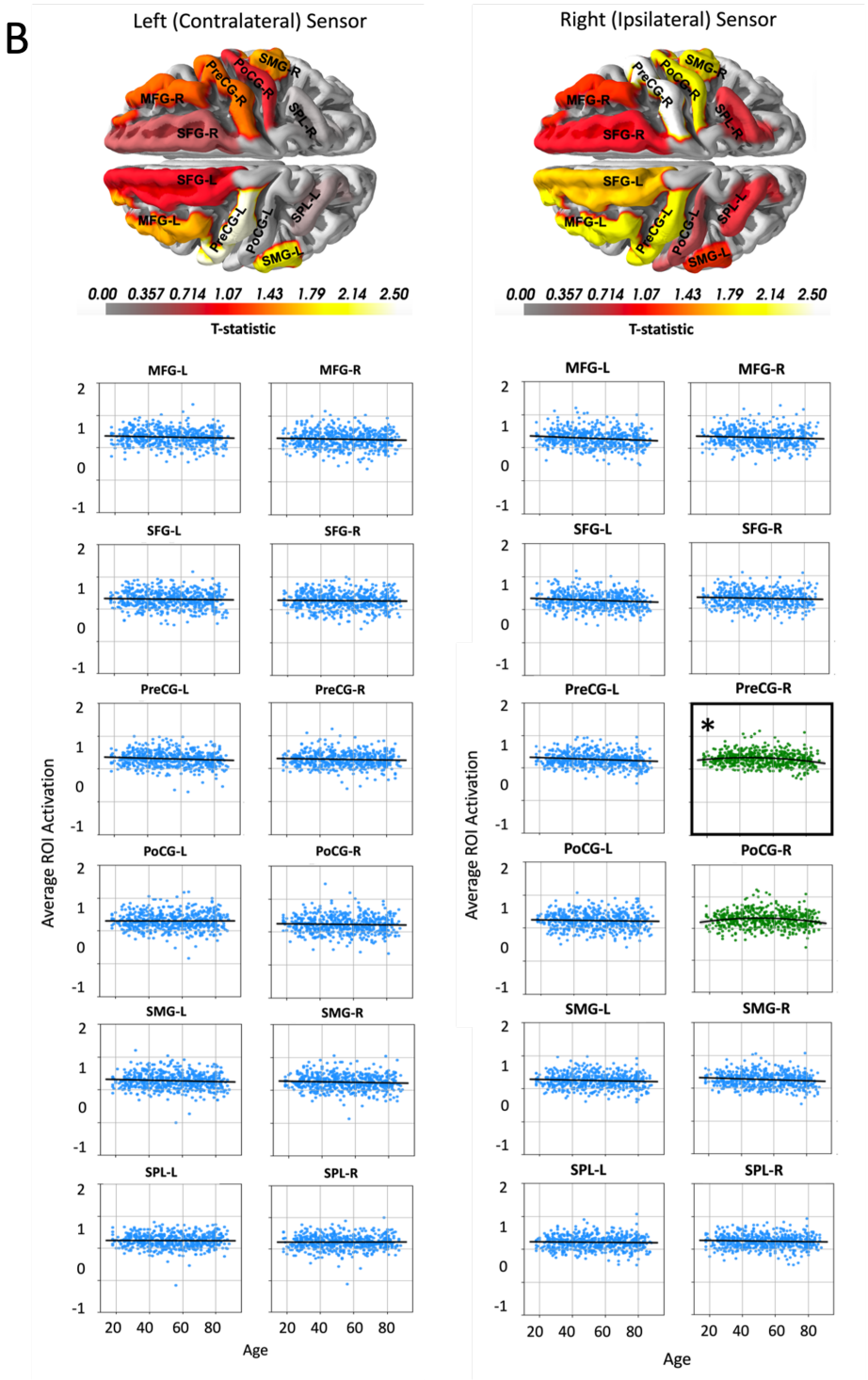
B
Left (Contralateral) Sensor
Right (Ipsilateral) Sensor
MFG-R
SFG-R
PreCG-R
PoCG-R
SMG-R
SPL-R
SFG-L
MFG-L
PreCG-L
PoCG-L
SMG-L
SPL-L
0.00 0.357 0.714 1.07 1.43 1.79 2.14 2.50
T-statistic
Average ROI Activation
Age
*

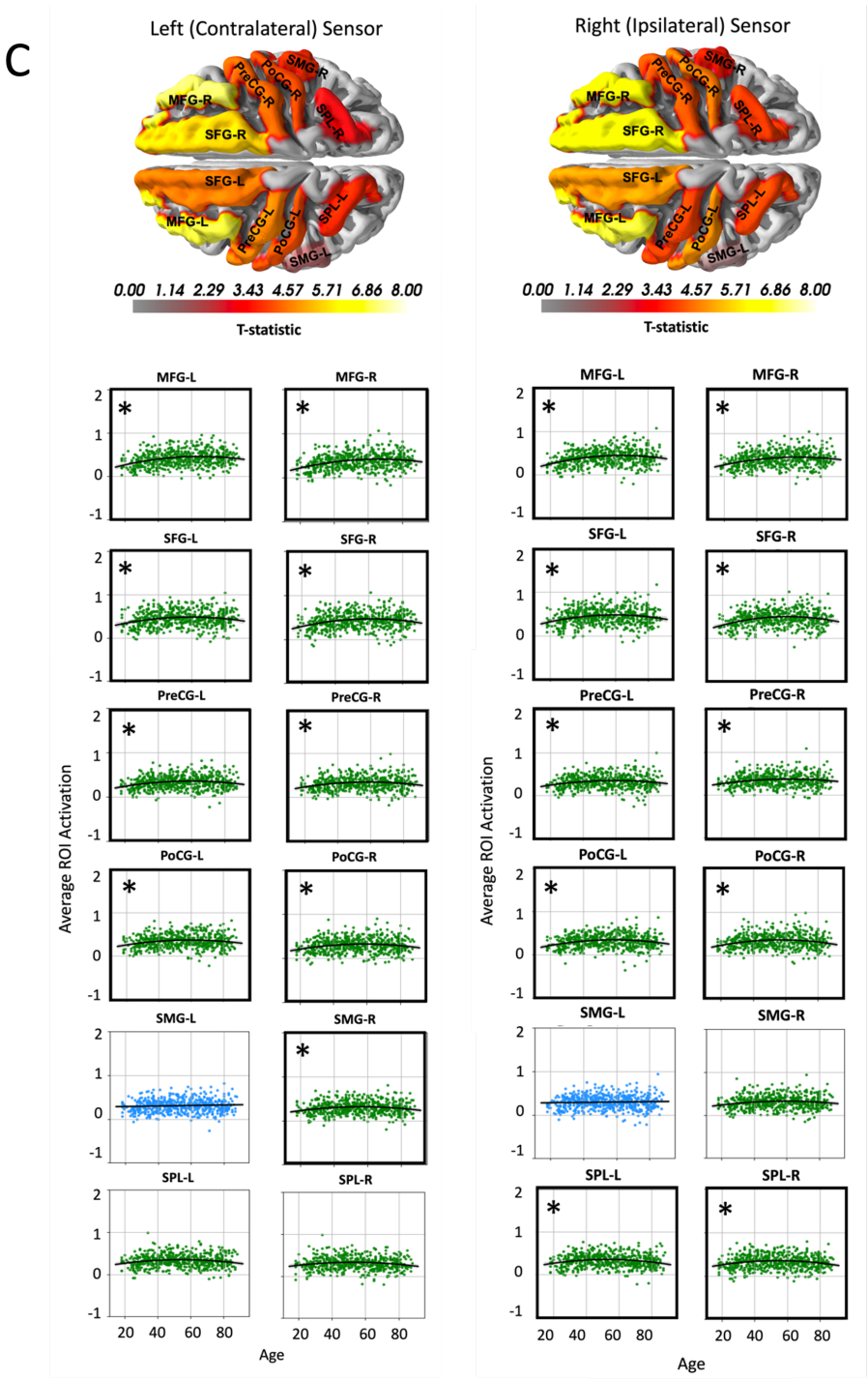

Figure A.3 The best-fit regression models for each of 12 anatomical regions of interest. The average beta burst power values detected by the DICS beamformer source estimation method for each region of interest are plotted against age along with the best-fit regression model (linear: blue; quadratic: green). The t-statistics associated with the chosen models are plotted using a colour bar on the dorsal view of the 3-dimensional head model. Data is shown from 561 healthy participants during (A) resting state, (B) pre-movement, and (C) post-movement from the left and right sensors.

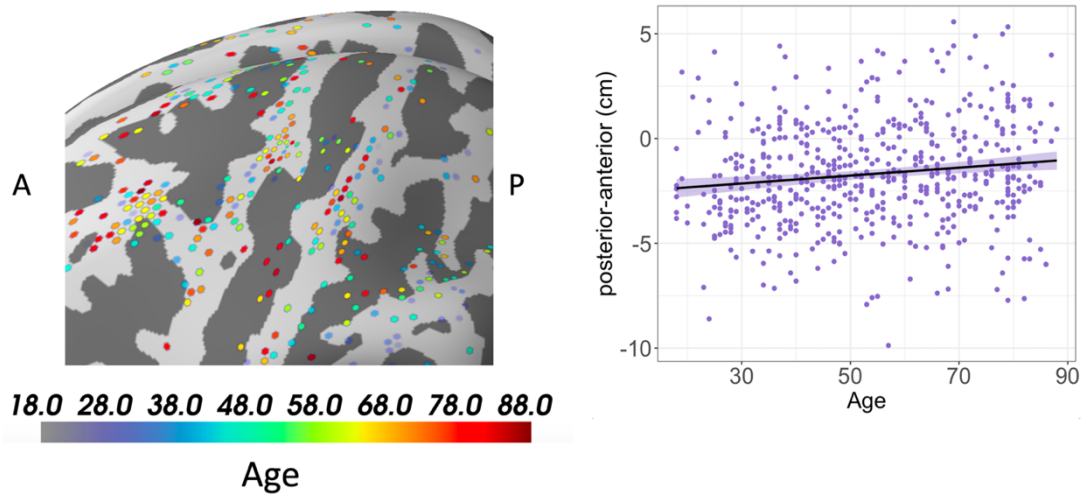

Figure A.4 Significant trends in peak location with age. Peak location of transient beta bursts detected by the DICS beamformer method at the left (contralateral) sensor during the post-movement condition. Points on the 3-dimensional average brain model (left) show the peak location for each participant, with colour representing the age of the participant. Pictured here is a section of the left central brain region, enlarged to show the shift in peak position in this region. “A” and “P” labels indicate the anterior and posterior ends of the section. Non-significant conditions are not shown in this figure.

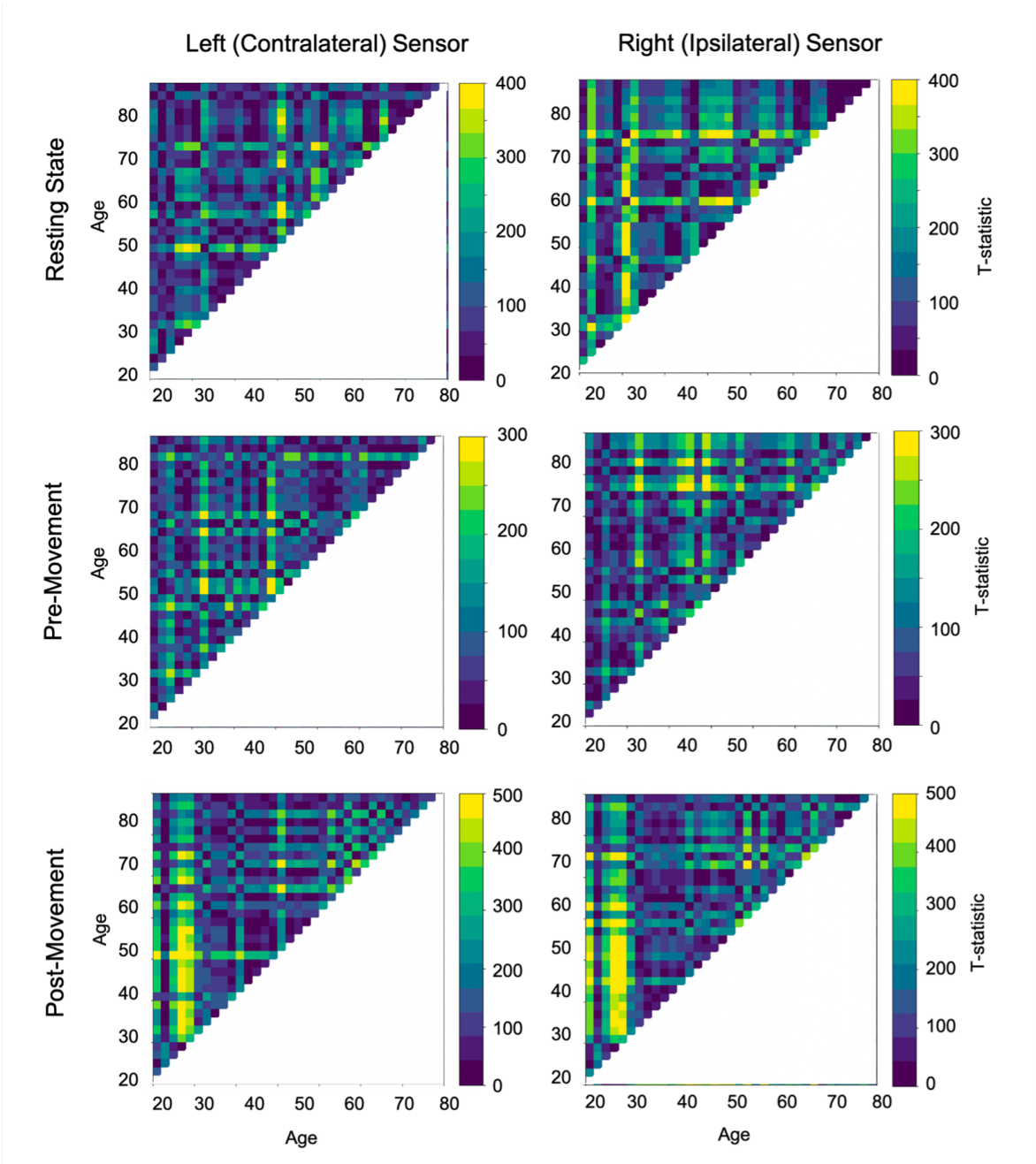

Figure A.5 T-statistics computed by conducting paired samples t-tests between the average source power maps of all 2-year age groups for bursts detected by the left (contralateral) and right (ipsilateral) sensors. The colour bar represents the t-statistic with purple representing low values (similar maps) and yellow representing high values (dissimilar maps). Note the differences in scale between conditions. Data is shown for resting state (top), pre-movement (middle) and post-movement (bottom) conditions.

Supplementary MNE Figures

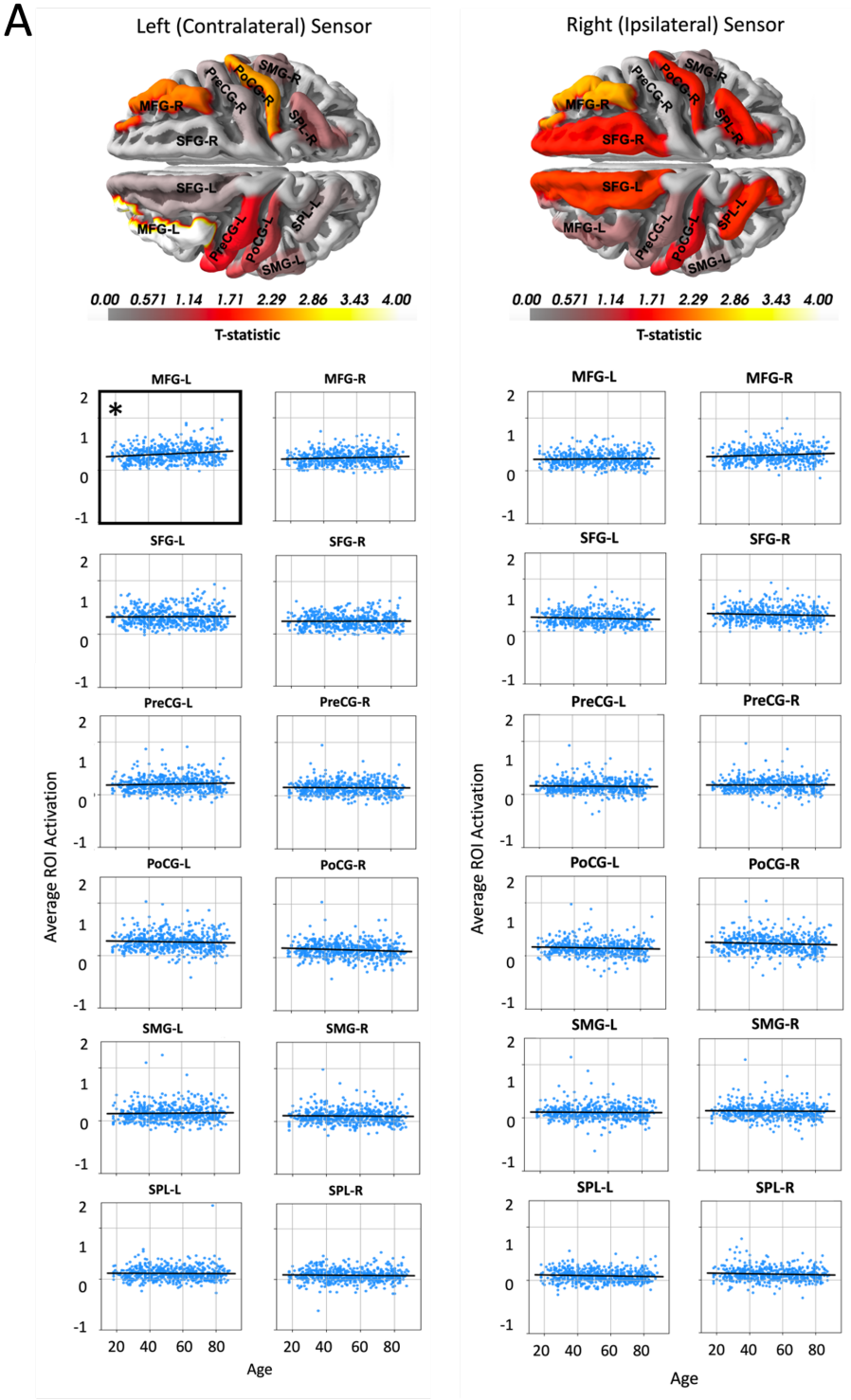

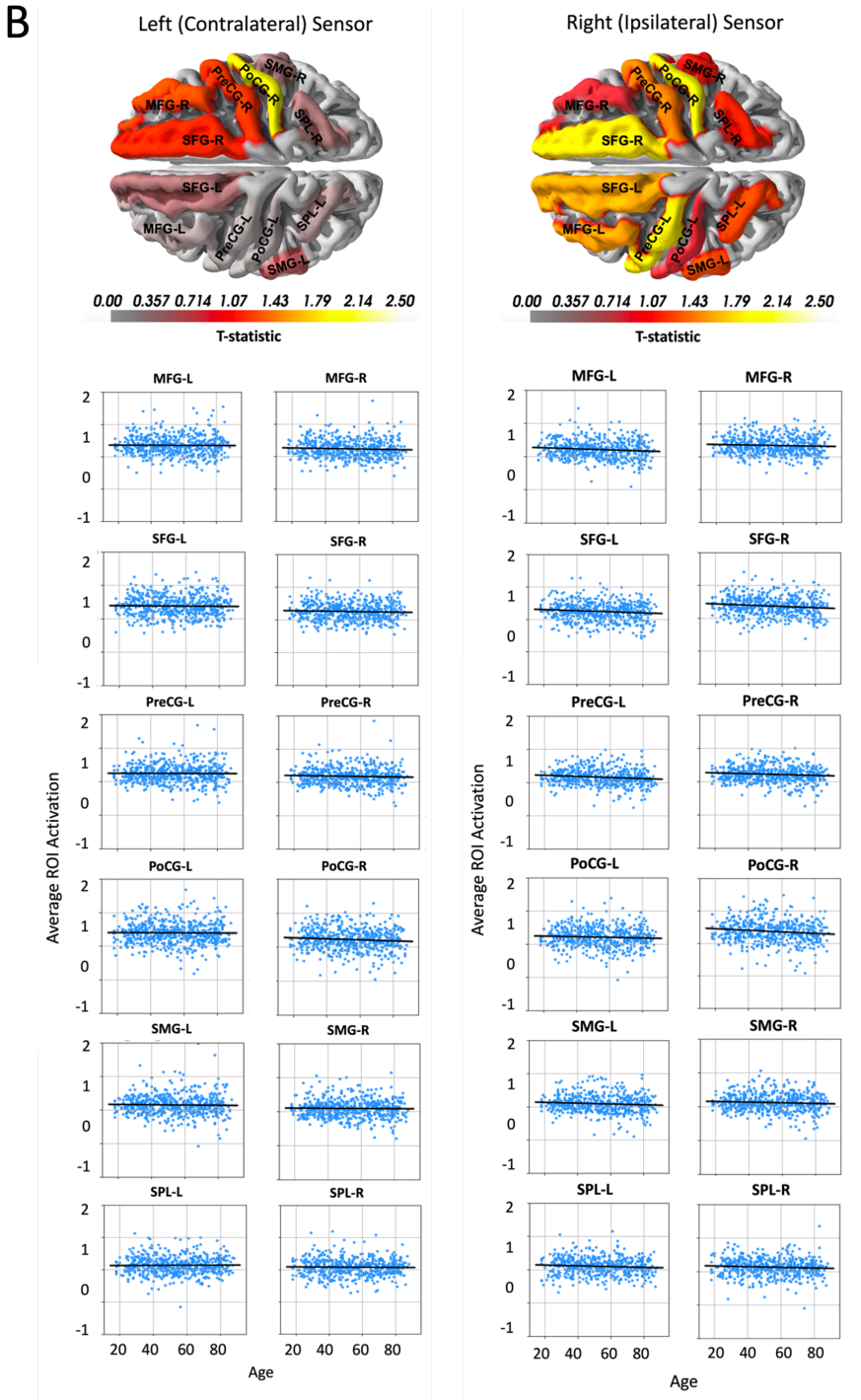

Figure A.6 The best-fit regression models for each of 12 anatomical regions of interest. The average beta burst power values detected by the MNE source estimation method for each region of interest are plotted against age along with the best-fit regression model (linear: blue; quadratic: green). The t-statistics associated with the chosen models are plotted using a colour bar on the dorsal view of the 3-dimensional head model. Data is shown from 561 healthy participants during (A) resting state and (B) pre-movement from the left and right sensors.

Appendix B: Chapter 3 Supplementary Material

Supplementary Equations

Multivariate CSC (Grosse et al., 2007) consists of solving the following optimization problem:

Equation B.1
$$\min_{D_k, z_k^n} \sum_{n=1}^{N} \frac{1}{2} \left\| X^n - \sum_{k=1}^{K} z_k^n * D_k \right\|_2^2 + \lambda \sum_{k=1}^{K} \|z_k^n\|_1,$$
$$s.t. \|D_k\|_2^2 \leq 1 \; and \; z_k^n \geq 0$$

Where:

$\{X^n\}_{n=1}^N \subset \mathbb{R}^{P \times T}$ are the observed signals,

$\{D_k\}_{k=1}^K \subset \mathbb{R}^{P \times L}$ are the spatiotemporal atoms,

$\{z_k^n\}_{k=1}^K \subset \mathbb{R}^{\tilde{T}}$ are the sparse activation vectors associated with $X^n, \tilde{T} = T - L + 1$,

$\lambda > 0$ is the regularization parameter

Multivariate CSC with rank-1 constraint (Dupré la Tour et al., 2018) consists of minimizing the following objective function, where here the atoms are formed by the outer product between a topography u_k and the temporal waveform v_k,
i.e., $D_k = u_k v_k{}^\intercal \in \mathbb{R}^{P \times L}$

Equation B.2
$$\min_{u_k, v_k, z_k^n} \sum_{n=1}^{N} \frac{1}{2} \left\| X^n - \sum_{k=1}^{K} z_k^n * (u_k v_k{}^\intercal) \right\|_2^2 + \lambda \sum_{k=1}^{K} \|z_k^n\|_1,$$
$$s.t. \|u_k\|_2^2 \leq 1, \|v_k\|_2^2 \leq 1 \; and \; z_k^n \geq 0$$

Where $u_k \in \mathbb{R}^P$ is the pattern over channels (sensors) and $v_k \in \mathbb{R}^L$ is the pattern over time.

Supplementary Tables

Table B.1

Summary table of subjects excluded as they do not show enough variety in their extracted atoms as described in Section 3.4.3.

Subject ID	Age	Sex	Number of Clusters
CC110037	18	Male	12
CC110182	18	Female	12
CC121397	27	Male	10
CC121428	26	Female	8
CC220506	35	Female	8
CC220610	32	Female	10
CC221209	29	Female	12
CC320850	47	Female	11
CC322186	47	Male	12
CC410325	54	Female	11
CC420061	57	Male	10
CC420167	51	Female	9
CC420261	54	Female	9
CC420348	57	Female	7
CC420396	53	Male	9
CC510043	58	Male	12
CC520517	65	Male	12
CC521040	63	Female	11
CC610052	77	Male	9
CC610292	72	Female	12
CC610469	73	Female	12
CC620129	75	Male	12

Subject ID	Age	Sex	Number of Clusters
CC620490	74	Female	8
CC621642	73	Male	11
CC720497	80	Female	12

Table B.2

Summary of the attributes of each cluster.

Cluster	Number of Atoms	Number of Participants	Peak Frequency (Hz)	ECD Position (mm)	ECD Orientation Unit Vector
LO_alpha	366	210	10.5	(0.52,-2.7,6.6)	(0.23,0.67,0.71)
RO_alpha	311	183	10.0	(-0.017,-3.1,6.6)	(-0.26,0.60,0.76)
MOP_alpha	324	171	9.4	(0.19,-1.9,8.0)	(0.00011,0.81,0.58)
RC_mu	305	194	10.5	(4.1,2.1,8.3)	(-0.40,0.90,0.18)
LT_alpha	230	168	9.4	(-4.0,-0.51,4.2)	(-0.065,0.50,0.86)
LPreC_beta	243	146	17.6	(-3.0,0.20,8.7)	(0.30,0.95,-0.072)
LPostC_beta	219	144	16.4	(-3.5,0.26,7.7)	(0.34,0.82,0.47)

Supplementary Figures

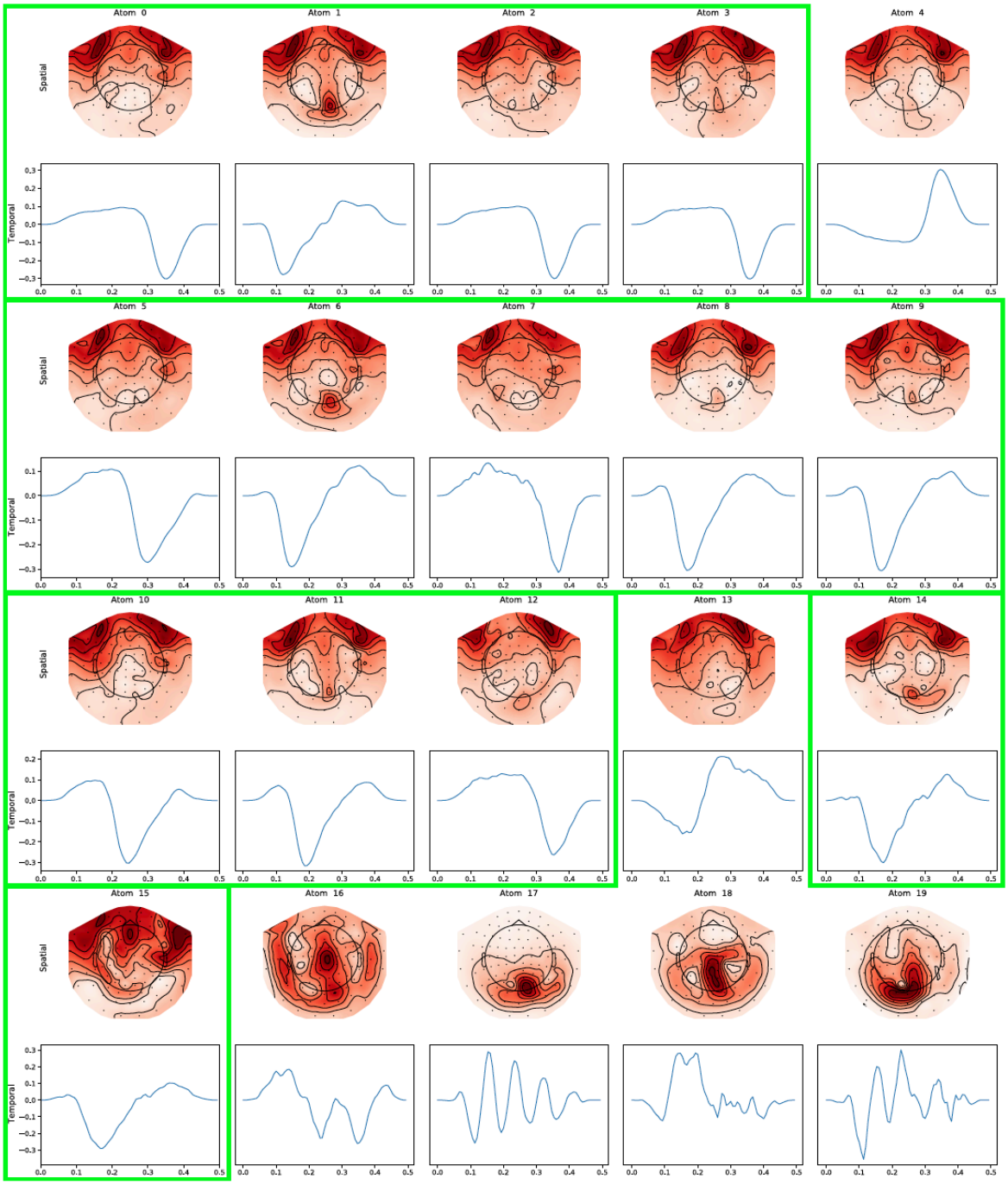

Figure B.1 Spatial and temporal representation of the 20 atoms extracted from the subject CC121428, that obtained 7 clusters. Framed atoms are part of a single intra-subject cluster. One can observe the low variability in the atoms obtained from the CDL step, showing the prevalence of artifacts in the recording.

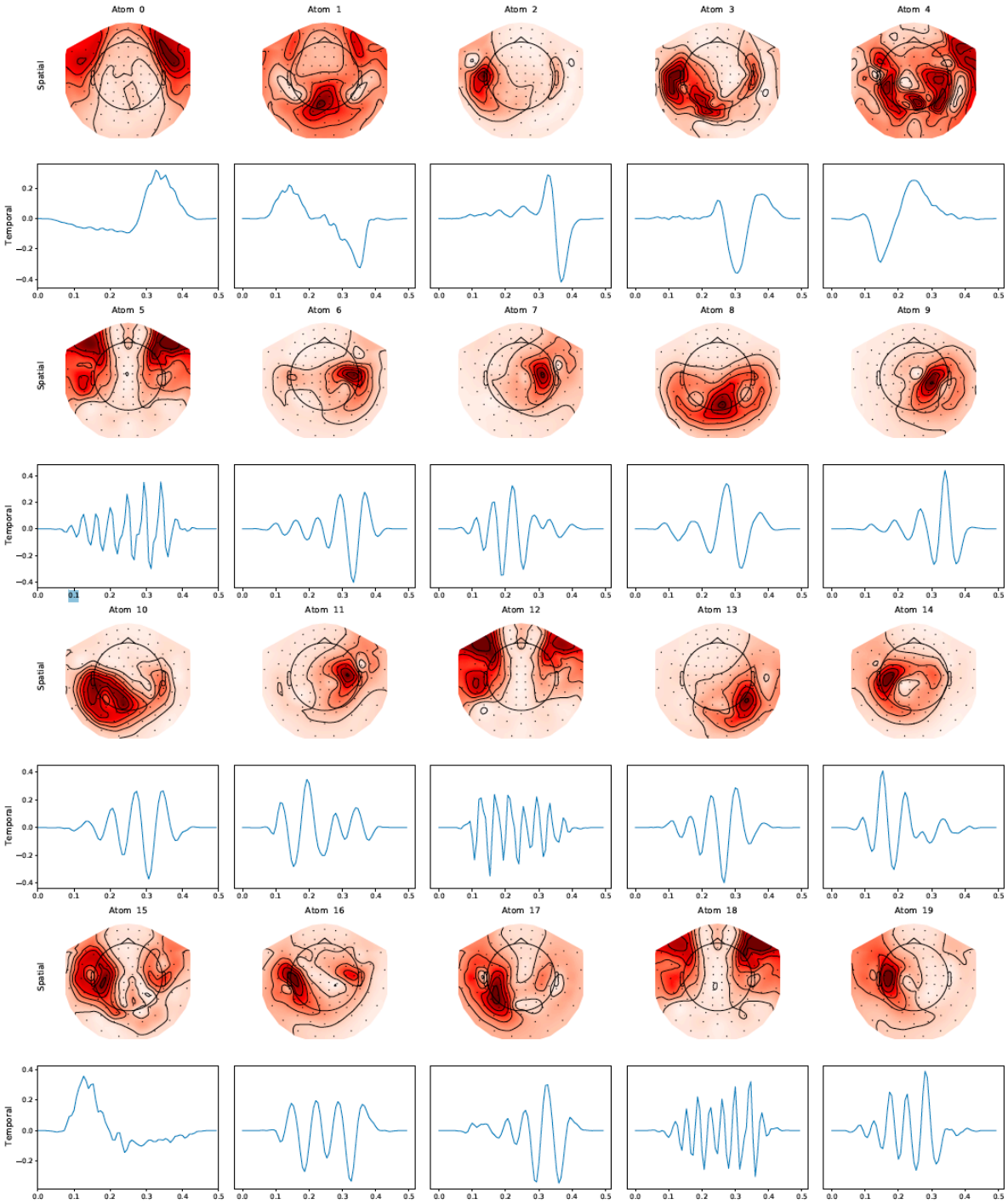

Figure B.2 Spatial and temporal representation of the 20 atoms extracted from the subject CC723395, that obtained 20 clusters. One can observe the high variability in the atoms.

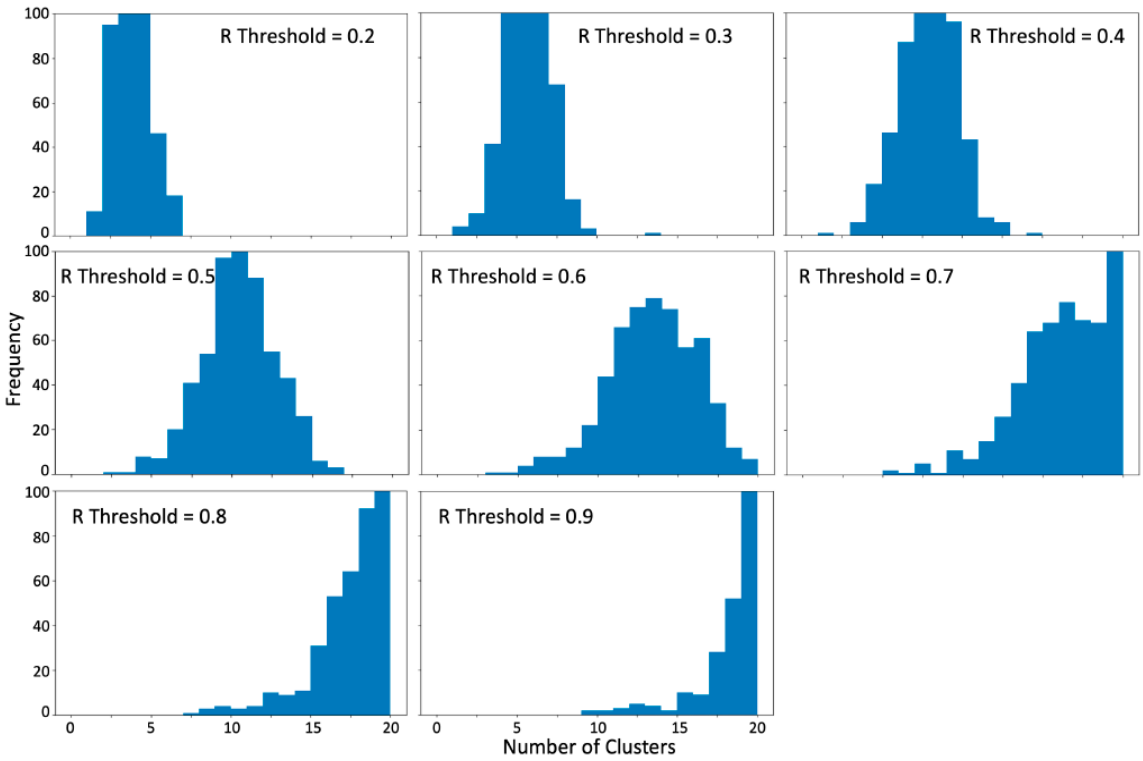

Figure B.3 Histograms showing the distribution of the number of groups per participant as the correlation coefficient is increased for the single subject clustering methods. Thresholds of 0.2 to 0.5 show approximately normal distributions with a single mode that shifts to a higher number of clusters as the threshold increases. Thresholds of 0.6 and above begin to show a left-skewed distribution. Thresholds of 0.8 and 0.9 show abnormal behaviour in the tail of the distribution such that a second small peak emerges that likely represents those participants with abnormal data that should be excluded.

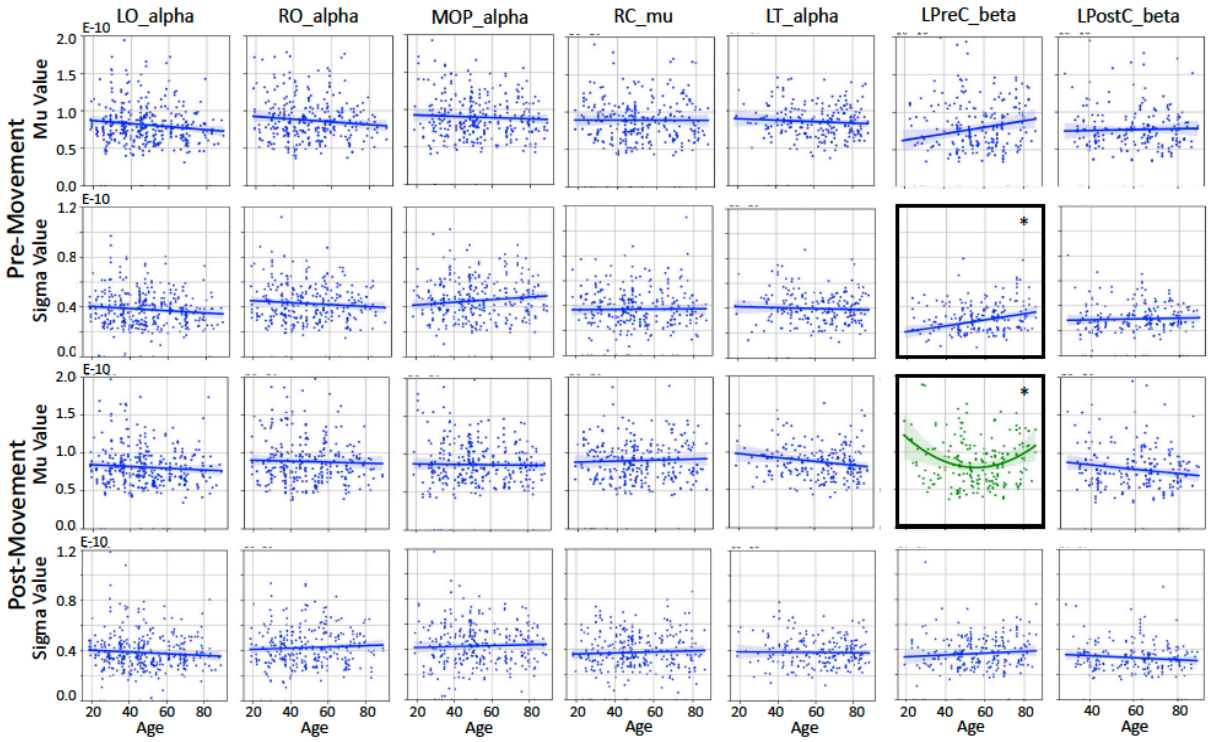

Figure B.4 The mean value (mu) and the standard deviation (sigma) of the distribution of activation values for each atom as a function of age for the pre-movement interval (top) and the post-movement interval (bottom). Mu and Sigma values were regressed against age. Blue plots represent those that were modelled by a linear fit and green plots were modelled by a quadratic fit. Asterisks indicate clusters and intervals for which the best fit regression was significant (Bonferroni corrected alpha < 0.007).

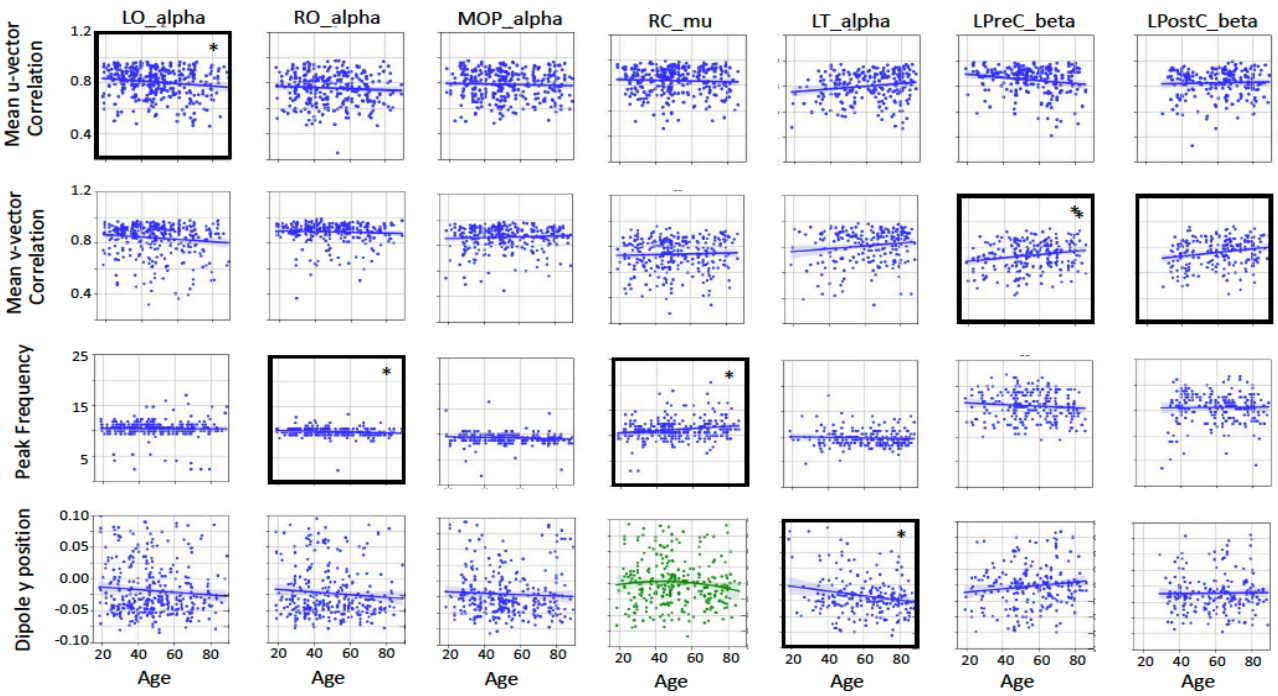

Figure B.5 Results of linear and quadratic regression of several burst characteristics with age. Blue plots represent those that were modelled by a linear fit and green plots were modelled by a quadratic fit. Asterisks indicate clusters and intervals for which the best fit regression was significant (Bonferroni corrected alpha < 0.007).

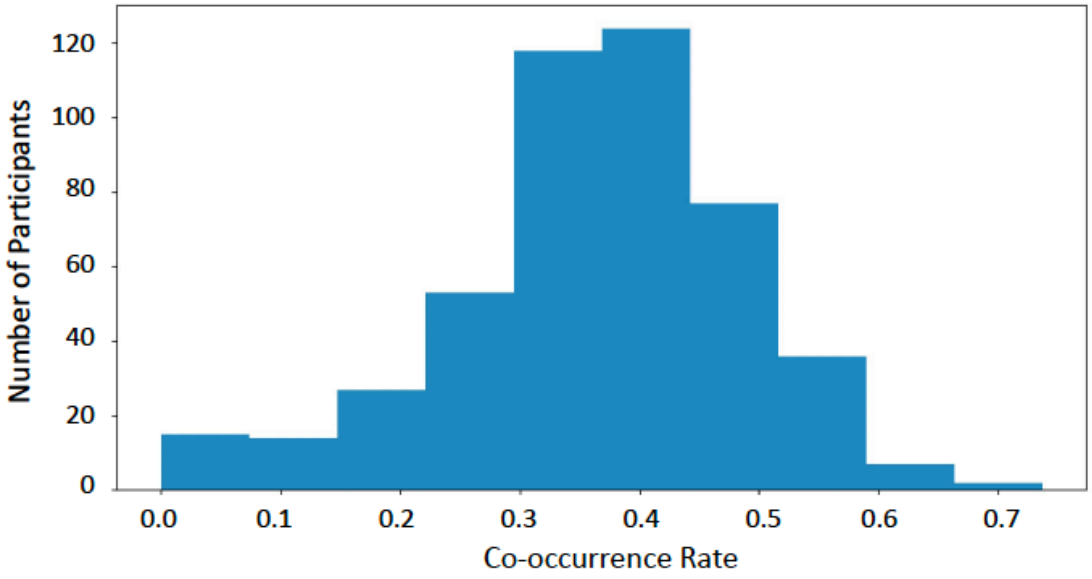

Figure B.6 Histogram of the cooccurrence rate of task-related atoms for all participants. The median cooccurrence rate across participants was 0.37.

Supplementary Analysis

While large cluster sizes were necessary for the current work to assess cross-sectional ageing trends, other applications of CDL and the associated clustering methods may not require this. An alternative method for presenting CDL cluster results is thus described below. This approach may be preferred for smaller datasets or in cases where you wish to appreciate more of the variability between atom clusters.

Following global clustering as described in Section 3.4.3, all detected clusters underwent task-based filtering as described in Section 3.4.4 resulting in a total of 79 task-related clusters. In this case no top cluster criteria was imposed to dictate a minimum cluster size. A representative atom was then generated for each of the 79 task-related clusters using the procedure described in Section 3.4.5 The representative atoms for each of the task-related clusters then underwent an additional round of clustering, using the methods described in Section 3.4.3 to roughly group clusters into sets based on similarity. This resulted in several sets of clusters each associated with a different class of brain activity (e.g., "left central beta", "occipital alpha", etc.) We could then select sets of interest and analyse all clusters within those sets to appreciate additional inter-subject variability in the atoms. The results from 3 sets identified by this method (right-central beta, left-central beta, and occipito-temporal alpha) are shown in Figure B.7.

Here, the frequency, activation strength, and age distribution of each cluster can be compared within a set. The age distribution in the Cam-CAN dataset is approximately flat, therefore investigating deviations from the flat age distribution provides meaningful information about age dynamics within clusters. This type of analysis allows for between-cluster comparison and can provide insight into the characteristics of participants who tend to have certain variations of atoms.

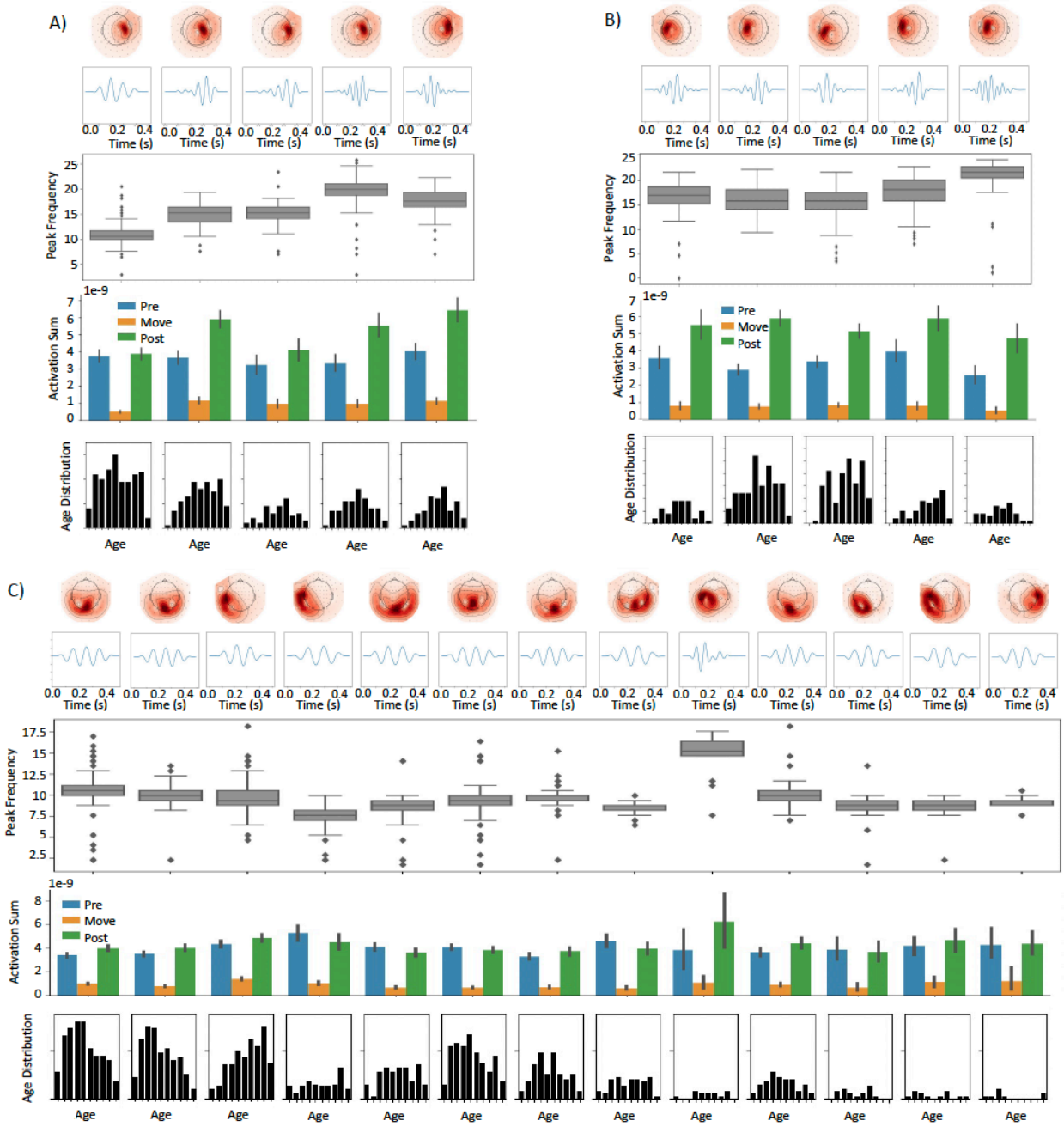

Figure B.7 Cluster sets identified resembling (A) right central beta, (B) left central beta, and (C) occipito-temporal alpha activity. For each set, representative atoms (spatial topographies and temporal waveforms) are shown for each cluster within the set. Box plots show the distribution of frequencies of the atoms composing each cluster. Bar plots show the summed activation in the pre-movement (blue), movement (orange), and post-movement (green) phases for each cluster. Finally, to facilitate demographic comparisons, the age distribution of each cluster is shown.

Appendix C: Chapter 4 Supplementary Material

Supplementary Figures

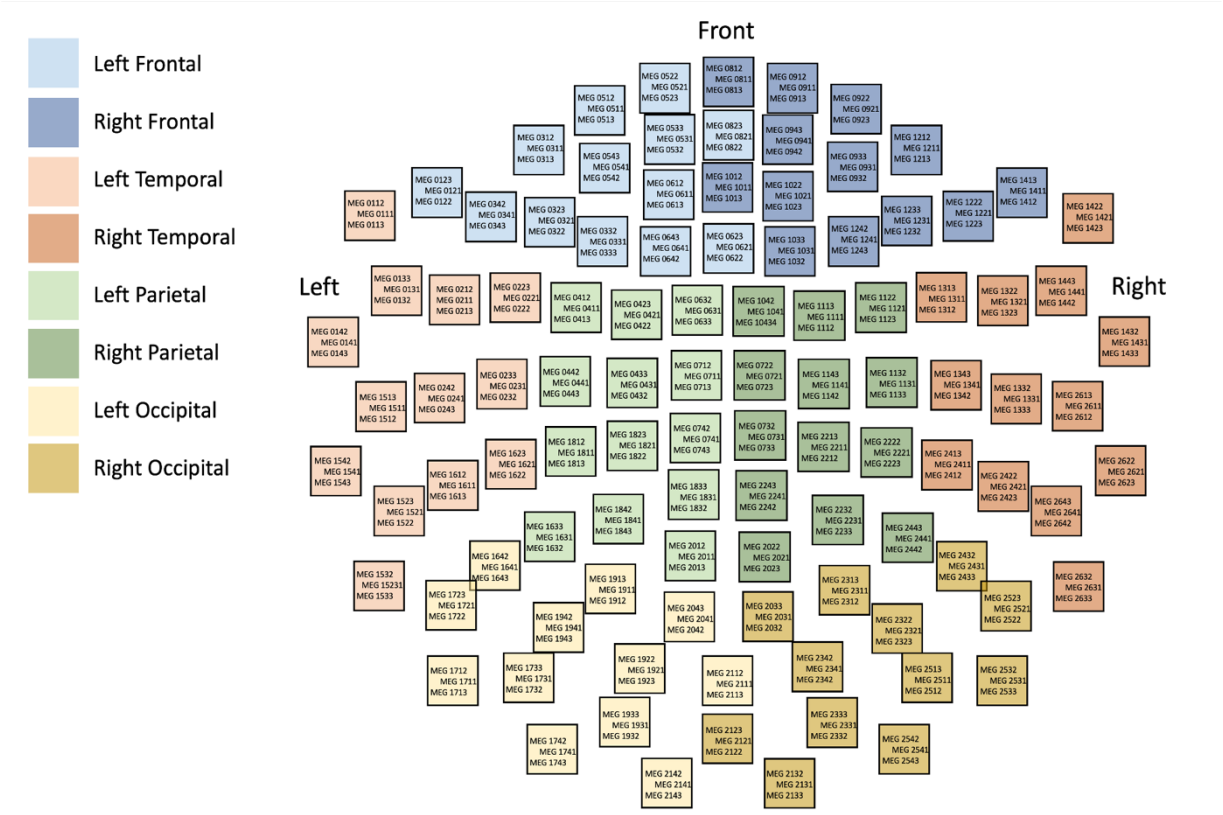

Figure C.1 The MEG channels included in each of the 8 spatial regions. Note that frontal, temporal, and parietal regions include 13 sets of channels (1 magnetometer and 2 gradiometers), while the occipital regions include 12 sets of channels.

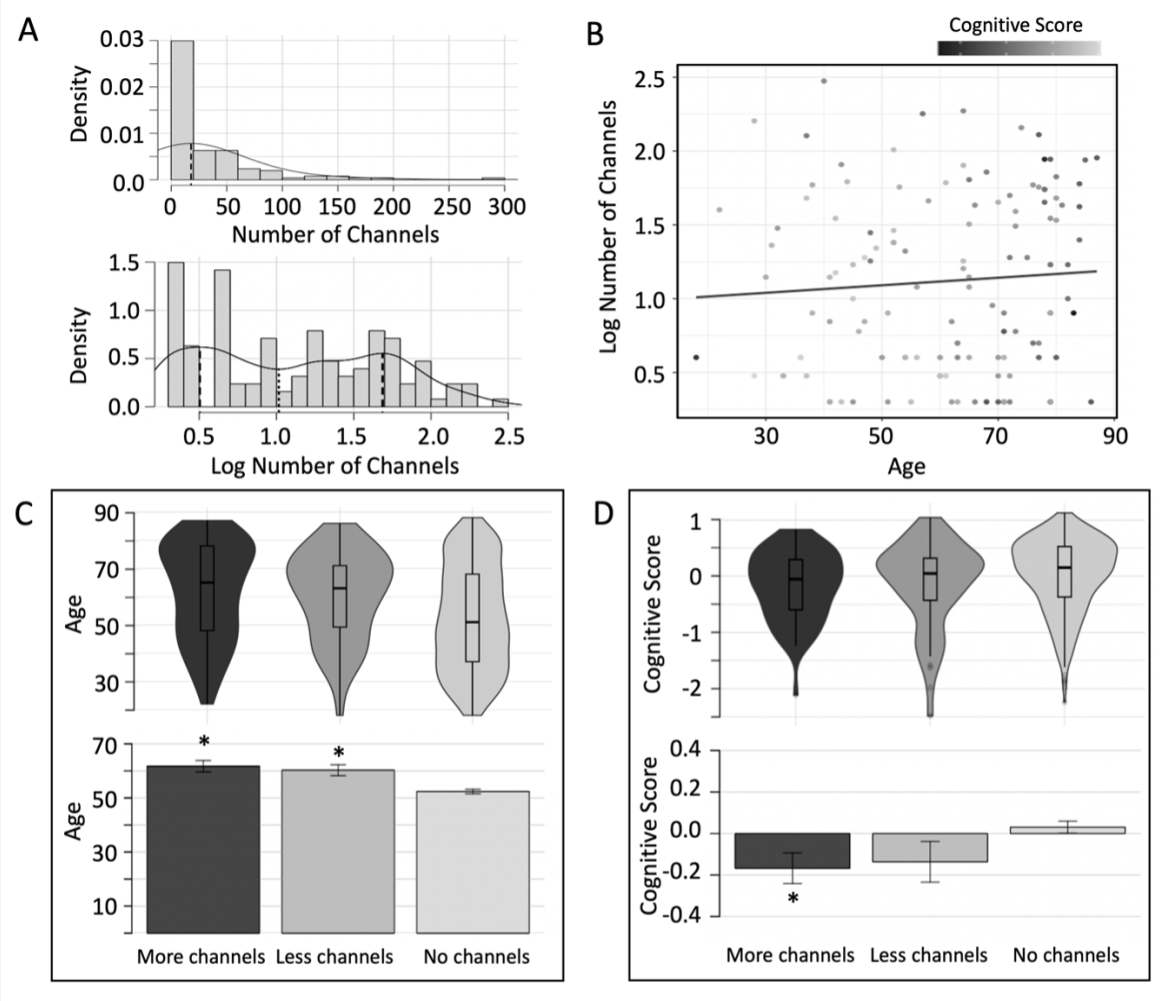

Figure C.2 The relationship between PSWE spread and participant age and aggregate cognitive score. (A) The distribution of number of channels before and after applying a log transform to the data. The histogram shows the actual values, and the black line shows a best fit curve. Dashed lines indicate the locations of modes and local minima for each distribution. (B) Results of a multiple linear regression relating age and cognitive performance to the log-transformed number of channels values. Each point represents a single person, and the greyscale color of the point indicates their cognitive score. The solid black line is the best fit regression for this data. (C) Ages of participants with no channels (light grey), less channels (medium grey), and more channels (dark grey). Violin plots (top) show age distribution and bar plots (bottom) show mean and standard error (error bars) of participant age for each group. (D) Cognitive scores for participants in each PSWE spread group. Asterisks indicate a significant effect.

Supplementary Analysis

To contextualize the PSWE findings in relation to traditional metrics, model comparisons between linear models of 1-6 Hz average power, 1-6 Hz root mean square (RMS), and time in events with age were conducted. Linear models were constructed using the entire CamCAN cohort (N=623). Average power and RMS were calculated and analysed separately for magnetometers and gradiometers.

This analysis revealed that time in PSWEs explained the most variance in age (see Figure C.3, Table C.1). This finding suggests that the time in PSWEs metric is more sensitive to age-related effects than other traditional metrics, and thus provides novel and valuable information about age-related brain activity.

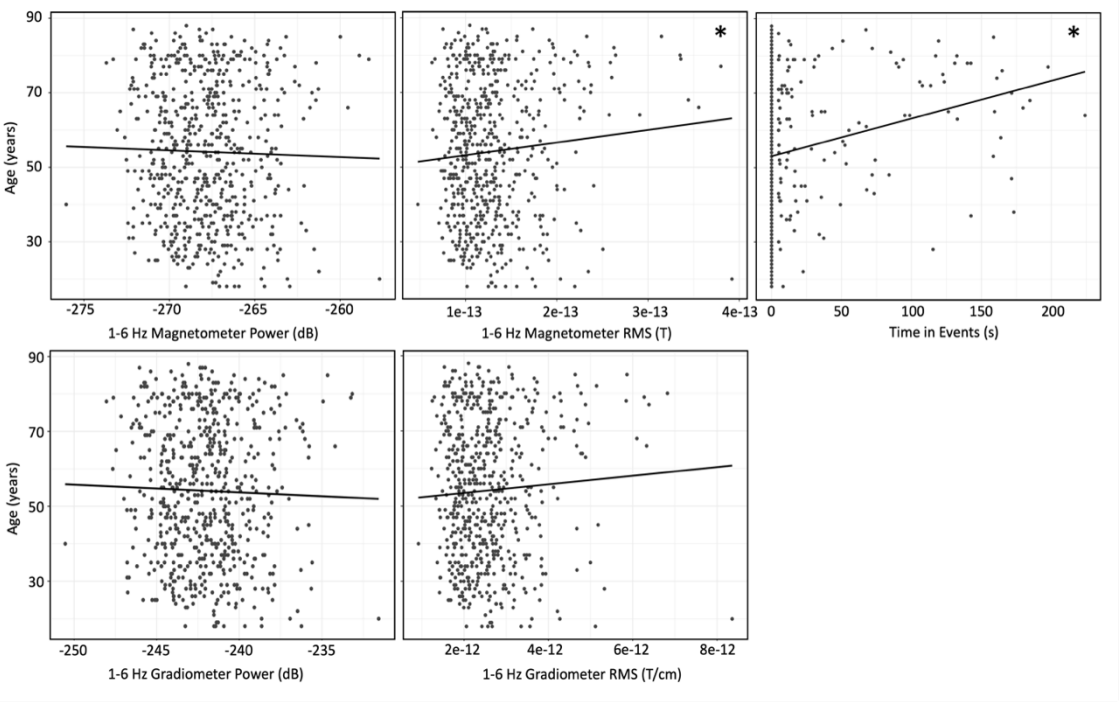

Figure C.3 Linear regression plots showing the relationship between 1-6 Hz magnetometer and gradiometer power, 1-6 Hz magnetometer and gradiometer root mean squares (RMS), and time in PSWEs. Significant effects are indicated by an asterisk. All Cam-CAN participants (N=623) are included in this analysis.

Table C.1

Model comparison between linear models of power, RMS, and time in PSWEs with age for all Cam-CAN participants.

Model	R	F-statistic	P-value	AIC
Grad Power x Age	-0.0282	0.505	0.478	5406.49
Mag Power x Age	-0.0316	0.374	0.541	5406.62
Grad RMS x Age	0.0375	1.88	0.171	5405.11
Mag RMS x Age	0.0731	4.34	0.0377*	5402.65
Time in PSWEs x Age	0.180	21.8	**3.69e-6***	**5385.49**

PSWEs were localized using the methods for transient event source localization described in Power et al., (2021). Briefly, a source estimate was computed in the 1-6 Hz frequency band using minimum norm estimation. Then, for each PSWE, source power during the first 5 seconds of the event was compared to a 5 second baseline interval preceding the event using the formula: log2(active/baseline). A 20484-vertex map was created for each participant with detectable PSWEs using the participant's T1-weighted MRI from the Cam-CAN dataset. To create summary maps across participants, the number of participants who had voxel activation surpassing the 75th percentile was counted at each voxel.

Although source estimation was attempted, these results were not included in the main body due to lack of confidence in the reliability of these findings. The source estimation resulted in high activity primarily in ventral regions of the cortex. MEG source estimation generally has low accuracy for the ventral and/or deep sources and therefore we were not confident in the accuracy of these activation maps. This, combined with our sensor-level spatial findings that suggested that PSWEs could be simultaneously recorded from distant sensors, caused us to question the validity of these source localization results. As such, these results should be interpreted with caution.

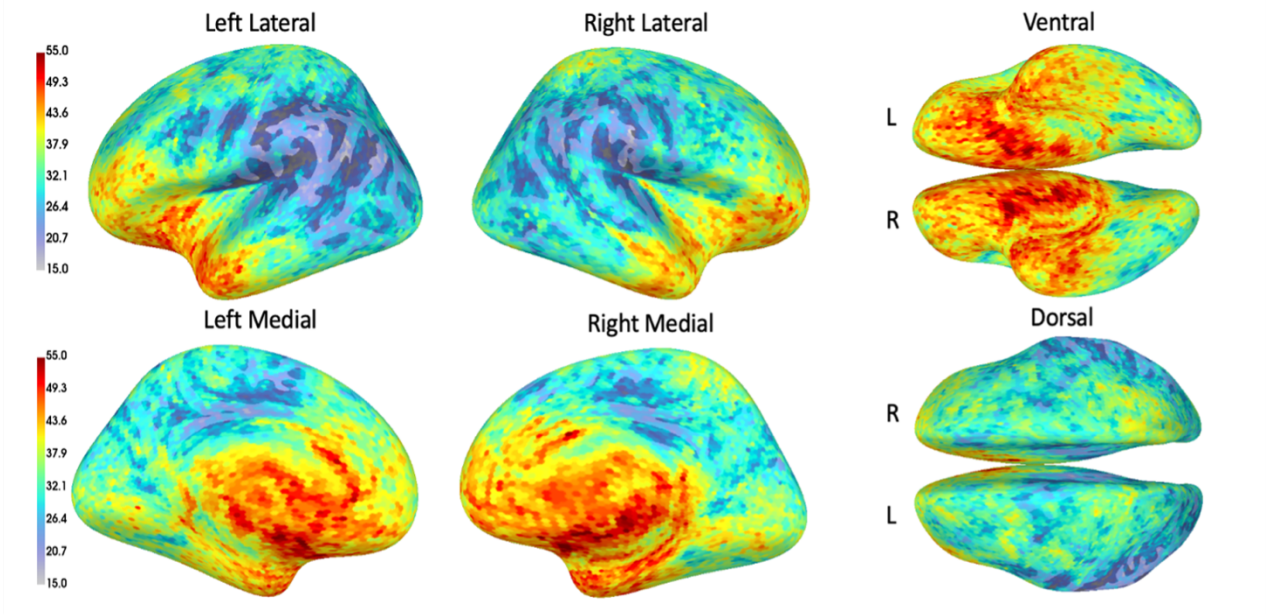

Figure C.4 Conjunction maps of PSWE source activity for 127 participants with PSWEs. Colour represents the count of participants with high (>75th percentile) activation.

Appendix D: Copyright Statement

Chapters 2, 3, and 4, as well as Figure 1.3 are reproduced from previously published content. All of these works were published *open access* in *Elsevier* journals. Based on Elsevier's copyright policy, as an author of these articles, I have the right to include them in my thesis. Letters of copyright permission are not required. Information regarding Elsevier's copyright policies for authors is available at: https://www.elsevier.com/about/policies-and-standards/copyright#1-author-rights